



The
University
Of
Sheffield.

Structure – property relationship in spinel and rock salt

Li-Mn-Mg-O phases

By:

Wan Fareen Shazli Bin Wan Sulong

A thesis submitted in partial fulfilment of the requirements for the degree of
Doctor of Philosophy

Supervisor: Professor Anthony R. West

The University of Sheffield
Faculty of Engineering
Department of Materials Science and Engineering

April 2019

Declaration

This thesis is submitted in consideration for the award of Doctor of Philosophy. It is believed to be completely original, except where references have been made.

Wan Sulong

April 2019

Acknowledgements

I would like to express my deepest gratitude to Professor Anthony R. West for his continuous support and guidance throughout my research. His patience and dedication have been tremendous help in making my Ph.D. thesis possible. I would like to thank Dr. Ron Smith for his support in neutron diffraction work in Polaris, ISIS and Professor Alan V. Chadwick for his support in XANES work in Diamond. Also, I would like to thank Dr. Nik Reeves-McLaren for sharing his expertise in crystallography.

I am also grateful to my colleagues from the Electroceramics Research Group, for their unfailing support and assistance: Mr Andrew Mould, Dr. Bo Dong, Dr. Linhao Li, Dr. Yun Dang, Dr. Xavier Vendrell, Dr. Fan Yang, Dr. Rebecca Boston, Dr. Whitney Schmidt, Dr. Ahmad Azmin Bin Mohamad and others.

I would like to express my sincere gratitude to Majlis Amanah Rakyat (MARA) of Malaysia for funding the Ph.D. research.

Last but not least, my special thanks to my family for their moral and emotional support in my life: my wife, Mrs Hasni Farlina; my children, Miss Wan Nurin Afiqah, Mr Wan Irfan Haziq, Mr Wan Irfan Hakim; my parents, Mr Wan Sulong and Mrs Fatimah; and my parents-in-law, Mr Abdul Hasim and Mrs Salbiah.

Abstract

A pseudo-binary phase diagram of $\text{MnO}_8\text{-MgO}$ has been constructed using a combination of X-ray powder diffraction data on quenched samples, high-temperature X-ray powder diffraction and differential scanning calorimetry. Study on the phase diagram was carried out with general formula $\text{Mg}_x\text{Mn}_{1-x}\text{O}_8$. Samples were prepared through solid-state synthesis and quenched in liquid nitrogen over a temperature range 600 to 1200 °C. Phase characterization revealed the formation of an extensive solid solution of Mg_6MnO_8 and the existence of two tetragonal spinel polymorphs (T1 and T2) which contradicts the reported literature.

Both tetragonal spinel polymorphs were indexed using $I4_1/amd$ space group and showed significantly different lattice parameters. High-temperature X-ray powder diffraction showed a transition of low-temperature (T1) to high-temperature cubic spinel (C1), which could not be preserved on quenching. Instead, a high-temperature polymorph (T2), which appears to be metastable, was formed during quenching. It is proposed that the rapid transition of C1 to T2 involves orientational distortion and therefore assumed that the cation distributions are the same in C1 and T2. Structural analysis on T2 confirmed the partial cation site exchange between tetrahedral and octahedral sites, which are very dependent in composition x .

Mg_6MnO_8 (C2) solid solution was observed over the entire range of $0.50 \leq x \leq 0.80$ between 900 and 1000 °C, instead of a single line-phase as reported in the literature. Below ~ 850 °C, the solid solution is unstable and decomposed into two separate cubic compositions governed by an immiscibility dome. Neutron powder diffraction confirmed the space group for C2 to be $Fm\bar{3}m$. Structural studies showed an increase in occupancy of an unoccupied tetrahedral Mn3 (32f) and a decreased occupancy of Mg1 (24d) and O2 (24e) with decreasing x . Since the Mn3 and Mg1 sites are partially occupied, the structure is regarded as highly disordered due to the possibility of cation site-exchange between these sites. As a result, it is not feasible to refine these sites since there are three occupancy variables exist in any one site: Mg, Mn and vacancy.

Impedance measurements showed that the conductivity of T2 is several orders of magnitude higher than that of T1 (at room temperature). The conductivity of T1 is independent of composition x . The conductivity of T2 increased with increasing x up to $x = 0.40$. The conductivity of C2 decreased with increasing x . The highest conductivity was observed at $x = 0.50$, $\sim 4 \times 10^{-6} \text{ S cm}^{-1}$ (at room temperature) over the entire range $0.05 \leq x \leq 0.80$. T2 and C2 showed similar activation energy, $0.42 \sim 0.44 \text{ eV}$. Based on the result of the impedance measurement, it is proposed that the partial cation site-exchange in T2 may trigger disproportionation of Mn^{3+} to Mn^{2+} and Mn^{4+} pairs at the octahedral sites. Therefore, the proposed compensation mechanism for T2 involves partial cation site exchange and disproportionation of Mn^{3+} ions.

A solid solution of Mg-doped Li_2MnO_3 was prepared by solid state reaction with two possible general formulae, $\text{Li}_{2+2m}\text{Mg}_m\text{Mn}_{1-m}\text{O}_3$ and $\text{Li}_2\text{Mg}_m\text{Mn}_{1-m}\text{O}_{3-m}$, $0 \leq m \leq 0.10$. The compensation mechanism is proposed to involve the reduction in Mn oxidation states and creation of oxygen vacancies, $\text{Li}_2\text{Mn}_{1-3z}^{4+}\text{Mn}_{2z}^{3+}\text{Mg}_z^{2+}\text{O}_{3-2z}$, with the assumption that there is no lithia loss and the Mn is initially in tetravalent state. Impedance spectroscopy analysis showed an increase in conductivity was observed for Mg-doped sample compared to the undoped Li_2MnO_3 . The presence of mixed valence Mn provide a conduction pathway for electronic hopping. Further increase in conductivity was observed on quenched Mg-doped Li_2MnO_3 ($\sim 10^{-8} \text{ S cm}^{-1}$). The electrical properties of Mg-doped Li_2MnO_3 are therefore depend on the number of mobile charge carrier, Mn^{3+} - Mn^{4+} pair. It is speculated that an increase in electrochemical behaviour is expected.

Table of Contents

Chapter 1: Literature Review	1
1.1 Introduction	1
1.2 Lithium-ion batteries	3
1.3 Cathode materials	5
1.3.1 Layered transition metal	7
1.4 Manganese oxide system	11
1.5 MgO-MnO ₈ system.....	17
1.5.1 The phase diagram.....	17
1.5.2 MgMn ₂ O ₄	20
1.5.3 Mg ₂ MnO ₄	25
1.5.4 Mg ₆ MnO ₈	26
1.5.5 MgMnO ₃	27
1.6 Aims and objectives	28
1.7 References	29
Chapter 2: Experimental techniques.....	37
2.1 Solid state synthesis.....	37
2.2 X-ray diffraction (XRD).....	37
2.3 Neutron diffraction (ND).....	40
2.4 Rietveld refinement ^[5-8]	42
2.5 X-ray Absorption Near Edge Structure (XANES) ^[9, 10]	46
2.6 Thermal analysis ^[2]	48
2.7 Impedance spectroscopy (IS) ^[12]	48
2.8 References	53
Chapter 3: Synthesis and characterisation of magnesium - doped lithium manganate, Li ₂ MnO ₃	54
3.1 Introduction	54

3.2 Experimental.....	55
3.3 Phase analysis and characterisation of slow-cooled Li_2MnO_3	58
3.3.1 Phase analysis of slow-cooled Li_2MnO_3	58
3.3.2 Impedance spectroscopy analysis on slow-cooled Li_2MnO_3	60
3.3.3 Impedance spectroscopy analysis on Li_2MnO_3 quenched from 1000 °C.....	62
3.3.4 Arrhenius plots of Li_2MnO_3	64
3.4 Phase analysis and characterisation of Mg-doped Li_2MnO_3	66
3.4.1 Synthesis and phase analysis of Mg-doped Li_2MnO_3	66
3.4.2 Impedance spectroscopy analysis on slow-cooled 10 mol % Mg-doped Li_2MnO_3	69
3.4.3 Impedance spectroscopy analysis on quenched 10 mol % Mg-doped Li_2MnO_3	73
3.5 Arrhenius plots	75
3.6 Discussion.....	77
3.7 Conclusions	79
3.8 References	80
Chapter 4: Subsolidus phase equilibria in the $\text{MnO}_\delta - \text{MgO}$ system	81
4.1 Introduction	81
4.2 Experimental.....	83
4.3 Slow-cooled samples	84
4.4 Quenched samples	89
4.4.1 Effect of temperature on composition $x = 0.20$ for $\text{Mg}_x\text{Mn}_{1-x}\text{O}_\delta$	89
4.4.2 Effect of composition on T1 phase quenched from 850 °C	94
4.4.3 Effect of temperature on composition $x = 0.40$ for $\text{Mg}_x\text{Mn}_{1-x}\text{O}_\delta$	96
4.4.4 Effect of composition on samples quenched from 1050 °C	97
4.4.5 Effect of composition on samples quenched from 1000 °C	99
4.4.6 Effect of composition on samples quenched from 900 °C	100

4.4.7 Effect of composition on samples quenched from 700 °C	105
4.5 Differential Scanning Calorimetry (DSC).....	107
4.5.1 DSC of MnO ₂	107
4.5.2 DSC of $x = 0.05, 0.10, 0.20$ and 0.30 of Mg _{x} Mn _{$1-x$} O _{δ}	111
4.5.3 DSC of T2, $x = 0.20$ of Mg _{x} Mn _{$1-x$} O _{δ}	113
4.6 High-Temperature X-ray Diffraction (HTXRD).....	114
4.6.1 HTXRD on MnO ₂	114
4.6.2 HTXRD on $x = 0.20$ and 0.30 of Mg _{x} Mn _{$1-x$} O _{δ}	117
4.7 Pseudo-binary phase diagram in the system of MnO _{δ} -MgO in air at 700 – 1100 °C.....	119
4.8 Discussion.....	122
4.9 Conclusions	127
4.10 References	129
Chapter 5: Structural analysis of tetragonal polymorphs T1 and T2.....	131
5.1 Structural refinement of Mn ₃ O ₄	131
5.2 Structural refinement of T1 tetragonal spinel polymorphs.....	135
5.2.1 T1 tetragonal spinel quenched from 500 °C ($x = 0.20$)	136
5.2.2 T1 tetragonal spinel quenched from different temperature ($x = 0.20$)	140
5.2.3 T1 tetragonal spinel quenched from 850 °C with different compositions ($x = 0.05, 0.10$ and 0.20)	142
5.3 Structural refinement of T2 tetragonal spinel polymorphs.....	147
5.3.1 T2 tetragonal spinel quenched from 1050 °C ($x = 0.20$)	147
5.3.2 T2 tetragonal spinel quenched from 1050 °C with different compositions ($x = 0.20, 0.30, 0.33, 0.36$ and 0.40)	152
5.4 XANES analysis of tetragonal spinel polymorphs	157
5.5 Conclusions	161
5.6 References	163

Chapter 6: Structural analysis of a cubic solid solution	165
6.1 Introduction	165
6.2 Neutron diffraction on a cubic solid solution	167
6.3 Structural refinement of cubic solid solutions.....	169
6.3.1 Structural refinement of $x = 0.80$ quenched from $950\text{ }^{\circ}\text{C}$	170
6.3.2 Structural refinement of $x = 0.50, 0.60, 0.67$ and 0.70 quenched from $950\text{ }^{\circ}\text{C}$	175
6.4 Conclusions	179
6.5 References	180
Chapter 7: Electrical properties of tetragonal polymorphs (T1 and T2) and C2 cubic solid solution	181
7.1 Introduction	181
7.2 Experimental.....	182
7.3 Electrical properties of tetragonal spinel polymorphs.....	183
7.3.1 Effect of composition on conductivity of slow-cooled T1 polymorph	183
7.3.2 Effect of temperature on conductivity of $x = 0.20\text{ Mg}_x\text{Mn}_{1-x}\text{O}_\delta$	188
7.3.3 Effect of composition on conductivity of T2 polymorph.....	193
7.4 Electrical properties of C2 cubic solid solution.....	198
7.4.1 Effect of temperature on conductivity of $x = 0.50\text{ Mg}_x\text{Mn}_{1-x}\text{O}_\delta$	198
7.4.2 Effect of composition on conductivity of C2 cubic solid solution.....	203
7.5 Discussion.....	208
7.6 Conclusions	213
7.7 References	214
Chapter 8: Conclusions and future work	214
8.1 Mg-doped Li_2MnO_3	214
8.2 Phase diagram of the MnO_δ -MgO system.....	214
8.3 Structural analysis of T1 and T2 solid solution.....	215

8.4 Structural analysis on cubic spinel-Suzuki phase, C2 solid solution	216
8.5 Electrical properties of T1, T2 and C2 solid solutions	217
8.6 Suggestion for future work	218
8.6.1 Mg-doped Li_2MnO_3	218
8.6.2 $\text{Mg}_x\text{Mn}_{1-x}\text{O}_\delta$	219
Appendices	220
Part A Spinel types	220
1.1.1 Normal spinel structure	220
1.1.2 Inverse spinel structure	221
1.1.3 Jahn-Teller distortions in a spinel structure.....	222
1.1.4 References	226

Chapter 1: Literature Review

1.1 Introduction

The increase in awareness on the effect of global warming towards the environment and our social life has led to a tremendous increase in the development of alternative renewable energy technologies and to be less dependent on the finite-energy resources such as coal and oil. The projected growing demands for these renewable energy sources such as solar, wind, hydropower or geothermal over the next several decades require the development of a more efficient sustainable energy storage system (figure 1.1). These energy storage systems could be used effectively in portable electrical devices, electric vehicles and even in power grid applications ^[1-4].

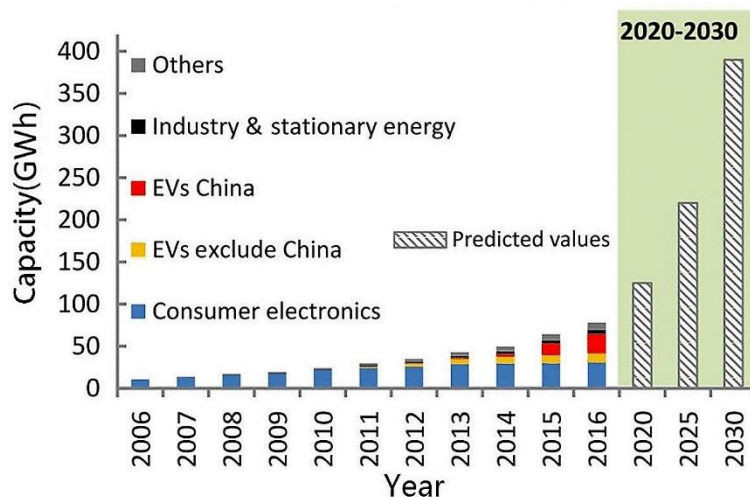


Figure 1.1 Present and future market for Lithium-ion batteries (LIB) including electric vehicles (EV) ^[5]

Current battery technologies have been hovering around lithium-ion batteries (LIB), lead-acid batteries, Ni-MH and Ni-Cd but are still incapable of coping with the requirement of future demands. Interest in the development of LIB has been spurred by the discovery of the possibility of lithium-ion (Li-ion) insertion and extraction from intercalation compounds in the 1980s ^[6] which subsequently led to the commercialization of the world's first LIB in the early 1990s ^[7].

Significant attention has been given to the development of LIB as the main electrochemical energy storage in the last two decades due to its high specific and volumetric energy density, measured in Wh kg^{-1} and Wh l^{-1} respectively, which represent the amount of energy that a battery could store with respect to its mass and volume (figure 1.2) [8]. Due to these outstanding features, LIB has been seen to be used as the main power source in a wide variety of applications such as mobile phones, laptops, power tools and electric vehicles.

The current commercialized LIB, however, is still facing several challenges such as the limited lithium (Li) supply, high cost, safety issue, hazardous (the use of cobalt (Co)) to the environment and low practical energy density [9, 10]. Several possible alternatives were proposed such as the use of alternative metal ions instead of Li^+ such as monovalent alkali metals (Na^+) [11], divalent alkaline earth metals (Mg^{2+}) [2] and multivalent cations (Al^{3+} and Zn^{2+}) [12] (table 1.1). Others such as the use of an environmentally benign and abundant active materials such as manganese were proposed. Therefore, it is necessary to have some understanding on their crystal structure and their thermodynamic stability with respect to variation in composition and temperature, hence their phase diagram, to utilise them as a potential battery material.

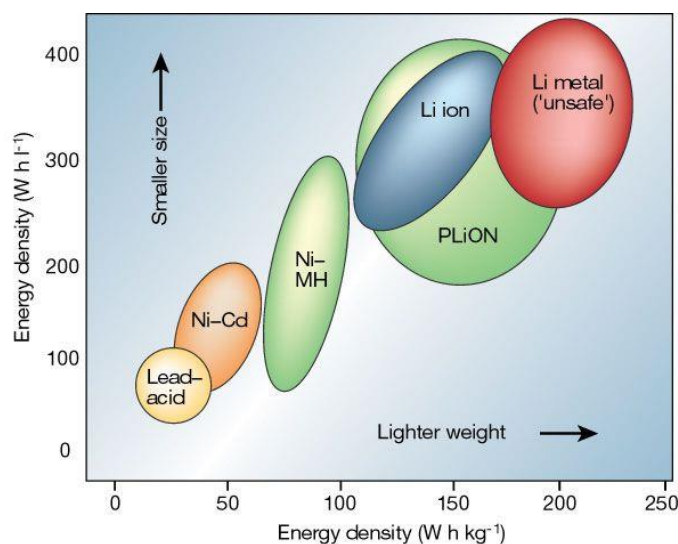


Figure 1.2 Energy storage comparison of different battery types [8]

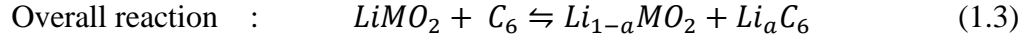
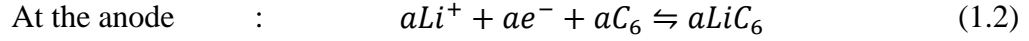
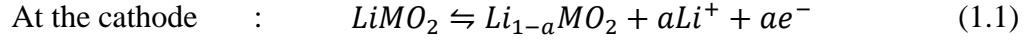
Table 1.1 Comparison between various metals for batteries: theoretical capacity, reduction potential and effective ionic radius ^[4]

Element	Specific capacity (mA h g ⁻¹)	Volumetric capacity (mA h mL ⁻¹)	Reduction potential (V vs. SHE)	Effective ionic radius (Å)
Li	3861	2026	-3.04	0.76
Na	1165	1128	-2.71	1.02
K	685	591	-2.93	1.38
Mg	2205	3833	-2.37	0.72
Ca	1337	2073	-2.87	1.00
Zn	820	5851	-2.20	0.74
Al	2980	8040	-1.67	0.54

1.2 Lithium-ion batteries

A battery system is an electrochemical cell that converts stored chemical energy into electrical energy through oxidation and reduction reactions. There are three main components in a battery system; the anode which is the source of electrons, the cathode where the electrons sink and the electrolyte which allows the diffusion of metal ions but prevents electron transport. The separator acts as a barrier to avoid contact between the electrodes while allowing the ions to pass freely through them. Aluminum (Al) and copper (Cu) are used for current collectors for the cathode and anode, respectively.

A typical rechargeable LIB system (figure 1.3), involves reversible insertion and extraction of lithium (Li⁺) ions into/from an electrode. During charging, Li⁺ ions are de-intercalated from the cathode and travel through the electrolyte to the anode. At the same time, electrons from the cathode are forced to travel through the external circuit and re-join with Li⁺ ions at the anode. The electrochemical reactions that take place during charging are as shown:



where M is transition metal (Co, Ni or Mn).

During discharging, an exact reverse process takes place. Ideally, the electrodes should provide a good conductivity for both electrons and ions to pass through. Conversely, the electrolyte should have good ionic conductivity but be an electronic insulator to avoid any self-discharge.

The overall battery performance is largely dependent on these three main components which give the energy density, cyclability and its safety.

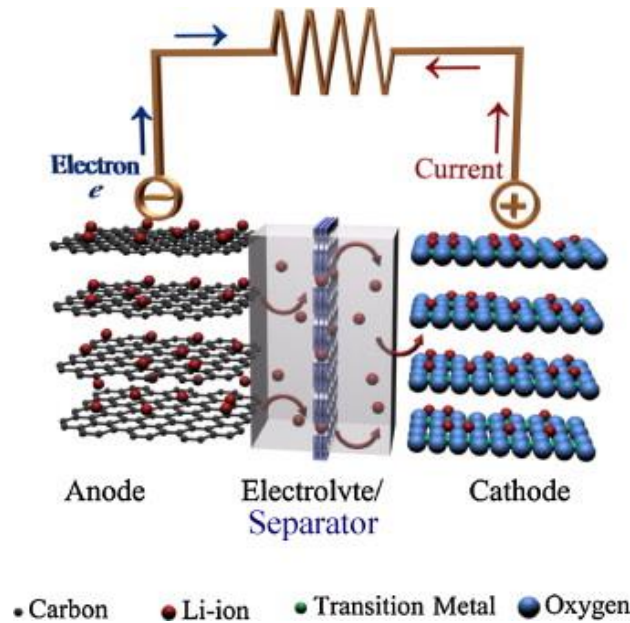


Figure 1.3 Schematic illustration of a typical lithium-ion battery during discharge ^[13]

1.3 Cathode materials

Current electrode materials used in commercialized LIB are based on intercalation materials. These intercalation materials are chosen because of their capability to store Li^+ ions in their solid host network and at the same time provide pathways for Li^+ ions to diffuse/remove into/from the host network reversibly during electrochemical process. The typical host network in LIB is either of transition metal oxides, polyanion compounds or metal chalcogenides. The latter have been widely studied and among many types, LiTiS_2 (LTS) has been commercialized by EXXON due to its high gravimetric energy density and good cycle life. However, due to its low voltage, the usage has been limited to low-powered consumer products [7].

The research on intercalation materials for cathodes has been focussed on the transition metal oxides and polyanion compounds due to high gravimetric and operating voltage (table 1.2). These compounds can be further divided into different crystal structures: such as layered rock salt, spinel and olivine, which correspond to the well-known cathodes: LiCoO_2 [6], LiMn_2O_4 [14] and LiFePO_4 [15], respectively (figure 1.4)

Table 1.2 Commercialised cathode compounds, their specific capacity and average voltage [7]

Crystal structure	Cathode compound	Specific capacity (mA h g^{-1}) (theoretical/experimental)	Volumetric capacity (mA h cm^{-3}) (theoretical/commercial)	Average voltage (V)
Layered	LiTiS_2	225/210	697	1.9
	LiCoO_2	274/148	131363/550	3.8
	$\text{LiNi}_{0.33}\text{Mn}_{0.33}\text{Co}_{0.33}\text{O}_2$	280/160	1333/600	3.7
	$\text{LiNi}_{0.8}\text{Co}_{0.15}\text{Al}_{0.05}\text{O}_2$	279/199	1284/700	3.7
Spinel	LiMn_2O_4	148/120	596	4.1
Olivine	LiFePO_4	170/165	589	3.4

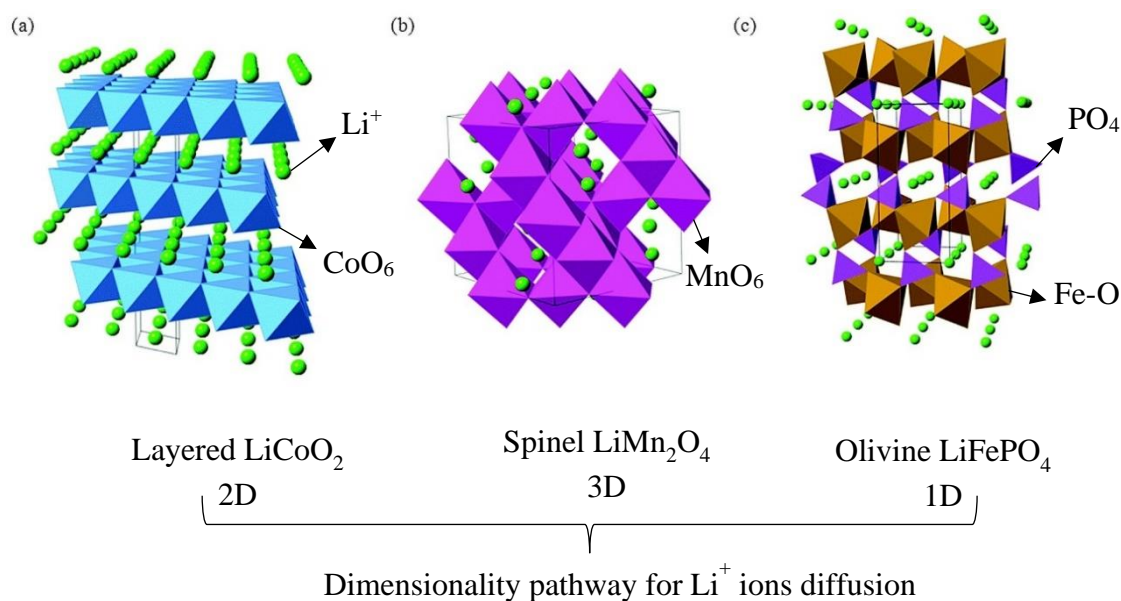


Figure 1.4 Schematics of different crystal structures of intercalation compound and their Li^+ ions diffusion pathways for LIB: (a) Layered rock-salt (LiCoO_2), (b) Spinel (LiMn_2O_4) and (c) Olivine (LiFePO_4)^[16]

There are several requirements for a material to be selected as a cathode in a rechargeable battery system^[17]:

- i. It should have a good ionic and electronic conductivity to give high current and power density.
- ii. It should have a high conducting ion (Li^+) to molecular weight ratio to give high capacity, coupled with high cell voltage to produce high energy density.
- iii. It should exhibit reversible (de)intercalation without or with minimum reversible structural changes to prolong battery cycle life.
- iv. It should have good intercalation properties to allow easy insertion and extraction of conducting ions during the electrochemical reaction.
- v. It should have a low molecular weight and high density to give high capacity and easy portability.
- vi. It should be chemically stable and not react with the electrolyte.
- vii. It should have electrochemical potential within the electrolyte energy band to prevent any unwanted oxidation of electrolyte (at the cathode) or reduction (at the anode) from forming a passivation layer of solid electrolyte interface (SEI) (figure 1.5)^[18].

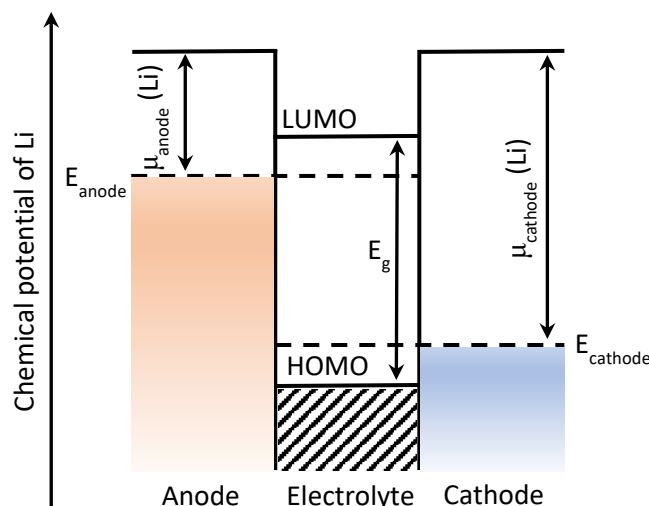


Figure 1.5 Schematic diagram of energy levels in LIB. HOMO and LUMO represent the highest occupied molecular orbital and the lowest unoccupied molecular orbital respectively. μ : chemical potential and E_g : energy gap ^[18]

1.3.1 Layered transition metal

Compounds with the layered rock salt crystal structure are the preferred cathode materials for Li-ion batteries because not only do they exhibit a high potential against the lithium anode but have good structural stability during the electrochemical process. They have general formula LiMO_2 ($M = \text{Co}, \text{Ni}, \text{Mn}, \text{etc}$) of a layered rock salt structure which is identical to the $\alpha\text{-NaFeO}_2$ structure with space group $R\bar{3}m$. Both Li^+ and M^{3+} occupy the octahedral sites of alternate (111) planes ^[19, 20] (figure 1.4).

One of the earliest layered rock salt structures that use transition metal oxides was LiCoO_2 . It was introduced by Goodenough ^[6] in 1980 and due to its outstanding electrochemical properties, SONY started to commercialize it and until today, this type of battery is still in use in many consumer devices.

LiCoO_2 has a relatively high theoretical specific capacity of 274 mA h g^{-1} , thus making this material very attractive. However, the typical capacity of LiCoO_2 is relatively low (145 mA h g^{-1}) with an average voltage of 3.8 V ^[7]. This is attributed to the phase transformation from hexagonal to monoclinic symmetry when the Li^+ ion content drops

below 50%, thus resulted in capacity fading ^[21]. In order to avoid such issue, the de-lithiation of $\text{Li}_{1-y}\text{CoO}_2$ is therefore limited to $1-y < 0.5$.

Due to the increased concern for the environment and cost, researchers are looking for an alternative material to replace Co. LiNiO_2 and LiMnO_2 have been proposed since they are isostructural to LiCoO_2 . However, preparation of stoichiometric LiNiO_2 is rather challenging since Ni^{2+} tends to replace Li^+ instead of oxidizing to Ni^{3+} , thus blocking the pathway for Li^+ ion diffusion and results in poor electrochemical performance ^[22].

LiMnO_2 also showed a poor cycling performance owing to the structural transformation into a spinel structure during de-lithiation. This is attributed to the disproportionation of Mn^{3+} to Mn^{2+} and Mn^{4+} ^[7] followed by the migration of Mn^{2+} ions into the vacant sites within the Li layers resulting in a significant structural change.

1.3.1.1 Li_2MnO_3 as a cathode in LIB

Li_2MnO_3 has a layered rock salt structure with a monoclinic symmetry and space group $C2/m$. It has a slightly different composition in the transition metal layer compared to LiCoO_2 . Rearranging the chemical formula to give $\text{Li}(\text{Li}_{1/3}\text{Mn}_{2/3})\text{O}_2$, shows that Li occupies 1/3 of the positions in Mn-plane to form an ordered LiMn_2 layer while still maintaining Li/Mn ratio of 2:1 (figure 1.6). Due to its higher content of Li, this layered compound generates a higher theoretical specific capacity of 458 mA h g^{-1} with an average voltage of 3.8 V ^[7].

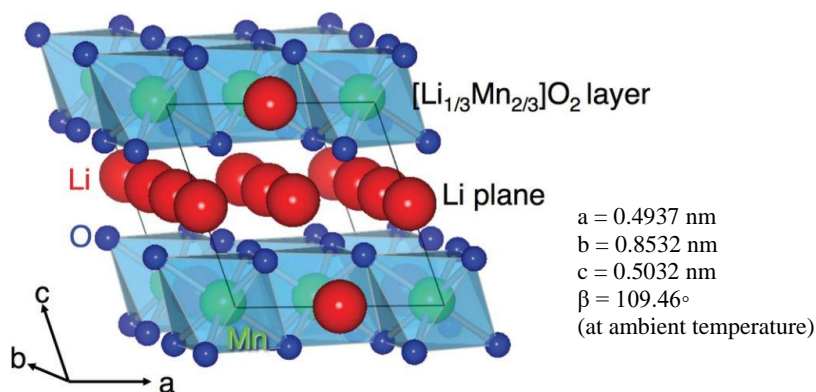


Figure 1.6 Crystal structure of Li_2MnO_3 ^[23]

Despite having such high theoretical capacity (if all Li^+ ions are extracted), Li_2MnO_3 does possess a major drawback. Li_2MnO_3 is electrochemically inactive^[24] since Mn^{4+} cannot be further oxidized to a higher valency as shown by Kubobuchi *et al.*^[25]. This is because the Mn^{4+} is considered stable in the octahedral environment^[26]. However, some anomalous electrochemical activities have been observed and suggestions have been put forward to explain this behavior. Kalyani *et al.*^[27] reported that it might indeed be due to the presence of stable Mn^{5+} and Robertson *et al.*^[28] said that it might be due to oxidation of electrolyte at the cathode that causes an ionic exchange between Li^+ and H^+ to occur.

Pasero *et al.*^[29] proposed that the anomalous electrochemical activities were attributed to the oxygen deficiency in $\text{Li}_2\text{MnO}_{3-\delta}$ and as a result, Mn^{4+} was partially reduced to Mn^{3+} . The presence of mixed valency of Mn enhances the electronic conductivity through the ease of electrons hopping between them. Therefore, during electrochemical charging, this Mn^{3+} will be oxidized to Mn^{4+} , releasing one electron. At the same time, Li^+ ions de-intercalate and diffuse through the electrolyte to the anode. Thus, the amount of Mn^{3+} ions present in the material controls the electrochemical activity.

Electrochemical data on Li_2MnO_3 prepared in various conditions showed that the capacity increases with increasing oxygen deficiency (table 1.3). Although the values obtained are significantly less than the theoretical value, it proves the vital effect of oxygen content on the electrochemical behavior of electrode materials.

Table 1.3 Li_2MnO_3 prepared in various conditions and its relation to oxygen deficiency and capacity^[29]

Li_2MnO_3 Sample	Oxygen deficiency, δ (± 0.003)	Capacity (after 20 cycles) mA h g^{-1} (± 0.5)
High O_2 partial pressure	0.001	0.5
Solid-state reaction at 900°C	0.009	4
Quenched 1000°C	0.013	6
Quenched 1100°C	0.027	13

Cathodes are generally electronic insulators in their discharge state. There are several ways to improve their electronic conductivity such as using additives (carbon), generation of mixed valency by oxygen non-stoichiometry or generation of mixed valency by doping. Doping has been investigated by several authors in order to improve the conductivity of Li_2MnO_3 [30, 31].

The use of Mg as a dopant in the layered rock salt structure has been studied by Tukamoto and West [32] with LiCoO_2 . An increase in electronic conductivity by over two orders of magnitude at room temperature was observed. A reduction in discharge capacity with increasing Mg content was seen which was attributed to the reduction in the number of Co^{3+} in the material. However, the possible use of Mg as a dopant in Li_2MnO_3 is not yet known to be reported.

Based on the compositional triangle of $\text{Li}_2\text{O}-\text{MnO}_\delta-\text{MgO}$ system (figure 1.7), there are three main stoichiometries on the $\text{Li}_2\text{O}-\text{MnO}_\delta$ join that have been widely studied for potential cathode materials: Li_2MnO_3 (monoclinic, $C2/m$), LiMnO_2 (orthorhombic, $Pmnm$) and LiMn_2O_4 (cubic, $Fd\bar{3}m$) [33]. The first two have the same rock-salt structure but with different lattice type and the last one has the spinel structure. The subscript δ in MnO_δ indicates that the composition has a variable oxygen non-stoichiometry which results in different stoichiometries, structures and polymorphisms.

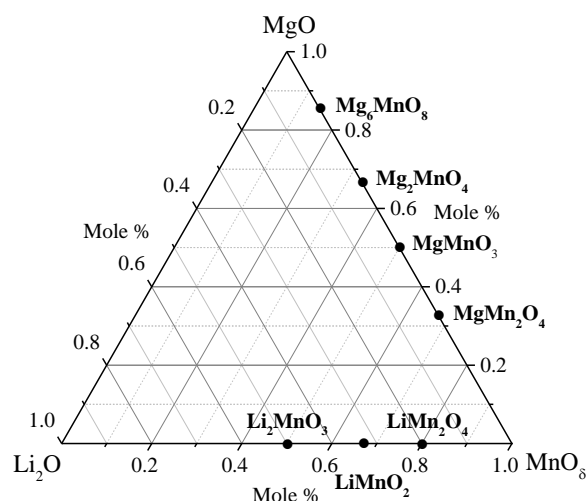


Figure 1.7 Composition triangle of the $\text{Li}_2\text{O}-\text{MgO}-\text{MnO}_\delta$ system with known phases on the joins $\text{Li}_2\text{O}-\text{MnO}_\delta$ and $\text{MgO}-\text{MnO}_\delta$

1.4 Manganese oxide system

The Mn-O system contains four known stable phases: MnO₂, Mn₂O₃, Mn₃O₄ and MnO, and several other metastable phases, which exist over appropriate ranges of temperature and oxygen partial pressure. Unlike stable phases, metastable phases are phases that could be thermodynamically metastable or unstable but kinetically stable. What this means is that the reaction rate to transform into a stable state is slow, thus requires a certain amount of energy to move from metastable state to a more stable state. Moreover, this amount of energy could be referred to as activation energy or energy barrier (figure 1.8).

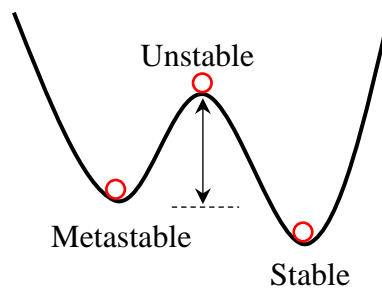
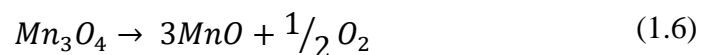
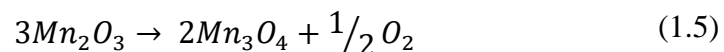
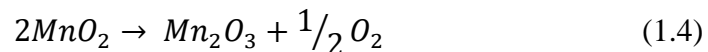


Figure 1.8 Schematic diagram showing three states of stability with an arrow indicating an energy barrier in moving from metastable to a stable state.

The complexity of the Mn-O system is due to the presence of variable oxidation states of Mn cations: Mn⁴⁺, Mn³⁺ and Mn²⁺. These different valencies of Mn arise from different oxygen non-stoichiometry within the system. With an increase in temperature, MnO₂ undergoes thermal decomposition to Mn₂O₃, Mn₃O₄, and finally to MnO [34] as shown by the following reactions:



The transformations between various manganese oxides under different conditions are shown in figure 1.9. MnO_2 exists in many polymorphs, but the most stable phase is known as pyrolusite ($\beta\text{-MnO}_2$), which has a simple tetragonal rutile (TiO_2) structure [35]. At temperatures of 535 to 700 °C, $\beta\text{-MnO}_2$ transformed into Mn_2O_3 . Mn_2O_3 exists in two stable polymorphs: α -kurnakite ($\alpha\text{-Mn}_2\text{O}_3$) and β -kurnakite/bixbyite ($\beta\text{-Mn}_2\text{O}_3$) [36]. $\beta\text{-Mn}_2\text{O}_3$ is commonly observed at a higher temperature but can transform to $\alpha\text{-Mn}_2\text{O}_3$ below ~ 35 °C [37, 38]. Like Mn_2O_3 , Mn_3O_4 known as hausmannite, also has two stable polymorphs: $\alpha\text{-Mn}_3\text{O}_4$ and $\beta\text{-Mn}_3\text{O}_4$. At ambient temperature, the $\alpha\text{-Mn}_3\text{O}_4$ has a distorted spinel structure due to the presence of Mn^{3+} ions in the octahedral-site with formula $(\text{Mn}^{2+})^{\text{tet}}[\text{Mn}^{3+}]_2^{\text{oct}}\text{O}_4$ [39, 40]. At ~ 1170 °C, $\alpha\text{-Mn}_3\text{O}_4$ transforms to $\beta\text{-Mn}_3\text{O}_4$, with a cubic spinel structure [41]. MnO which has a cubic rock salt structure, exists above ~ 1560 °C. [38]. Most of these phases in the Mn-O system have been well established with the exception of a few metastable phases [42-44].

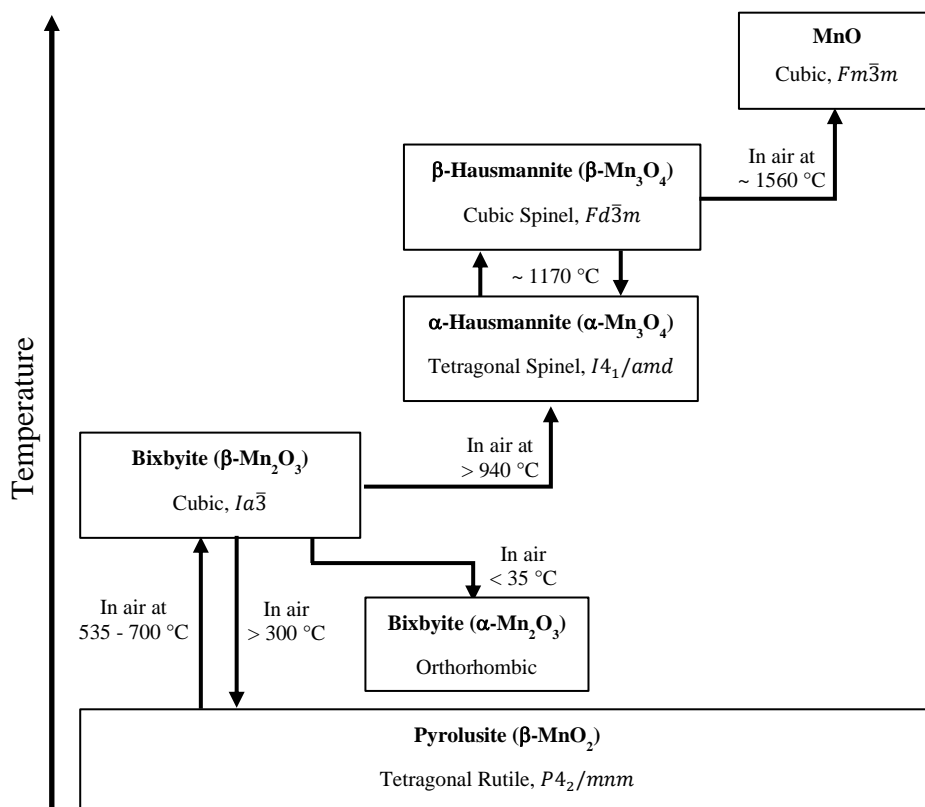
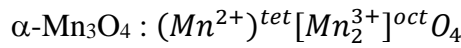


Figure 1.9 Schematic diagram showing the transformation of stable phases of manganese oxide with temperature taken from literature data [37, 38]

The calculated phase equilibria for the Mn-O system have been described by Wang and Sundman^[45] (figure 1.10) and Grundy *et al.*^[37] (figure 1.11). The β -MnO₂, β -Mn₂O₃, α - and β -Mn₃O₄ phases are oxygen-stoichiometric as there is no report described otherwise^[37]. There were variations in the recorded temperature at which the phase transitions of these phases were observed (table 1.4). The phase transition of β -MnO₂ to β -Mn₂O₃ and β -Mn₂O₃ to α -Mn₃O₄ were reported to be between 350 to 670 °C^[41, 46-49] and 685 to 1077 °C^[41, 47-50] respectively. The transformation of α -Mn₃O₄ (tetragonal spinel) to β -Mn₃O₄ (cubic spinel) was observed to be between 1095 to 1200 °C, but a larger number of measurements reported values of 1170 to 1177 °C^[37, 41, 49, 51-58].

The reversible transformation between α - and β -Mn₃O₄ polymorphs does not involve any decomposition reaction. Doris and Mason^[59] suggested that these polymorphs, in fact, have a different ionic configuration, with Mn³⁺ in β -Mn₃O₄ undergoing partial disproportionation: $2Mn_{oct}^{3+} \leftrightarrow Mn_{oct}^{2+} + Mn_{oct}^{4+}$, which explained the cubic structure formation at higher temperature and the observed small increase in conductivity. They proposed the chemical formulae for the hausmannite polymorphs to be:



Driessens^[60] proposed two mechanisms that could explain the formation of cubic spinel at high temperature:

- (a) The distorted spinel α -Mn₃O₄ has Mn³⁺ ions in the octahedral site, which accommodates the fourth 3d electron in the d_{z^2} orbital. With an increase in temperature, the number of Mn³⁺ ions with the fourth 3d electron in the $d_{x^2-y^2}$ orbital also increases. The presence of electrons in $d_{x^2-y^2}$ has a tendency to distort the crystal structure in the opposite direction ($c/a < 1$). As a consequence, the energy gap between these two orbitals reduces. Therefore, it was proposed that at a certain temperature, a sudden transition to the cubic phase is possible when both orbitals have the same energy.

- (b) The possibility of cationic distribution between tetrahedral and octahedral sites, which reduces the number of Mn^{3+} ions in the octahedral sites was also proposed to be responsible for the distorted spinel structure.

Between these two suggestions, the latter was chosen as the most probable cause by the author with a probability of a small degree of inversion at high temperature. The author dismissed any possibility of disproportionation at high temperature, thus gave both α - and β - Mn_3O_4 phases similar Mn^{2+} and Mn^{3+} oxidation states. Several other authors also have a similar opinion, with no change in charge states proposed for the α - to β - Mn_3O_4 transition [53, 61-63].

Further descriptions on the spinel structure and Jahn-Teller effect are described in the appendices of this thesis.

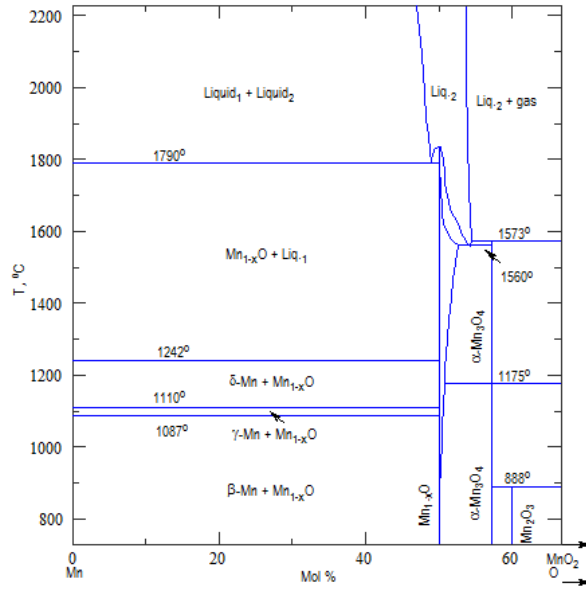


Figure 1.10 The calculated phase equilibria of partial binary diagram between $0 \leq$ mole fraction of oxygen ≤ 0.67 from Wang and Sundman [45]

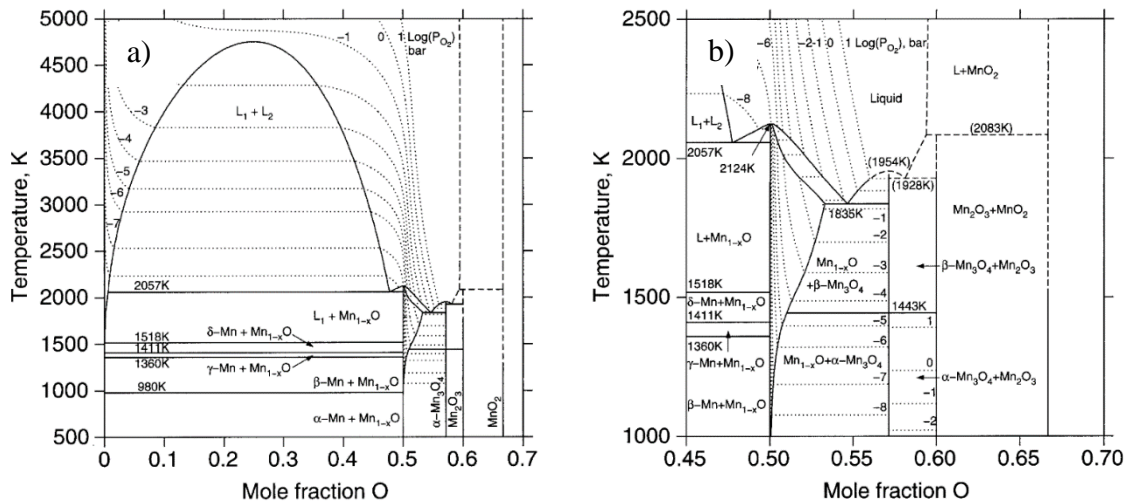


Figure 1.11 (a) The calculated phase equilibria of partial binary diagram between $0 \leq$ mole fraction of oxygen ≤ 0.70 from Grundy *et al.* [37] (b) The enlargement of the phase equilibria between $0.45 \leq$ mole fraction of oxygen ≤ 0.70 and $1000 \text{ K} \leq T \leq 2500 \text{ K}$

Table 1.4 The phase transitions and their respective temperatures
(from literature data)

Phase Transition	Temperature (°C) in air	References
$\alpha\text{-Mn}_3\text{O}_4 - \beta\text{-Mn}_3\text{O}_4$	1200	Schmier and Sterr ^[54]
	1177	Ramana Rao and Tare ^[55]
	1172	Southard and Moore ^[51]
	1172	Pankratz ^[49]
	1170	McMurdie and Golovato ^[41]
	1170	Irani <i>et al.</i> ^[53]
	1170	Grundy <i>et al.</i> ^[37]
	1160	Van Hook and Keith ^[52]
	1157	Metselaar <i>et al.</i> ^[57]
	1134	Keller and Dieckmann ^[58]
	1095	Tromel <i>et al.</i> ^[56]
$\beta\text{-Mn}_2\text{O}_3 \rightarrow \alpha\text{-Mn}_3\text{O}_4$	1077	Pankratz ^[49]
	970	Kissinger <i>et al.</i> ^[46]
	950	McMurdie and Golovato ^[41]
	884	Ingraham ^[50]
	685	Klingsberg and Roy ^[48]
$\beta\text{-MnO}_2 \rightarrow \beta\text{-Mn}_2\text{O}_3$	670	McMurdie and Golovato ^[41]
	570	Dubois and Urbain ^[47]
	550	Kissinger <i>et al.</i> ^[46]
	527	Pankratz ^[49]
	350	Klingsberg and Roy ^[48]

1.5 MgO-MnO₈ system

The MgO-MnO₈ system contains four phases that have been reported: MgMn₂O₄^[64], MgMnO₃^[65], Mg₂MnO₄^[66] and Mg₆MnO₈^[67] (figure 1.7). Mg₆MnO₈ has a cubic rock salt structure as reported by Kasper and Prener^[67]. Both MgMn₂O₄ and Mg₂MnO₄ have a spinel structure and the latter is an inverse of the former. MgMnO₃ has a cubic spinel with defect structure, recently reported by Sehra *et al.*^[65]. Out of these four phases, only MgMn₂O₄ has Mn in the trivalent state.

1.5.1 The phase diagram

A pseudo-binary phase diagram of MgO-MnO₈ has been described by Barkhatov *et al.*^[68] over the temperature range 800-1200 °C (figure 1.12(a)). Samples were heated for a period of 120-340 h in air and quenched to room temperature. The phase diagram was constructed together with the combined data from the literature^[67, 69]. However, only a few details were given to comprehend the work made by the author.

Joshi *et al.*^[70] reported that the current phase diagram is not well established due to insufficient data for temperatures below 800 °C. The authors were interested in the tetragonal to cubic spinel region of the phase diagram. In-situ high-temperature x-ray diffraction and quenched data on several compositions combined with previous literature were used to construct the phase diagram shown in figure 1.12 (b).

The two phase diagrams (a, b) are different from each other, especially in the high temperature Mn-rich region. However, both reported that there is a phase transition from low-temperature tetragonal spinel to high-temperature cubic spinel at high Mn content. For composition Mn = 2/3 (MgMn₂O₄), a mixture of tetragonal and a cubic spinel was observed over the temperature range 600-900 °C. The cubic region was dependent on the Mg content and extended to a lower temperature region with increasing Mg content.

Both diagrams also showed that Mg₆MnO₈ is a single line phase up to ~ 1050 °C. However, data collected by Joshi *et al.* at this composition between 900-1150 °C indicated the presence of MgO over that temperature range. A mixture of Mg₆MnO₈ and

cubic spinel region was observed between Mn ~ 0.15 to 0.45 below temperature ~ 1050 °C.

The spinel structure in the Mn₃O₄-MgMn₂O₄ solid solution has attracted considerable interest because of its high electronic conductivity due to a hopping mechanism associated with the presence of multivalent cations (Mn²⁺, Mn³⁺ and Mn⁴⁺) as reported by Panda and Ho Jung ^[71]. MgMn₂O₄ which is structurally analogous to LiMn₂O₄ has also been studied as a potential cathode material in magnesium-ion batteries (MIB) ^[72-74]. However, the study was constrained by the slow Mg²⁺ ion diffusion due to its bivalency and small ionic radius that resulted in a strong cation-anion electrostatic attractions ^[75, 76]. The electrostatic attraction energy, E_e , can be defined as the amount of energy required to separate the ionic species and is governed by Coulomb's law:

$$E_e = -\frac{Z_+Z_-e^2}{4\pi\epsilon_0r} \quad (1.7)$$

where,

Z_+, Z_- = magnitude of ionic charges

e = electronic charge, 1.602×10^{-19} C

ϵ_0 = electric permittivity of free space, 8.854×10^{-14} F cm⁻¹

r = cation-anion distance

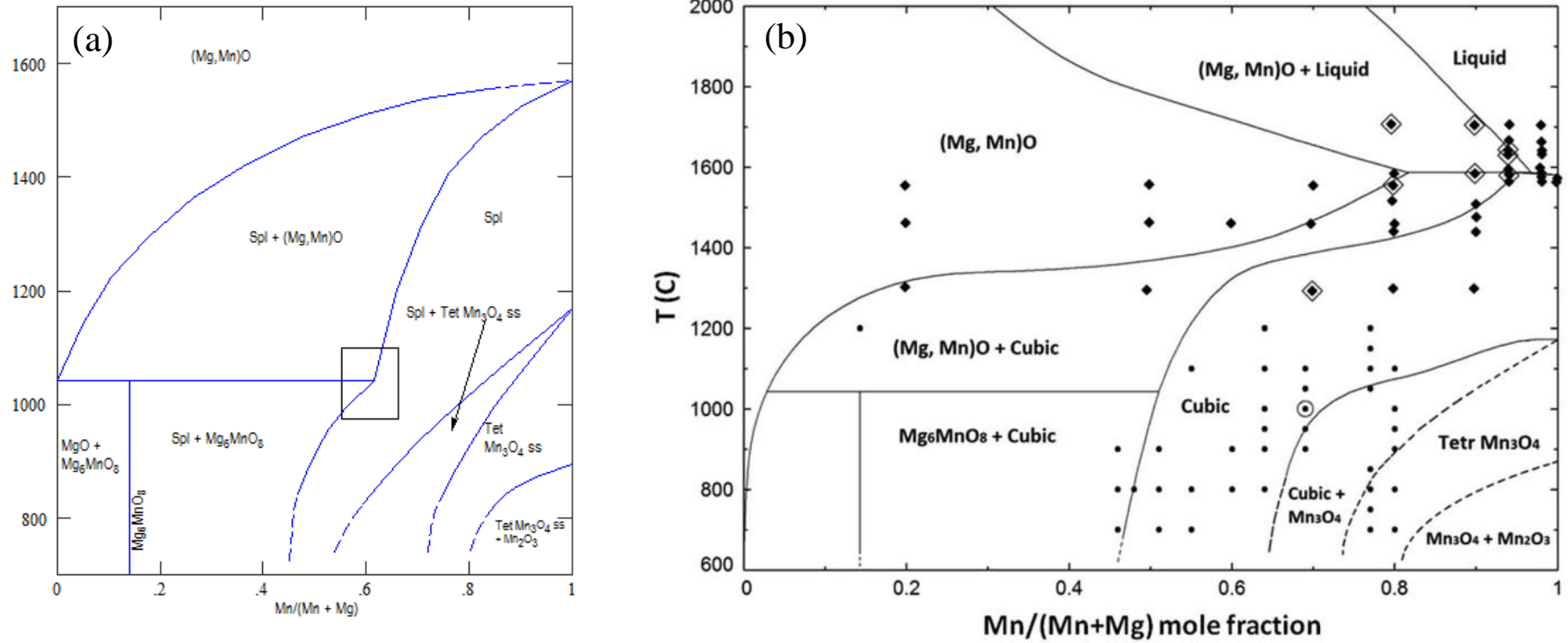


Figure 1.12 A pseudo-binary phase diagram for MgO-MnO₈ system described by (a) Barkhatov *et al.* [68] 1980 and (b) Joshi *et al.* [70] 2014

1.5.2 MgMn₂O₄

Numerous studies have been reported on MgMn₂O₄ spinel with a particular interest in structural properties, the degree of inversion and electronic properties. MgMn₂O₄ has been reported to exhibit two polymorphs analogous to α - and β -Mn₃O₄. At room temperature, MgMn₂O₄ possesses a tetragonal spinel structure, isomorphous with the hausmannite structure with $I4_1/amd$ space group, and lattice parameters $a = 5.721$ (1) Å, $c = 9.315$ (1) Å and $c/a = 1.6282$ (5) [64, 77, 78]. The Mg and Mn cations are distributed over the $4b$ -tetrahedral and $8c$ -octahedral sites respectively within a cubic closed packed oxygen array ($16h$) (figure 1.13): $(Mg^{2+})^{tet}[Mn_2^{3+}]^{oct}O_4$. The presence of Mn³⁺ ions in the octahedral environment is responsible for the crystal distortion due to the Jahn-Teller effect [78].

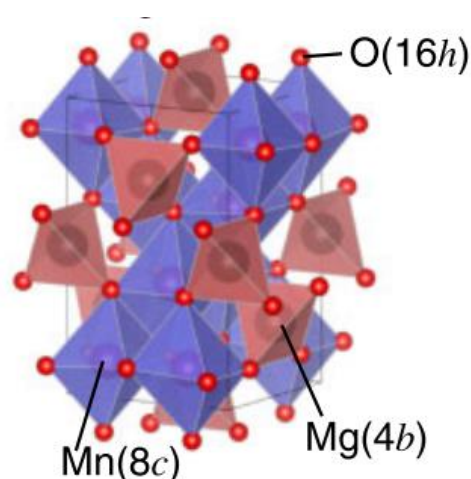
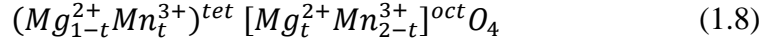


Figure 1.13 The crystal structure of MgMn₂O₄ [79]

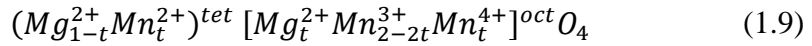
At higher temperature, the tetragonal spinel of MgMn₂O₄ transformed into a cubic structure. Several authors have proposed mechanisms for this transition.

Irani *et al.* [53] reported that the transition from tetragonal to cubic spinel of MgMn₂O₄ occurs abruptly at a critical temperature ~ 850 °C, where a sudden drop of axial c/a ratio to near unity was observed. They proposed that this anomalous behavior was due to the conjugate action of: (a) the partial migration of Mn³⁺ ions from octahedral to tetrahedral sites, and (b) the randomization of the orientation of the distorted octahedra. This is consistent with the theoretical expectations of Wojtowicz [80] and Kanamori [81].

The cation distribution triggers a structural transformation from tetragonal to cubic spinel and resulted in a degree of inversion reaction. The proposed general formula is:



Rosenberg and Nicolau ^[82] reported that the transition occurs in a narrow temperature range of 880 – 950 °C. They proposed that the cubic spinel formation is due to the migration of Mg²⁺ ions to the octahedral sites which then triggers the disproportionation of $2Mn_{oct}^{3+} \leftrightarrow Mn_{oct}^{2+} + Mn_{oct}^{4+}$. Consequently, all the Mn²⁺ ions have then migrated to the tetrahedral site. This disproportionation reduces the number of Mn³⁺ ions in the octahedral site and a cubic-like structure was therefore observed. They are also reported that the slow-cooled MgMn₂O₄, still revealed some cation distribution but to a lesser degree. Their proposed general formula was:



Mănăilă and Păușescu ^[78] reported that the transition from tetragonal to cubic spinel is similar to that proposed by Rosenberg and Nicolau ^[82] but with a broader two-phase domain between 760 °C and 950 ~ 1000 °C. The first occurrence of cubic spinel at 760 °C was facilitated by the inversion process which decreases the number of Mn³⁺ ions and increases the number of non-distorting Mg²⁺ and Mn⁴⁺ ions in the octahedral site. This reduces the ability for the structure to retain its collective tetragonal orientation and hence reduces the transition temperature.

Rosenberg *et al.* ^[77] also studied the transition temperature with variation in Mg content within the $Mg_yMn_{3-y}O_4$ system between $0 \leq y \leq 1$. A linear decrease in transition temperature with increasing y was observed which is similar to the expectation of Wojtowicz ^[80]. In addition, a slight decrease in the lattice c/a ratio was also observed for the slow-cooled samples (with tetragonal spinel structure) with increasing y . They claimed that the reduction in lattice c/a ratio was attributed to the presence of a small fraction of Mg²⁺ ions on the octahedral site, thus reducing the Mn³⁺ ions, after heat treatment at 1200 °C.

Barkhatov *et al.* [83] claimed similar disproportionation of Mn^{3+} ions in the octahedral site but with the additional possibility of partial migration of Mn^{2+} from octahedral to the tetrahedral site instead of a full migration. Therefore, a mixture of Mn^{2+} , Mn^{3+} and Mn^{4+} in the octahedral site is then possible. This gives general formula:



In principle, the arguments over which mechanism of the cubic spinel formation is preferable depend upon whether the octahedral site is occupied with Mn^{3+} cation or with a mixture of Mn^{2+} and Mn^{4+} cations as previously described.

The inversion degree, γ , which can be referred to as the cation migration of either Mn or Mg to tetrahedral or octahedral sites respectively in the tetragonal spinel $MgMn_2O_4$ has been studied by several authors [78, 82, 84]. Radhakrishnan and Biswas [85] using neutron diffraction on quenched samples showed that the cation migration occurred from 550 °C onwards, below which any cationic redistribution is unnoticeable (figure 1.14). Beyond 550 °C, the inversion degree increased rapidly owing to the increasing number of Mg^{2+} migrated to the octahedral site.

However, only a few authors have reported on the inversion degree in the high-temperature cubic spinel region of $MgMn_2O_4$. Irani *et al.* [53] reported that at the transition temperature, an inversion of $\lambda = 0.225$ was observed. Mănăilă and Păușescu [78] reported an inversion of $\lambda = 0.489$ (3) was observed for the sample quenched from 1250 °C.

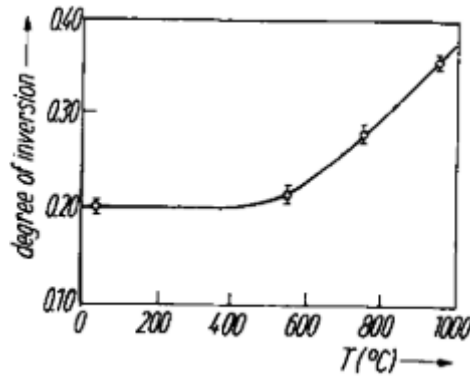


Figure 1.14 The variation of the degree of inversion with temperature for $MgMn_2O_4$ reported by Radhakrishnan and Biswas [85]

Barkhatov *et al.* [83] also measured the inversion degree of the cubic spinel using in-situ x-ray diffraction with various Mg content within the $Mg_yMn_{3-y}O_4$ system between $0.5 < y \leq 1.4$. The inversion degree was observed to decrease linearly with increasing y between $1 \leq y \leq 1.4$.

Many researchers had attempted to prepare a single phase of $MgMn_2O_4$ by various methods. Malavasi *et al.* [84] and Aazoni *et al.* [86] (figure 1.15) carried out solid state reaction with the final calcination temperature at 1200 °C for at least six days. Based on the XRD pattern, a single phase of $MgMn_2O_4$ was successfully prepared.

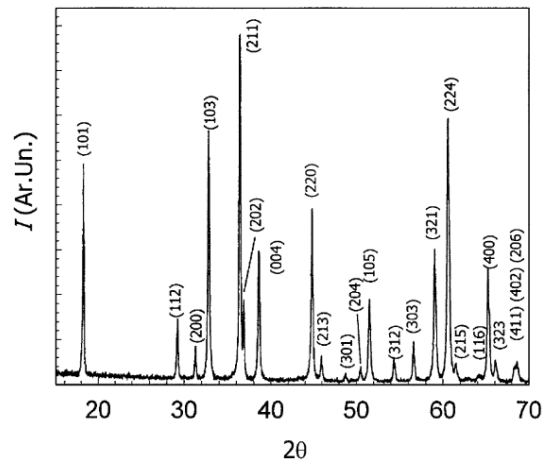


Figure 1.15 The XRD pattern of $MgMn_2O_4$ [84, 86]

Several others, Kim *et al.* [87], Rahman and Gerosa [88], Liu *et al.* [89] and Yagi *et al.* [79], however, had prepared this composition by various methods and the XRD patterns showed an extra set of peaks which appears to be separated from the known tetragonal $MgMn_2O_4$ spinel reflections (figure 1.16). Yagi *et al.* [79] reported that this extra reflection was due to impurity while others [87-89] claimed that they had successfully prepared a pure phase of tetragonal $MgMn_2O_4$. These extra peaks can generally be observed at 2θ ca 36°, 44°, 58° and 63° with Cu $K\alpha$ radiation, depending on the quality of the data. Yagi *et al.* [79] used different radiation wavelength ($\lambda = 0.7737\text{-}0.7739$ Å) and hence the 2θ position is different to the others, but is at similar 2θ positions if converted to Cu $K\alpha$ radiation.

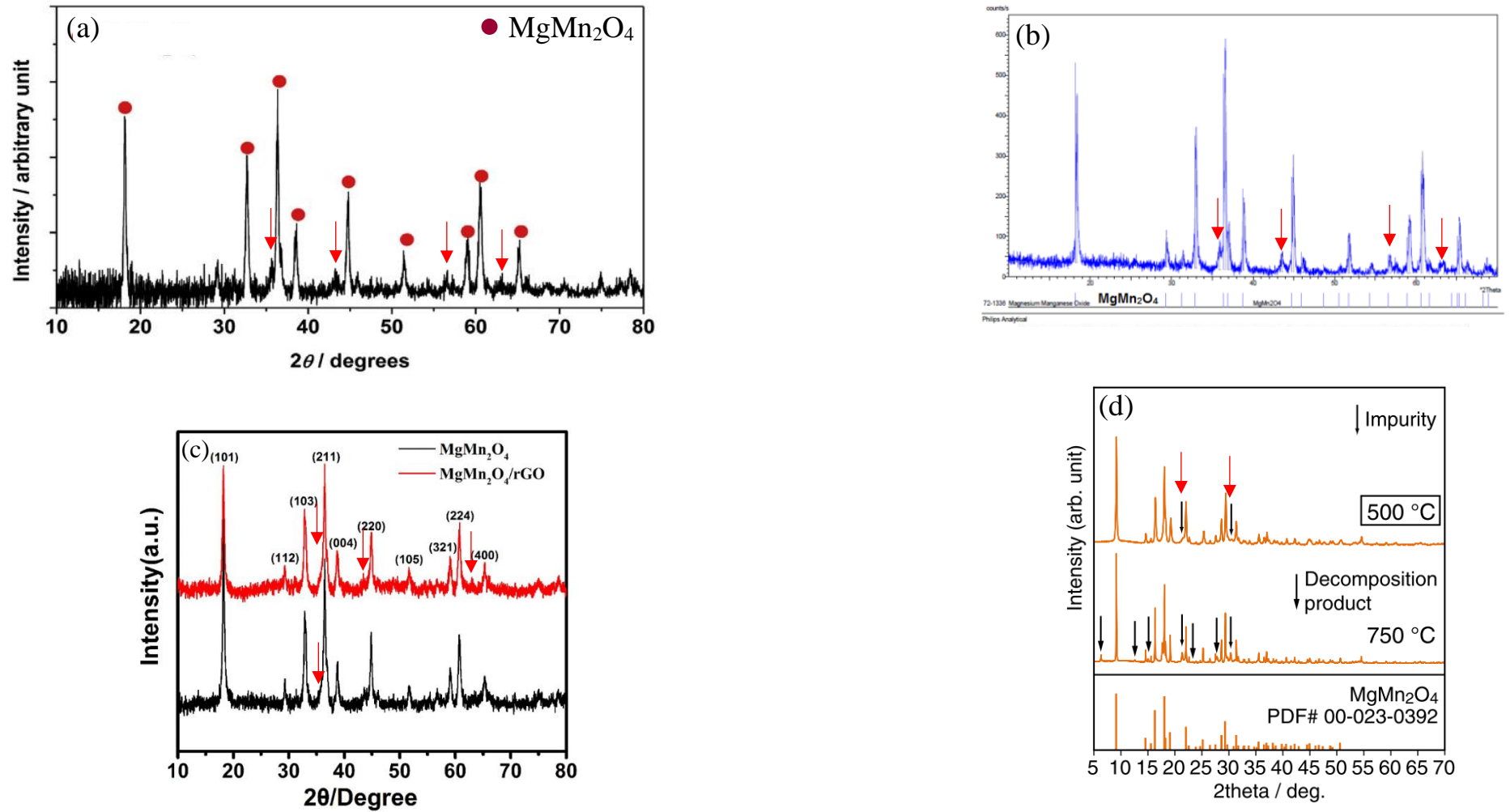


Figure 1.16 The XRD patterns of MgMn_2O_4 showing an extra set of reflection (red arrow) from different literature data:

(a) Kim *et al.* [87], (b) Rahman and Gerosa [88], (c) Liu *et al.* [89] and (d) Yagi *et al.* [79]

1.5.3 Mg₂MnO₄

Mg₂MnO₄ is an inverse spinel, can be described by $(Mg^{2+})^{tet}[Mg^{2+}Mn^{4+}]^{oct}O_4$ where one-eighth of the tetrahedral sites are occupied by Mg²⁺ and half of the octahedral sites are occupied by Mg²⁺ and Mn⁴⁺ ions in an oxide array environment (figure 1.17). Unlike normal MgMn₂O₄, the Mn in this inverse spinel is in tetravalent state [66]. Therefore, with the absence of Mn³⁺ ions in the octahedral environment, no Jahn-Teller distortion can be expected. Hence, Mg₂MnO₄ formed a cubic structure with $Fd\bar{3}m$ space group with lattice parameter [90] as shown in table 1.5.

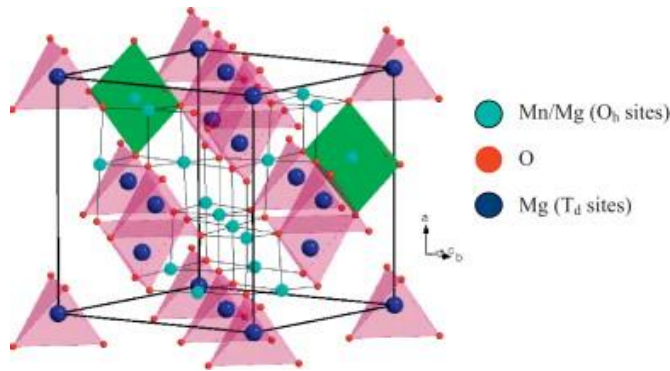


Figure 1.17 The Mg₂MnO₄ crystal structure [90]

Table 1.5 Comparison between three different compositions with spinel structure within the MgO-MnO₈ system

	Mn₃O₄	MgMn₂O₄	Mg₂MnO₄
	Normal spinel	Normal spinel	Inverse spinel
General formula	AB ₂ O ₄	AB ₂ O ₄	B(AB)O ₄
Tetrahedral site	Mn ²⁺	Mg ²⁺	Mg ²⁺
Octahedral site	Mn ³⁺	Mn ³⁺	Mg ²⁺ , Mn ⁴⁺
Structure	Tetragonal	Tetragonal	Cubic
Space group	<i>I4₁/amd</i>	<i>I4₁/amd</i>	<i>Fd$\bar{3}m$</i>
<i>a</i> (Å)	5.71	5.721 (1)	8.336 (3)
<i>c</i> (Å)	9.35	9.315 (1)	-
<i>c/a</i>	1.64	1.63	-
Reference	Jensin and Nielsen [91]	Mănăilă and Păușescu [78]	Garg <i>et al.</i> [90]

1.5.4 Mg₆MnO₈

Mg₆MnO₈, which is known as ‘Suzuki-phase’, after Kazuo Suzuki who described the structure of Na₆Cd□Cl₈ [92], where □ denotes as vacancy, was first discovered by Kasper and Prener [67] in 1953. During the same period, another example, Cu₆PbO₈, with similar structure was discovered by Christ and Clark [93], and Fahey [94].

As reported by Kasper and Prener [67], Mg₆MnO₈ has a rock salt superstructure with lattice parameter, $a = 8.381(2) \text{ \AA}$, with $Fm\bar{3}m$ space group, which is double that of cubic MgO (4.203 Å). The main characteristic of this structure is that it contains a high number of ordered cation and cation vacancies in the octahedral sites of a cubic close packed oxide array and thus the formula can be rewritten as Mg₆Mn□O₈. It appears that the close-packed arrangement contains 32 oxygens in a unit cell which are distributed over 8*c*- and 24*e*-sites. Since the Mn occupied 4*a*-site and the Mg occupied 24*d*-site, this leaves the ordered cation vacancies to be at 4*b*-site (figure 1.18).

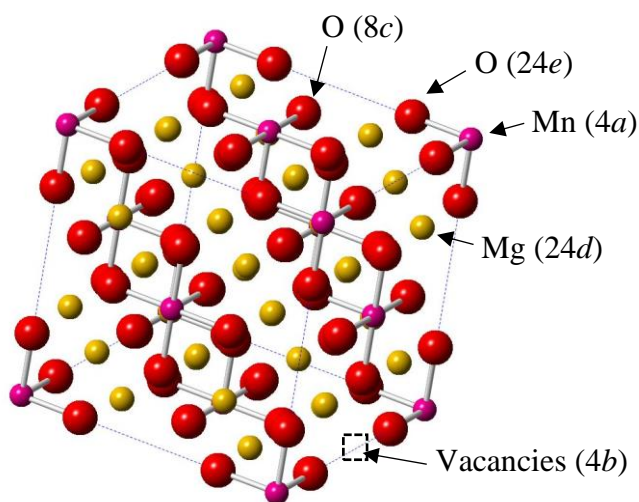


Figure 1.18 Crystal structure of Mg₆MnO₈

The possibility of using this material as a potential electrode in an energy storage system has apparently not yet to be reported. A study on the magnetic and optical properties has been made by Porta and Valigi [95]. Taguchi *et al.* [96] reported on the success of doping with lithium in (Mg_{6-y}Li_y)MnO₈ for $0 \leq y \leq 0.3$ and as a result, partial oxidation of Mn⁴⁺ to Mn⁵⁺ was proposed. However, no data were collected on its electrical properties.

1.5.5 MgMnO₃

MgMnO₃ was reported by Chamberland *et al.* [97] to be an Ilmenite-type compound (FeTiO₃) with a general formula AMn⁴⁺O₃, where A = Ni [98], Co [99] and Zn [97]. It has a hexagonal structure with lattice parameter $a = 4.945 \text{ \AA}$ and $c = 13.73 \text{ \AA}$, and may require a high pressure to form. Attempts to prepare it at ambient pressure may result in a cubic structure with oxygen-deficiency after heat treatment between 600-1000 °C. Arjomand and Machin [100] reported that hexagonal MgMnO₃ could in fact be formed at 1 bar pressure when heated at 900 °C, but beyond this temperature, an oxygen-deficient cubic structure was observed. However, prolonged heat treatment at 900 °C for seven days showed that there was no evidence of hexagonal MgMnO₃ present in the sample as reported by Pavlyuchkov *et al.* [101].

The oxygen-deficient cubic structure of MgMnO_{3-δ} could be considered as either (a) the structure possesses a mixture of Mn³⁺ and Mn⁴⁺ in the crystal lattice described by $(Mg^{2+})^{tet}[Mg_{0.5}^{2+}Mn^{3+}Mn_{0.5}^{4+}]^{oct}O_4$ or (b) it has ordered cation vacancies described by $Mg^{2+}Mn^{4+}\square O_3$ [65], where \square denotes a vacancy. These models have respectively, a cubic spinel and a cubic defect spinel structure with both belong to the same space group of $Fd\bar{3}m$. The latter can be rewritten as $(Mg^{2+})^{tet}[Mg_{1/3}^{2+}Mn_{4/3}^{4+}\square_{1/3}]^{oct}O_4$ [65, 102, 103]. Seehra *et al.* [65] reported that this cubic defect spinel has a lattice parameter $a = 8.2923 \text{ \AA}$.

1.6 Aims and objectives

The Li-Mn-O system contains two phases that are important for lithium battery applications, the spinel LiMn_2O_4 and the layered rock salt Li_2MnO_3 . There are problems to be solved and uncertainties concerning optimisation of the properties of both phases, and the effect of dopants. Li_2MnO_3 has been reported to show some anomalous electrochemical behaviour and further investigation on this phase is planned. The initial objective at the beginning of this study was to investigate the effect of dopant, Mg, on (i) solid solution formation within the pseudoternary phase diagram of $\text{Li}_2\text{O-MgO-MnO}_8$ system, and (ii) their electrical properties (chapter 3). This was based on the success of doping a layered rock salt LiCoO_2 with Mg and the observed increased in conductivity [32].

Unlike the $\text{Li}_2\text{O-MnO}_8$ system, studies on MgO-MnO_8 has not been equally extensive. In this thesis, several compositions were prepared initially on the MgO-MnO_8 join and showed contradicting results from the reported literature [68]:

- (i) the formation of a wide cubic solid solution at intermediary temperature over the range $0.50 \leq x \leq 0.80$ of $\text{Mg}_x\text{Mn}_{1-x}\text{O}_8$ instead of a phase mixture.
- (ii) the formation of high temperature tetragonal spinel polymorph (on quenching) instead of a cubic spinel at low Mg content.

Based on these results, the objectives were redefined as (i) to investigate and construct the pseudo-binary phase diagram of the MgO-MnO_8 system (chapter 4), (ii) to study the relevant crystal structures and their possible doping mechanisms (chapter 5 and 6), and (iii) to investigate the electrical properties and their relationship to the crystal structures (chapter 7).

1.7 References

1. Larcher, D. and J.-M. Tarascon, *Towards greener and more sustainable batteries for electrical energy storage*. Nature chemistry, 2015. **7**(1): p. 19.
2. Saha, P., M.K. Datta, O.I. Velikokhatnyi, A. Manivannan, D. Alman, and P.N. Kumta, *Rechargeable magnesium battery: Current status and key challenges for the future*. Progress in Materials Science, 2014. **66**: p. 1-86.
3. Yoo, H.D., I. Shterenberg, Y. Gofer, G. Gershinsky, N. Pour, and D. Aurbach, *Mg rechargeable batteries: an on-going challenge*. Energy & Environmental Science, 2013. **6**(8): p. 2265-2279.
4. Wang, Y., R. Chen, T. Chen, H. Lv, G. Zhu, L. Ma, C. Wang, Z. Jin, and J. Liu, *Emerging non-lithium ion batteries*. Energy Storage Materials, 2016. **4**: p. 103-129.
5. Zubi, G., R. Dufo-López, M. Carvalho, and G. Pasaoglu, *The lithium-ion battery: State of the art and future perspectives*. Renewable and Sustainable Energy Reviews, 2018. **89**: p. 292-308.
6. Mizushima, K., P. Jones, P. Wiseman, and J. Goodenough, *Li_xCoO_2 ($0 < x \leq 1$): A new cathode material for batteries of high energy density*. Solid State Ionics, 1981. **3**: p. 171-174.
7. Nitta, N., F. Wu, J.T. Lee, and G. Yushin, *Li-ion battery materials: present and future*. Materials today, 2015. **18**(5): p. 252-264.
8. Armand, M. and J. Tarascon, *Issues and challenges facing rechargeable batteries*. Nature, 2001. **414**: p. 359-367.
9. Slater, M.D., D. Kim, E. Lee, and C.S. Johnson, *Sodium-ion batteries*. Advanced Functional Materials, 2013. **23**(8): p. 947-958.
10. Park, M.S., J.G. Kim, Y.J. Kim, N.S. Choi, and J.S. Kim, *Recent advances in rechargeable magnesium battery technology: a review of the field's current status and prospects*. Israel Journal of Chemistry, 2015. **55**(5): p. 570-585.
11. Kundu, D., E. Talaie, V. Duffort, and L.F. Nazar, *The emerging chemistry of sodium ion batteries for electrochemical energy storage*. Angewandte Chemie International Edition, 2015. **54**(11): p. 3431-3448.
12. Xu, C., Y. Chen, S. Shi, J. Li, F. Kang, and D. Su, *Secondary batteries with multivalent ions for energy storage*. Scientific reports, 2015. **5**: p. 14120.
13. Song, M.-K., S. Park, F.M. Alamgir, J. Cho, and M. Liu, *Nanostructured electrodes for lithium-ion and lithium-air batteries: the latest developments, challenges, and perspectives*. Materials Science and Engineering: R: Reports, 2011. **72**(11): p. 203-252.

14. Thackeray, M., P. Johnson, L. De Picciotto, P. Bruce, and J. Goodenough, *Electrochemical extraction of lithium from LiMn_2O_4* . *Materials Research Bulletin*, 1984. **19**(2): p. 179-187.
15. Chung, S.-Y., J.T. Bloking, and Y.-M. Chiang, *Electronically conductive phospho-olivines as lithium storage electrodes*, in *Materials For Sustainable Energy: A Collection of Peer-Reviewed Research and Review Articles from Nature Publishing Group*. 2011, World Scientific. p. 205-210.
16. Islam, M.S. and C.A. Fisher, *Lithium and sodium battery cathode materials: computational insights into voltage, diffusion and nanostructural properties*. *Chemical Society Reviews*, 2014. **43**(1): p. 185-204.
17. Whittingham, M.S., *Materials challenges facing electrical energy storage*. *Mrs Bulletin*, 2008. **33**(4): p. 411-419.
18. Goodenough, J.B. and Y. Kim, *Challenges for rechargeable Li batteries*. *Chemistry of materials*, 2009. **22**(3): p. 587-603.
19. Thackeray, M., *Lithium-ion batteries: An unexpected conductor*. *Nature materials*, 2002. **1**(2): p. 81.
20. Van Schalkwijk, W. and B. Scrosati, *Advances in lithium ion batteries introduction*, in *Advances in Lithium-Ion Batteries*. 2002, Springer. p. 1-5.
21. Reimers, J.N. and J. Dahn, *Electrochemical and in situ X-ray diffraction studies of lithium intercalation in Li_xCoO_2* . *Journal of The Electrochemical Society*, 1992. **139**(8): p. 2091-2097.
22. Rougier, A., P. Gravereau, and C. Delmas, *Optimization of the Composition of the $\text{Li}_{1-z}\text{Ni}_{1+z}\text{O}_2$ Electrode Materials: Structural, Magnetic, and Electrochemical Studies*. *Journal of The Electrochemical Society*, 1996. **143**(4): p. 1168-1175.
23. Sugiyama, J., K. Mukai, H. Nozaki, M. Harada, M. Månsson, K. Kamazawa, D. Andreica, A. Amato, and A.D. Hillier, *Antiferromagnetic spin structure and lithium ion diffusion in Li_2MnO_3 probed by $\mu^+\text{SR}$* . *Physical Review B*, 2013. **87**(2): p. 024409.
24. Denis, Y., K. Yanagida, Y. Kato, and H. Nakamura, *Electrochemical activities in Li_2MnO_3* . *Journal of The Electrochemical Society*, 2009. **156**(6): p. A417-A424.
25. Kubobuchi, K., M. Mogi, H. Ikeno, I. Tanaka, H. Imai, and T. Mizoguchi, *Mn $L_{2,3}$ -edge X-ray absorption spectroscopic studies on charge-discharge mechanism of Li_2MnO_3* . *Applied Physics Letters*, 2014. **104**(5): p. 053906.
26. Ammundsen, B. and J. Paulsen, *Novel lithium-ion cathode materials based on layered manganese oxides*. *Advanced Materials*, 2001. **13**(12-13): p. 943-956.
27. Kalyani, P., S. Chitra, T. Mohan, and S. Gopukumar, *Lithium metal rechargeable cells using Li_2MnO_3 as the positive electrode*. *Journal of power sources*, 1999. **80**(1-2): p. 103-106.

28. Robertson, A.D., A.R. Armstrong, A.J. Paterson, M.J. Duncan, and P.G. Bruce, *Nonstoichiometric layered $\text{Li}_x\text{Mn}_y\text{O}_2$ intercalation electrodes - a multiple dopant strategy*. Journal of Materials Chemistry, 2003. **13**(9): p. 2367-2373.
29. Pasero, D., V. McLaren, S. De Souza, and A. West, *Oxygen nonstoichiometry in Li_2MnO_3 : An alternative explanation for its anomalous electrochemical activity*. Chemistry of materials, 2005. **17**(2): p. 345-348.
30. Tabuchi, M., Y. Nabeshima, T. Takeuchi, K. Tatsumi, J. Imaizumi, and Y. Nitta, *Fe content effects on electrochemical properties of Fe-substituted Li_2MnO_3 positive electrode material*. Journal of Power Sources, 2010. **195**(3): p. 834-844.
31. Lu, Z. and J.R. Dahn, *Understanding the anomalous capacity of $\text{Li}/\text{Li}[\text{Ni}_x\text{Li}_{(1/3-2x/3)}\text{Mn}_{(2/3-x/3)}]\text{O}_2$ cells using in situ X-ray diffraction and electrochemical studies*. Journal of The Electrochemical Society, 2002. **149**(7): p. A815-A822.
32. Tukamoto, H. and A. West, *Electronic conductivity of LiCoO_2 and its enhancement by magnesium doping*. Journal of The Electrochemical Society, 1997. **144**(9): p. 3164-3168.
33. Park, S.-H., Y. Sato, J.-K. Kim, and Y.-S. Lee, *Powder property and electrochemical characterization of Li_2MnO_3 material*. Materials chemistry and physics, 2007. **102**(2-3): p. 225-230.
34. Terayama, K. and M. Ikeda, *Study on thermal decomposition of MnO_2 and Mn_2O_3 by thermal analysis*. Transactions of the Japan institute of metals, 1983. **24**(11): p. 754-758.
35. Baur, W.H., *Rutile-type compounds. V. Refinement of MnO_2 and MgF_2* . Acta Crystallographica Section B: Structural Crystallography and Crystal Chemistry, 1976. **32**(7): p. 2200-2204.
36. Geller, S., *Structure of $\alpha\text{-Mn}_2\text{O}_3$, $(\text{Mn}_{0.983}\text{Fe}_{0.017})_2\text{O}_3$ and $(\text{Mn}_{0.37}\text{Fe}_{0.63})_2\text{O}_3$ and relation to magnetic ordering*. Acta Crystallographica Section B: Structural Crystallography and Crystal Chemistry, 1971. **27**(4): p. 821-828.
37. Grundy, A.N., B. Hallstedt, and L.J. Gauckler, *Assessment of the Mn-O system*. Journal of phase equilibria, 2003. **24**(1): p. 21-39.
38. Jacob, K., A. Kumar, G. Rajitha, and Y. Waseda, *Thermodynamic data for Mn_3O_4 , Mn_2O_3 and MnO_2* . High Temperature Materials and Processes, 2011. **30**(4-5): p. 459-472.
39. Satomi, K.i., *Oxygen positional parameters of tetragonal Mn_3O_4* . Journal of the Physical Society of Japan, 1961. **16**(2): p. 258-266.
40. Jahn, H.A. and E. Teller, *Stability of polyatomic molecules in degenerate electronic states-I—Orbital degeneracy*. Proceedings of the Royal Society of London. Series A-Mathematical and Physical Sciences, 1937. **161**(905): p. 220-235.

41. McMurdie, H.F. and E. Golovato, *Study of the modifications of manganese dioxide*. Journal of Research of the National Institute of Standards and Technology, 1948. **41**: p. 589-600.
42. Picard, C. and P. Gerdanian, *High temperature study of manganese monoxide*. Journal of Solid State Chemistry France, 1974. **11**: p. 190-202.
43. Fritsch, S. and A. Navrotsky, *Thermodynamic properties of manganese oxides*. Journal of the American Ceramic Society, 1996. **79**(7): p. 1761-1768.
44. Zaki, M., M. Hasan, L. Pasupulety, and K. Kumari, *Thermochemistry of manganese oxides in reactive gas atmospheres: Probing catalytic MnO_x compositions in the atmosphere of CO+O₂*. Thermochimica acta, 1998. **311**(1-2): p. 97-103.
45. Wang, M. and B. Sundman, *Thermodynamic assessment of the Mn-O system*. Metallurgical Transactions B, 1992. **23**(6): p. 821-831.
46. Kissinger, H., H. McMurdie, and B. Simpson, *Thermal decomposition of manganous and ferrous carbonates*. Journal of the American Ceramic Society, 1956. **39**(5): p. 168-172.
47. Dubois, M. and M. Urbain, *Hydrates and allotropic variations of manganese sesquioxide*. Cryst. Rev, 1934. **199**: p. 1416-18.
48. Klingsberg, C. and R. ROY, *Solid-Solid and Solid-Vapor Reactions and a New Phase in the System Mn-O*. Journal of the American Ceramic Society, 1960. **43**(12): p. 620-626.
49. Pankratz, L., *Thermodynamic properties of elements and oxides*. United States Bureau of Mines Bull., 1982. **509**.
50. Ingraham, T., *Thermodynamics of the Mn-SO system between 1000 K and 1250 K*. Canadian Metallurgical Quarterly, 1966. **5**(2): p. 109-122.
51. Southard, J. and G. Moore, *High-temperature Heat Content of Mn₃O₄, MnSiO₃ and Mn₃C*. Journal of the American Chemical Society, 1942. **64**(8): p. 1769-1770.
52. Van Hook, H. and M. Keith, *The system Fe₃O₄-Mn₃O₄*. American Mineralogist: Journal of Earth and Planetary Materials, 1958. **43**(1-2): p. 69-83.
53. Irani, K., A. Sinha, and A. Biswas, *Effect of temperature on the structure of manganites*. Journal of Physics and Chemistry of Solids, 1962. **23**(6): p. 711-727.
54. Schmier, A. and G. Sterr, *Beitrag zur Kenntnis der Hausmannitphase*. Zeitschrift für anorganische und allgemeine Chemie, 1966. **346**(3-4): p. 181-187.
55. Rao, A.R. and V. Tare, *Determination of Free Energy of Formation, Heat and Temperature of Transformation of Mn₃O₄*. Trans. Inst. Mining Metall, 1973. **82**: p. C34-37.
56. Trömel, G., W. Fix, K. Koch, and F. Schaberg, *The Phase Diagram of the Manganese-Oxygen System*. Erzmetall, 1976. **29**: p. 234-237.

57. Metselaar, R., R. Van Tol, and P. Piercy, *The electrical conductivity and thermoelectric power of Mn_3O_4 at high temperatures*. Journal of Solid State Chemistry, 1981. **38**(3): p. 335-341.
58. Keller, M. and R. Dieckmann, *Defect Structure and Transport Properties of Manganese Oxides:(II) The Nonstoichiometry of Hausmannite ($Mn_{3-\delta}O_4$)*. Berichte der Bunsengesellschaft für physikalische Chemie, 1985. **89**(10): p. 1095-1104.
59. Dorris, S. and T.O. Mason, *Electrical properties and cation valencies in Mn_3O_4* . Journal of the American Ceramic Society, 1988. **71**(5): p. 379-385.
60. Driessens, F., *Place and valence of the cations in Mn_3O_4 and some related manganates*. Inorganica Chimica Acta, 1967. **1**: p. 193-201.
61. McClure, D.S., *The distribution of transition metal cations in spinels*. Journal of Physics and Chemistry of Solids, 1957. **3**(3-4): p. 311-317.
62. Dunitz, J.t. and L. Orgel, *Electronic properties of transition-metal oxides-II: cation distribution amongst octahedral and tetrahedral sites*. Journal of Physics and Chemistry of Solids, 1957. **3**(3-4): p. 318-323.
63. Irani, K., A. Sinha, and A. Biswas, *Crystal distortion in spinels containing Mn^{3+} ions*. Journal of Physics and Chemistry of Solids, 1960. **17**(1-2): p. 101-111.
64. Sinha, A., N. Sanjana, and A. Biswas, *On the structure of some anganites*. Acta Crystallographica, 1957. **10**(6): p. 439-440.
65. Seehra, M., V. Singh, S. Thota, B. Prasad, and J. Kumar, *Synthesis and magnetic properties of nanocrystals of cubic defect spinel $MgMnO_3$* . Applied Physics Letters, 2010. **97**(11): p. 112507.
66. Miyai, Y., K. Ooi, and S. Katoh, *Preparation and ion-exchange properties of ion-sieve manganese oxide based on Mg_2MnO_4* . Journal of colloid and interface science, 1989. **130**(2): p. 535-541.
67. Kasper, J. and J. Prener, *The crystal structure of Mg_6MnO_8* . Acta Crystallographica, 1954. **7**(3): p. 246-248.
68. Barkhatov, V.P., Y.V. Golikov, A.G. Zalazinskii, V.F. Balakirev, and G.I. Chufarov, *System Mg-Mn-O*. Dokl. Chem., 1980. **252**(2): p. 370-370.
69. Riboud, P. and A. Muan, *Melting Relations of CaO-Manganese Oxide and MgO-Manganese Oxide Mixtures in Air*. Journal of the American Ceramic Society, 1963. **46**(1): p. 33-36.
70. Joshi, S., C. Silva, P. Wang, Y. Mozharivskyj, and A. Petric, *Copper-Magnesium-Manganese spinel coatings for solid oxide fuel cell interconnects*. Journal of The Electrochemical Society, 2014. **161**(3): p. F233-F238.
71. Panda, S.K. and I.H. Jung, *Critical Evaluation and Thermodynamic Modeling of the Mg-Mn-O (MgO - MnO - MnO_2) System*. Journal of the American Ceramic Society, 2014. **97**(10): p. 3328-3340.

72. Ling, C. and F. Mizuno, *Phase stability of post-spinel compound AMn_2O_4 ($A = Li, Na, \text{ or } Mg$) and its application as a rechargeable battery cathode*. Chemistry of Materials, 2013. **25**(15): p. 3062-3071.
73. Cabello, M., R. Alcantara, F. Nacimiento, G. Ortiz, P. Lavela, and J. Tirado, *Electrochemical and chemical insertion/deinsertion of magnesium in spinel-type $MgMn_2O_4$ and $\lambda\text{-}MnO_2$ for both aqueous and non-aqueous magnesium-ion batteries*. CrystEngComm, 2015. **17**(45): p. 8728-8735.
74. Huie, M.M., D.C. Bock, E.S. Takeuchi, A.C. Marschilok, and K.J. Takeuchi, *Cathode materials for magnesium and magnesium-ion based batteries*. Coordination Chemistry Reviews, 2015. **287**: p. 15-27.
75. Yin, J., A.B. Brady, E.S. Takeuchi, A.C. Marschilok, and K.J. Takeuchi, *Magnesium-ion battery-relevant electrochemistry of $MgMn_2O_4$: crystallite size effects and the notable role of electrolyte water content*. Chemical Communications, 2017. **53**(26): p. 3665-3668.
76. Rajput, N.N., X. Qu, N. Sa, A.K. Burrell, and K.A. Persson, *The coupling between stability and ion pair formation in magnesium electrolytes from first-principles quantum mechanics and classical molecular dynamics*. Journal of the American Chemical Society, 2015. **137**(9): p. 3411-3420.
77. Rosenberg, M., P. Nicolau, R. Manaila, and P. Păușescu, *Preparation, electrical conductivity and tetragonal distortion of some manganite-systems*. Journal of Physics and Chemistry of Solids, 1963. **24**(12): p. 1419-1434.
78. Mănăilă, R. and P. Păușescu, *Structural changes in $MgMn_2O_4$ at high temperatures*. physica status solidi (b), 1965. **9**(2): p. 385-394.
79. Yagi, S., Y. Ichikawa, I. Yamada, T. Doi, T. Ichitsubo, and E. Matsubara, *Synthesis of binary magnesium–transition metal oxides via inverse coprecipitation*. Japanese Journal of Applied Physics, 2013. **52**(2R): p. 025501.
80. Wojtowicz, P.J., *Theoretical model for tetragonal-to-cubic phase transformations in transition metal spinels*. Physical Review, 1959. **116**(1): p. 32.
81. Kanamori, J., *Crystal distortion in magnetic compounds*. Journal of Applied Physics, 1960. **31**(5): p. S14-S23.
82. Rosenberg, M. and P. Nicolau, *Electrical properties and cation migration in $MgMn_2O_4$* . physica status solidi (b), 1964. **6**(1): p. 101-110.
83. Barkhatov, V., V. Balakirev, Y.V. Golikov, and E. Kostitsin, *X-ray diffraction investigation of cation distribution in high-temperature cubic spinels of the Mg-Mn-O system*. physica status solidi (a), 1983. **76**(1): p. 57-63.
84. Malavasi, L., P. Ghigna, G. Chiodelli, G. Maggi, and G. Flor, *Structural and transport properties of $Mg_{1-x}Mn_xMn_2O_{4+\delta}$ spinels*. Journal of Solid State Chemistry, 2002. **166**(1): p. 171-176.

85. Radhakrishnan, N. and A. Biswas, *A neutron diffraction study of the cation migration in $MgMn_2O_4$* . *physica status solidi (a)*, 1976. **37**(2): p. 719-722.
86. Azzoni, C.B., M.C. Mozzati, L. Malavasi, P. Ghigna, and G. Flor, *Magnetic and X-ray diffraction investigation on $Mg_{1-x}Mn_{2+x}O_4$ spinels*. *Solid state communications*, 2001. **119**(10-11): p. 591-595.
87. Kim, J.-S., W.-S. Chang, R.-H. Kim, D.-Y. Kim, D.-W. Han, K.-H. Lee, S.-S. Lee, and S.-G. Doo, *High-capacity nanostructured manganese dioxide cathode for rechargeable magnesium ion batteries*. *Journal of Power Sources*, 2015. **273**: p. 210-215.
88. Rahman, M. and D. Gerosa, *Synthesis and characterization of cathode material for rechargeable magnesium battery technology*. *Optoelectronics and Advanced Materials-Rapid Communications*, 2015. **9**(9-10): p. 1204-1207.
89. Liu, G., Q. Chi, Y. Zhang, Q. Chen, C. Zhang, K. Zhu, and D. Cao, *Superior high rate capability of $MgMn_2O_4$ /rGO nanocomposites as cathode materials for aqueous rechargeable magnesium ion batteries*. *Chemical Communications*, 2018. **54**(68): p. 9474-9477.
90. Garg, N., K.V. Ramanujachary, S.E. Lofland, and A.K. Ganguli, *Nanostructured dimagnesium manganese oxide (Spinel): Control of size, shape and their magnetic and electro catalytic properties*. *Journal of Solid State Chemistry*, 2013. **197**: p. 392-397.
91. Jensen, G. and O. Nielsen, *The magnetic structure of Mn_3O_4 Hausmannite between 4.7 K and Neel point, 41 K*. *Journal of Physics C: Solid State Physics*, 1974. **7**(2): p. 409.
92. Suzuki, K., *X-ray studies on precipitation of metastable centers in mixed crystals $NaCl-CdCl_2$* . *Journal of the Physical Society of Japan*, 1961. **16**(1): p. 67-78.
93. Christ, C. and J.R. Clark, *The crystal structure of murdochite*. 1955, Mineralogical Society of America.
94. Fahey, J.J., *Murdochite, a new copper lead oxide mineral*. *American Mineralogist: Journal of Earth and Planetary Materials*, 1955. **40**(9-10): p. 905-906.
95. Porta, P. and M. Valigi, *Magnetic and optical investigation of Mg_6MnO_8* . *Journal of Solid State Chemistry*, 1973. **6**(3): p. 344-347.
96. Taguchi, H., A. Ohta, M. Nagao, H. Kido, H. Ando, and K. Tabata, *Crystal structure and magnetic properties of $(Mg_{6-x}Li_x)MnO_8$* . *Journal of Solid State Chemistry*, 1996. **124**(2): p. 220-223.
97. Chamberland, B., A. Sleight, and J. Weiher, *Preparation and characterization of $MgMnO_3$ and $ZnMnO_3$* . *Journal of Solid State Chemistry*, 1970. **1**(3-4): p. 512-514.
98. Bertaut, E. and F. Forrat, *Structure and ferrimagnetism of the ilmenite compound $MnNiO_3$* . *Journal of Applied Physics*, 1958. **29**(3): p. 247-248.

99. Swoboda, T., R. Toole, and J. Vaughan, *New magnetic compounds of the ilmenite-type structure*. Journal of Physics and Chemistry of Solids, 1958. **5**(4): p. 293-298.
100. Arjomand, M. and D. Machi, *The preparation and magnetic properties of ternary oxides ABO_3 (A= alkaline earth metal, B= Ti, Zr, Mn, Fe, Co) and quaternary oxides $ATi_{1-x}(Zr_{1-x})B_xO_3$* . Journal of the Less Common Metals, 1978. **61**(1): p. 133-149.
101. Pavlyuchkov, D., D. Dilner, G. Savinykh, and O. Fabrichnaya, *Phase equilibria in the ZrO_2 - MgO - MnO_x system*. Journal of the American Ceramic Society, 2016. **99**(9): p. 3136-3145.
102. Thota, S., K. Singh, B. Prasad, J. Kumar, C. Simon, and W. Prellier, *Formation mechanism, optical and magneto-dielectric studies of new cubic spinel $MgMnO_3$* . AIP Advances, 2012. **2**(3): p. 032140.
103. Singh, V., M. Seehra, A. Manivannan, and P. Kumta, *Magnetic characteristics of a new cubic defect spinel $Li_{0.5}Mg_{0.5}MnO_3$* . Journal of Applied Physics, 2012. **111**(7): p. 07E302.

Chapter 2: Experimental techniques

2.1 Solid state synthesis

Samples were prepared by solid-state synthesis using precursors (with their respective drying temperature) as shown in table 2.1. Reagents were weighed in their stoichiometric amounts, mixed and ground with acetone in an agate mortar and pestle for 45 minutes to form a paste. The mixtures were then put in gold/platinum boats and heated in a muffle furnace at 650 °C to 1000 °C before slowly cooling to room temperature at 5 °C/min.

Table 2.1 Reagents, purity, supplier and drying temperature

Reagent	Purity	Supplier	Drying temperature (°C)
Li ₂ CO ₃	≥ 99%	Sigma Aldrich	180
MnO ₂	≥ 99%	Sigma Aldrich	180
Mg(NO ₃) ₂ ·6H ₂ O	≥ 99%	Sigma Aldrich	-

2.2 X-ray diffraction (XRD)

XRD is an important technique that is widely used in solid state chemistry for qualitative and quantitative analysis. It is also known as the *fingerprint* technique for the qualitative identification of crystalline phase(s) or compound(s) presents which is done by comparing with the known diffraction patterns in the database. In this case, the reference used was the *Powder Diffraction File* (PDF) compiled by the International Center for Diffraction Data (ICDD) that contains more than 350,000 diffraction patterns to date ^[1]. Usually different crystalline phases have their own unique diffraction pattern but it is not uncommon for them to have similar patterns. In practice, the fingerprint identification of experimental diffraction patterns should focus on the peak positions (i.e. *d*-spacing) with relatively correct intensity and compared with known PDF data. Lattice parameters of a phase or compound can also be measured accurately with an internal

standard for peak position calibration. For quantitative analysis, the peak intensities of a diffraction pattern could be used to determine average crystal structure of the crystalline phase(s) present.

When an incident x-ray beam interacts with matter, the beam can be either absorbed or scattered. The scattered beam can either be diffracted coherently (with same wavelength) or incoherently (with longer wavelength than the incident beam). This coherent scattering is therefore used for x-ray diffraction experiment. When adjacent beams are scattered in-phase, a constructive interference occurs as a result of which satisfy the Bragg's law (figure 2.1) (equation (2.1)).

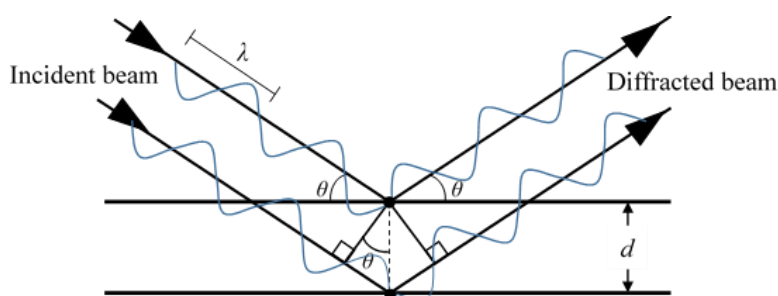


Figure 2.1 Derivation of Bragg's Law ^[2]

$$\text{Bragg's law:} \quad n\lambda = 2d\sin\theta \quad (2.1)$$

where:

- n = order of reflection,
- λ = wavelength of incident beam,
- d = d -spacing,
- θ = Bragg's angle.

In this work, three different diffractometers were used: STOE STADI P X-ray diffractometer with Mo $K\alpha_1$ ($\lambda = 0.7093 \text{ \AA}$) and Cu $K\alpha_1$ ($\lambda = 1.5405 \text{ \AA}$) radiations with linear position sensitive detector (PSD) with 2θ angle range 5° to 40° and 10° to 80° respectively, and *in-situ* high temperature X-ray diffraction (HTXRD) Siemens D5000 with Cu $K\alpha$ radiation ($\lambda = 1.5418 \text{ \AA}$) with 2θ angle range 10° to 90° (table 2.2).

Table 2.2 Diffractometers used, their radiation and analysis

Diffractometer	Radiation	2θ	Analysis
STOE Stadi P	Mo $K\alpha_1$	5~40°	Phase analysis, lattice parameter measurement, structural refinement
STOE Stadi P	Cu $K\alpha_1$	10~80°	Phase analysis
Siemens D5000	Cu $K\alpha_{av}$	10~90°	Phase analysis (<i>in-situ</i>)

In HTXRD, the powdered sample was dispersed sparsely onto a Pt sheet heater and the temperature was monitored through the thermocouple connected to the bottom of the Pt sheet. The heating was done in air with rate of 200 °C/min (3.33 °C/s) and the data were collected after an equilibration time of 3 to 4 hours.

In order to determine the unit cell symmetry, size and shape of a crystalline phase or compound, indexing (assigning Miller indices) of individual Bragg reflection and lattice parameter measurement of a diffraction pattern was done using the software WinXPOW (version 3.0.5 of STOE & Cie GmbH, Germany). A silicon standard of SRM 640e from National Institute of Standard and Technology (NIST) was used as internal standard for 2θ peak position calibration. The indexing and lattice parameter calculation can also be done manually using the $\sin^2\theta$ ratio method by combining Bragg's law (equation (2.1)) and the equation that relates the interplanar spacing and unit cell size (equation (2.2)). However, manual calculation tends to get more tedious and complicated for a lower symmetry lattice type when the angles are not 90° and the use of software is desirable.

The relationship between interplanar spacings, d , adjacent planes (hkl) for a cubic lattice type is given by:

$$\frac{1}{d^2} = \frac{h^2 + k^2 + l^2}{a^2} \quad (2.2)$$

Therefore, combining equation (2.1) and (2.2) would give:

$$\sin^2 \theta = \frac{n^2 \lambda^2}{4a^2} (h^2 + k^2 + l^2) \quad (2.3)$$

where, $\frac{n^2 \lambda^2}{4a^2}$ is constant and by taking the ratio of $\sin^2 \theta$, the values of $(h^2 + k^2 + l^2)$ could be determined.

2.3 Neutron diffraction (ND)

The ND technique is similar to XRD and follows the same Bragg's diffraction law but uses different radiation type that provides different information. It is an expensive technique that utilises a nuclear reactor neutron source or a pulsed spallation neutron source (ISIS, Rutherford-Appleton Laboratory, Oxford) in order to produce a very highly intense neutron beam for *time-of-flight* (TOF) analysis.

Neutrons have no charge and unlike XRD, interact with atomic nuclei instead of with electrons. Therefore, the neutron scattering length is independent of $\sin\theta/\lambda$, and the general decrease in intensity with increasing 2θ angle, as observed in XRD patterns, is no longer observed. In addition, ND can also detect light elements (such as Li, H) better than XRD, since they are strong neutron scatterers, especially in the presence of heavy elements. Neighbouring atoms in the periodic table or ions with similar number of electrons (such as Mg^{2+} and O^{2-}) could also be easily distinguishable using ND, but not using XRD (figure 2.2).

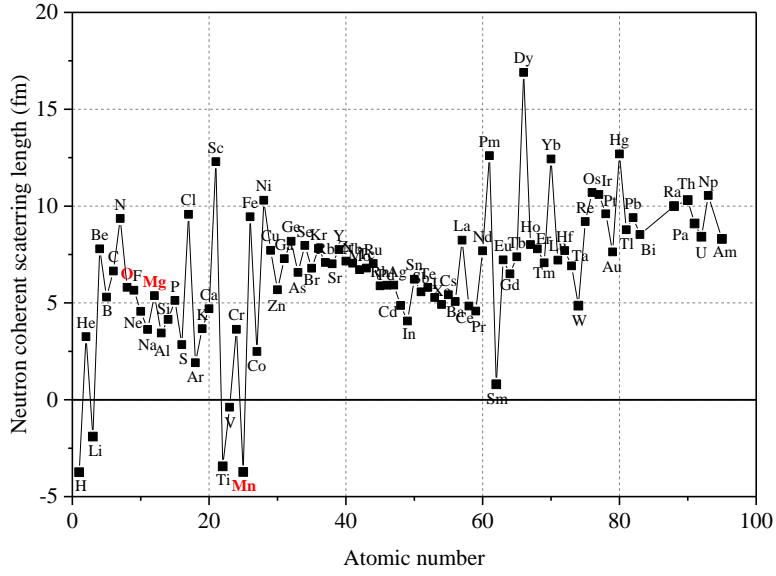


Figure 2.2 Neutron coherent scattering length as a function of atomic number [3]

In TOF [4], the diffraction angle, θ is fixed and the entire neutron spectrum (with variable wavelength, λ) is used. It measures the time taken for neutrons to reach the detector from the source with known distance between the source, the sample and the detector. The neutron wavelength depends on velocity given by the de Broglie relation:

From Planck's equation;

$$E = \frac{hc}{\lambda} \quad (2.4)$$

Einstein's equation;

$$E = mc^2 \quad (2.5)$$

But neutron has mass, therefore $c = v$, de Broglie equation;

$$\lambda = \frac{h}{mv} \quad (2.6)$$

Since $v = L/t$,

$$\lambda = \frac{ht}{mL} \quad (2.7)$$

Substituting equation (2.1) to (2.7);

$$t = \left(\frac{2m}{h}\right) L \sin\theta \cdot d \quad (2.8)$$

where;

t = the total time of flight,

m = the neutron mass,

h = the Planck's constant (6.62607×10^{-34} J/s),

L = the total flight path from source to sample to detector,

θ = half the Bragg scattering angle (2θ),

d = d-spacing

The TOF ND data in this work were collected using the Polaris powder diffractometer with incident wavelength in the range of 0.1 to 6.0 Å. Five separate detector banks were positioned at each side of the beamline to collect the scattered neutron data: three at low angles (10° to 60°), one at right angle (85° to 95°) and one at back scattering angle (130° to 160°). Powder samples were filled into a vanadium canister of volume $\sim 1.5 \text{ cm}^3$. Data were collected over duration of 350 $\mu\text{A h}$ (as a guide, 170 $\mu\text{A h}$ is equivalent to ~ 1 hour in the neutron beam).

2.4 Rietveld refinement ^[5-8]

The Rietveld refinement method was adopted to refine the structure of the crystalline materials. The refinement was done through series of minimisations of the least square calculation to match the calculated theoretical profile to the observed experimental profile (data from XRD or ND) over the whole diffraction pattern. Essentially, a good starting model (relatively similar to the expected structure) is required in order to proceed with the refinement, although this is not always the case (for an unknown structure). The GSAS (General Structure Analysis System) with graphical user interface EXPGUI was used in this work.

A good high resolution XRD or ND data set is often required for the refinement. This is to ensure that all the individual intensities can be determined since the peak's intensities tend to overlap, especially at lower 2θ angle (high d -space). Due to this, a longer data acquisition time (especially using Mo radiation) is essential and since the refinement also includes the background contribution, a good signal to noise ratio is important to avoid any unaccounted peak intensities.

The goodness of fit given by the reliability factor and the difference profile were used as quality indicators in the refinement. The latter is preferred as it can be observed visually. However, expressing them in numerical terms helps to guide the refinement process in the right direction. Therefore, several reliability factors: R_p , R_{wp} , R_{exp} and χ^2 were used to highlight the refinement quality between the calculated and observed data.

R-factor

$$R_p = \frac{\sum_i |y_i (obs) - y_i (calc)|}{\sum_i |y_i (obs)|} \quad (2.9)$$

Weighted R-factor

$$R_{wp} = \left\{ \frac{\sum w_i [y_i (obs) - y_i (calc)]^2}{\sum w_i [y_i (obs)]^2} \right\}^{\frac{1}{2}} \quad (2.10)$$

R-expected

$$R_{exp} = \left\{ \frac{N - P}{\sum w_i [y_i (obs)]^2} \right\}^{\frac{1}{2}} \quad (2.11)$$

Goodness-of-fit

$$\chi^2 = \frac{R_{wp}}{R_{exp}} \quad (2.12)$$

where,	$y_i (obs)$	= observed intensity data at step i
	$y_i (calc)$	= calculated intensity data at step i
	w_i	= weighting factor at step i
	N	= number of observations / data points
	P	= number of parameters

During the refinement, the numerator term in R_p and R_{wp} are minimised. The expression indicates the difference between the observed and calculated data. Both reliability factors are often quoted in the refinement result and usually include the background contribution. The mismatch in intensity between observed and calculated data might contain contributions from structural or instrumentation factors and R_p eliminates the dependencies of the peak profile shape factor. Ideally, the refined R_{wp} values should approach the statistical R_{exp} value but this is not always the case.

Several parameters were used in the refinement as shown below:

1. Scale factor.

The scale factor is the first parameter to be refined as it adjusts the calculated profile to be on the same scale as the observed pattern. Usually, the scale factor is allowed to refine in every cycle of refinement.

2. Background.

The background parameter is used to fit the background of the observed diffraction pattern. Several polynomial functions with different terms are available but the Shifted Chebyshev was preferred since it fit the background rather well with most refinement data. The number of terms initially used was 6 and this could be varied depending on the quality of fit. This parameter was allowed to refine in every cycle of refinement.

3. Unit cell / lattice parameter.

The unit cell parameter is used to fit the Bragg peaks position to the observed diffraction pattern. The peak positions (d -space) are ideally determined by the lattice parameter and the unit cell symmetry. This parameter was also allowed to refine in every cycle of refinement.

4. 2θ zero.

The zero-shift is used for the specimen displacement parameter correction in the transmission geometry. For Bragg-Brentano setup, the shift (shft) and / or transparency (trns) parameter should be refined instead.

For ND, DIFA can be refined instead of 2θ zero and is dependent on the detector bank position.

5. Profile parameters (peak-shape function).

The peak-shape profile is governed by the sample and instrumental factors and is usually best described using the pseudo-Voigt function (combination of Gaussian and Lorentzian functions).

$$\text{Gaussian:} \quad \text{FWHM}^2 = U \tan^2 \theta + V \tan \theta + W \quad (2.13)$$

$$\text{Lorentzian:} \quad \text{FWHM} = X \tan \theta + Y / \cos \theta \quad (2.14)$$

where FWHM is the full width of a Bragg peak at half maximum of its height and U, V, W, X and Y terms are related to crystallite size, strain broadening, etc which together, describe the average peak-shapes over the whole pattern. For ND, sig-1, sig-2 and gam-1, gam-2 can be refined instead, which describe the Gaussian and Lorentzian parts of the pseudo-Voigt function.

6. Atomic positions.

The fractional coordinates (x, y, z) of each atom in the unit cell can be refined based on their scattering power (XRD) or scattering length (ND). Normally, atoms in ‘special positions’ (eg. (0, 0, 0) or ($\frac{1}{2}, \frac{1}{2}, \frac{1}{2}$)) cannot be refined as they are fixed by the unit cell symmetry. If more than one atom occupies the same site, a constraint can be set up for their atomic positions, occupancies and thermal parameters.

7. Fractional occupancies.

The fractional occupancies of each atom in the unit cell can be refined to check the possibility of partial replacement by other atoms or the presence of site-vacancies. An occupancy constraint can be applied if more than one atom

occupies the same site and the sum of the individual occupancy should equal 1 on the assumption that the site is fully occupied.

8. Thermal displacement coefficient.

The thermal parameter, U_{iso} (\AA^2), is a measure of the magnitude of an atom's vibration/ displacement at a particular site. A high U_{iso} value usually indicates that the site may have some vacancies or may require a lighter atom to be present. Thus, thermal parameters are highly correlated to the fractional occupancies and U_{iso} s are usually the last parameter to be refined. The value for the U_{iso} is generally between 0.005 and 0.025 \AA^2 .

A damping factor is applied whenever necessary in the early steps of refinement to avoid the refined model drifting too far away from the initial value which could lead to a false minimum.

2.5 X-ray Absorption Near Edge Structure (XANES) ^[9, 10]

X-rays interact with matter through elastic scattering (as used in x-ray diffraction), inelastic scattering (known as Compton scattering, which contributes to the background radiation) and absorption (electronic transition within atoms). The absorption of x-ray can be used to study the local structure of the material such as the oxidation states, bond lengths and coordination numbers. Thus, the study requires a high energy x-ray source and in this project was conducted at the Diamond Light Source, Oxford.

The XANES technique is used to study the possible oxidation states of elements present in a sample. It uses the absorption edge (usually K -edge) of the electronic structure and compares it with the standard edges. The K -edge in this context represents the minimum energy required to ionise an electron from its $1s$ ground state. In the presence of two components (mixed oxidation states), the K -edge may show the average of the two components. However, this is not a straightforward comparison especially when the reference compound does not have mixed oxidation states to begin with. As the oxidation state increases, the K -edge spectrum is displaced to a higher energy, due to the increase in difficulty to ionise K shell electrons.

In this work, 10 mg of samples were mixed thoroughly with 150 mg of cellulose (Avicel® PH-101 (~ 50 µm particle size) from Sigma Aldrich) in an agate mortar and pestle. Then the samples were pressed in a 13 mm die using a uniaxial press. All the pellets (including the reference pellets) were placed in a plastic holder in the beam line of the instrument. Athena software was used for data analysis ^[11].

Standard samples with known oxidation states of Mn were prepared using the same method described above (table 2.3).

Table 2.3 Standard samples, purity, supplier and their valence(s) used for XANES

Reagent	Purity	Supplier	Valence(s)
MnO ₂	≥ 99%	Sigma Aldrich	4+
Mn ₂ O ₃	99.9%	Sigma Aldrich	3+
Mn ₃ O ₄	97%	Sigma Aldrich	2+, 3+
MnO	99%	Sigma Aldrich	2+

According to the Beer-Lambert law, the transmitted x-ray beam is given by:

$$I_t = I_0 e^{-\mu t} \quad (2.15)$$

where:

I_t = the transmitted intensity

I_0 = the incident beam intensity

μ = linear absorption coefficient

t = thickness of sample

Based on equation (2.15), the linear absorption coefficient is very much dependent on the atomic number, Z and hence the number of electrons. The lower the number of electrons, the more penetrating the x-rays will be and as a result, the linear absorption decreases.

2.6 Thermal analysis ^[2]

Differential scanning calorimetry (DSC) was used to investigate any thermal events that might occur and their reversibility during heating and cooling (figure 2.3). A thermal event can be caused by many factors such as melting, decomposition or a polymorphic transition. It is a powerful technique to study phase diagrams in conjunction with x-ray diffraction.

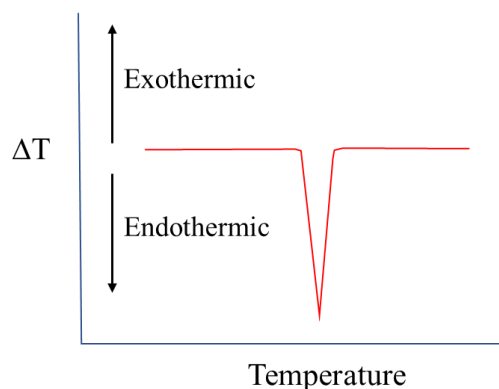
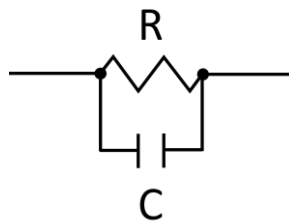


Figure 2.3 A typical DSC endothermic peak profile ^[2]

Samples wrapped in Pt foil were placed in an alumina crucible heated from 25 to 1300 °C at 10 to 50 °C/min heating/cooling rate and the sample temperature compared with that of an inert reference material (in this case an empty alumina crucible). The data were collected using a NETZSCH 404C instrument and analysed using Proteus Analysis software.

2.7 Impedance spectroscopy (IS) ^[12]

Impedance spectroscopy is a non-destructive technique that can be used to measure the electrical properties (normally resistance, R and capacitance, C) of ceramic materials. When a small alternating (AC) voltage was applied over a set frequency range, different electroactive regions/components could be characterised such as grains, grain boundaries and sample-electrode interface. This is because each region/component has its own characteristic time constant, τ , where $\tau = RC$, and this can be represented by a series equivalent circuit of parallel RC elements (figure 2.4).

Figure 2.4 A schematic of a parallel RC element

Since τ is related to frequency, f , the parallel RC element can be further represented by:

$$\omega_{max}RC = 1 \quad (2.16)$$

$$\omega_{max} = 2\pi f_{max} \quad (2.17)$$

where ω_{max} represents the relaxation frequencies of different regions/components (different parallel RC element). What this means is that at low frequency, current will flow mainly through R . As the frequency increases, capacitance becomes more ‘leaky’ and current starts to flow through C . At a certain frequency, f_{max} , equal amounts of current flow through both R and C . Therefore, a wide frequency range is needed to investigate the effect of different electroactive regions/components.

An impedance complex plane plot (also known as a Nyquist plot), Z'' vs Z' , gives a semicircle for a parallel RC element (figure 2.5). The resistance value can be obtained from the intercept on the Z' axis whilst the capacitance value can be calculated from ω_{max} using equation (2.16).

When there is more than one component present, the impedance complex plane plot displays two or more semi-circles. Each semi-circle represents parallel RC element (which represent a component) and they are usually connected in series.

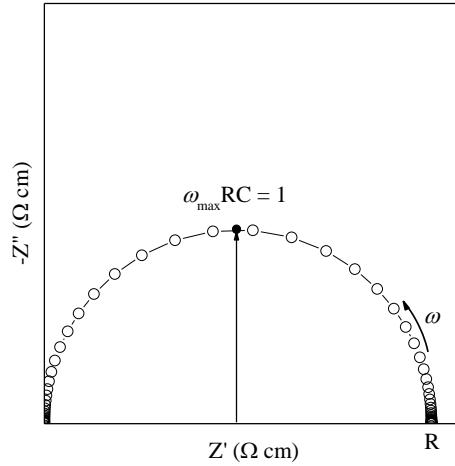


Figure 2.5 A typical impedance complex plane plot for a parallel RC element

Different regions/components give different capacitance values that can be used to identify their electroactive regions. A capacitance is given by:

$$C = \epsilon_0 \epsilon_r \frac{A}{d} \quad (2.18)$$

where: C = Capacitance

ϵ_0 = permittivity of free space ($8.854 \times 10^{-14} \text{ F cm}^{-1}$)

ϵ_r = relative permittivity of sample

A = surface area of sample or electrode contact

d = thickness of region sample or electrode separation

Each region/component has different thickness which as a result would give different capacitance value. Generally, a capacitance value in the order of $10^{-12} \text{ F cm}^{-1}$ is expected (for a material with typical permittivity value of ~ 10) to be associated with the bulk properties of the sample. A summary of capacitance values with their possible electroactive regions is listed in table 2.4.

Impedance data can be represented in different graphical forms: complex impedance plot, Z^* , capacitance vs frequency plot (C' vs f) and combination of impedance and electric modulus vs frequency plot.

Table 2.4 Capacitance values and their possible interpretation ^[12]

Capacitance (F cm ⁻¹)	Responsible regions
10 ⁻¹²	Bulk
10 ⁻¹¹	Minor, second phase
10 ⁻¹¹ - 10 ⁻⁸	Grain boundary
10 ⁻¹⁰ - 10 ⁻⁹	Bulk Ferroelectric
10 ⁻⁹ - 10 ⁻⁷	Surface layer
10 ⁻⁷ - 10 ⁻⁵	Sample - electrode interface
10 ⁻⁴	Electrochemical reactions

In this work, sample powder was mixed with a small amount (10 %) of PVA binder by grinding them in an agate pestle and mortar. Next, the powder was pressed into a pellet with 0.5 tons of pressure using the uniaxial cold press. Then, the sample was sintered at its respective reaction temperature for 10 h in a muffle furnace. The dimensions (thickness and diameter) and weight of the sample were measured. After that, either a gold (Au) or indium gallium (InGa) paste were applied to the opposite faces of the pellet.

If the Au paste was used, the pellet was heated in furnace at 850 °C for 2 h to eliminate any organic component. If InGa was used, the impedance experiments were carried out directly without the necessity to dry the electrode. In and Ga are both two solids at room temperature but become liquid in contact with each other as shown in the phase diagram (figure 2.6). The best ratio for the electrode In:Ga is 0.17:0.83 In:Ga as both solids are transformed into liquid at room temperature at this eutectic composition.

The advantage of using InGa is that it can be applied to a pellet directly after preparation or quenching and measurement can be carried out immediately. However, the disadvantage is that the maximum operating temperature of InGa for impedance measurement is around 200 °C before the electrode loses its integrity.

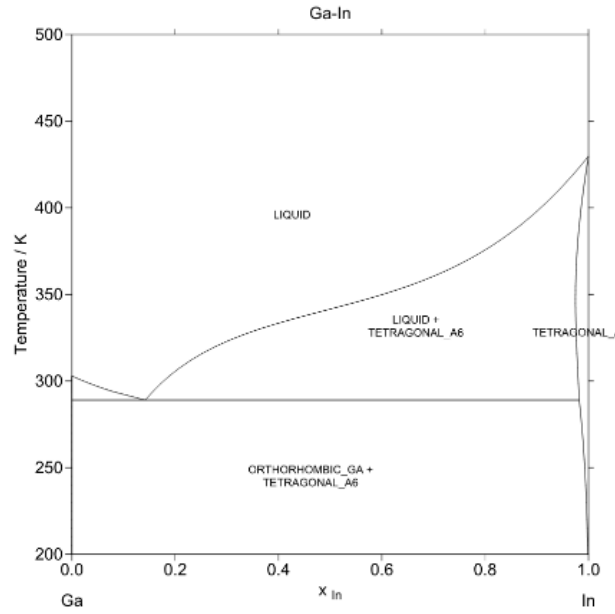


Figure 2.6 Ga-In phase diagram ^[13]

Data were collected using a Solartron Modulab Impedance Analyser with 100mV alternating voltage, over frequency range 10 mHz to 1 MHz. Low temperature impedance measurements were carried out using an Oxford Instrument cryocooler and data collected using an Agilent E4980A Precision LCR meter over the frequency range of 20 Hz to 1 MHz with 100 mV alternating voltage.

2.8 References

1. ICDD (2018) and PDF-4+ 2019 (Database), *International Centre for Diffraction Data*. Newtown Square, Pennsylvania, USA, edited by Dr. Soorya Kabekkodu, 2018.
2. West, A.R., *Solid state chemistry and its applications*. 2014: John Wiley & Sons.
3. Furrer, A., J. Mesot and T. Strässle, *Neutron scattering in condensed matter physics*. 2009: World Scientific Publishing Company.
4. Hull, S., R. Smith, W. David, A. Hannon, J. Mayers, and R. Cywinski, *The POLARIS powder diffractometer at ISIS*. *Physica B: Condensed Matter*, 1992. **180**: p. 1000-1002.
5. McCusker, L., R. Von Dreele, D. Cox, D. Louër, and P. Scardi, *Rietveld refinement guidelines*. *Journal of Applied Crystallography*, 1999. **32**(1): p. 36-50.
6. Toby, B.H., *R factors in Rietveld analysis: how good is good enough?* *Powder diffraction*, 2006. **21**(1): p. 67-70.
7. Finger, L., D. Cox, and A. Jephcoat, *A correction for powder diffraction peak asymmetry due to axial divergence*. *Journal of Applied Crystallography*, 1994. **27**(6): p. 892-900.
8. Buchsbaum, C. and M.U. Schmidt, *Rietveld refinement of a wrong crystal structure*. *Acta Crystallographica Section B: Structural Science*, 2007. **63**(6): p. 926-932.
9. Henderson, G.S., F.M. De Groot, and B.J. Moulton, *X-ray absorption near-edge structure (XANES) spectroscopy*. *Reviews in Mineralogy and Geochemistry*, 2014. **78**(1): p. 75-138.
10. Manceau, A., M.A. Marcus, and S. Grangeon, *Determination of Mn valence states in mixed-valent manganates by XANES spectroscopy*. *American Mineralogist*, 2012. **97**(5-6): p. 816-827.
11. B. Ravel and M. Newville, *ATHENA, ARTEMIS, HEPHAESTUS: data analysis for X-ray absorption spectroscopy using IFEFFIT*, *Journal of Synchrotron Radiation* 12, 537–541 (2005)
12. Irvine, J.T., D.C. Sinclair, and A.R. West, *Electroceramics: characterization by impedance spectroscopy*. *Advanced Materials*, 1990. **2**(3): p. 132-138.
13. Anderson, T. and I. Ansara, *The Ga-In (gallium-indium) system*. *Journal of phase equilibria*, 1991. **12**(1): p. 64-72.

Chapter 3: Synthesis and characterisation of magnesium - doped lithium manganate, Li_2MnO_3

3.1 Introduction

Li_2MnO_3 has been proposed as an alternative source of cathode materials not only due to its high theoretical capacity of 458 mA h g^{-1} but also due to the environmentally benign nature of manganese compared with cobalt or nickel ^[1]. The manganese present in the Li_2MnO_3 exists in the tetravalent state and therefore, it has not been possible to extract Li^+ electrochemically as the manganese is unlikely to be oxidised to Mn^{5+} in the octahedral environment ^[2]. However, some anomalous electrochemical activities have been reported ^[3-5] and several suggestions have been put forward to explain this behaviour.

Pasero *et al.* ^[6] proposed that oxygen deficiency within Li_2MnO_3 was the main cause of partial reduction of Mn^{4+} to Mn^{3+} , which was dependent on the processing conditions. The presence of mixed valency of Mn led to increased electronic conductivity. During electrochemical charging, Mn^{3+} is oxidised to Mn^{4+} , and at the same time, Li^+ ions de-intercalate and diffuse through the electrolyte to the anode. Thus, the anomalous electrochemical activity observed was proposed to be dependent on the amount of Mn^{3+} present in the sample.

The use of Mg as a dopant in the layered rock salt structure (LiCoO_2) has been studied by Tukamoto and West ^[7]. An increase in conductivity by over two orders of magnitude at room temperature was observed. However, discharge capacity shows some reduction as the Mg content increases. This was attributed to the reduction of the Co^{3+} content in the material.

In this work, in order to promote the conductivity of Li_2MnO_3 , Mg was introduced to the undoped sample through solid state synthesis by four possible ionic compensation mechanisms. These involved creation of: Li vacancies, Li interstitials, self-compensation, and O vacancies. Phase analysis was conducted to determine the possible success of doping and the electrical conductivity was measured.

3.2 Experimental

Samples were prepared by solid-state synthesis. Precursors were initially dried overnight to eliminate moisture and stored in a vacuum desiccator (table 3.1). The pristine sample of Li_2MnO_3 was prepared by using Li_2CO_3 and MnO_2 precursors. These precursors were weighed in their stoichiometric compositions based on their calculated molecular weights. Next, they were mixed and ground with acetone using an agate mortar and pestle. Then, these mixtures were put inside a gold (Au) boat and heated over the temperature range 600 to 950°C. Intermittent regrinding and phase analysis was carried out after each temperature step.

Table 3.1 Reagents (all from Sigma Aldrich), their purity and drying temperature

Precursor	Purity	Drying temperature
Li_2CO_3	$\geq 99\%$	180°C
MnO_2	$\geq 99\%$	180°C
$\text{Mg}(\text{NO}_3)_2 \cdot 6\text{H}_2\text{O}$	$\geq 99\%$	-

Four mechanisms of formation were investigated in order to synthesize Mg-doped Li_2MnO_3 (table 3.2). $\text{Mg}(\text{NO}_3)_2 \cdot 6\text{H}_2\text{O}$ was used as the source of MgO. Samples of $m = 0.05$ and 0.10 were prepared for all mechanisms using similar conditions as outlined above. The mixtures were initially heated at 150°C for 4 h, 350°C for 10 h and finally at 650°C for 10 h in order to expel water, NO_2 and CO_2 respectively. Subsequent heating in air for all samples was at 750, 850 and 950 °C for 10 hours with intermediate regrinding and phase analysis.

Table 3.2 Mechanisms of formation to synthesize Mg-doped Li_2MnO_3

	Mechanism of formation	General Formula	Remarks
Join 1	$2\text{Li}^+ \rightarrow \text{Mg}^{2+} + \text{V}_{\text{Li}}'$	$\text{Li}_{2-2m}\text{Mg}_m\text{MnO}_3$	Creation of Li vacancies
Join 2	$\text{Mn}^{4+} \rightarrow \text{Mg}^{2+} + 2\text{Li}^+$	$\text{Li}_{2+2m}\text{Mg}_m\text{Mn}_{1-m}\text{O}_3$	Creation of Li interstitials
Join 3	$2\text{Li}^+ + \text{Mn}^{4+} \rightarrow 3\text{Mg}^{2+}$	$\text{Li}_{2-2m}\text{Mg}_{3m}\text{Mn}_{1-m}\text{O}_3$	Self-compensation
Join 4	$\text{O}^{2-} + \text{Mn}^{4+} \rightarrow \text{Mg}^{2+} + \text{V}_{\text{O}}''$	$\text{Li}_2\text{Mg}_m\text{Mn}_{1-m}\text{O}_{3-m}$	Creation of O vacancies

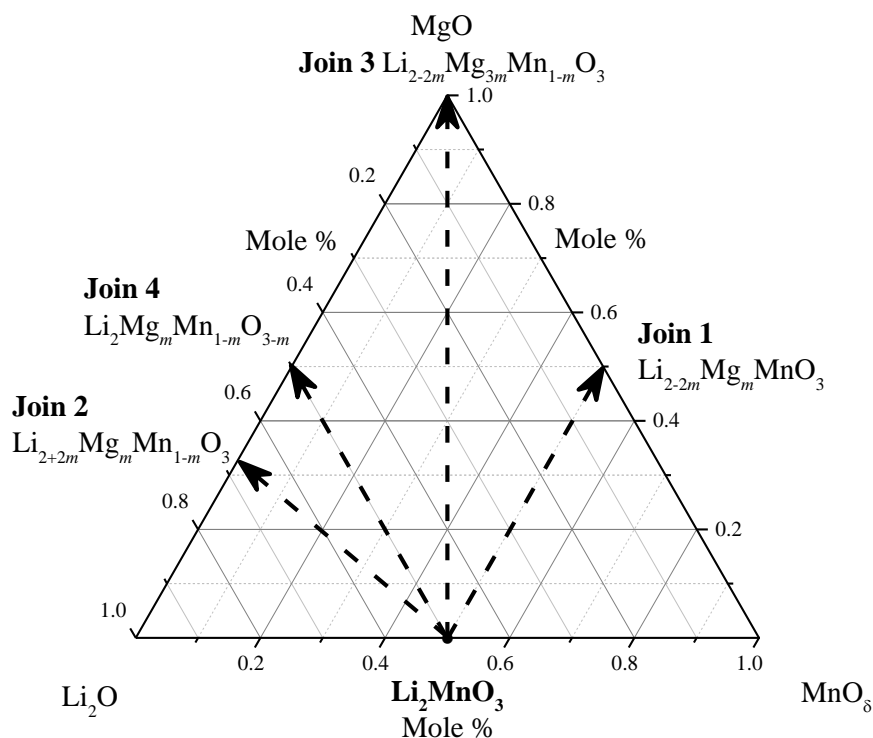


Figure 3.1 A composition triangle $\text{Li}_2\text{O}-\text{MgO}-\text{MnO}_8$ showing the possible solid solution loci of Mg-doped Li_2MnO_3

Phase analysis used a STOE Stadi P x-ray diffractometer, $\text{Mo K}\alpha_1$ ($\lambda = 0.70930\text{\AA}$) with linear position sensitive detector (PSD) at an accelerating voltage of 20 kV and tube current of 5 mA. Data were recorded over the 2θ scan range $5^\circ - 40^\circ$ with a step of 0.1° . Ge monochromator was used to remove $\text{K}\alpha_2$ and $\text{K}\beta$, thus giving monochromatic $\text{K}\alpha_1$ radiation.

Qualitative analysis of the XRD patterns used WinXPOW software package version 3.0.2.1 and PDF-4+ 2014 by comparing with data from the International Centre for Diffraction Data (ICDD).

Pellets of calcined samples were prepared by grinding the powdered samples with a drop of Polyvinyl Alcohol (PVA) binder and pressed using a 10 mm diameter die in a uniaxial press up to 1.0 tons. Pellets were put into Au boats, sintered in air at 1000°C for 10 h and slow-cooled in the furnace to room temperature. Au paste electrodes were printed on opposite faces of the pellets and dried at 800°C for 2 h. Impedance data were

recorded using Solartron Modulab Impedance Analyzer with 100 mV of alternating current (AC) with a frequency range of 10 mHz to 1 MHz.

In order to study the effect of possible oxygen deficiency in the samples, the same pellets were re-sintered at 1000 °C overnight and removed from the furnace in order to “freeze-in” their structure. Their electrical properties were re-measured.

3.3 Phase analysis and characterisation of slow-cooled Li_2MnO_3

3.3.1 Phase analysis of slow-cooled Li_2MnO_3

The XRD patterns of Li_2MnO_3 synthesised at 950°C are shown in figure 3.2. At 950°C , the diffraction peaks are the most intense and the sharpest indicating a well-crystallised material is formed especially for peaks between 9° to $16^\circ 2\theta$ related to Li and Mn ordering in the transition metal layers [2, 8-11]. All peaks at 950°C of the XRD pattern are in good accordance with the reported literature of Li_2MnO_3 (PDF 01-084-8630) [12] – a layered rock salt structure indexed on monoclinic $C2/m$ space group (table 3.3).

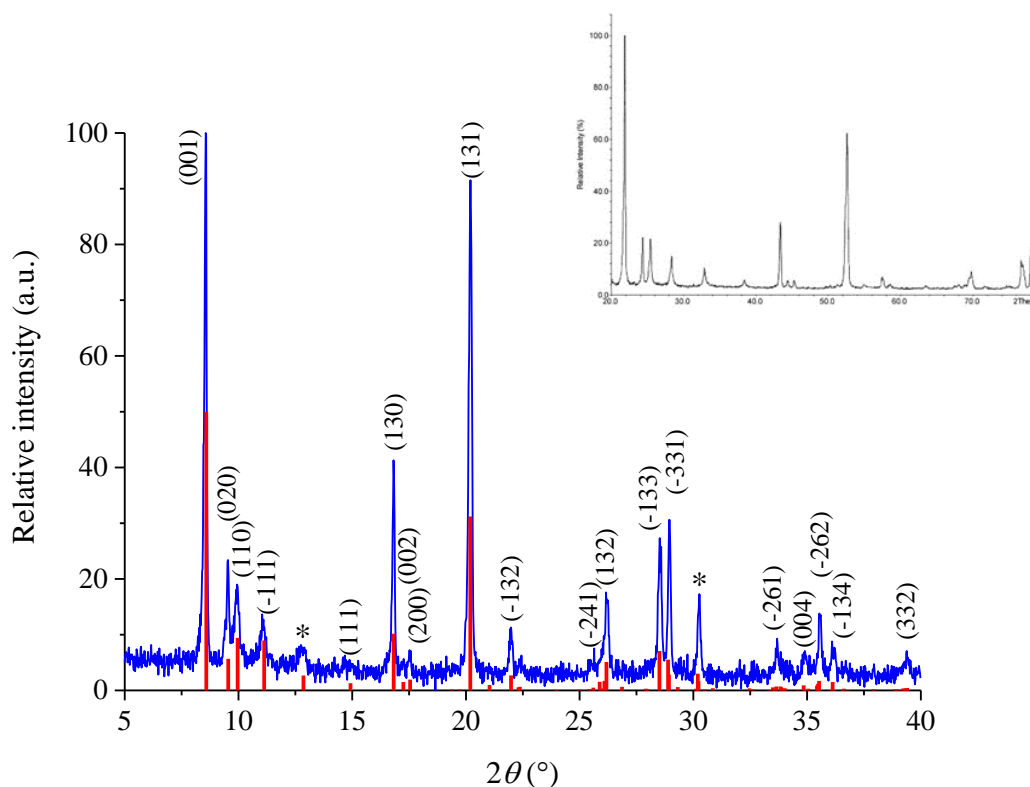


Figure 3.2 XRD pattern for slow-cooled Li_2MnO_3 at 950°C . Vertical red bars indicate the pattern from ICDD PDF 01-084-8630. Inset shows XRD pattern from the literature [6] at 900°C .

Peak (*) was not indexed since it coincides with reference silicon peak

Table 3.3 Indexing data for slow-cooled Li₂MnO₃ heated at 950 °C

No	$2\theta_{\text{obs}}$ (°)	h	k	l	$2\theta_{\text{calc}}$ (°)	$\Delta 2\theta$ (°)	Intensity	d_{obs} (Å)	d_{calc} (Å)
1	8.578	0	0	1	8.583	-0.0044	100.0	4.742	4.740
2	9.548	0	2	0	9.537	0.0112	26.5	4.261	4.266
3	9.966	1	1	0	9.965	0.0010	27.4	4.083	4.083
4	11.091	-1	1	1	11.106	-0.0152	17.5	3.670	3.665
5	14.938	1	1	1	14.949	-0.0109	8.3	2.728	2.726
6	16.810	1	3	0	16.809	0.0012	38.8	2.426	2.426
7	17.205	-1	1	2	17.208	-0.0035	9.2	2.371	2.371
		0	0	2	17.214	-0.0091			2.370
8	17.531	-1	3	1	17.516	0.0151	9.5	2.327	2.329
		2	0	0	17.547	-0.0159			2.325
9	20.182	1	3	1	20.196	-0.0143	82.8	2.024	2.023
10	21.951	-1	3	2	21.937	0.0135	13.7	1.863	1.864
11	24.039	2	2	1	24.030	0.0090	6.2	1.703	1.704
12	25.559	-2	4	1	25.563	-0.0050	7.6	1.603	1.603
13	26.071	-1	5	1	26.058	0.0137	15.0	1.572	1.573
		2	4	0	26.079	-0.0075			1.572
14	26.173	1	3	2	26.187	-0.0133	18.1	1.566	1.566
15	26.816	-3	1	2	26.823	-0.0070	6.7	1.530	1.529
16	27.909	-2	4	2	27.917	-0.0081	6.8	1.471	1.470
17	28.458	-1	3	3	28.459	-0.0002	26.6	1.443	1.443
18	28.885	-3	3	1	28.874	0.0118	35.3	1.422	1.423
		0	6	0	28.882	0.0037			1.422
19	33.605	-2	6	1	33.591	0.0142	9.6	1.227	1.227
		-4	0	1	33.601	0.0044			1.227
20	33.879	3	3	1	33.867	0.0120	7.8	1.217	1.218
21	34.833	-2	2	4	34.821	0.0121	10.0	1.185	1.185
		0	0	4	34.832	0.0005			1.185
22	35.479	-2	6	2	35.459	0.0193	16.2	1.164	1.165
23	36.071	-1	3	4	36.067	0.0046	9.8	1.146	1.146
24	36.587	2	6	1	36.604	-0.0171	6.7	1.130	1.129
25	39.286	3	3	2	39.279	0.0067	8.3	1.055	1.055

Symmetry: Monoclinic, Space group: C2/m, Final 2θ window: 0.02. $a = 4.928$ (2) Å, $b = 8.533$ (3) Å, $c = 5.023$ (2) Å, $\beta = 109.34^\circ$ (2) and Volume = 199.31 (7) Å³

3.3.2 Impedance spectroscopy analysis on slow-cooled Li_2MnO_3

The electrical conductivity on pristine slow-cooled Li_2MnO_3 was determined by impedance spectroscopy analysis. The impedance complex plane, Z^* plot of Li_2MnO_3 and their respective spectroscopic Y' , C' and $-Z''$, M'' plots at two temperatures, 350 and 375 °C are shown in figure 3.3.

The Z^* plots show two semicircles in which the larger high-frequency arc is attributed to the bulk response and the smaller low-frequency arc is attributed to either the grain boundary response or the sample-electrode interface response. The resistance of the sample decreased with increasing temperature as shown by the Z' values.

The conductivity (Y') plots as a function of frequency show two plateaux observed at low and intermediate frequency and a dispersion at high frequency at both temperatures. The high-frequency dispersion could be associated with a power law behaviour.

The capacitance (C') against frequency plots show a nearly frequency independent plateau ($6.2 \times 10^{-13} \text{ F cm}^{-1}$) at higher frequency attributed to the bulk response, followed by a broad dispersion at an intermediate frequency. A capacitance (at $\sim 10^{-8} \text{ F cm}^{-1}$) observed at low frequency could probably represents the sample-electrode interface response.

The Z'' and M'' plots as a function of frequency show two distinct Z'' maxima at low and high frequencies. The low-frequency Z'' maximum may be attributed to the sample-electrode interface response. The nearly coincident peak maxima of Z'' and M'' at higher frequency indicate the bulk response of the sample.

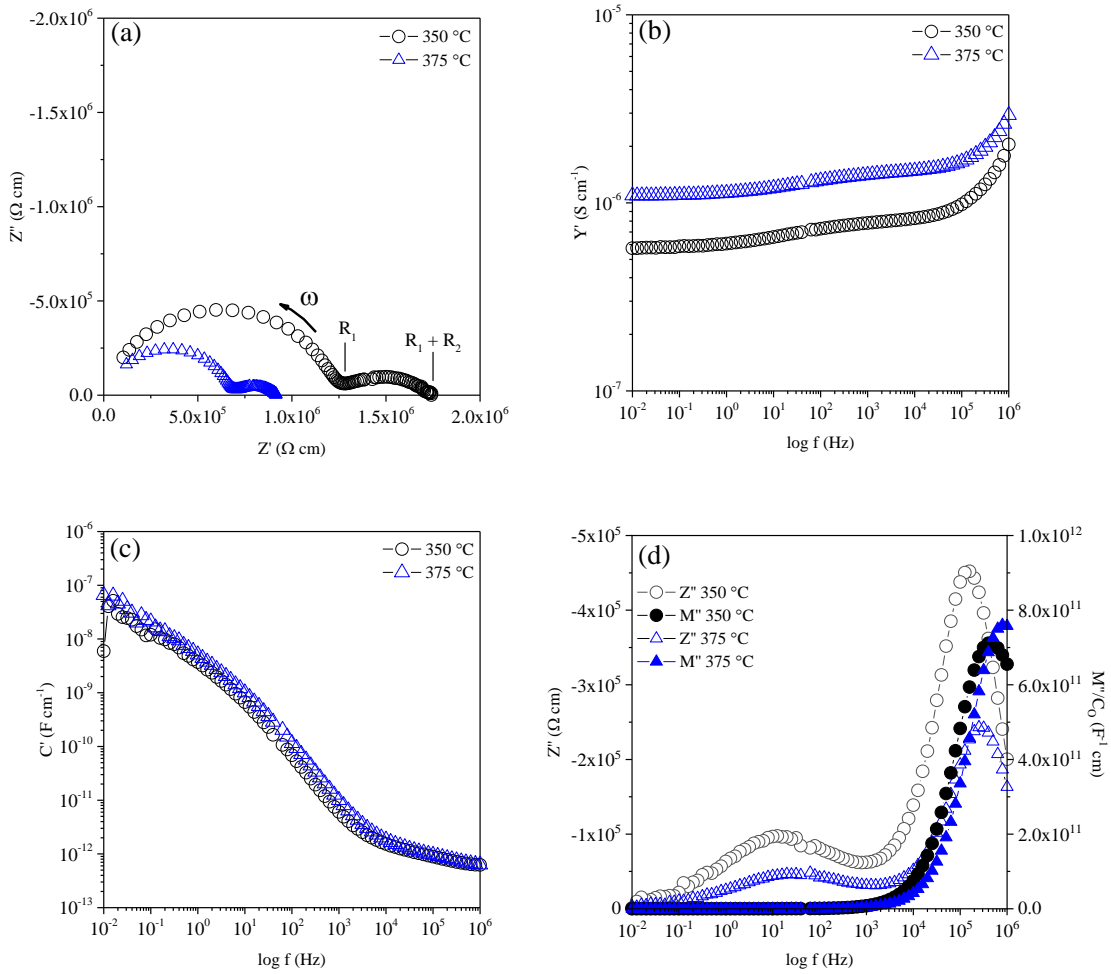


Figure 3.3 Li_2MnO_3 : (a) Impedance complex plane, Z^* plot and spectroscopic plots (b) Y' , (c) C' , (d) $-Z''$ and M'' at 350 °C and 375 °C

3.3.3 Impedance spectroscopy analysis on Li_2MnO_3 quenched from 1000 °C

The impedance complex plane, Z^* plot of Li_2MnO_3 quenched from 1000 °C in air and their respective spectroscopic Y' , C' and $-Z''$ and M'' plots are shown in figure 3.4.

The Z^* plots show a more well-defined large semicircle and a residual tail that becomes a depressed semicircle and finally a nearly flat response at lower frequency range on the Z' axis. The nearly ideal semicircle at 275 °C is attributed to the bulk response (with an associated capacitance of $1.5 \times 10^{-12} \text{ F cm}^{-1}$), together with a residual tail probably attributed to the sample-electrode interface impedance (with the capacitance of $3.4 \times 10^{-8} \text{ F cm}^{-1}$).

The Y' plots as a function of frequency show that there is a nearly frequency independent plateau at the intermediate frequency with a dispersion at a higher frequency at both temperatures. A small low-frequency dispersion can be seen at 300 °C.

The C' against frequency plots show a similar pattern to the slow-cooled sample with a plateau at high frequency attributed to the bulk response, followed by a large dispersion at intermediate frequency. A capacitance observed at low frequency may be attributed to the sample-electrode interface response.

The Z'' and M'' *versus* frequency plots also show similar characteristics to the slow-cooled sample. The lower frequency peaks of Z'' becomes less apparent and the Z'' and M'' maxima at higher frequency show better-overlapping peaks indicating good electrical homogeneity of the sample.

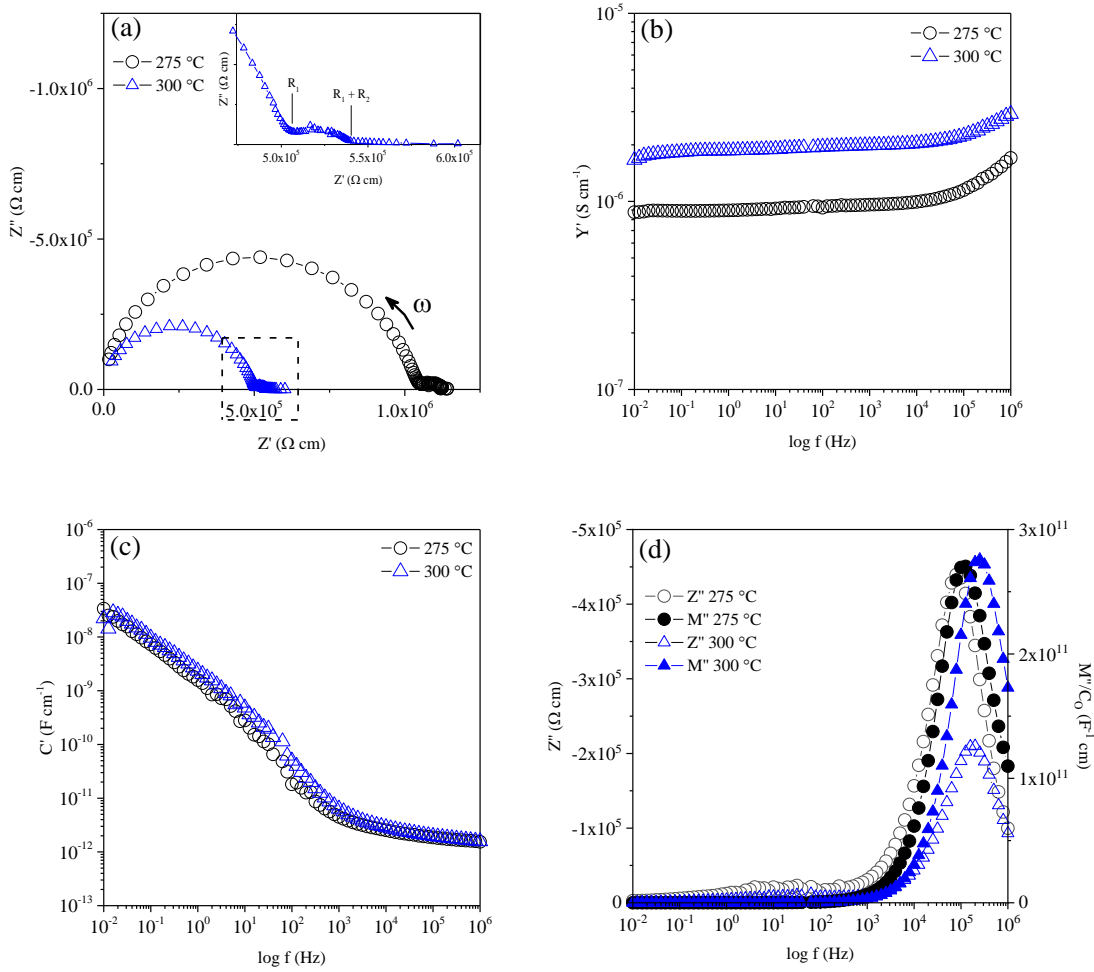


Figure 3.4 Li_2MnO_3 quenched from 1000 °C: (a) Impedance complex plane, Z^* plot (inset showing low frequency response at 300 °C) and spectroscopic plots (b) Y' , (c) C' , (d) $-Z''$ and M'' at 275 °C and 300 °C

3.3.4 Arrhenius plots of Li_2MnO_3

The resistance of the bulk response was extracted from the bulk semicircle at the intercept point on the Z' axis of the Z^* plot and the conductivity were derived from the Arrhenius equation (3.1).

$$\sigma = A \exp\left(\frac{-E_a}{RT}\right) \quad (3.1)$$

where,

σ = Conductivity (S cm^{-1})

E_a = Activation energy (eV)

R = Universal gas constant ($8.314 \text{ J mol}^{-1} \text{ K}^{-1}$)

T = Temperature (K)

A = Constant

Both slow-cooled and quenched Li_2MnO_3 show a linear behaviour on the Arrhenius plot (figure 3.5 (a)). The conductivity of the quenched sample is higher compared to the slow-cooled sample, accompanied by a small reduction in activation energy from 0.835 (4) to 0.75 (1) eV. The increase in conductivity of quenched Li_2MnO_3 is probably associated with the small amount of oxygen loss in the sample. As a result, a partial reduction of Mn^{4+} to Mn^{3+} is expected for electroneutrality. The presence of mixed valence state of Mn thus provides a possible conduction pathway for electron hopping ^[6].

The activation energy (0.75 eV) of the sample quenched in air is in good agreement with the literature data (figure 3.5 (b)), where it lies in-between as-prepared sample (1.28 eV) and sample quenched in mercury (0.11 eV). This shows that the conductivity of any given sample is likely depends on the amount of oxygen content, i.e. synthesis conditions.

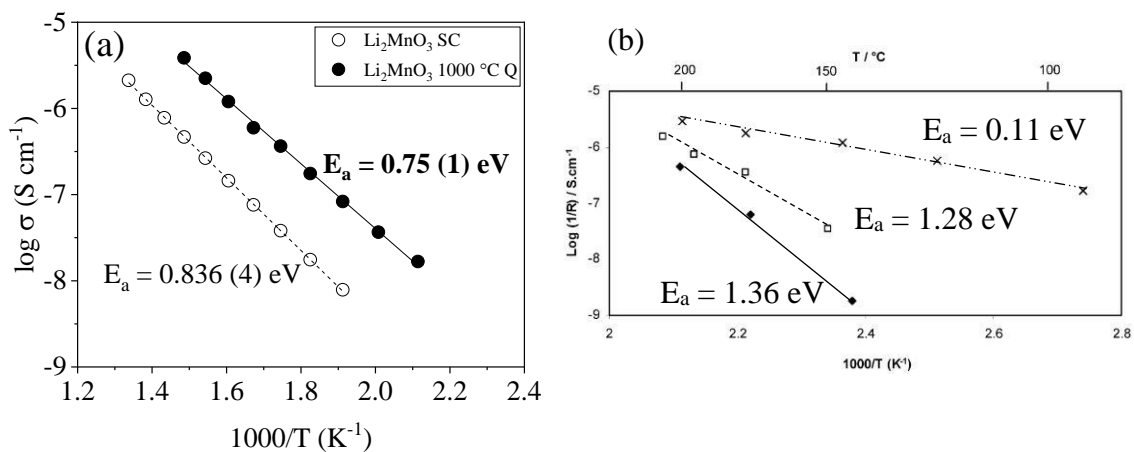


Figure 3.5 Arrhenius plot of Li_2MnO_3 : (a) Slow-cooled (SC) and quenched (Q) from 1000 °C (in air). (b) Literature data ^[6] for sample prepared in different conditions:
 ◆ High O_2 content, □ As-prepared and × Quenched from 1000 °C (into mercury)

3.4 Phase analysis and characterisation of Mg-doped Li_2MnO_3

3.4.1 Synthesis and phase analysis of Mg-doped Li_2MnO_3

The phase analysis summary for 5 and 10 mol % Mg-doped Li_2MnO_3 can be represented in the composition triangle of $\text{Li}_2\text{O-MgO-MnO}_8$ (figure 3.6). A single phase of Mg-doped Li_2MnO_3 was observed on joins 2 and 4 (table 3.4) (figure 3.7).

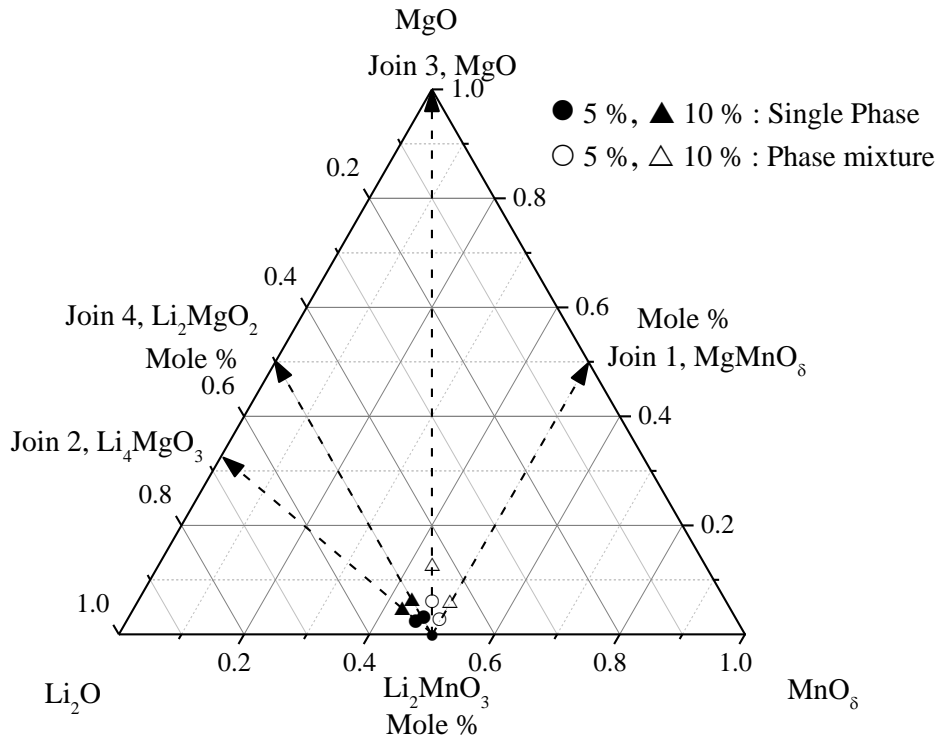


Figure 3.6 A composition triangle of $\text{Li}_2\text{O-MgO-MnO}_8$ showing summary of phase analysis on joins 1 to 4 for Mg-doped Li_2MnO_3

Table 3.4 Results of 10 mol % Mg-doped Li_2MnO_3 at 950°C in air

	Mechanism of formation	Expected formula	Phase(s) present
Join 1	$2\text{Li}^+ \rightarrow \text{Mg}^{2+} + \text{V}_{\text{Li}}'$	$\text{Li}_{1.8}\text{Mg}_{0.1}\text{MnO}_3$	$\text{Li}_2\text{MnO}_3, \text{LiMn}_2\text{O}_4$
Join 2	$\text{Mn}^{4+} \rightarrow \text{Mg}^{2+} + 2\text{Li}^+$	$\text{Li}_{2.2}\text{Mg}_{0.1}\text{Mn}_{0.9}\text{O}_3$	Li_2MnO_3
Join 3	$2\text{Li}^+ + \text{Mn}^{4+} \rightarrow 3\text{Mg}^{2+}$	$\text{Li}_{1.8}\text{Mg}_{0.3}\text{Mn}_{0.9}\text{O}_3$	$\text{Li}_2\text{MnO}_3, \text{MgO}$
Join 4	$\text{O}^{2-} + \text{Mn}^{4+} \rightarrow \text{Mg}^{2+} + \text{V}_{\text{O}}''$	$\text{Li}_2\text{Mg}_{0.1}\text{Mn}_{0.9}\text{O}_{2.9}$	Li_2MnO_3

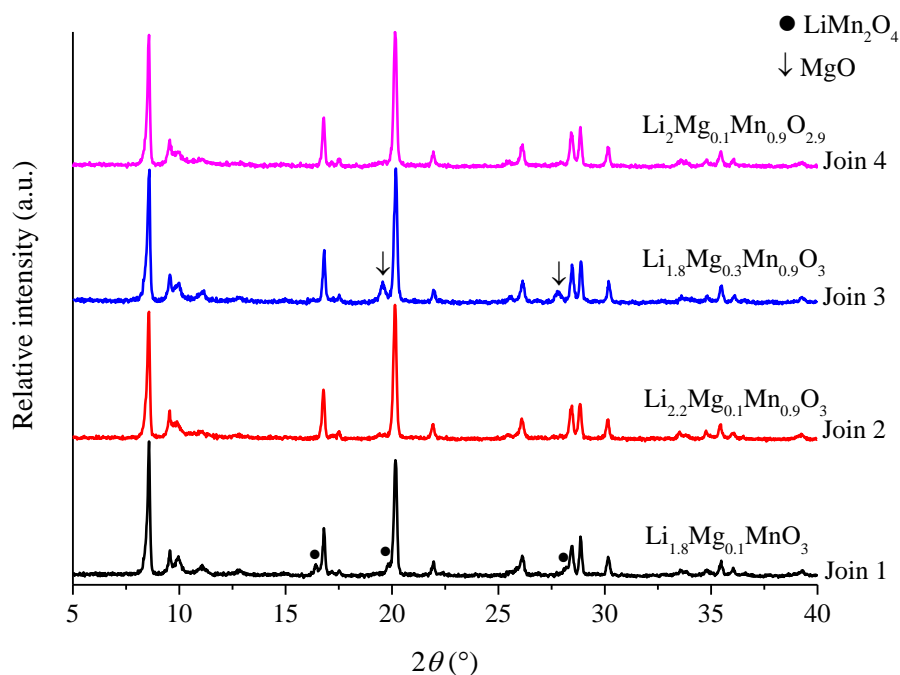


Figure 3.7 Comparison of XRD patterns for join 1 to 4 of 10 mol % Mg-doped Li_2MnO_3 heated at 950 C for 10 h and slowly cooled to room temperature. Phase pure samples were observed for joins 2 and 4

The creation of lithium vacancies on join 1 somehow triggered a possible partial reduction of Mn^{4+} to $\text{Mn}^{3.5+}$ for charge balance, thus causing the formation of secondary phase LiMn_2O_4 . Double cation substitution increased the Mg content in join (3) and resulted in the appearance of MgO as second phase.

Both joins 2 and 4 were indexed using monoclinic space group $C2/m$ and it can be concluded that these compositions were single phase. Table 3.5 shows indexing data for join 2.

The lattice parameters for both joins 2 and 4 for slow-cooled samples were plotted against pristine Li_2MnO_3 (figure 3.8). Both joins show a relatively minimal change in lattice parameter.

Table 3.5 Indexing data for slow-cooled join 2, $\text{Li}_{2.2}\text{Mg}_{0.1}\text{Mn}_{0.9}\text{O}_3$

No	$2\theta_{\text{obs}}$ (°)	h	k	l	$2\theta_{\text{calc}}$ (°)	$\Delta 2\theta$ (°)	Intensity	d_{obs} (Å)	d_{calc} (Å)
1	8.571	0	0	1	8.571	-0.0004	92.3	4.746	4.746
2	9.552	0	2	0	9.543	0.0090	22.7	4.259	4.263
3	9.937	1	1	0	9.935	0.0022	16.5	4.095	4.096
4	11.070	-1	1	1	11.091	-0.0210	11.4	3.677	3.670
5	16.799	1	3	0	16.799	-0.0002	41.1	2.428	2.428
6	17.174	0	0	2	17.190	-0.0161	8.2	2.375	2.373
		-1	1	2	17.195	-0.0210			2.372
7	17.523	-1	3	1	17.514	0.0089	10.4	2.328	2.330
8	20.165	1	3	1	20.170	-0.0051	100.0	2.026	2.025
9	21.944	2	0	1	21.918	0.0261	15.3	1.863	1.866
		-1	3	2	21.932	0.0116			1.864
10	26.140	1	3	2	26.145	-0.0046	20.6	1.568	1.568
11	27.959	1	5	1	27.955	0.0041	8.5	1.468	1.468
12	28.450	-1	3	3	28.445	0.0048	31.7	1.443	1.444
		2	0	2	28.448	0.0018			1.443
13	28.880	0	6	0	28.902	-0.0217	35.6	1.422	1.421
14	33.595	-2	6	1	33.581	0.0141	9.8	1.227	1.228
15	34.811	0	0	4	34.783	0.0277	10.6	1.186	1.187
		-2	2	4	34.794	0.0175			1.186
		-3	5	1	34.818	-0.0069			1.185
16	35.465	-2	6	2	35.455	0.0101	17.2	1.164	1.165
17	36.060	-1	3	4	36.042	0.0171	10.3	1.146	1.146
		2	0	3	36.056	0.0031			1.146
18	36.569	2	6	1	36.566	0.0026	7.4	1.130	1.131
		3	1	2	36.569	0.0000			1.130
19	39.287	-2	6	3	39.312	-0.0252	9.0	1.055	1.054

Symmetry: Monoclinic, Space group: $C2/m$, Final 2θ window: 0.03. $a = 4.946$ (3) Å, $b = 8.527$ (3) Å, $c = 5.027$ (5) Å, $\beta = 109.3^\circ$ (1) and Volume = 200.17 (14) Å³

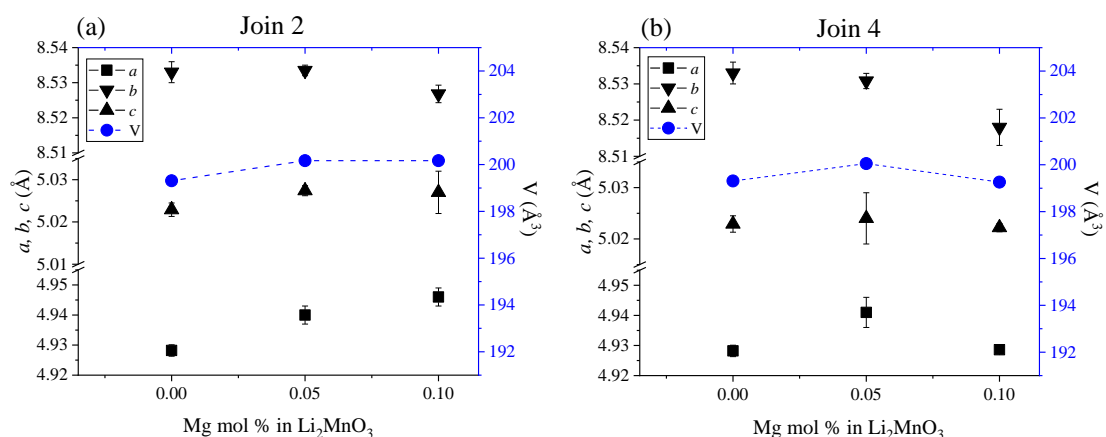


Figure 3.8 Lattice parameter, a , b , c and cell volume, V : (a) join 2, $\text{Li}_{2.2}\text{Mg}_{0.1}\text{Mn}_{0.9}\text{O}_3$ and (b) join 4, $\text{Li}_2\text{Mg}_{0.1}\text{Mn}_{0.9}\text{O}_{2.9}$ slow-cooled from 950 °C

3.4.2 Impedance spectroscopy analysis on slow-cooled 10 mol % Mg-doped Li_2MnO_3

The impedance spectroscopy analysis was conducted on single phase samples: join 2 ($\text{Li}_{2.2}\text{Mg}_{0.1}\text{Mn}_{0.9}\text{O}_3$) and join 4 ($\text{Li}_2\text{Mg}_{0.1}\text{Mn}_{0.9}\text{O}_{2.9}$). The pellets were heated at 950 °C for 10 h and slowly cooled to room temperature.

3.4.2.1 $\text{Li}_{2.2}\text{Mg}_{0.1}\text{Mn}_{0.9}\text{O}_3$ (join 2)

The impedance complex plane, Z^* plot of join 2 $\text{Li}_{2.2}\text{Mg}_{0.1}\text{Mn}_{0.9}\text{O}_3$ and their respective spectroscopic Y' , C' and $-Z''$, M'' plots at two temperatures, 179 and 206 °C are shown in figure 3.9.

The Z^* plots show two semicircles in which the well-defined higher frequency arc is attributed to the bulk response and the smaller low-frequency arc is attributed to either the grain boundary response or the sample-electrode interface response. The absence of a low-frequency spike in the Z^* plot indicating that the mobile charge carrier is dominated by electronic conduction.

The Y' plots as a function of frequency show two nearly same plateaux at intermediate frequency with a dispersion at a higher frequency observed at both temperature.

The C' against frequency plots show a plateau at high frequency attributed to the bulk response ($\sim 1.1 \times 10^{-12} \text{ F cm}^{-1}$), followed by a large dispersion at lower frequency. The low-frequency capacitance of $\sim 10^{-8} \text{ F cm}^{-1}$ may be attributed to the sample-electrode interface response.

The Z'' and M'' versus frequency plots show nearly overlapping peak of Z'' and M'' maxima at high frequency, indicating the bulk response of the sample.

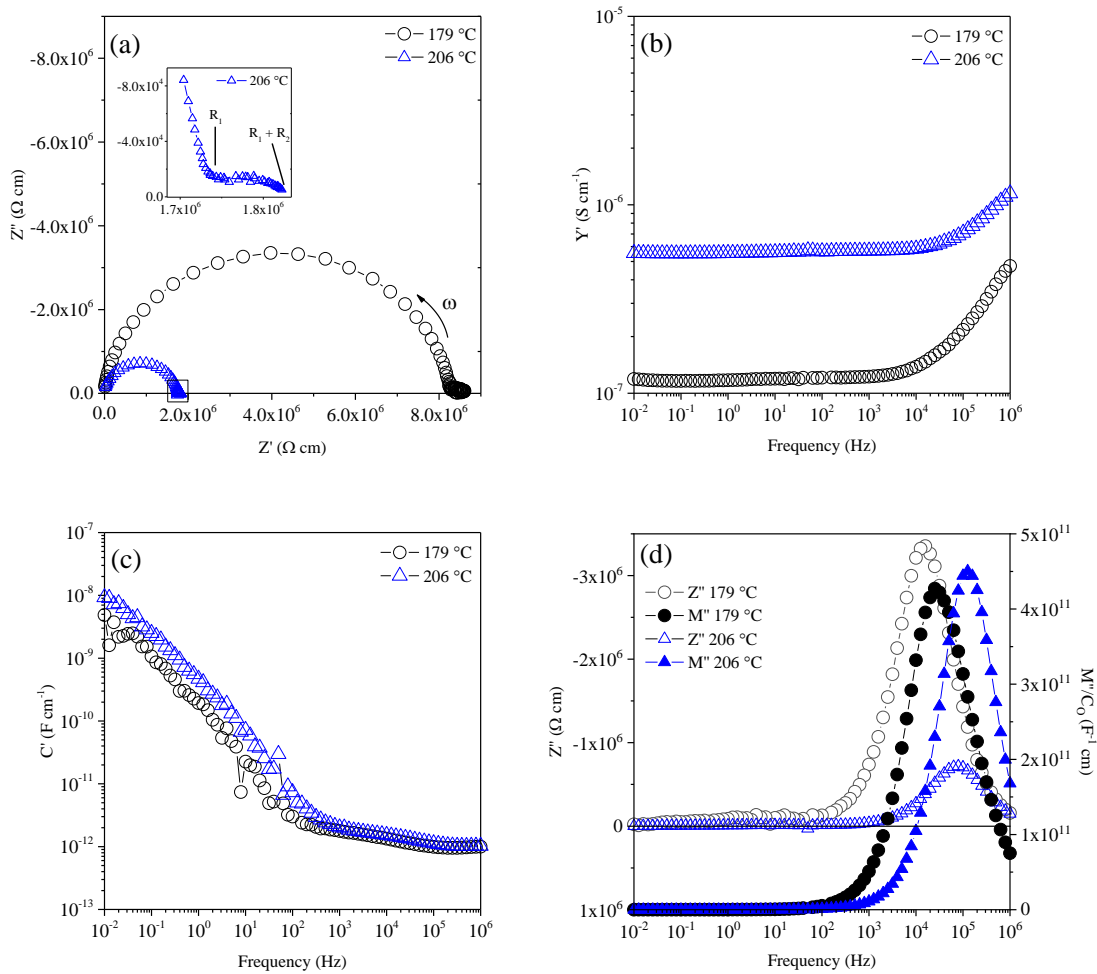


Figure 3.9 $\text{Li}_{2.2}\text{Mg}_{0.1}\text{Mn}_{0.9}\text{O}_3$ (join 2) slow-cooled: (a) Impedance complex plane, Z^* plot (inset shows small low-frequency arc at 206 °C) and spectroscopic plots (b) Y' , (c) C' , (d) $-Z''$ and M'' at 179 °C and 206 °C

3.4.2.2 $\text{Li}_2\text{Mg}_{0.1}\text{Mn}_{0.9}\text{O}_{2.9}$ (join 4)

The impedance complex plane, Z^* plot of join 4 $\text{Li}_2\text{Mg}_{0.1}\text{Mn}_{0.9}\text{O}_{2.9}$ and their respective spectroscopic Y' , C' and $-Z''$, M'' plots at temperatures 125, 150 and 175 °C are shown in figure 3.10.

The Z^* plots show an overlapping of two semicircles which attributed to the grain boundary and the bulk response at low and high frequency respectively. The arc for the grain boundary response is larger than the bulk response.

The Y' plots as a function of frequency show two frequency independent plateaux at intermediate and high frequency.

The C' against frequency plots show two plateaux observed at intermediate and high frequency attributed to the grain boundary and bulk response respectively, followed by a noisy dispersion towards lower frequency.

The Z'' and M'' *versus* frequency plots show separate peak of Z'' and M'' maxima at high frequency. This indicates that the sample does not have electrical homogeneity.

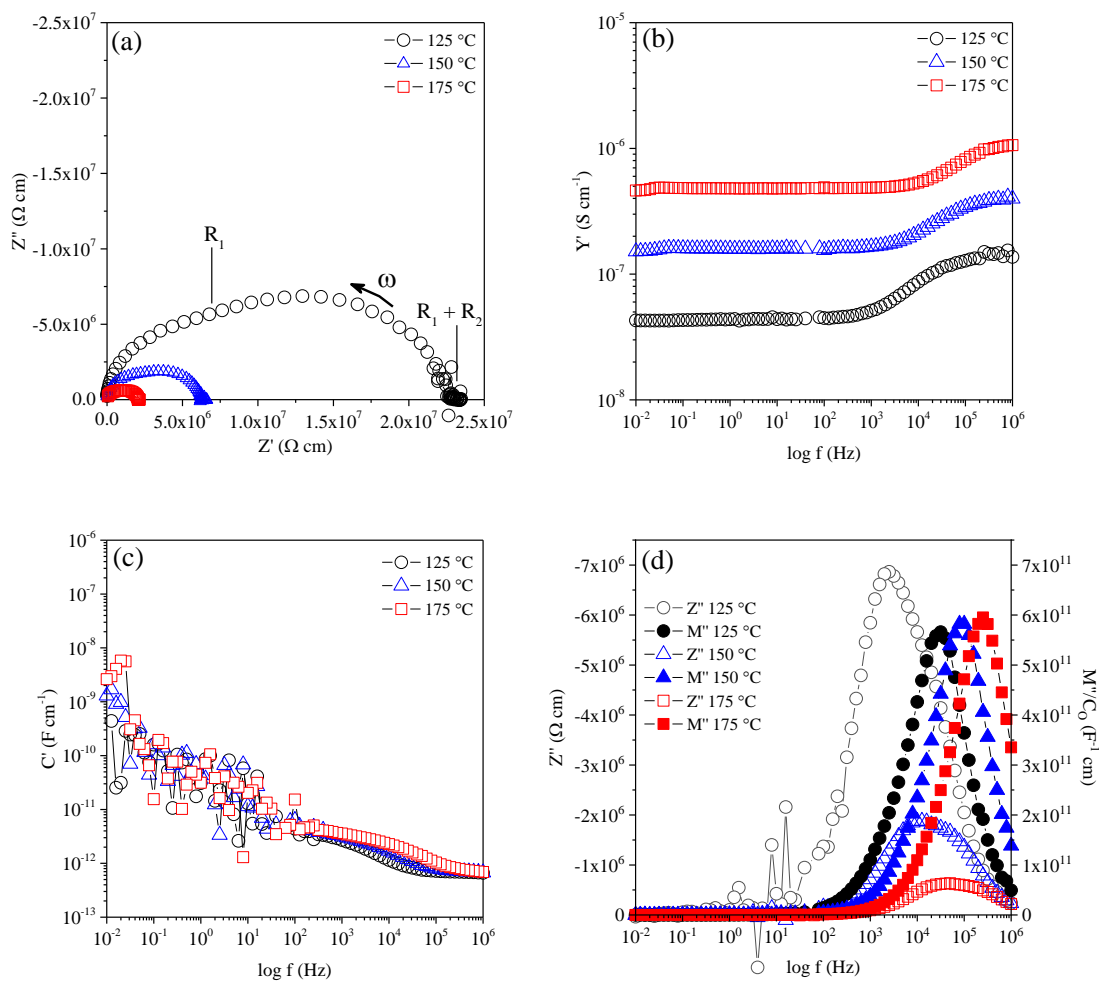


Figure 3.10 $\text{Li}_2\text{Mg}_{0.1}\text{Mn}_{0.9}\text{O}_{2.9}$ (join 4) slow-cooled: (a) Impedance complex plane, Z^* plot and spectroscopic plots (b) Y' , (c) C' , (d) $-Z''$ and M'' at 125 °C, 150 °C and 175 °C

3.4.3 Impedance spectroscopy analysis on quenched 10 mol % Mg-doped Li_2MnO_3

The impedance spectroscopy analysis was conducted on quenched samples: join 2 ($\text{Li}_{2.2}\text{Mg}_{0.1}\text{Mn}_{0.9}\text{O}_3$) and join 4 ($\text{Li}_2\text{Mg}_{0.1}\text{Mn}_{0.9}\text{O}_{2.9}$). The pellets were heated at 1000 °C for 10 h and quenched to room temperature (in air).

The impedance complex plane, Z^* plots of joins 2 and 4 with their respective spectroscopic Y' , C' and $-Z''$, M'' plots are shown in figure 3.11 and figure 3.12 respectively.

The Z^* plots for both quenched samples show similar characteristics. Two arcs were observed which could be attributed to the grain boundary and bulk response at low and high frequency respectively. Again, no low-frequency spike was observed on both samples which could be associated with the ionic conduction. Therefore, the conductivity is dominated by electronic conduction.

The Y' plots as a function of frequency for both samples show two frequency independent plateaux at the intermediate frequency. A high-frequency dispersion was observed and shifted out of the measured window with increasing temperature.

The C' against frequency plots show two plateaux which could be attributed to the bulk and the grain boundary response at high and intermediate frequency respectively. A low-frequency dispersion was noisy at low temperature and the signal became better with increasing temperature as the sample becomes less resistive. The low-frequency capacitance of $\sim 10^{-8}$ to 10^{-7} F cm^{-1} may be attributed to the sample-electrode interface response.

The Z'' and M'' *versus* frequency plots show double peaks on the Z'' spectra and a single peak on the M'' spectra. The low and high-frequency maxima on the Z'' spectra correspond to the grain boundary and bulk response thus indicating the electrical heterogeneity of the sample.

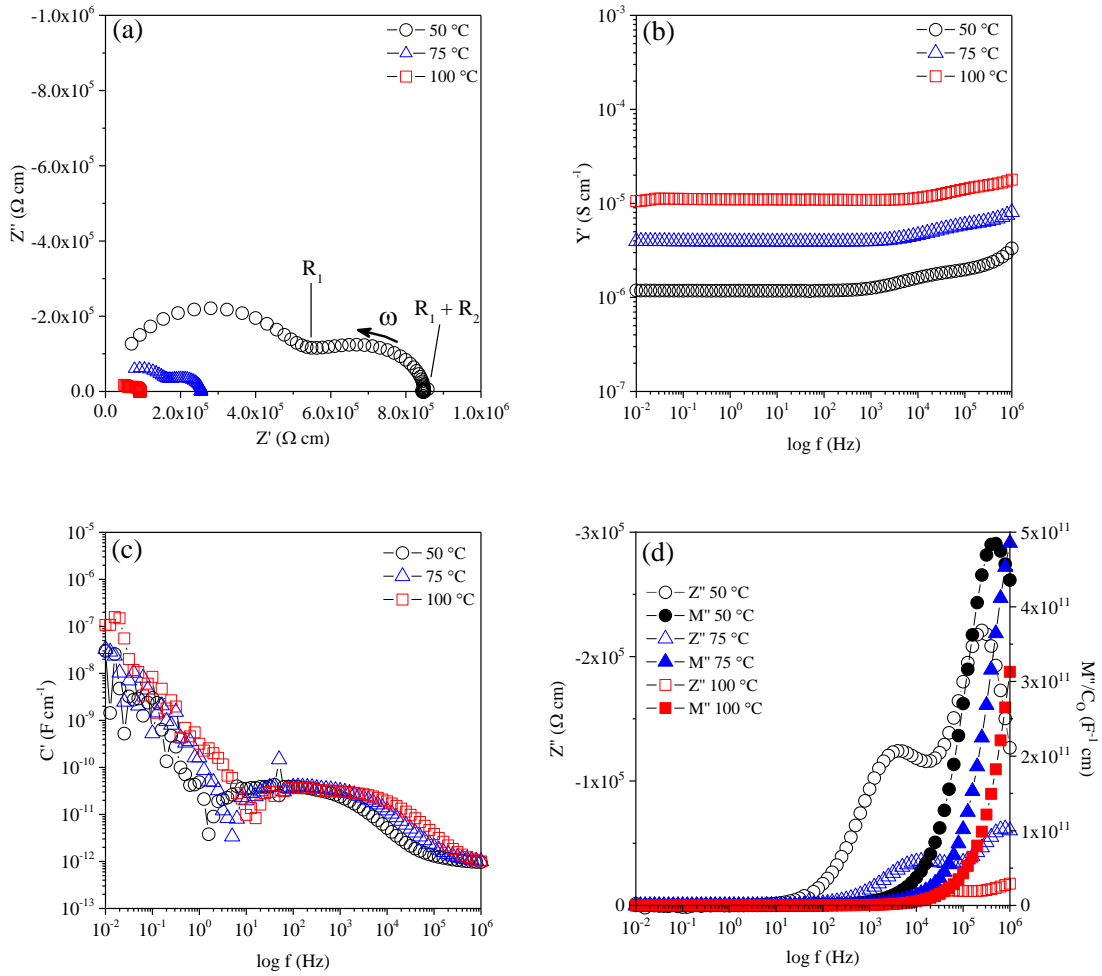


Figure 3.11 $\text{Li}_{2.2}\text{Mg}_{0.1}\text{Mn}_{0.9}\text{O}_3$ (join (2)) quenched: (a) Impedance complex plane, Z^* plot and spectroscopic plots (b) Y' , (c) C' , (d) $-Z''$ and M'' at 50 °C, 75 °C and 100 °C

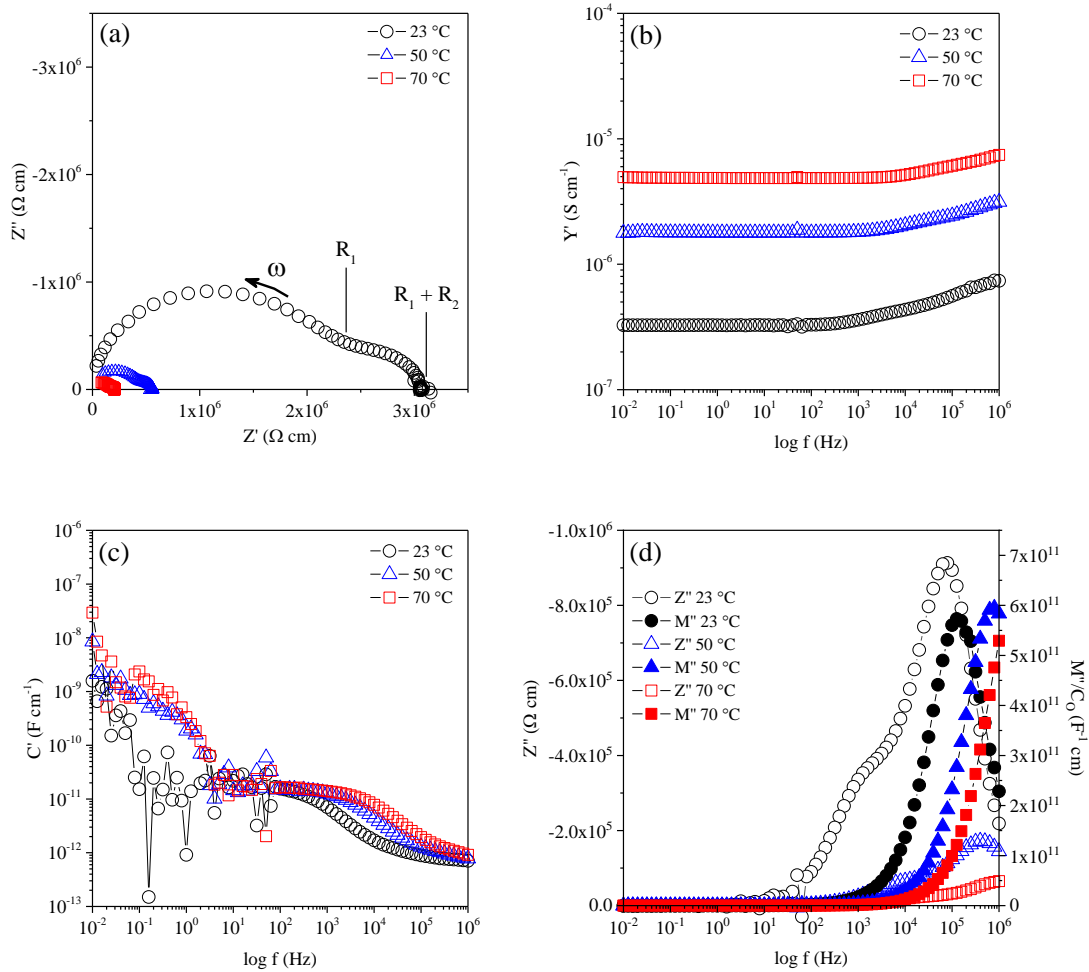


Figure 3.12 $\text{Li}_2\text{Mg}_{0.1}\text{Mn}_{0.9}\text{O}_{2.9}$ (join 4) quenched: (a) Impedance complex plane, Z^* plot and spectroscopic plots (b) Y' , (c) C' , (d) $-Z''$ and M'' at 23 °C, 50 °C and 70 °C

3.5 Arrhenius plots

Generally, all samples show a linear behaviour on the Arrhenius plot (figure 3.13). The slow-cooled Li_2MnO_3 has the lowest conductivity with activation energy, E_a of 0.835 (4) eV, followed by its quenched sample with E_a of 0.75 (1) eV, within the temperature range 150 to 400 °C.

The slow-cooled 10% Mg-doped Li_2MnO_3 on joins 2 and 4 show higher conductivity than the pristine Li_2MnO_3 . Join 4 shows conductivity an order of magnitude higher than join 2 and with similar activation energy, within errors. The increase in

conductivity is probably due to an increase in partial reduction of Mn^{4+} to Mn^{3+} with increasing Mg content.

The quenched samples of 10% Mg-doped Li_2MnO_3 on joins 2 and 4 show the highest conductivity at a temperature range 20 to 200 °C as compared to the slow-cooled samples. Both samples showed an activation energy of 0.43 eV, which are about half of their respective E_a on their slow-cooled samples. This is probably due to the similar effect shown by the quenched Li_2MnO_3 .

Table 3.6 summarises the activation energy and conductivity data of samples prepared. It also includes the conductivity value extrapolated to room temperature based on the Arrhenius plots (assuming that the conductivity behaves linearly with temperature and there is no change in the activation energy). At room temperature, the projected conductivity for the quenched sample of 10 mol % Mg-doped Li_2MnO_3 for joins 2 and 4 is expected to be in the order of three to four orders of magnitudes ($\sim 10^{-8}$ S cm^{-1}) compared to the slow-cooled samples ($\sim 10^{-11}$ to 10^{-12} S cm^{-1}).

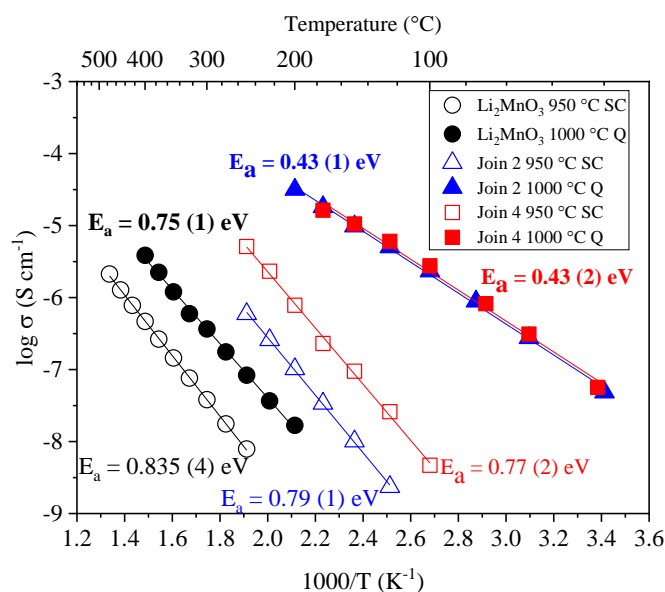


Figure 3.13 Arrhenius plot of Li_2MnO_3 , $\text{Li}_{2.2}\text{Mg}_{0.1}\text{Mn}_{0.9}\text{O}_3$ (join 2) and $\text{Li}_2\text{Mg}_{0.1}\text{Mn}_{0.9}\text{O}_{2.9}$ (join 4) for slow-cooled (SC) and quenched (Q) samples with their respective activation energy, E_a

Table 3.6 Comparison of activation energy and its conductivities (measured and extrapolated)

Sample	State	Activation Energy (eV)	Conductivity (S cm ⁻¹) at T (°C)	Conductivity (S cm ⁻¹) at T (°C) extrapolated
Li ₂ MnO ₃	Slow-cooled	0.835 (4)	1.1 × 10 ⁻⁹ (200)	6.3 × 10 ⁻¹⁵ (25)
	Quenched (in air)	0.75 (1)	1.6 × 10 ⁻⁸ (200)	2.6 × 10 ⁻¹³ (25)
Li _{2.2} Mg _{0.1} Mn _{0.9} O ₃ Join (2)	Slow-cooled	0.79 (1)	9.6 × 10 ⁻⁹ (150)	1.0 × 10 ⁻¹² (25)
	Quenched (in air)	0.43 (1)	1.0 × 10 ⁻⁵ (150)	7.1 × 10 ⁻⁸ (25)
Li ₂ Mg _{0.1} Mn _{0.9} O _{2.9} Join (4)	Slow-cooled	0.77 (2)	9.0 × 10 ⁻⁸ (150)	1.1 × 10 ⁻¹¹ (25)
	Quenched (in air)	0.43 (2)	1.2 × 10 ⁻⁵ (150)	8.3 × 10 ⁻⁸ (25)

3.6 Discussion

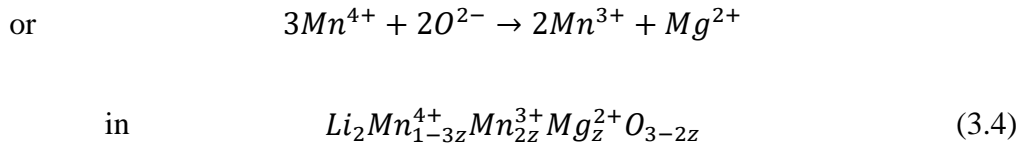
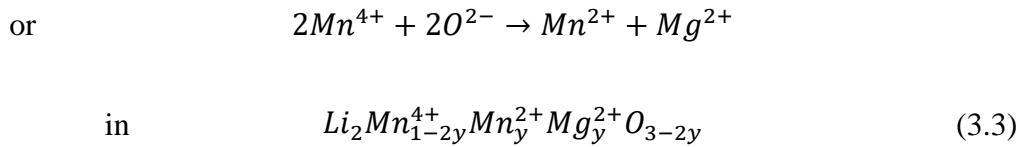
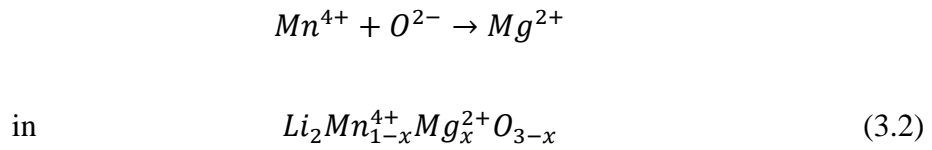
From the XRD and electrical property results, it is clear that Li₂MnO₃ has been successfully doped with Mg, but the doping mechanism(s) is not obvious. This is because there are two uncertainties associated with the synthesis procedure and subsequent results.

First, samples may lose some Li₂O during heating in an open environment, especially those on join 2. Thus, although single phase products were obtained on both joins 2 and 4, the products in both cases may approximate to join 4. If the join 2 products were single phase and contained interstitial Li⁺ ions, this would be an unusual result since rock-salt related, lithium-based oxides are usually restricted to a maximum cation:oxygen stoichiometry of 1:1 as any extra cations would occupy interstitial tetrahedral sites which share faces with occupied octahedral sites. The mechanism proposed for join 2 is unlikely, therefore.

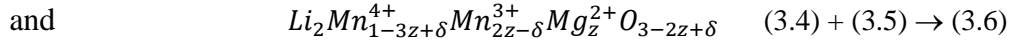
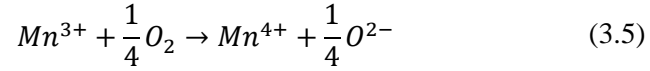
Second, the Mn oxidation state in the solid solution products may not be exclusively 4+. Most Mn-based oxides, with the exception of Li₂MnO₃, have Mn oxidation states less than 4+ at high temperature. For example, Mn oxides pass through the sequence MnO₂ → Mn₂O₃ → Mn₃O₄ → MnO on heating. Li₂MnO₃, is unusual in that it contains Mn⁴⁺ and is stable at high temperatures, to at least 1200 °C. It is therefore possible that Mg-doped Li₂MnO₃ may have a reduction in the oxidation state of Mn. Indirect evidence for this is obtained from the electrical property results in which the

conductivity of the quenched samples is several orders of magnitude higher than that of slow-cooled samples; the implication is that at high temperatures, samples lose oxygen, giving mixed valence 3+, 4+ of Mn, which is regained during slow cooling.

From the location of join 4 on the phase diagram, it appears that the doping mechanism involves replacement of Mn by Mg, in a probable 1:1 ratio, but without change in Li content. This therefore requires either the creation of oxygen vacancies or (possible) reduction of Mn oxidation state to achieve charge balance. Possible mechanisms ideally include:



Since samples appear to pick up oxygen during slow cooling, this is good evidence that charge compensation involves oxygen vacancy creation as shown by all mechanisms (3.2) to (3.4) and that quenched samples have mixed valence Mn as shown by mechanisms (3.3) and (3.4). Of these two mechanisms, (3.4) is more likely since Mn³⁺ is the oxidation state to be accessed first during doping or oxygen loss. We therefore proposed that mechanism (3.4) may be the preferred compensation mechanism at high temperatures combined with the possibility of oxygen uptake during slow cooling, to give:



3.7 Conclusions

In summary, the Li_2MnO_3 has been successfully doped with Mg with the observation of a single phase on join 2 and join 4. It was proposed that the compensation mechanism involves the creation of oxygen vacancies and as a direct consequence, a partial reduction of Mn^{4+} to Mn^{3+} was expected for charge balance.

Impedance measurements on all sintered pellets does not indicate any low frequency spike in impedance complex plane plots which could be associated with the ionic conduction blocking at the sample-electrode interface. Hence, the charge carrier is dominated by the electronic conduction.

An increase in conductivity was observed for all quenched samples compared to their respective slow-cooled counterpart. For the oxygen-deficient samples of 10% Mg-doped, both joins show a significant increase in the conductivity, accompanied by a reduction in activation energy. A further loss in oxygen results in an increase in Mn^{3+} - Mn^{4+} pair which create an easier conduction pathway for electrons to ‘hop’ between the Mn valency state and as a result, the electronic conductivity increases by several orders of magnitude (compared to the slow-cooled undoped Li_2MnO_3).

It can be concluded at this point that the use of Mg as dopant in Li_2MnO_3 cathode material can improve the electronic conductivity of the samples. This shows that the role of oxygen non-stoichiometry in Mg-doped Li_2MnO_3 has significant effect to the conductivity. Although, their electrochemical properties are not yet known, based on the impedance measurements, an increase in electrochemical activity is expected.

3.8 References

1. Nitta, N., F. Wu, J.T. Lee, and G. Yushin, *Li-ion battery materials: present and future*. *Materials today*, 2015. **18**(5): p. 252-264.
2. Robertson, A.D. and P.G. Bruce, *Mechanism of electrochemical activity in Li_2MnO_3* . *Chemistry of Materials*, 2003. **15**(10): p. 1984-1992.
3. Kalyani, P., S. Chitra, T. Mohan, and S. Gopukumar, *Lithium metal rechargeable cells using Li_2MnO_3 as the positive electrode*. *Journal of power sources*, 1999. **80**(1-2): p. 103-106.
4. Robertson, A.D., A.R. Armstrong, A.J. Paterson, M.J. Duncan, and P.G. Bruce, *Nonstoichiometric layered $\text{Li}_x\text{Mn}_y\text{O}_2$ intercalation electrodes - a multiple dopant strategy*. *Journal of Materials Chemistry*, 2003. **13**(9): p. 2367-2373.
5. Kim, J.-S., C.S. Johnson, J.T. Vaughey, M.M. Thackeray, S.A. Hackney, W. Yoon, and C.P. Grey, *Electrochemical and Structural Properties of $x\text{Li}_2\text{M}'\text{O}_3.(1-x)\text{LiMn}_{0.5}\text{Ni}_{0.5}\text{O}_2$ Electrodes for Lithium Batteries ($\text{M}' = \text{Ti, Mn, Zr}$; $0 \leq x \leq 0.3$)*. *Chemistry of Materials*, 2004. **16**(10): p. 1996-2006.
6. Pasero, D., V. McLaren, S. De Souza, and A. West, *Oxygen nonstoichiometry in Li_2MnO_3 : An alternative explanation for its anomalous electrochemical activity*. *Chemistry of materials*, 2005. **17**(2): p. 345-348.
7. Tukamoto, H. and A. West, *Electronic conductivity of LiCoO_2 and its enhancement by magnesium doping*. *Journal of The Electrochemical Society*, 1997. **144**(9): p. 3164-3168.
8. JuHee Kang, I.O., ChaeHwan Jeong, SeongJae Boo, TaeWon Kim, MooSung Lee and Ho-Sung Kim, *A Study of Electrochemical Behavior for the Pure Li_2MnO_3 Material via the Synthesis Methods and the Effect of the Composite Materials*. *International Conference on Power and Energy Systems*, 2012. **13**: p. 390-395.
9. Denis, Y., K. Yanagida, Y. Kato, and H. Nakamura, *Electrochemical activities in Li_2MnO_3* . *Journal of The Electrochemical Society*, 2009. **156**(6): p. A417-A424.
10. Wang, R., X. He, L. He, F. Wang, R. Xiao, L. Gu, H. Li, and L. Chen, *Atomic Structure of Li_2MnO_3 after Partial Delithiation and Re-Lithiation*. *Advanced Energy Materials*, 2013. **3**(10): p. 1358-1367.
11. Boulineau, A., L. Croguennec, C. Delmas, and F. Weill, *Structure of Li_2MnO_3 with different degrees of defects*. *Solid State Ionics*, 2010. **180**(40): p. 1652-1659.
12. ICDD (2018) and PDF-4+ 2019 (Database), *International Centre for Diffraction Data*. Newtown Square, Pennsylvania, USA, edited by Dr. Soorya Kabekkodu, 2018.

Chapter 4: Subsolidus phase equilibria in the MnO_8 – MgO system

4.1 Introduction

The binary system Li_2O - MnO_8 has been widely studied for lithium-ion battery applications as an alternative to materials containing toxic cobalt (Co) and nickel (Ni). Several known electrode materials are present within this system such as layered LiMnO_2 and spinel LiMn_2O_4 . MgO could be an exciting dopant for this system as it has been reported by Tukamoto and West ^[1] that it helps to improve the conductivity of LiCoO_2 by more than two orders of magnitude at room temperature. The initial study in this thesis (chapter 3) showed that a partial solid solution formed when Li_2MnO_3 was doped with Mg up to ~ 10 mol %.

The compositional triangle of the subsolidus pseudo-ternary system Li_2O - MnO_8 - MgO was constructed as shown in figure 4.1. The join between MgO - MnO_8 shows three distinct known phases which are MgMn_2O_4 , Mg_2MnO_4 and Mg_6MnO_8 . MgMn_2O_4 ^[2, 3] has been studied as a potential electrode material in magnesium ion batteries particularly since it has a similar structure to the lithium counterpart. It is not yet known whether Mg_6MnO_8 has been studied as an alternative electrode material especially for lithium-ion battery applications. This may be due to the difficulty to obtain a single phase of Mg_6MnO_8 ^[4, 5].

A phase diagram for the MgO - MnO_8 system has been reported (figure 4.2). At low Mg content (< 40 mol %), above 700 °C, two solid solutions were observed: tetragonal spinel at low temperature and cubic spinel at higher temperature. At 86 mol % Mg , Mg_6MnO_8 appeared as a single line phase which subsequently decomposes into a two-phase mixture of cubic spinel and $(\text{Mg}, \text{Mn})\text{O}$ when heated above ~ 1050 °C ^[6, 7].

During initial study of the MgO - MnO_8 system, it was found serendipitously that Mg_6MnO_8 is not just a single line phase but a solid solution over a wide compositional range. Further to this, at low Mg content (< 40 mol %), a new tetragonal spinel polymorph was observed when heated at higher temperature instead of a cubic spinel. Following

these new findings, a more extensive study of the subsolidus phase equilibria in the MgO-MnO₈ system was made.

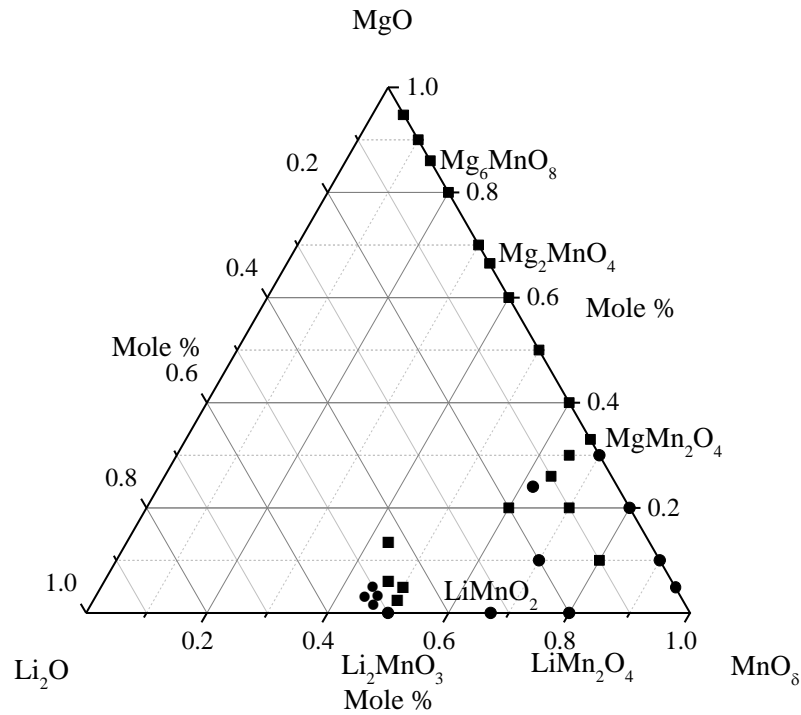


Figure 4.1 Partial pseudo-ternary compositional triangle of Li₂O-MnO₈-MgO.

● Single-phase; ■ Phase-mixture

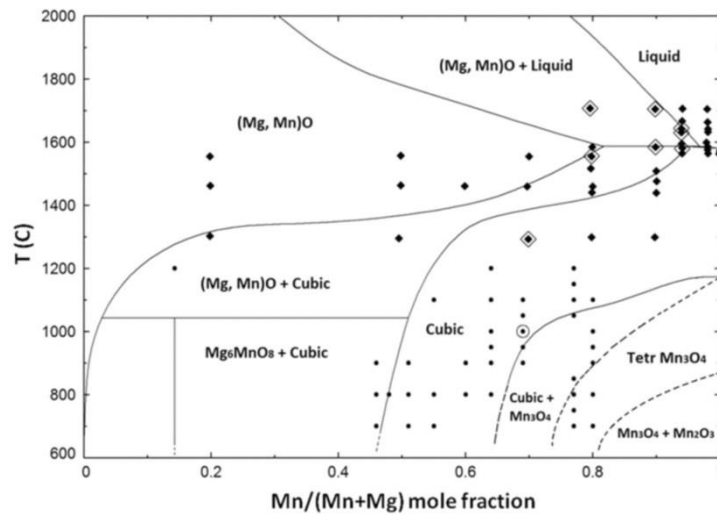


Figure 4.2 Binary phase diagram of the Mg-Mn-O system in air showing possible phase boundaries as reported by Joshi *et al.*^[7]

4.2 Experimental

Samples were prepared by solid-state synthesis using precursors of $\text{Mg}(\text{NO}_3)_2 \cdot 6\text{H}_2\text{O}$ ($\geq 99\%$) and MnO_2 ($\geq 99\%$, dried at 180°C). Both (from Sigma-Aldrich), were weighed in their stoichiometric amounts according to the formula $\text{Mg}_x\text{Mn}_{1-x}\text{O}_\delta$, mixed and ground with acetone in an agate mortar and pestle. The mixtures were put in alumina boats and heated at 150°C for 4 h and 350°C for 10 h to eliminate water and NO_2 . Finally, the samples were heated at 1000°C for 6 days with intermittent regrinding.

For the purpose of phase diagram studies, compositions were prepared with $x = 0, 0.05, 0.1, 0.2, 0.3, 0.33, 0.4, 0.5, 0.6, 0.7, 0.8, 0.86, 0.9$ and 0.95 . Small portions of the reacted batch samples were wrapped in Pt foil and heated isothermally in a vertical tube furnace at temperatures in the range 600°C to 1200°C and quenched into liquid nitrogen at the end of the heat treatment (approximate cooling rate 200°C s^{-1}) [8].

Phase characterization used a STOE Stadi P X-ray diffractometer using $\text{Mo K}\alpha_1$ radiation with a linear position sensitive detector. Initial phase analysis and lattice parameter measurement used the STOE WinX^{POW} software package.

Thermal analysis was conducted on a small portion of $x = 0, 0.05, 0.1, 0.2$ and 0.3 using the NETZSCH 404C instrument and was analyzed using Proteus Analysis software. Samples were heated from 25 to 1300°C at $10^\circ\text{C}/\text{min}$ heating/cooling rate.

HTXRD was conducted on a small portion of $x = 0, 0.2,$ and 0.3 using Siemens D5000 with $\text{Cu K}\alpha_{(\text{average})}$ radiation ($\lambda = 1.5418 \text{ \AA}$) with 2θ angle range between 10° and 90° .

4.3 Slow-cooled samples

The XRD results for slow-cooled samples of $0.05 \leq x \leq 0.30$ at rate $0.1 \text{ }^\circ\text{C}/\text{min}$, showed a similar pattern (figure 4.3). All reflections from one composition $x = 0.30$ were indexed using the tetragonal space group $I4_1/amd$ (141), $a = b = 5.7256$ (3) \AA , $c = 9.3176$ (9) \AA , $V = 305.45$ (3) \AA^3 , lattice c/a ratio = 1.6274 (2), and thus it can be concluded that these compositions were single phase (table 4.1). Several reflections showed an increase in intensity such as (101), (004), (220), (213) and others showed a decrease in intensity such as (112), (200), (204), (312) with increasing x . A shift in peak positions to higher 2θ angles was observed for all reflections up to $x = 0.30$, inset figure 4.3.

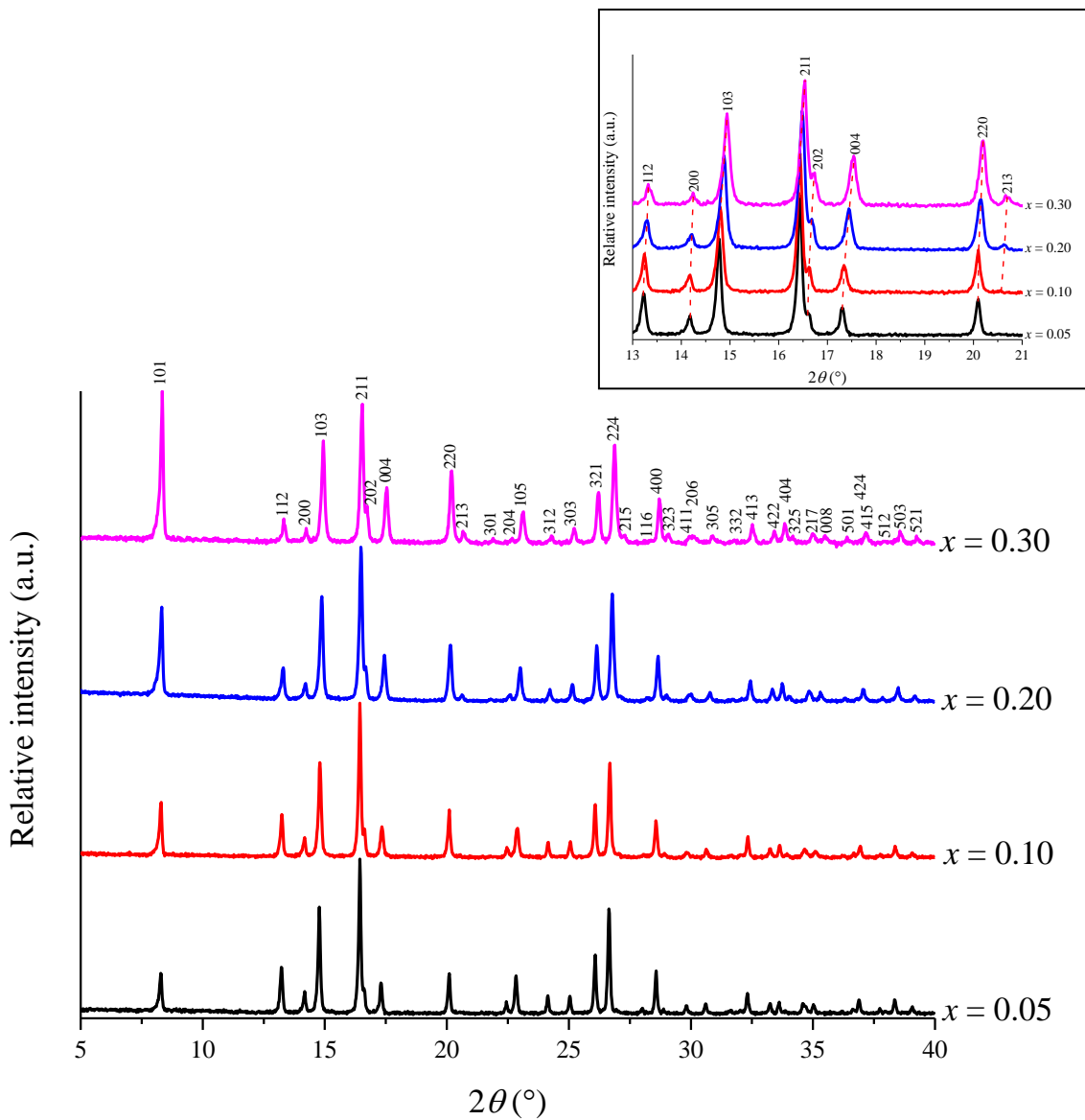


Figure 4.3 XRD patterns for slow-cooled $\text{Mg}_x\text{Mn}_{1-x}\text{O}_8$ for $0.05 \leq x \leq 0.30$. Inset shows peak shifting to higher 2θ angle over the range $13^\circ \leq 2\theta \leq 21^\circ$

Table 4.1 Indexing data for $x = 0.30$ slow-cooled from 1000 °C

No	$2\theta_{\text{obs}}$ (°)	h	k	l	$2\theta_{\text{calc}}$ (°)	$\Delta 2\theta$ (°)	Intensity	d_{obs} (Å)	d_{calc} (Å)
1	8.343	1	0	1	8.338	0.0049	96.9	4.875	4.878
2	13.327	1	1	2	13.329	-0.0019	24.1	3.056	3.056
3	14.232	2	0	0	14.232	-0.0008	16.2	2.863	2.863
4	14.928	1	0	3	14.928	-0.0003	78.1	2.730	2.730
5	16.516	2	1	1	16.517	-0.0013	100.0	2.469	2.469
6	16.717	2	0	2	16.721	-0.0038	30.6	2.440	2.439
7	17.512	0	0	4	17.515	-0.0022	42.7	2.330	2.329
8	20.176	2	2	0	20.180	-0.0045	51.8	2.025	2.024
9	20.677	2	1	3	20.682	-0.0048	14.3	1.976	1.976
10	21.856	3	0	1	21.868	-0.0128	9.4	1.871	1.870
11	22.635	2	0	4	22.639	-0.0041	10.6	1.807	1.807
12	23.088	1	0	5	23.090	-0.0023	27.0	1.772	1.772
13	24.257	3	1	2	24.262	-0.0055	12.0	1.688	1.688
14	25.194	3	0	3	25.195	-0.0009	17.1	1.626	1.626
15	26.183	3	2	1	26.188	-0.0051	37.0	1.566	1.565
16	26.841	2	2	4	26.842	-0.0012	67.4	1.528	1.528
17	27.212	2	1	5	27.228	-0.0153	13.0	1.508	1.507
18	28.690	4	0	0	28.691	-0.0004	36.3	1.431	1.431
19	29.050	3	2	3	29.053	-0.0029	12.9	1.414	1.414
20	29.942	4	1	1	29.928	0.0143	11.7	1.373	1.374
21	30.110	2	0	6	30.118	-0.0074	11.9	1.365	1.365
22	30.850	3	0	5	30.851	-0.0016	12.4	1.333	1.333
23	31.757	1	0	7	31.750	0.0069	8.9	1.296	1.297
		3	3	2	31.757	0.0001			1.296
24	32.489	4	1	3	32.491	-0.0025	18.4	1.268	1.268
25	33.388	4	2	2	33.390	-0.0023	14.9	1.235	1.235
26	33.812	4	0	4	33.812	-0.0001	19.7	1.220	1.220
27	34.126	3	2	5	34.126	0.0000	11.1	1.209	1.209
28	34.963	2	1	7	34.950	0.0134	13.4	1.181	1.181
29	35.463	0	0	8	35.456	0.0074	11.6	1.165	1.165
30	36.369	5	0	1	36.364	0.0047	9.6	1.136	1.137
31	36.861	4	2	4	36.854	0.0080	9.1	1.122	1.122
32	37.146	4	1	5	37.145	0.0018	14.9	1.113	1.114
33	37.914	3	0	7	37.911	0.0025	8.6	1.092	1.092
		5	1	2	37.917	-0.0033			1.092
34	38.552	5	0	3	38.548	0.0039	14.2	1.074	1.074
35	39.237	5	2	1	39.234	0.0036	10.1	1.056	1.056

Symmetry: Body-centred tetragonal, Space group: $I4_1/amd$, Final 2θ window: 0.02
 $a = 5.7256$ (3) Å, $c = 9.3176$ (9) Å, $V = 305.45$ (3) Å³ and $c/a = 1.6274$ (2)

At higher values of x (> 0.30), a mixture of phases was present in the slow-cooled (at rate $0.1\text{ }^{\circ}\text{C}/\text{min}$) samples (figure 4.4). Thus, at $x = 0.33$, a small amount of the second phase started to appear with peaks observed at *ca* 16.3° , 19.6° and 27.9° 2θ which gave a mixture with tetragonal spinel. The peak intensity of this second phase (denoted as C1) increases with increasing x up to $x = 0.50$. At $x = 0.50$, another set of peaks (denoted as C2) which is similar to C1 appeared at angles slightly lower than the C1 and thus gave a three-phase mixture: tetragonal spinel, C1 and C2. In the range $0.70 \leq x \leq 0.80$, only a mixture of C1 and C2 was observed, with an increase in intensity for C2 with increasing x . Beyond $x \geq 0.86$, only a mixture of C2 and MgO was observed, with an increase in intensity for MgO with increasing x .

The powder XRD pattern for $x = 0.86$ (figure 4.5), showed the C2 reflections with the Miller indices according to Mg_6MnO_8 (Suzuki phase) with $Fm\bar{3}m$ space group. The Suzuki phase was reported to have a cubic rock salt structure with Mg^{2+} and Mn^{4+} octahedrally coordinated in the oxide array with six oxygen ions.

The C1 reflection has a similar pattern to C2 but at a slightly higher 2θ angle and therefore, has a cubic structure similar to C2 but with smaller unit cell size. The initial appearance of C1 at $x = 0.33$, could indicate the possibility of a cubic spinel structure that formed due to the reduction in the number of Mn^{3+} in the octahedral environment. Therefore, initial thoughts were that C1 and C2 could probably be assigned to a cubic spinel and a Suzuki phase structure respectively.

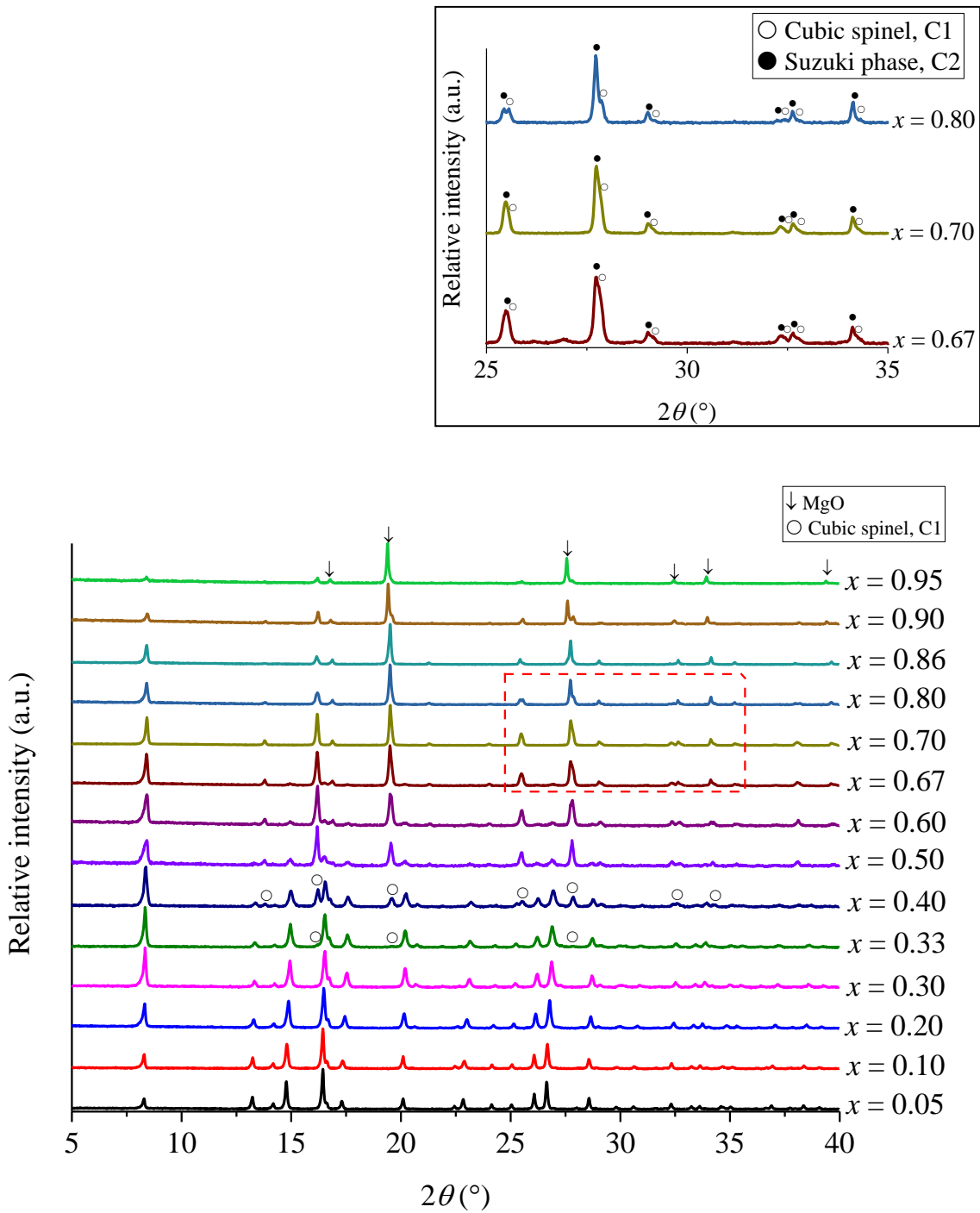


Figure 4.4 XRD patterns for slow-cooled $0.05 \leq x \leq 0.95$. Inset shows the mixture of C1 (cubic spinel) and C2 (Suzuki phase) phases for $0.67 \leq x \leq 0.80$ over the range $25^\circ \leq 2\theta \leq 35^\circ$

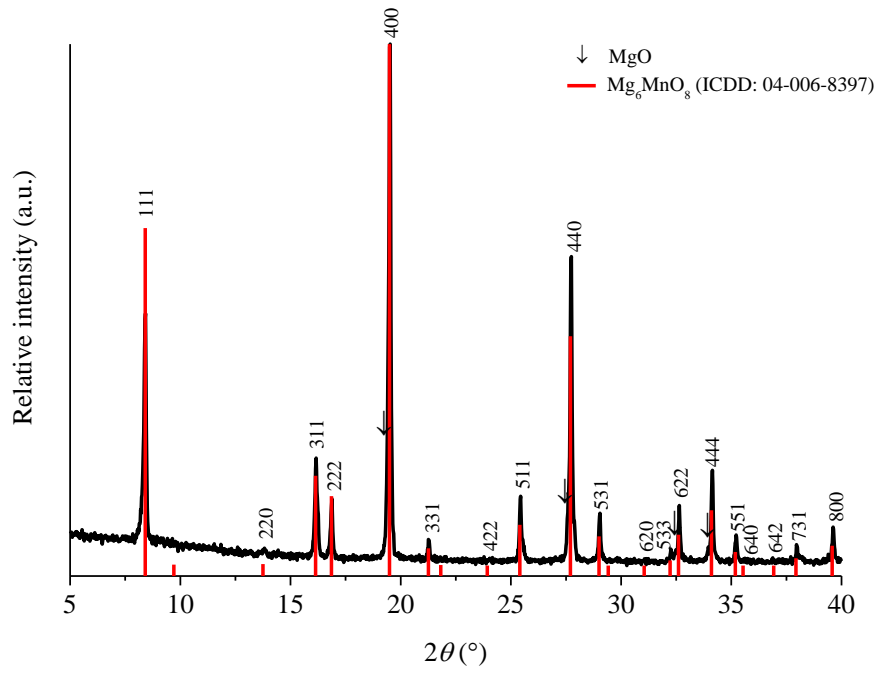


Figure 4.5 XRD pattern for slow-cooled $x = 0.86$. A mixture of Suzuki phase and MgO was observed

4.4 Quenched samples

From the result on the slow-cooled samples, it was suspected that in some cases, structural changes occurred during slow cooling. Experiments were therefore carried out on samples quenched from various temperatures.

4.4.1 Effect of temperature on composition $x = 0.20$ for $\text{Mg}_x\text{Mn}_{1-x}\text{O}_8$

Small quantities of $x = 0.20$ were heated in the temperature range 500 to 1200 °C and quenched into liquid nitrogen (figure 4.6). Two similar diffraction patterns were observed at low and high quench temperatures but with slightly different 2θ angles. At 900 °C and lower, the XRD patterns look similar to the tetragonal structure observed for the slow-cooled samples. A second phase started to form at around 950 °C and became a single phase from 1030 °C onwards.

The low temperature phase (sample quenched from 500 °C) was indexed using the tetragonal $I4_1/amd$ space group, $a = b = 5.7383$ (4) Å, $c = 9.3588$ (10) Å, $V = 308.17$ (3) Å³, $c/a = 1.6309$ (2), and so it can be concluded to be a single phase (table 4.2).

The high-temperature phase (sample quenched from 1050 °C) was also observed to have a similar pattern to the low-temperature assemblage but with different peak positions (2θ). Therefore, it was indexed using the same tetragonal $I4_1/amd$ space group, $a = b = 5.7866$ (7) Å, $c = 9.1466$ (15) Å, $V = 306.27$ (5) Å³, $c/a = 1.5806$ (3), and it can also be concluded as single phase (table 4.3). The lower and higher temperature phases of composition $x = 0.20$ are denoted as T1 and T2 respectively for easy reference.

It can be observed that the lattice parameters of these two phases were different (table 4.4). T2 has a parameter larger and c parameter smaller than T1. Therefore, for $x = 0.20$, the calculated lattice c/a ratios for T1 (at 500 °C) and T2 (at 1050 °C) were 1.63 and 1.58 respectively.

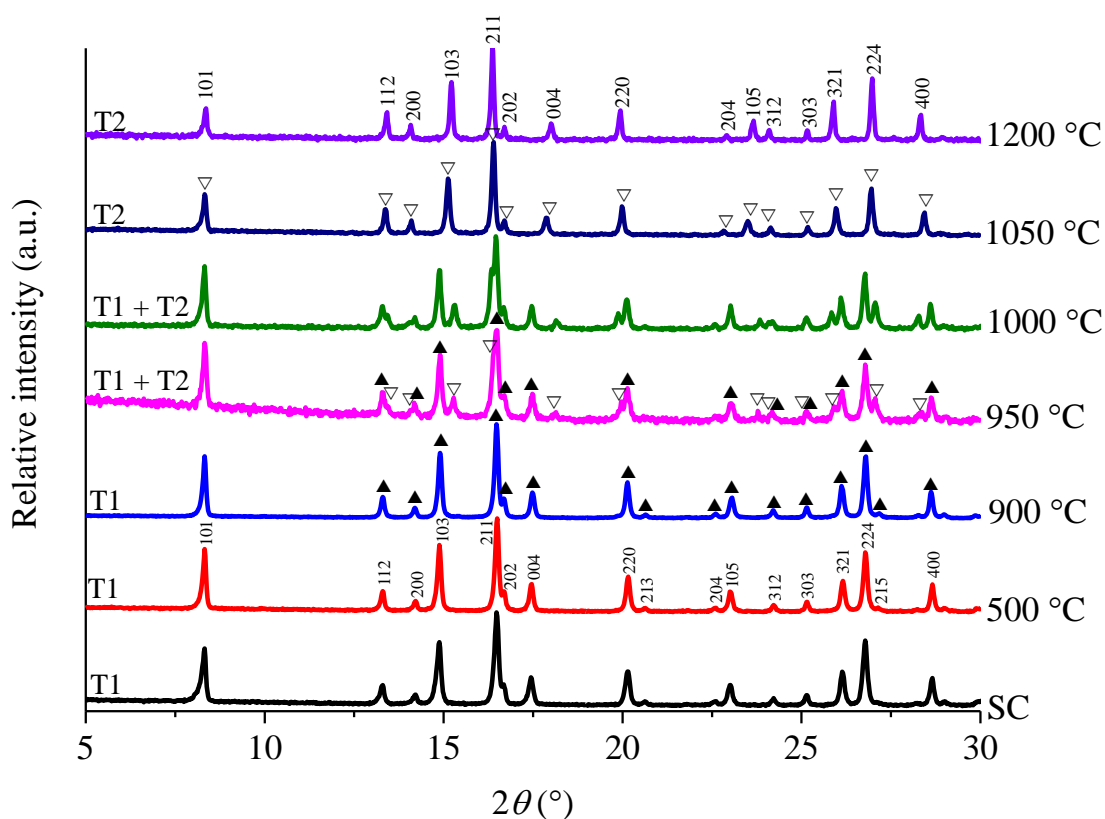


Figure 4.6 XRD patterns for $x = 0.20$ quenched from 500 to 1200 °C into liquid nitrogen. Two polymorphs T1 (▲) and T2 (▽) were observed.

SC = slow-cooled

In order to study the possible reversibility of transformation between these two phases as a function of temperature, a small quantity of powder of $x = 0.20$ was heated and quenched from 800 °C (step 1), then 1050 °C (step 2) and returned to 800 °C (step 3), for 10 h at each step. Similar XRD patterns were observed for T1 and T2 as shown in figure 4.6. Lattice parameter measurements were conducted at each step (table 4.5), and indicated that the transformation is reversible between T1 and T2.

Table 4.2 Indexing data for $x = 0.20$ quenched from 500 °C, T1 (▲)

N	$2\theta_{\text{obs}}$ (°)	h	k	l	$2\theta_{\text{calc}}$ (°)	$\Delta 2\theta$ (°)	Intensity	d_{obs} (Å)	d_{calc} (Å)
1	8.324	1	0	1	8.315	0.0094	60.8	4.886	4.892
2	13.279	1	1	2	13.287	-0.0071	27.9	3.067	3.066
3	14.196	2	0	0	14.201	-0.0045	19.0	2.870	2.869
4	14.868	1	0	3	14.870	-0.0018	70.0	2.741	2.741
5	16.474	2	1	1	16.478	-0.0038	100.0	2.475	2.475
6	16.665	2	0	2	16.674	-0.0086	28.6	2.447	2.446
7	17.434	0	0	4	17.437	-0.0028	34.2	2.340	2.340
8	20.131	2	2	0	20.135	-0.0040	42.2	2.029	2.029
9	20.608	2	1	3	20.617	-0.0096	11.4	1.983	1.982
10	22.559	2	0	4	22.558	0.0007	13.2	1.813	1.813
11	22.990	1	0	5	22.992	-0.0015	27.7	1.780	1.780
12	24.198	3	1	2	24.200	-0.0027	15.1	1.692	1.692
13	26.123	3	2	1	26.128	-0.0046	39.2	1.569	1.569
14	26.755	2	2	4	26.756	-0.0013	63.9	1.533	1.533
15	27.140	2	1	5	27.127	0.0132	12.2	1.512	1.512
16	28.196	1	1	6	28.197	-0.0008	10.7	1.456	1.456
17	28.622	4	0	0	28.626	-0.0036	38.1	1.435	1.435
		3	1	4	28.640	-0.0173			1.434
18	30.743	3	0	5	30.746	-0.0024	13.6	1.338	1.338
19	32.403	4	1	3	32.405	-0.0025	18.8	1.271	1.271
20	33.308	4	2	2	33.309	-0.0006	15.4	1.238	1.237
21	33.712	4	0	4	33.714	-0.0021	17.6	1.223	1.223
22	34.819	2	1	7	34.808	0.0113	14.5	1.185	1.186
23	35.290	0	0	8	35.295	-0.0047	11.9	1.170	1.170
24	37.027	4	1	5	37.029	-0.0022	14.9	1.117	1.117
25	38.447	5	0	3	38.449	-0.0013	16.2	1.077	1.077
26	39.160	5	2	1	39.142	0.0173	10.8	1.058	1.059

Symmetry: Body-centred tetragonal, Space group: $I4_1/amd$, Final 2θ window: 0.02
 $a = 5.7383$ (4) Å, $c = 9.3588$ (10) Å, $V = 308.17$ (3) Å³ and $c/a = 1.6309$ (2)

Table 4.3 Indexing data for $x = 0.20$ quenched from 1050 °C, T2 (∇)

N	$2\theta_{\text{obs}}$ (°)	h	k	l	$2\theta_{\text{calc}}$ (°)	$\Delta 2\theta$ (°)	Intensity	d_{obs} (Å)	d_{calc} (Å)
1	8.315	1	0	1	8.318	-0.0028	46.4	4.892	4.890
2	13.355	1	1	2	13.357	-0.0022	34.2	3.050	3.049
3	14.081	2	0	0	14.082	-0.0010	21.1	2.894	2.893
4	15.115	1	0	3	15.110	0.0044	63.1	2.697	2.697
5	16.375	2	1	1	16.376	-0.0015	100.0	2.490	2.490
6	16.676	2	0	2	16.680	-0.0041	22.4	2.446	2.445
7	17.852	0	0	4	17.845	0.0076	26.2	2.286	2.287
8	19.966	2	2	0	19.965	0.0005	37.7	2.046	2.046
9	22.797	2	0	4	22.803	-0.0064	12.6	1.795	1.794
10	23.470	1	0	5	23.463	0.0064	24.2	1.744	1.744
11	24.093	3	1	2	24.098	-0.0049	17.0	1.699	1.699
12	25.138	3	0	3	25.133	0.0047	18.6	1.630	1.630
13	25.929	3	2	1	25.930	-0.0012	40.4	1.581	1.581
14	26.905	2	2	4	26.901	0.0044	63.8	1.524	1.525
15	28.383	4	0	0	28.382	0.0012	33.1	1.447	1.447
16	30.514	2	0	6	30.492	0.0227	10.6	1.348	1.349
17	30.991	3	0	5	30.995	-0.0040	14.0	1.328	1.327
18	32.304	4	1	3	32.304	0.0000	19.5	1.275	1.275
		1	0	7	32.312	-0.0080			1.275
19	33.724	4	0	4	33.727	-0.0027	14.5	1.223	1.223
20	35.379	2	1	7	35.403	-0.0232	11.3	1.167	1.166
21	37.141	4	1	5	37.144	-0.0037	15.4	1.114	1.114
22	38.265	5	0	3	38.268	-0.0022	14.6	1.082	1.082
		3	0	7	38.275	-0.0091			1.082
23	38.827	5	2	1	38.819	0.0082	10.6	1.067	1.067

Symmetry: Body-centred tetragonal, Space group: $I4_1/amd$, Final 2θ window: 0.03
 $a = 5.7866$ (7) Å, $c = 9.1466$ (15) Å, $V = 306.27$ (5) Å³ and $c/a = 1.5806$ (3)

Table 4.4 T1 (\blacktriangle) and T2 (∇) at $x = 0.20$ lattice parameter and lattice c/a ratio vs temperature

	Quench temperature	a (Å)	c (Å)	Volume (Å ³)	c/a
T2	1200 °C	5.8030 (2)	9.0835 (5)	305.89 (2)	1.5653 (1)
	1100 °C	5.7786 (6)	9.1755 (15)	306.39 (4)	1.5878 (3)
	1050 °C	5.7866 (7)	9.1466 (15)	306.27 (5)	1.5806 (3)
	1030 °C	5.7845 (4)	9.1584 (12)	306.45 (3)	1.5833 (2)
T1	900 °C	5.7445 (5)	9.3456 (15)	308.40 (4)	1.6269 (3)
	850 °C	5.7450 (5)	9.3535 (14)	308.71 (4)	1.6281 (3)
	800 °C	5.7422 (6)	9.3502 (16)	308.30 (4)	1.6283 (3)
	700 °C	5.7399 (4)	9.3552 (10)	308.23 (4)	1.6298 (2)
	600 °C	5.7389 (4)	9.3557 (11)	308.13 (3)	1.6302 (2)
	500 °C	5.7383 (4)	9.3588 (10)	308.17 (3)	1.6309 (2)

Table 4.5 Lattice parameter and lattice c/a ratio measurement for reversibility study at $x = 0.20$ between T1 and T2

	Quench temperature	a (Å)	c (Å)	Volume (Å ³)	c/a	Phase observed
Step 1	800 °C	5.7418 (3)	9.3564 (9)	308.46 (3)	1.6295 (2)	T1
Step 2	1050 °C	5.7739 (4)	9.2168 (15)	307.26 (4)	1.5963 (3)	T2
Step 3	800 °C	5.7408 (3)	9.3503 (7)	308.15 (2)	1.6288 (2)	T1

In order to investigate any weight change between these two polymorphs, a pellet of composition $x = 0.20$ was prepared and sintered at 1100 °C and slowly cooled to room temperature at rate 5 °C/min. The pellet weight was recorded and was placed in a Pt envelope and reweighed. The pellet was then heated and quenched from 800 °C (step 1), 1050 °C (step 2) and returned to 800 °C (step 3). The weight of the Pt envelope together with the pellet was measured at each step, and no difference in weight was observed indicating that any oxygen loss might be minimal and undetectable by the method used (table 4.6).

Table 4.6 Weight loss study for $x = 0.20$ between T1 and T2.

SC = slow-cooled, Q = quenched

			Weight (g)	
			Pellet with Pt	Pellet
	Phase	Temperature		
	T1	1100 °C (SC)	0.5239 (2)	0.2212 (2)
Step 1	T1	800 °C (Q)	0.5239 (2)	0.2212 (2)
Step 2	T2	1050 °C (Q)	0.5239 (2)	0.2212 (2)
Step 3	T1	800 °C (Q)	0.5239 (2)	0.2212 (2)

4.4.2 Effect of composition on T1 phase quenched from 850 °C

A small quantity of $x = 0.05$, 0.10 and 0.20 was heated at 850 °C and quenched into liquid nitrogen. The observed diffraction patterns showed that all the peaks shifted to higher 2θ angle with increasing x (figure 4.7). Each diffraction pattern was indexed using the tetragonal $I4_1/amd$ space group and can be concluded to be single phase.

The peak shift indicates that there was a change in the d -spacings and hence the unit cell size. In order to investigate this change, lattice parameter measurements were conducted on samples containing silicon as an internal standard (for peak calibration) using a STOE Stadi P diffractometer with $\text{MoK}\alpha_1$ radiation. The lattice parameter, volume and axial c/a ratio against composition were plotted (figure 4.8).

Both lattice constants a and c decreased with increasing x . The axial c/a ratio also showed a slight decrease with increasing x .

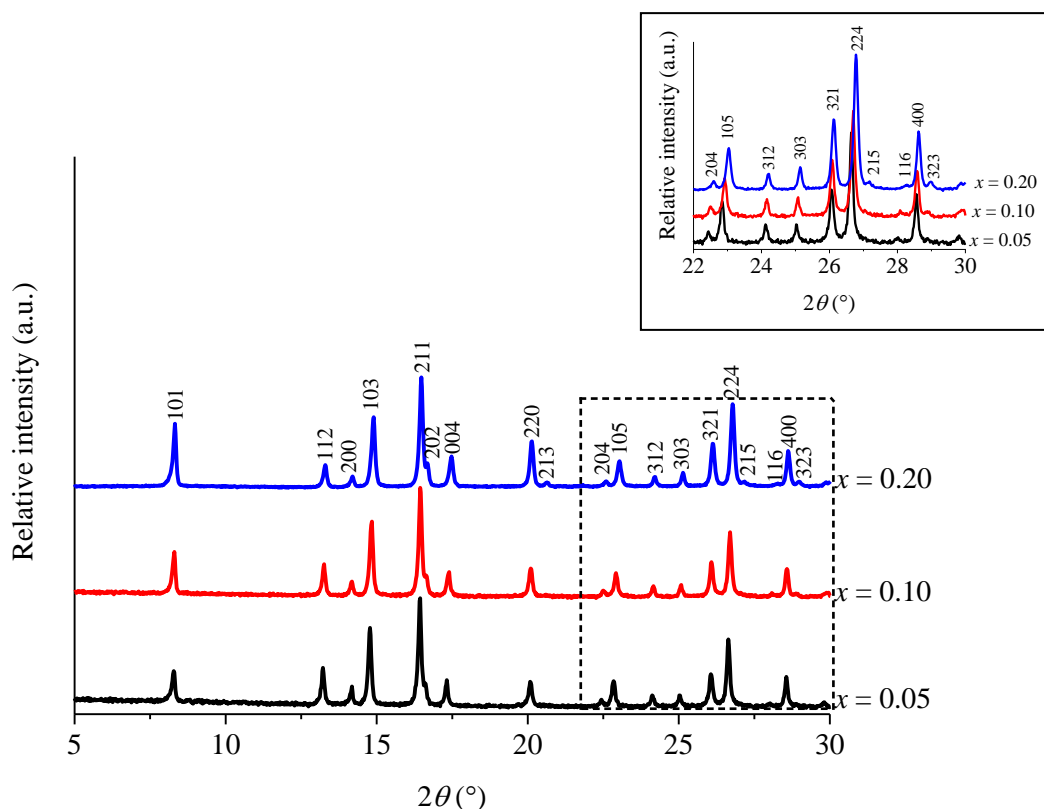


Figure 4.7 XRD patterns of T1, $x = 0.05, 0.10$ and 0.20 quenched from $850\text{ }^\circ\text{C}$ into liquid nitrogen. Inset shows peak shift to higher angle over the range $22^\circ \leq 2\theta \leq 30^\circ$

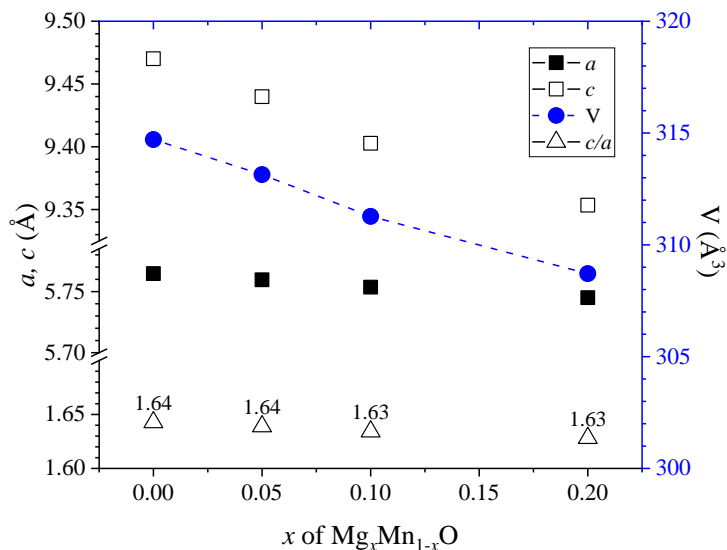


Figure 4.8 Lattice parameter, a , c , cell volume, V , and axial c/a ratio, of T1 for $0.05 \leq x \leq 0.20$ quenched from $850\text{ }^\circ\text{C}$ into liquid nitrogen, compared to Mn_3O_4 ($x = 0$) at room temperature. Error bars are smaller than the data points

4.4.3 Effect of temperature on composition $x = 0.40$ for $\text{Mg}_x\text{Mn}_{1-x}\text{O}_8$

At $x = 0.40$ (figure 4.9), a mixture of T1 and C1 was observed from 500 to 700 °C. At 800 °C, the XRD pattern shows a mixture of T1 and T2. A single phase of T2 was observed between 850 to 1100 °C. At 1200 °C, MgO started to form and gave a mixture with T2.

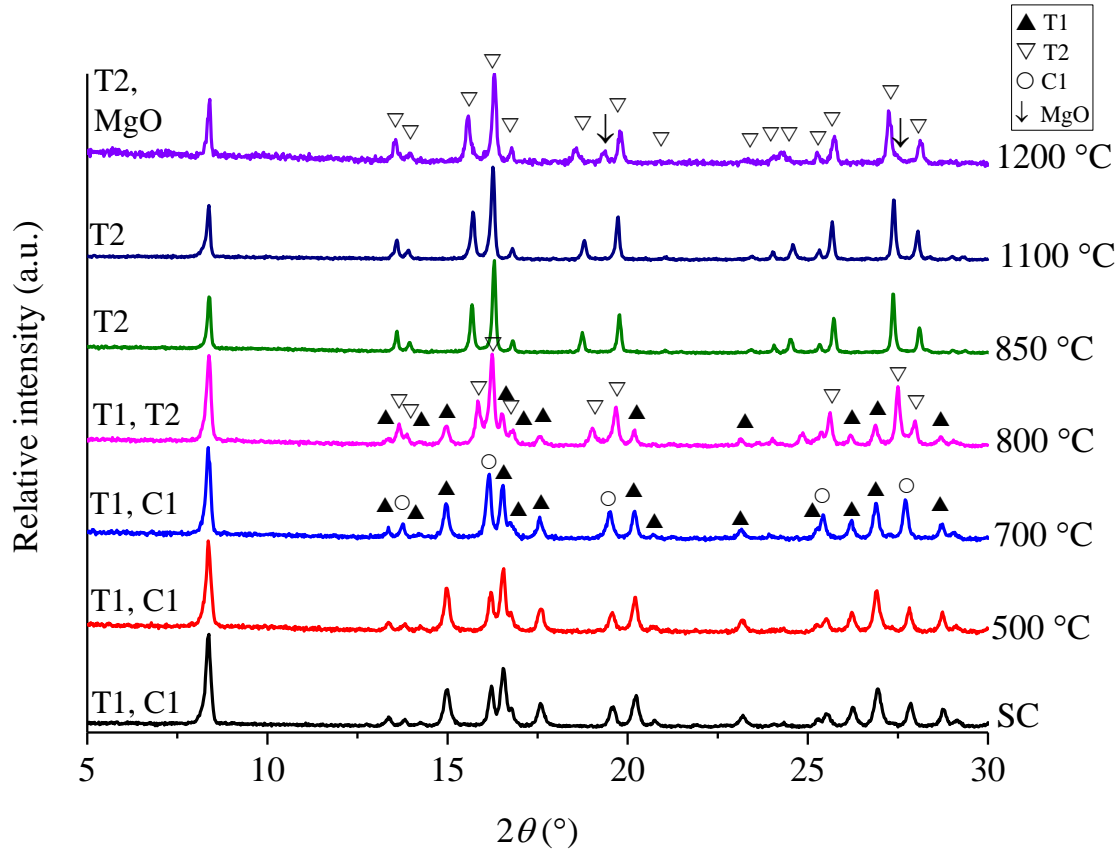


Figure 4.9 XRD patterns for $x = 0.40$ quenched from 500 to 1200 °C into liquid nitrogen, where SC = slow-cooled

4.4.4 Effect of composition on samples quenched from 1050 °C

A small quantity of samples between $0 \leq x \leq 0.95$ were heated at 1050 °C and quenched into liquid nitrogen. The XRD patterns for the entire range were analyzed (figure 4.10). In the range $0 \leq x \leq 0.10$, the spectra were identified as T1 with all the peaks shifted to a higher angle with increasing x .

A single phase of T2 was observed between $0.20 \leq x \leq 0.40$; peak shifts were seen both to lower and higher angles (figure 4.11). Inset patterns showed that peaks (112), (103), (202) and (004) were shifted to higher 2θ angles and the opposite for peaks (200), (211) and (220).

At $x = 0.50$, a mixture of T2 and MgO was observed until $x = 0.95$ with a decrease in intensity for T2.

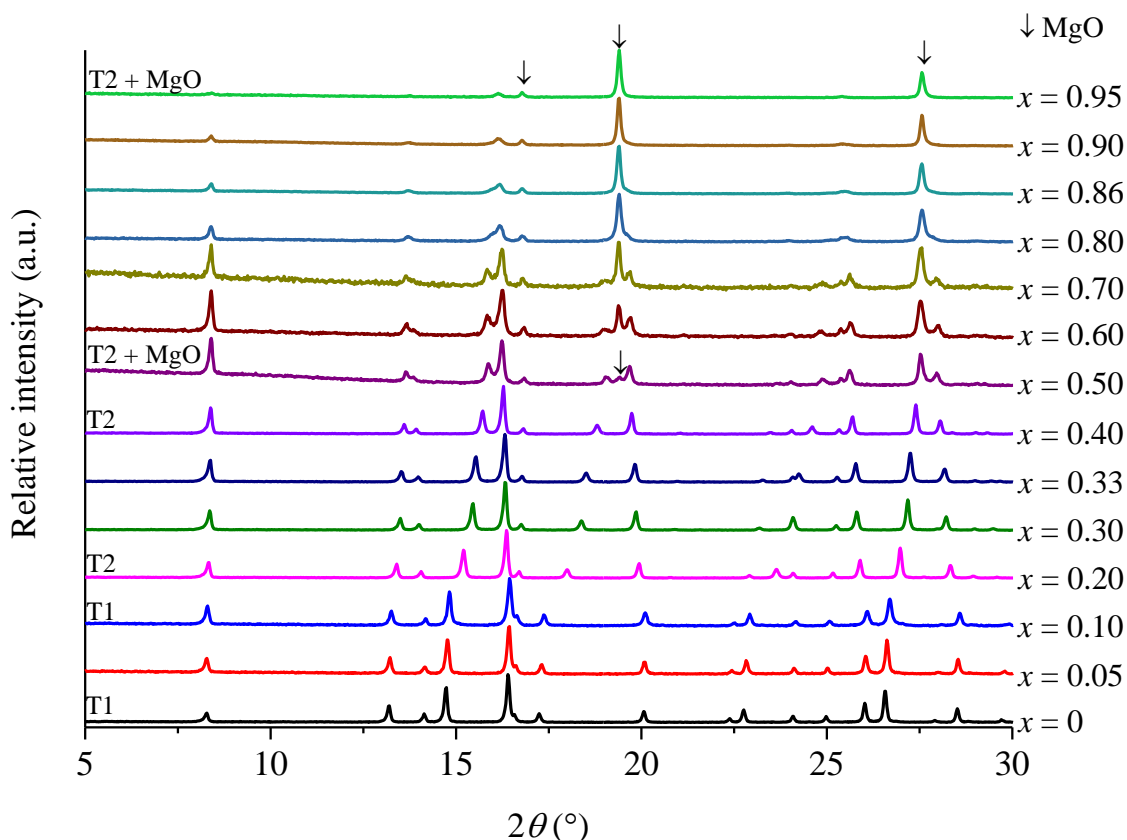


Figure 4.10 XRD patterns of $\text{Mg}_x\text{Mn}_{1-x}\text{O}_\delta$ quenched from 1050 °C into liquid nitrogen

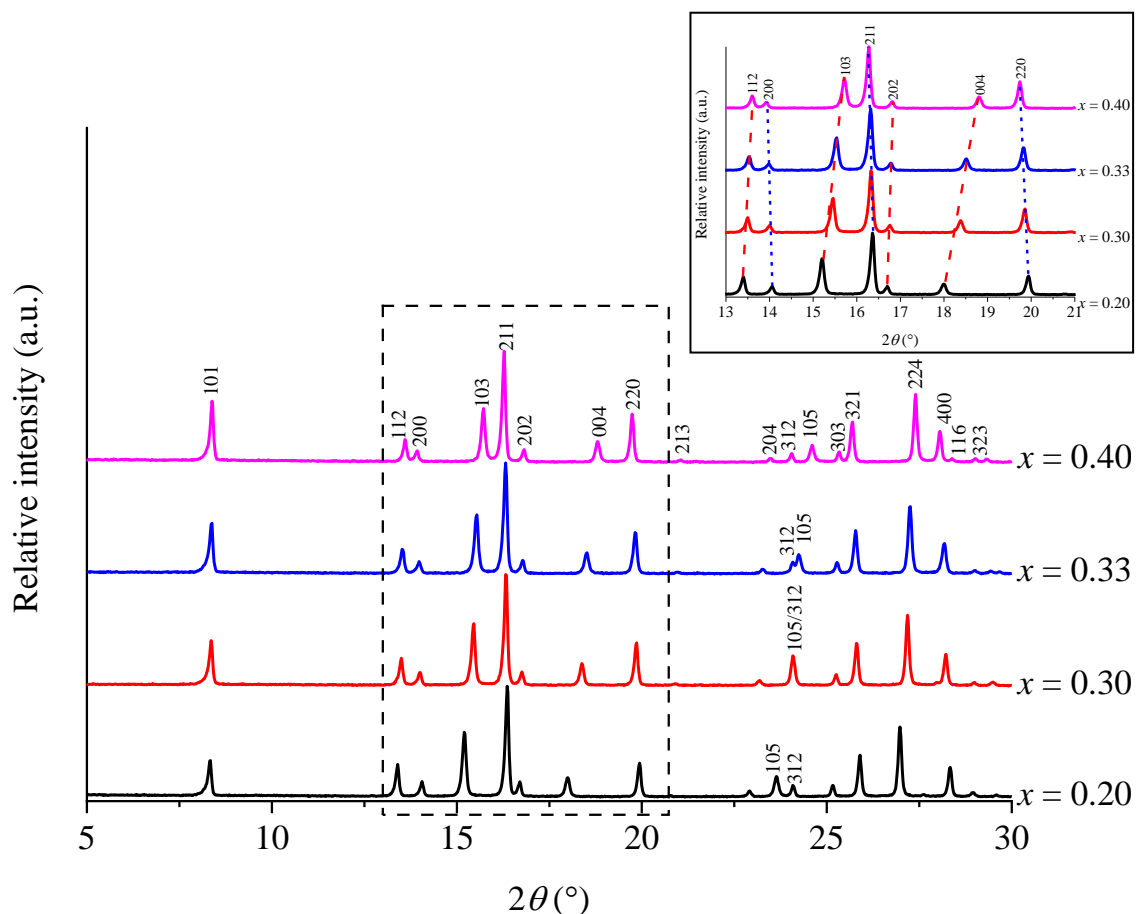


Figure 4.11 XRD patterns of T2 quenched from 1050 °C into liquid N₂ for $0.20 \leq x \leq 0.40$. Inset shows peaks shifted over the range $13^\circ \leq 2\theta \leq 21^\circ$

An additional composition was prepared at $x = 0.36$ in order to study further the change in lattice parameters for T2 tetragonal spinel solid solution. A small amount of powder of $x = 0.20, 0.30, 0.33, 0.36,$ and 0.40 was mixed with silicon (as internal standard) for diffraction angle calibration. Data of lattice constants, volume and axial c/a ratio against compositions were plotted in figure 4.12.

Lattice constant a and c show an increase and decrease respectively with increasing x . The axial c/a ratio also shows a decrease with increasing x .

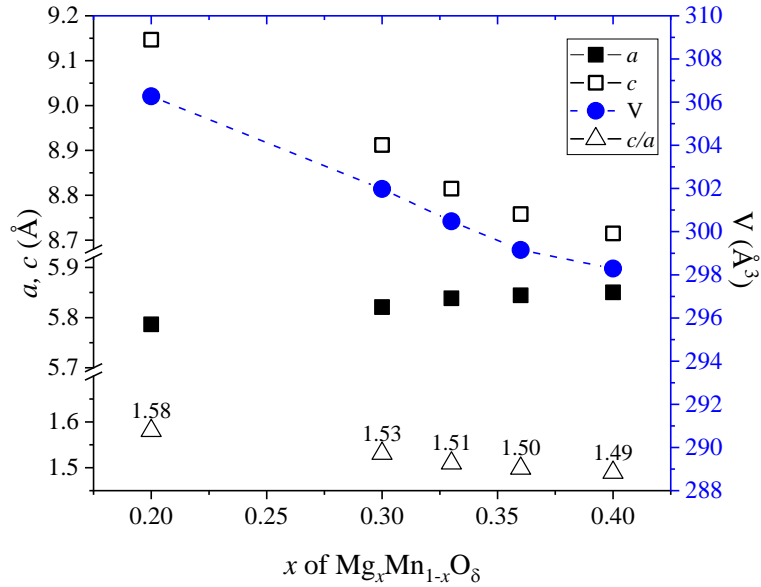


Figure 4.12 Lattice parameter, a , c , cell volume, V , and axial c/a ratio of the T2 for $0.20 \leq x \leq 0.40$ quenched from $1050\text{ }^{\circ}\text{C}$ into liquid nitrogen. Error bars are smaller than the data points

4.4.5 Effect of composition on samples quenched from $1000\text{ }^{\circ}\text{C}$

Samples quenched from $1000\text{ }^{\circ}\text{C}$ (figure 4.13) show similar changes to those observed quenched from $1050\text{ }^{\circ}\text{C}$ for $0.05 \leq x \leq 0.40$ except that at $x = 0.20$, a two-phase mixture of T1 and T2 was observed. Similar peak shift patterns were also observed as in $1050\text{ }^{\circ}\text{C}$ spectra for T1 and T2.

A C2 solid solution was observed between $0.50 \leq x \leq 0.80$, except at $x = 0.67$ where a three-phase mixture: C2, T2 and MgO was observed. The (311) and (400) reflections showed a decrease and increase in intensity respectively with increasing x .

At $x \geq 0.86$, a mixture of Suzuki phase and MgO was observed where MgO was more dominant at $x = 0.95$.

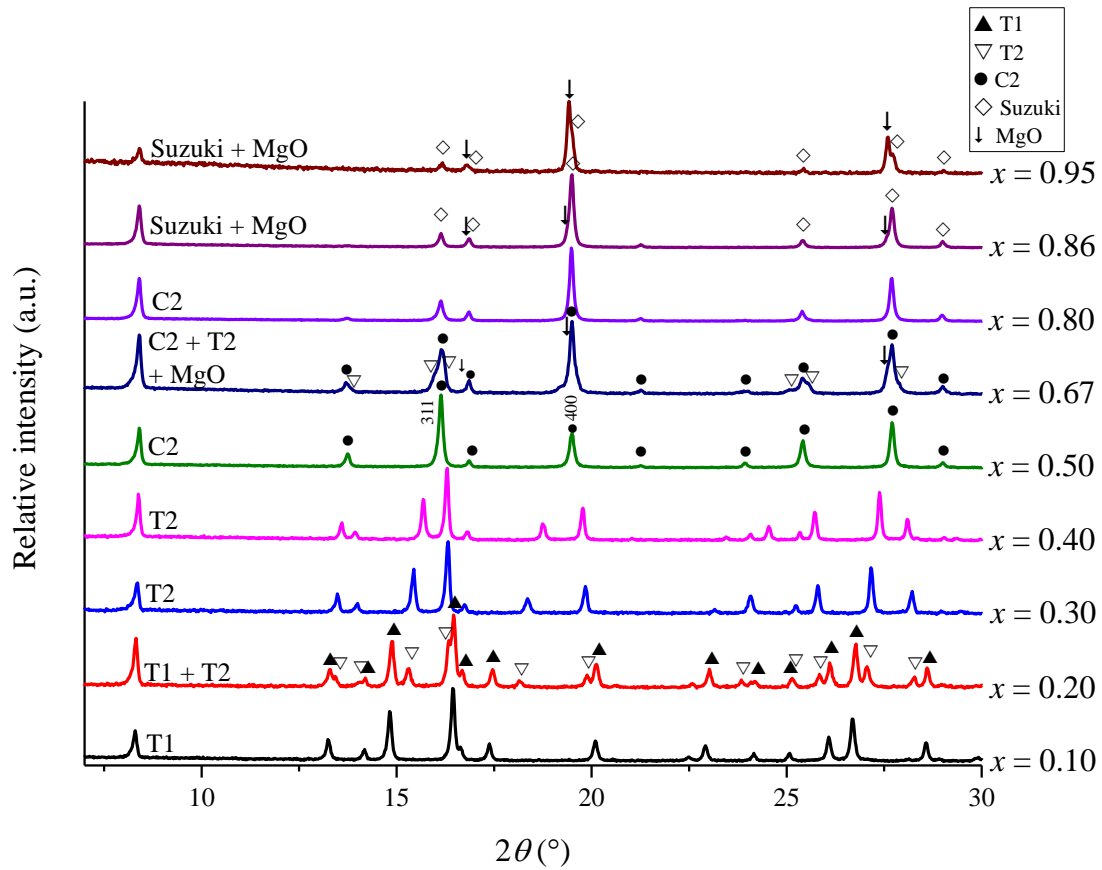


Figure 4.13 XRD patterns of $\text{Mg}_x\text{Mn}_{1-x}\text{O}_8$ quenched from 1000 °C into liquid N_2

4.4.6 Effect of composition on samples quenched from 900 °C

A similar phase transition pattern to that at 1000 °C was observed for samples quenched from 900 °C (figure 4.14) for $0.05 \leq x \leq 0.95$. Two distinct differences were that a mixture of T1 and T2 was now observed at $x = 0.30$ and the cubic solid solution was continuous from $x = 0.50$ to 0.80. No peak splitting was observed for the C2 reflection as compared to the slow-cooled samples. Pattern shifts and peak intensity variations are similar to that at 1000 °C.

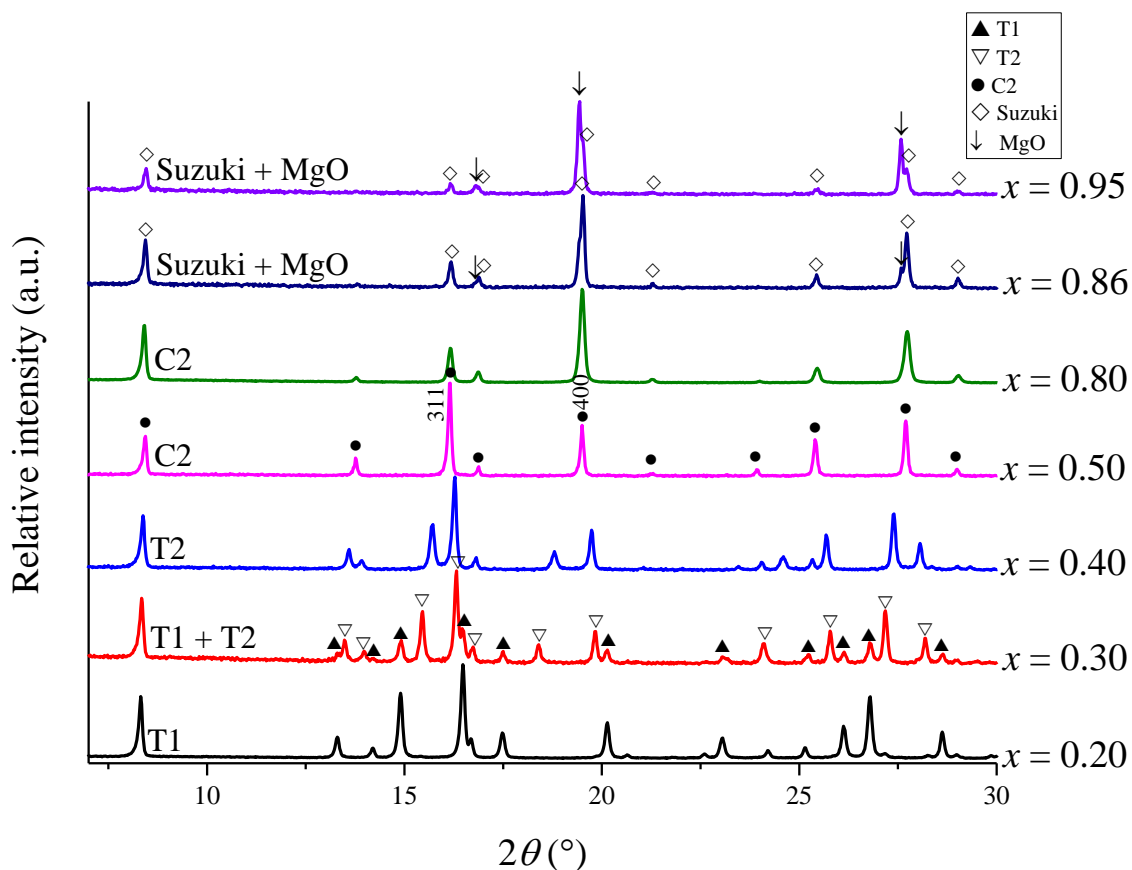


Figure 4.14 XRD patterns of $\text{Mg}_x\text{Mn}_{1-x}\text{O}_\delta$ quenched from 900 °C into liquid N_2

In order to study the transition from T2 to C2 ($0.40 \leq x \leq 0.50$) at 900 °C, four additional compositions were prepared with $x = 0.42, 0.44, 0.46$ and 0.48 . Samples were prepared using the same precursors and experimental methods.

XRD data (figure 4.15) for $x = 0.44$ to 0.48 showed a similar pattern with a similar intensity distribution that could probably indicate the reduced tetragonality of T2 with increasing x , instead of a two-phase mixture of T2 and cubic.

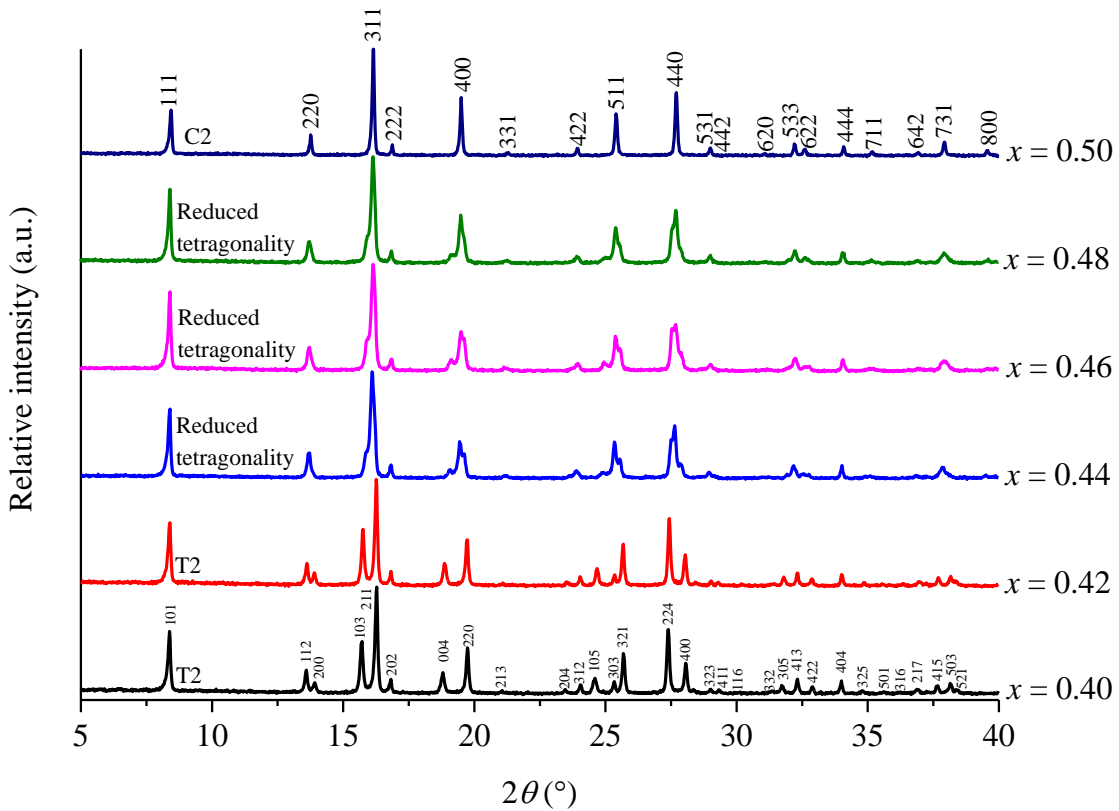


Figure 4.15 XRD patterns for $0.40 \leq x \leq 0.50$ quenched from 900°C into liquid N_2

The reflections from $x = 0.50$ were indexed with cubic space group $Fd\bar{3}m$ (227), $a = b = c = 8.3813(4) \text{ \AA}$, $V = 588.85(3) \text{ \AA}^3$, and thus it can be concluded that the composition $x = 0.50$ is a single phase (table 4.7). This reflection can also be indexed with cubic space group $Fm\bar{3}m$ (225) which resulted in the same refined lattice parameters. The difference between these two space groups is that $Fd\bar{3}m$ has an extra symmetry element of a body diagonal d -glide plane associated with its cubic structure. This extra symmetry results in an additional rule for reflection to be observed: $0kl: k+l = 4n$, where (hkl) are the Miller indices and n is an integer.

The XRD patterns observed (figure 4.16) do obey this additional rule of reflection whereby peaks correspond to $Fm\bar{3}m$ space group, (200), (420) and (640) over the range $5^\circ \leq 2\theta \leq 40^\circ$ were absent. However, the absence of these peaks could also mean that a destructive interference had occurred due to the resultant effect of the form factor, f , where $f_{\text{Mn}} \sim 2f_{\text{Mg}}$. In order to determine the suitable space group for C2, neutron diffraction

has been carried out. Tentative results showed that the reflections are best indexed using $Fm\bar{3}m$ space group instead of $Fd\bar{3}m$ and are described later in chapter 6.

Table 4.7 Indexing data for $x = 0.50$ quenched from 950 °C

N	$2\theta_{\text{obs}}$ (°)	h	k	l	$2\theta_{\text{calc}}$ (°)	$\Delta 2\theta$ (°)	Intensity	d_{obs} (Å)	d_{calc} (Å)
1	8.414	1	1	1	8.406	0.0088	45.0	4.834	4.839
2	13.751	2	2	0	13.747	0.0037	18.9	2.963	2.963
3	16.135	3	1	1	16.134	0.0009	100.0	2.527	2.527
4	16.857	2	2	2	16.857	0.0005	9.8	2.420	2.420
5	19.491	4	0	0	19.488	0.0023	55.4	2.095	2.095
6	23.930	4	2	2	23.927	0.0034	9.0	1.711	1.711
7	25.402	5	1	1	25.402	0.0004	47.2	1.613	1.613
8	27.699	4	4	0	27.697	0.0020	68.8	1.482	1.482
9	28.995	5	3	1	28.993	0.0015	10.9	1.417	1.417
10	31.039	6	2	0	31.044	-0.0044	5.3	1.326	1.325
11	32.219	5	3	3	32.217	0.0014	14.9	1.278	1.278
12	32.599	6	2	2	32.600	-0.0006	10.5	1.264	1.264
13	34.094	4	4	4	34.093	0.0011	11.3	1.210	1.210
14	35.176	7	1	1	35.176	0.0005	6.5	1.174	1.174
15	36.913	6	4	2	36.919	-0.0065	5.8	1.120	1.120
16	37.930	7	3	1	37.932	-0.0020	17.8	1.091	1.091

Symmetry: Face-centred cubic, Space group: $Fd\bar{3}m$, Final 2θ window: 0.01
 $a = 8.3813$ (4) Å and $V = 588.85$ (3) Å³

The C2 solid solution XRD patterns (figure 4.16) show a change in intensities with increasing x particularly for peaks (311) and (400). The peak (400) intensity increases and peak (311) intensity decreases.

Lattice parameters were measured for $x = 0.50, 0.60, 0.70$ and 0.80 (figure 4.17). The cubic solid solution observed a non-linear change with composition. The lattice constant a , shows a decrease with increasing x up to slightly less than 0.70 followed by a small increase until $x = 0.80$.

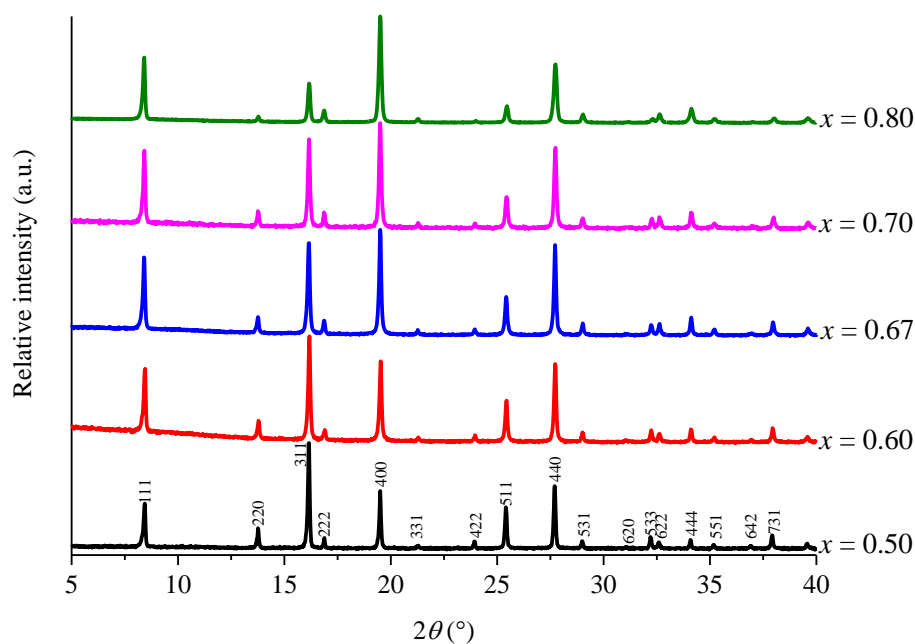


Figure 4.16 XRD patterns for $0.50 \leq x \leq 0.80$ quenched from 900°C into liquid N_2

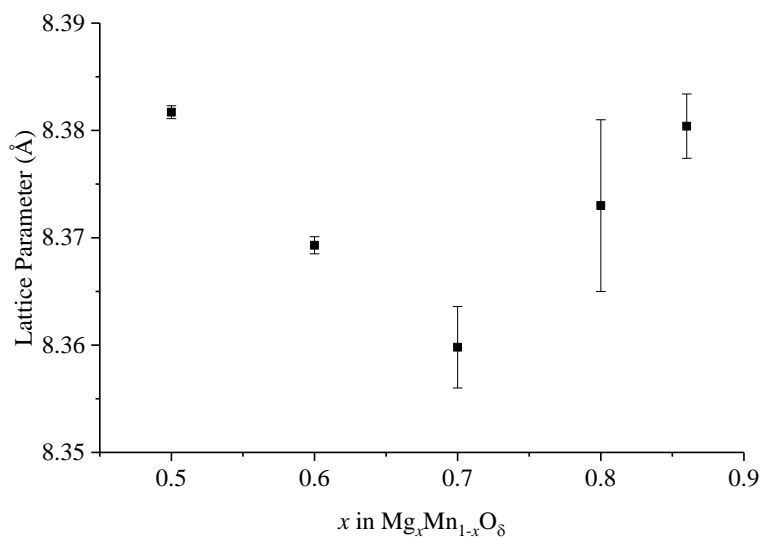


Figure 4.17 Lattice parameter measurement for the C2 cubic solid solution for $0.50 \leq x \leq 0.80$ quenched from 950°C into liquid nitrogen with statistical error bars of 2 e.s.d.s

4.4.7 Effect of composition on samples quenched from 700 °C

The diffraction patterns for samples quenched from 700 °C into liquid N₂ are shown in figure 4.18. A limited solid solution of T1 was observed over the range $0.05 \leq x \leq 0.20$. A cubic spinel phase is formed from $x = 0.30$ giving a mixture with T1 until $x = 0.40$. At $x = 0.50$, a C2 solid solution (ss) was observed. Over the range $0.60 \leq x \leq 0.80$, a mixture of cubic phases (C1 ss and C2 ss) coexist, which can be observed at a higher angle, $25^\circ \leq 2\theta \leq 30^\circ$. The identification of C1 ss and C2 ss was described in section 4.3. For $x \geq 0.86$, a mixture of Suzuki phase and MgO was observed.

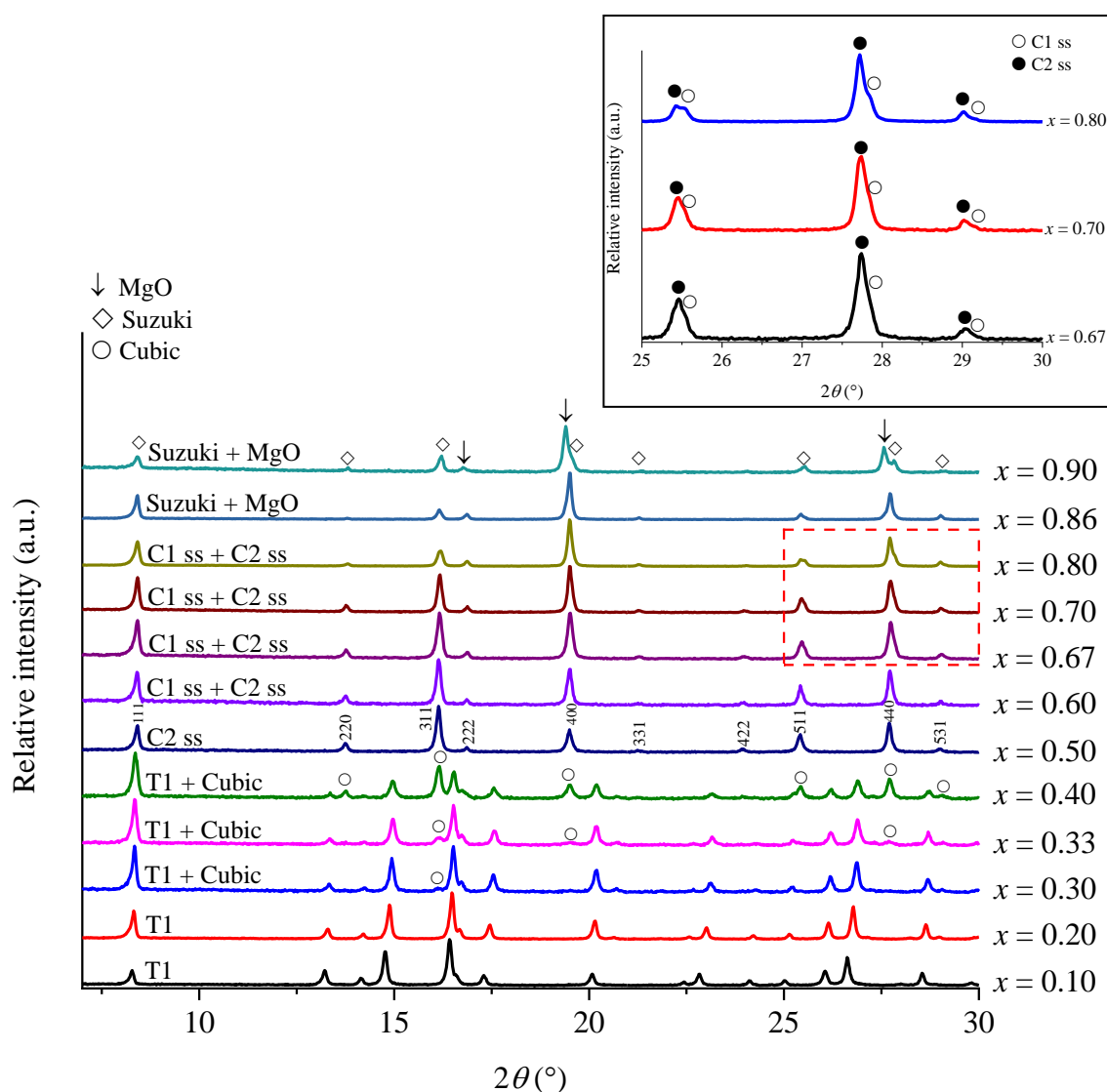


Figure 4.18 XRD patterns of $\text{Mg}_x\text{Mn}_{1-x}\text{O}_8$ quenched from 700 °C into liquid N₂. Inset shows two cubic phases (C1 ss and C2 ss) present over the range

$$25^\circ \leq 2\theta \leq 30^\circ$$

Since the reflections between C1 and C2 solid solutions are not well separated, inset figure 4.18, further phase characterization was carried out on a single composition $x = 0.67$ using STOE Stadi P X-ray diffractometer with Cu $K\alpha_1$ ($\lambda = 1.5405 \text{ \AA}$) radiation. Based on Bragg's law, with higher radiation wavelength, the reflections between C1 ss and C2 ss could be better resolved. Small amounts of powder were heated over the range $700 \sim 950 \text{ }^\circ\text{C}$ and quenched at $50 \text{ }^\circ\text{C}$ intervals into liquid nitrogen. Results (figure 4.19) showed that the amount of cubic ss phase is reduced with increasing temperature. A single phase of C2 ss was observed from 900 to $950 \text{ }^\circ\text{C}$.

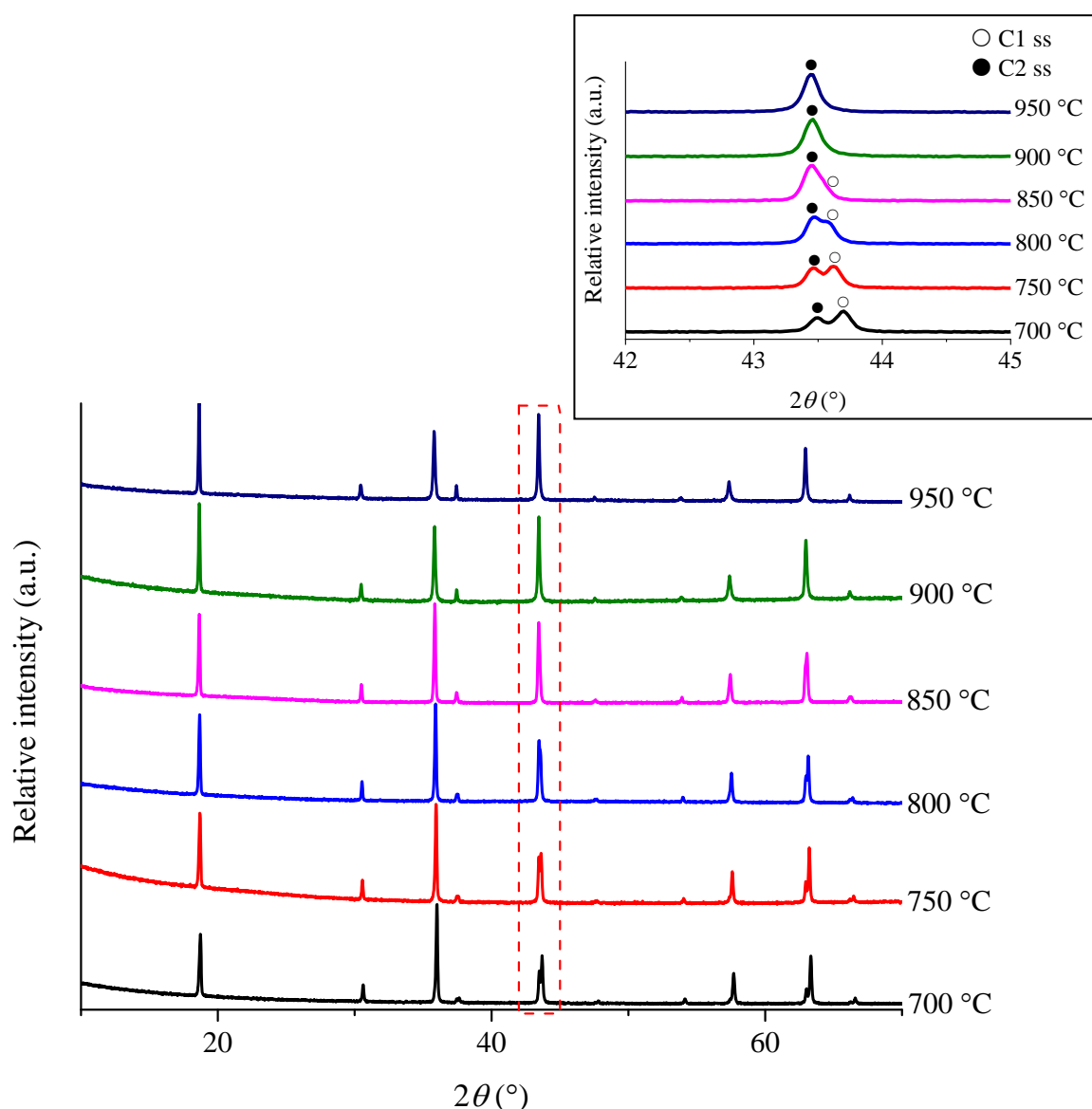


Figure 4.19 XRD patterns (Cu $K\alpha_1$ radiation) for $x = 0.67$ quenched from 700 to $950 \text{ }^\circ\text{C}$. Inset shows mixture of C1 ss and C2 ss over the range $42^\circ \leq 2\theta \leq 45^\circ$

4.5 Differential Scanning Calorimetry (DSC)

4.5.1 DSC of MnO₂

A DSC thermal analysis was conducted on pristine MnO₂ (figure 4.20). The sample was heated in argon/air at rate 10 °C/min from room temperature to 1300 °C and slowly cooled to room temperature using the same rate.

Three endothermic peaks and one exothermic peak were observed during heating and cooling respectively.

The first two endothermic peaks at 600 and 950 °C were attributable to the polymorphic transitions of MnO₂ to Mn₂O₃ and Mn₂O₃ to Mn₃O₄ tetragonal spinel respectively as shown by the XRD patterns of samples quenched from different temperatures (figure 4.21). The third endothermic peak at 1180 °C, does not indicate any polymorphic transition based on the XRD patterns observed. Tentative results on HTXRD (section 4.6.1) however, showed a formation of Mn₃O₄ cubic spinel at higher temperatures. This suggested that the third endothermic peak was attributed to the polymorphic transition of Mn₃O₄ tetragonal to cubic spinel.

All reflections of the sample quenched from 1300 °C were indexed using the tetragonal space group *I4₁/amd* (141), $a = b = 5.7664$ (5) Å, $c = 9.4658$ (12) Å, $V = 314.75$ (4) Å³, lattice c/a ratio = 1.6415 (3), and thus it can be concluded that the sample was single phase (table 4.8). Samples quenched from 1000 to 1300 °C showed similar XRD patterns to the T1 tetragonal spinel.

On cooling, the single exothermic peak at 1130 °C could therefore be attributed to the polymorphic transition of Mn₃O₄ cubic to tetragonal spinel (section 4.6.1). A small exothermic peak at *ca* 70 °C is probably due to some moisture absorption by the sample.

The endothermic and exothermic peaks at 1180 °C and 1130 °C respectively, were further investigated using HTXRD and are described later in section 4.6.1.

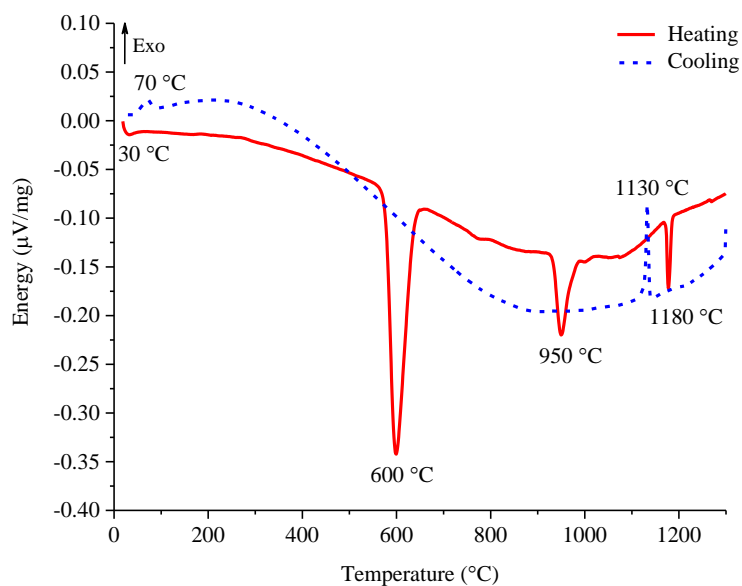
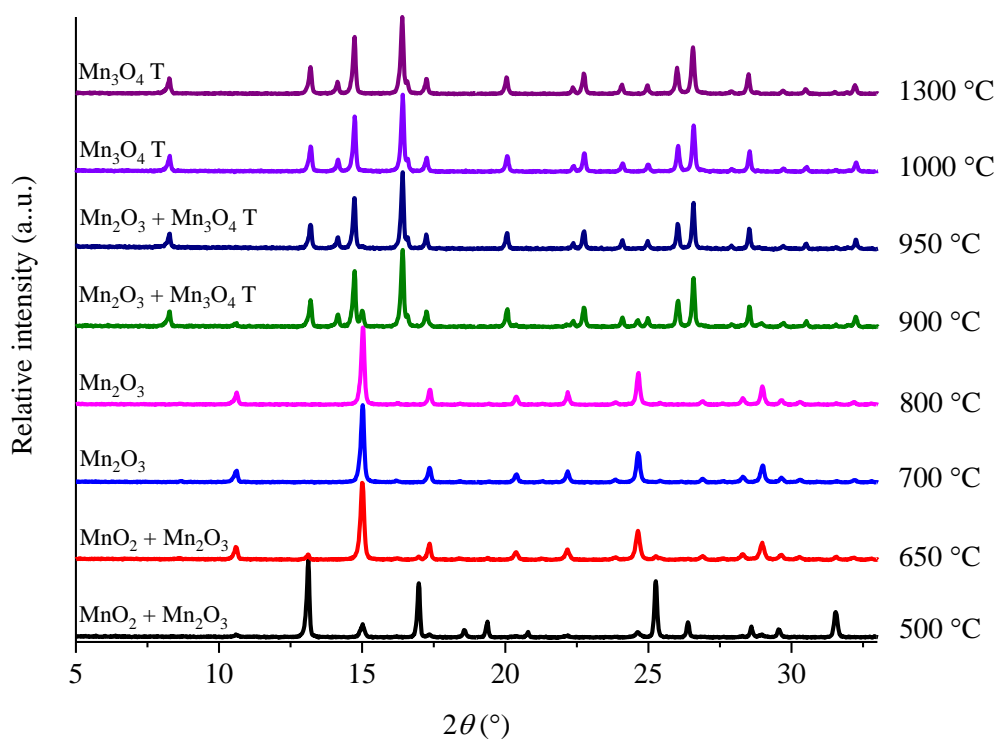
Figure 4.20 DSC curves for MnO_2 heated to 1300 °C

Figure 4.21 XRD patterns for pristine MnO_2 quenched over the range 500 to 1300 °C into liquid N_2 . Mn_3O_4 T represents tetragonal spinel. No evidence for cubic spinel or T2 was seen

Table 4.8 Indexing data for pristine Mn₃O₄ quenched from 1300 °C

No	2 θ_{obs} (°)	h	k	l	2 θ_{calc} (°)	$\Delta 2\theta$ (°)	Intensity	d _{obs} (Å)	d _{calc} (Å)
1	8.241	1	0	1	8.260	-0.0181	23.8	4.935	4.925
2	13.174	1	1	2	13.185	-0.0109	38.3	3.092	3.089
3	14.124	2	0	0	14.131	-0.0075	19.4	2.885	2.883
4	14.714	1	0	3	14.723	-0.0086	75.1	2.770	2.768
5	16.384	2	1	1	16.389	-0.0052	100.0	2.489	2.488
6	16.551	2	0	2	16.562	-0.0114	22.2	2.464	2.462
7	17.230	0	0	4	17.238	-0.0082	24.2	2.368	2.367
8	20.035	2	2	0	20.036	-0.0008	26.6	2.039	2.039
9	22.355	2	0	4	22.359	-0.0036	12.4	1.830	1.829
10	22.739	1	0	5	22.743	-0.0039	31.7	1.799	1.799
11	24.058	3	1	2	24.060	-0.0016	16.3	1.702	1.702
12	24.971	3	0	3	24.954	0.0168	18.2	1.640	1.642
13	25.994	3	2	1	25.993	0.0012	38.7	1.577	1.577
14	26.549	2	2	4	26.548	0.0012	68.5	1.545	1.545
15	27.898	1	1	6	27.896	0.0027	7.8	1.471	1.471
16	28.488	4	0	0	28.483	0.0051	29.8	1.441	1.442
17	29.697	2	0	6	29.695	0.0019	9.3	1.384	1.384
		4	1	1	29.705	-0.0081			1.384
18	30.495	3	0	5	30.489	0.0060	11.0	1.349	1.349
19	31.505	3	3	2	31.505	0.0001	6.3	1.306	1.306
20	31.939	4	2	0	31.930	0.0097	6.4	1.289	1.289
21	32.211	4	1	3	32.207	0.0037	16.1	1.278	1.279
22	33.112	4	2	2	33.126	-0.0140	11.6	1.245	1.244
23	33.481	4	0	4	33.484	-0.0028	10.5	1.231	1.231
24	34.457	2	1	7	34.451	0.0058	11.7	1.197	1.198
25	34.886	0	0	8	34.883	0.0028	9.3	1.183	1.183
26	36.755	4	1	5	36.755	0.0007	12.5	1.125	1.125
27	37.619	5	1	2	37.620	-0.0006	6.5	1.100	1.100
28	38.226	5	0	3	38.223	0.0024	12.1	1.083	1.083
29	38.939	4	0	6	38.932	0.0073	8.0	1.064	1.064
		5	2	1	38.940	-0.0006			1.064

Symmetry: Body-centred tetragonal, Space group: $I4_1/amd$, Final 2θ window: 0.02
 $a = 5.7664$ (5) Å, $c = 9.4658$ (12) Å, $V = 314.75$ (4) Å³ and $c/a = 1.6415$ (3)

In order to check the reversibility of transformation between polymorphs during heating and cooling, the experiment was repeated using pristine MnO_2 heated separately at $850\text{ }^\circ\text{C}$ and $1050\text{ }^\circ\text{C}$ (figure 4.22).

For sample heated at $850\text{ }^\circ\text{C}$, figure 4.22 (a), a single endothermic peak was observed, attributed to the polymorphic transition of MnO_2 to Mn_2O_3 . There was no exothermic peak was observed on cooling.

For sample heated at $1050\text{ }^\circ\text{C}$, figure 4.22 (b), two endothermic peaks were observed at $\sim 590\text{ }^\circ\text{C}$ and $\sim 900\text{ }^\circ\text{C}$ attributed to the polymorphic transitions of MnO_2 to Mn_2O_3 and Mn_2O_3 to Mn_3O_4 tetragonal spinel respectively. Again, no exothermic peak was observed on cooling.

At the end of each experiment, a phase analysis was conducted for both samples and showed a single phase of Mn_2O_3 and Mn_3O_4 tetragonal spinel, respectively.

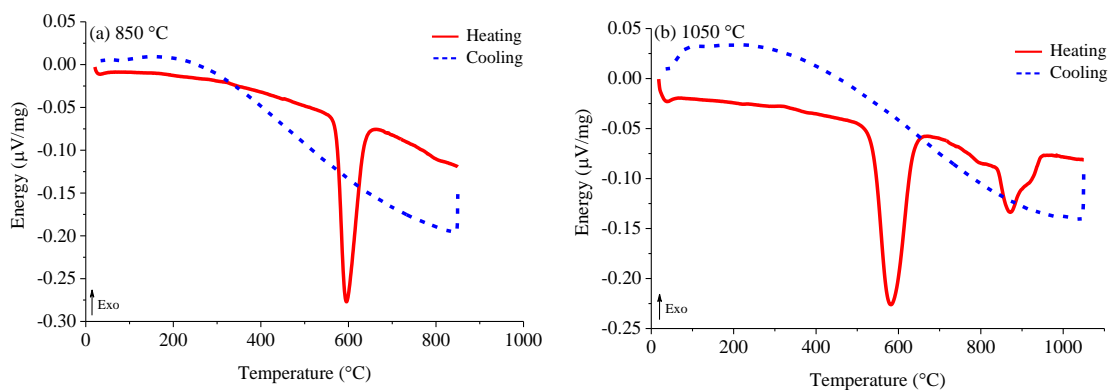
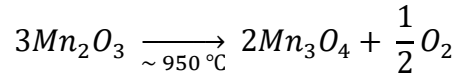
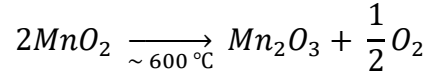


Figure 4.22 DSC curves for MnO_2 heated to: (a) $850\text{ }^\circ\text{C}$ and (a) $1050\text{ }^\circ\text{C}$

The irreversibility of the transitions $\text{MnO}_2 \rightarrow \text{Mn}_2\text{O}_3$ and $\text{Mn}_2\text{O}_3 \rightarrow \text{Mn}_3\text{O}_4$, are probably due to the decomposition of MnO_2 and Mn_2O_3 respectively by oxygen loss from the sample with increasing temperature. Therefore, any oxygen uptake during cooling is very slow and may be regarded as negligible.



4.5.2 DSC of $x = 0.05, 0.10, 0.20$ and 0.30 of $\text{Mg}_x\text{Mn}_{1-x}\text{O}_8$

A small portion of $x = 0.05, 0.10, 0.20$ and 0.30 was used for thermal analysis. Samples were heated in argon/air at rate $10^\circ\text{C}/\text{min}$ from room temperature to 1000 and 1300°C and slowly cooled to room temperature with the same rate.

A single endothermic and exothermic peak were observed for all samples (figure 4.23). However, the temperature range for the endothermic peaks are widened with increasing x for $0 \leq x \leq 0.30$. It was observed that at $x = 0.30$, the endothermic peak is so broad that the onset temperature was observed at about $\sim 500^\circ\text{C}$. Considering the tip of the endothermic peak at which a complete transition occurred, it can be seen that the transition temperature decreases with increasing x for $0 \leq x \leq 0.30$ (figure 4.24).

The exothermic peaks also showed a similar trend in which the peaks became broadened and reduced in height with increasing x for $0 \leq x \leq 0.30$.

The broadening of the endothermic peaks implied that the transition occurs at a wider range and passes through a two-phase region. This is consistent with the XRD patterns described in section 4.4.

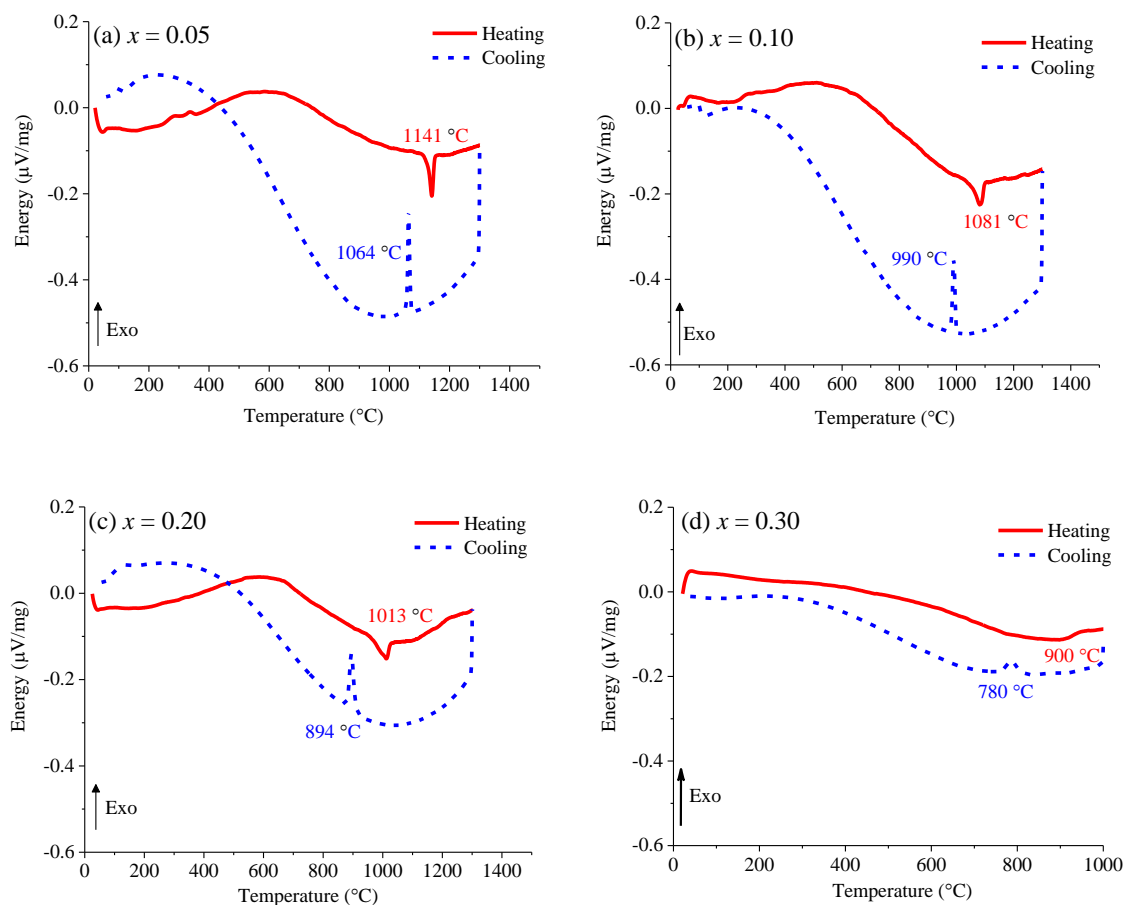


Figure 4.23 DSC curves for (a) $x = 0.05$, (b) $x = 0.10$, (c) $x = 0.20$ and (d) $x = 0.30$

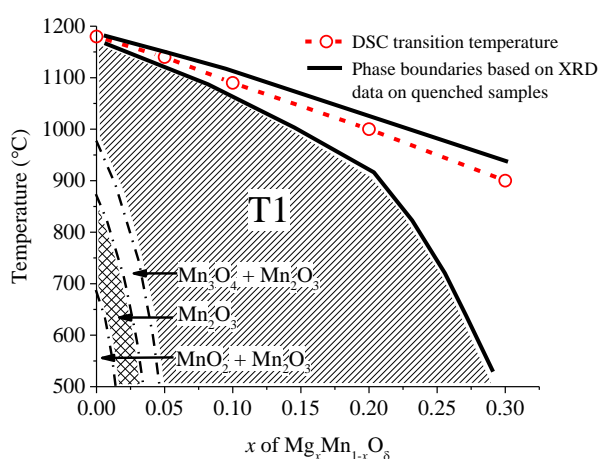


Figure 4.24 Transition temperatures from DSC endothermic peak maxima for $0 \leq x \leq 0.30$.

Solid lines are deduced from XRD data on quenched samples (discussed later). The dash-dot lines are the predicted phase boundaries of Mn_2O_3 and T1 solid solution of $x < 0.05$ since no measurement was carried out within this range.

4.5.3 DSC of T2, $x = 0.20$ of $\text{Mg}_x\text{Mn}_{1-x}\text{O}_\delta$

A small portion of $x = 0.20$ quenched from 1100 °C into liquid nitrogen was used for thermal analysis. Sample was heated in argon/air at rate 50 °C/min from room temperature to 1100 °C and rapidly cooled to room temperature with the same rate.

Small exothermic (~ 375 °C) and endothermic (~ 1018 °C) peaks were observed on heating, followed by a single exothermic (~ 870 °C) peak on cooling (figure 4.25).

The small exothermic peak observed on heating shows a possibility of phase transformation of the sample. In order to investigate further, the experiment was repeated with the same rate, heated up to 600 °C, a temperature slightly higher than the exothermic peak (on heating). A phase analysis was carried out on the same sample after the DSC measurement. The XRD pattern obtained is similar to the T1 sample (figure 4.26). This showed that the exothermic peak, at ~ 375 °C, could be attributed to the T2 (metastable) \rightarrow T1 (stable) transformation.

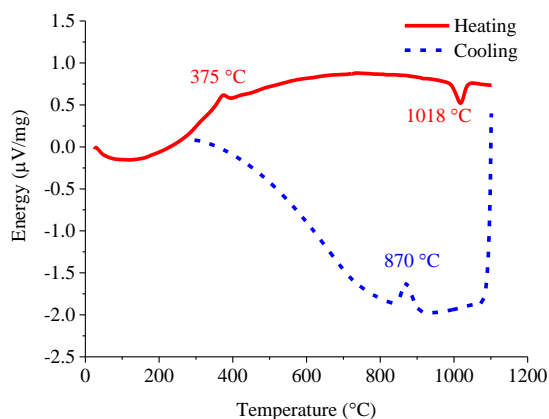


Figure 4.25 DSC curves for T2, $x = 0.20$ at rate 50 °C/min

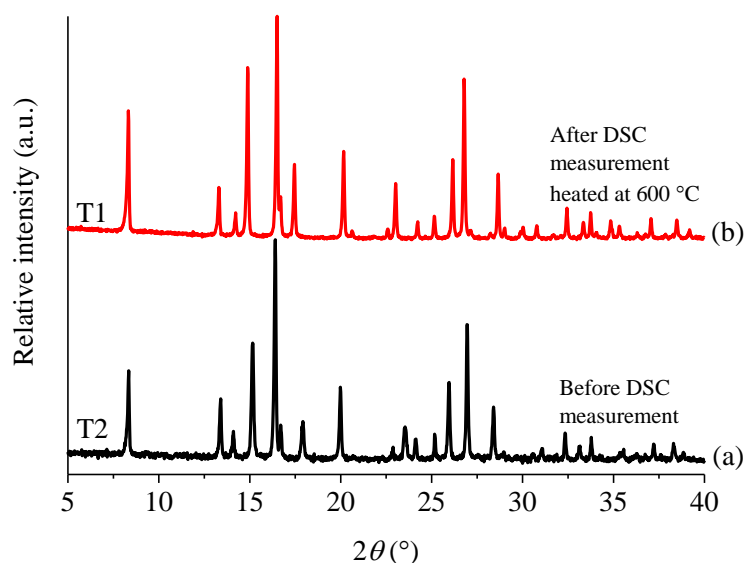


Figure 4.26 XRD patterns for T2, $x = 0.20$. (a) Reflection before DSC measurement (T2). (b) Reflection after DSC measurement heated to 600 °C at 50 °C/min and rapidly cooled to room temperature using the same rate

4.6 High-Temperature X-ray Diffraction (HTXRD)

4.6.1 HTXRD on MnO₂

An *in-situ* HTXRD was conducted on a small quantity of pristine MnO₂ and data were recorded at 30, 500, 800, 1100, 1300 and 1400 °C (figure 4.27). The sample was heated at rate 5 °C/min and was kept at the measurement temperature for four hours to allow equilibration before each measurement.

A single phase of MnO₂ was observed from room temperature to 500 °C. At 800 °C, a single phase of Mn₂O₃ was observed. A mixture of Mn₂O₃ and Mn₃O₄ tetragonal spinel was observed at 1100 °C. At 1300 °C, a cubic spinel of Mn₃O₄ (denoted as Mn₃O₄ C) was observed together with a small amount of Mn₃O₄ tetragonal spinel (denoted as Mn₃O₄ T). A single phase of Mn₃O₄ cubic spinel was observed at 1400 °C. Five extra peaks were observed at 2θ *ca* 39.3°, 45.7°, 66.7°, 80.3° and 84.8°, corresponding to Pt heating slab.

Phase analysis comparison between the quenched sample (figure 4.21) and HTXRD data showed that Mn_3O_4 cubic spinel formation was only observed in the HTXRD at a higher temperature (table 4.9). Therefore, from the DSC result (figure 4.20), it can be concluded that the endothermic peak observed at 1180 °C, was probably attributed to the polymorphic transition of Mn_3O_4 tetragonal to cubic spinel (since there was no evidence at higher temperature of T2 tetragonal phase).

In preparing the HTXRD experiment, the sample powder was spread on top of a Pt slab over a wide area. The temperature was recorded by a thermocouple attached to the bottom of the Pt slab at a specific point. The presence of a small quantity of Mn_2O_3 at 1100 °C and Mn_3O_4 T at 1300 °C could probably be due to the temperature gradient along the Pt slab which resulted in incomplete transformation. Despite this, the main phase observed was identifiable.

Table 4.9 Phase analysis data comparison between XRD on quenched MnO_2 and HTXRD. T represent tetragonal and C represent cubic

Temperature (°C)	Phase(s) present	
	XRD on the quenched sample	HTXRD
1400	-	Mn_3O_4 C
1300	Mn_3O_4 T	Mn_3O_4 C, Mn_3O_4 T (small amount)
1100	Mn_3O_4 T	Mn_3O_4 T, Mn_2O_3 (small amount)
800	Mn_2O_3	Mn_2O_3
500	MnO_2 , Mn_2O_3 (small amount)	MnO_2
30	MnO_2	MnO_2

The rapid polymorphic transition of Mn_3O_4 from tetragonal to cubic spinel could probably be because the Mn^{3+} ions are randomly oriented in the distorted octahedral sites at high temperature. This randomization could allow the cubic symmetry of Mn_3O_4 to be achieved statistically. On quenching, the Mn^{3+} ions are collectively returned to their favorable distorted orientation, where they align cooperatively in adjacent unit cells. Thus, a tetragonal spinel structure is formed.

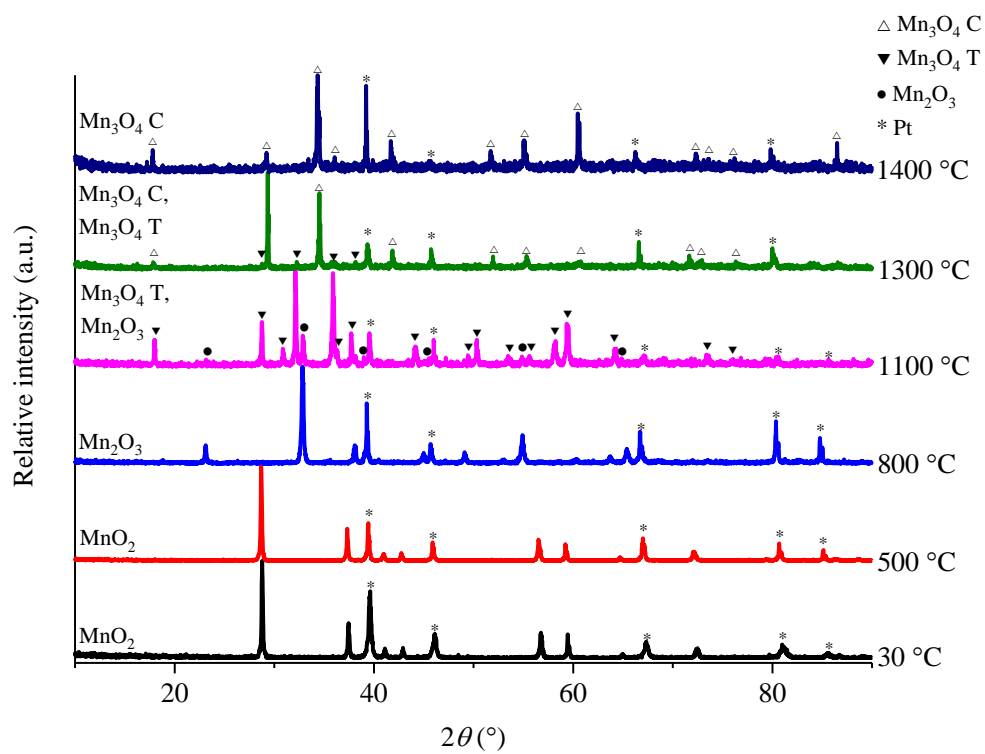


Figure 4.27 HTXRD patterns for MnO₂. Mn₃O₄ T represent tetragonal spinel and Mn₃O₄ C represents cubic spinel

4.6.2 HTXRD on $x = 0.20$ and 0.30 of $\text{Mg}_x\text{Mn}_{1-x}\text{O}_8$

HTXRD was conducted on $x = 0.20$ and 0.30 in order to investigate the possible presence of cubic spinel such as was shown by $x = 0$ (MnO_2) (figure 4.27). The samples were heated at $5\text{ }^\circ\text{C}/\text{min}$ and kept at a measured temperature for four hours to allow equilibration before each measurement.

For sample $x = 0.20$ (figure 4.28 (a)), a single phase of T1 tetragonal spinel was observed up to $900\text{ }^\circ\text{C}$. At $1000\text{ }^\circ\text{C}$, a cubic spinel (denoted as C1) formed and gave a mixture with T1. A single phase of C1 ss was observed at $1200\text{ }^\circ\text{C}$. No evidence of tetragonal T2 was observed.

For sample $x = 0.30$ (figure 4.28 (b)), a mixture of T1 and C2 was observed from 700 to $900\text{ }^\circ\text{C}$. A single phase of C1 ss was observed at $1100\text{ }^\circ\text{C}$. Again, no evidence of T2 was observed.

These HTXRD data indicate the presence of a C1 ss instead of a T2 as shown by the quenched samples. Again, the C1 ss was observed probably due to the random orientation of the Mn^{3+} ions, similar to the observed Mn_3O_4 cubic spinel described in the previous section.

However, on quenching, this C1 cubic spinel does not revert to T1 tetragonal structure, but undergoes an unavoidable cubic to T2 tetragonal spinel phase transition as shown by the XRD pattern (figure 4.6). This result differs from that of pure MnO_2 , and gave an early indication that the T2 tetragonal spinel might be a metastable phase.

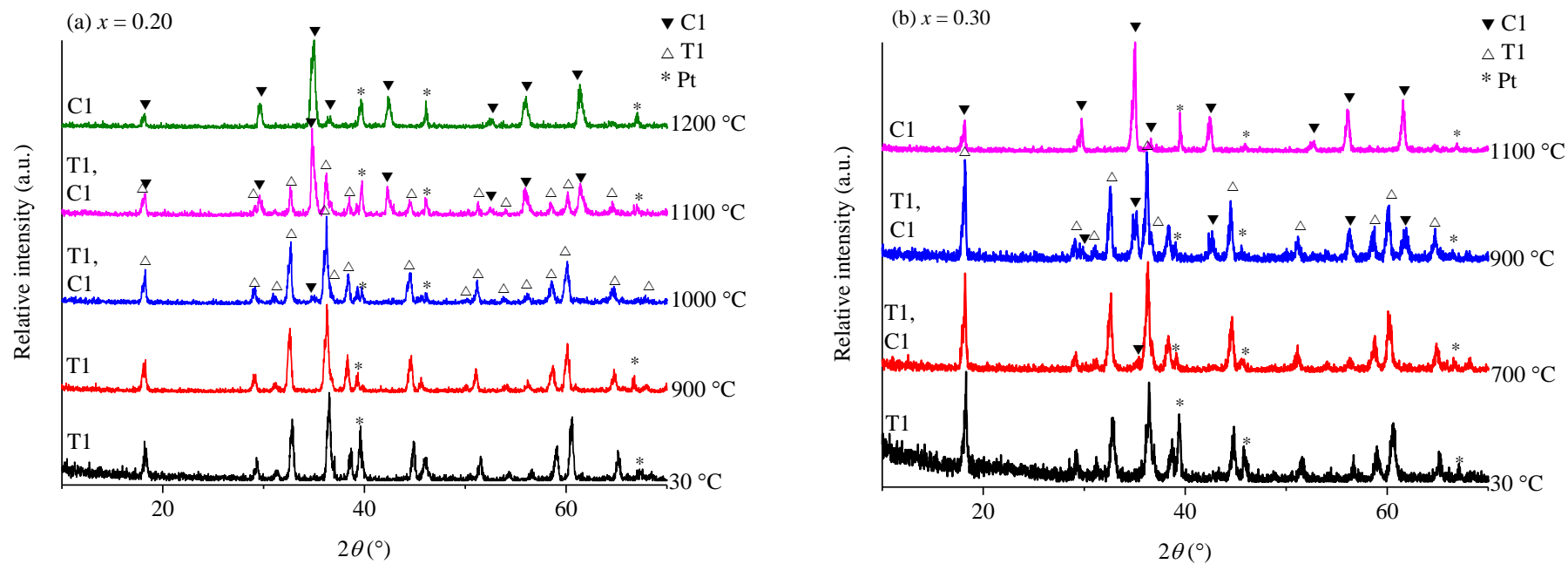
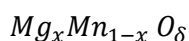


Figure 4.28 HTXRD (a) $x = 0.20$ and (b) $x = 0.30$ of $\text{Mg}_x\text{Mn}_{1-x}\text{O}_\delta$. T1 = tetragonal spinel; C1 = cubic spinel. No evidence of T2 tetragonal spinel was observed

4.7 Pseudo-binary phase diagram in the system of MnO_δ - MgO in air at 700 – 1100 °C

A combination of XRD results on quenched samples, DSC and HTXRD have enabled a phase diagram to be constructed (figure 4.29). Three large single-phase solid solution areas that exist under equilibrium conditions have been identified. These are: tetragonal spinel, T1; cubic spinel, C1; cubic spinel-Suzuki phase, C2. In addition, a second tetragonal spinel, T2 was prepared, by rapid transformation of C1 during quenching, which appears to be entirely metastable and does not appear on the equilibrium phase diagram.

The phase diagram was constructed from a variety of results on 19 different compositions x , described in section 4.2, with general formula:



Since Mn can adopt various oxidation states, the general formula does not specify the oxygen non-stoichiometry, δ .

Phase analysis are investigated using XRD data of quenched samples and HTXRD data, at various temperatures. The observed phase(s) are marked in an xy -plot of $\text{Mg}/(\text{Mg}+\text{Mn})$ mol fraction against temperature. Based on these plotted data, approximate phase boundaries were identified.

In addition, transition temperatures from DSC measurements, taken at the endothermic peak maxima of $x = 0.05, 0.10, 0.20$ and 0.30 , matched well with the phase boundary deduced from the XRD data on quenched samples, within errors (figure 4.24). However, it is still uncertain whether the endothermic peak on heating corresponds to a direct $\text{T1} \rightarrow \text{C1}$ transition, or a $\text{T1} \rightarrow \text{T2}$ transition.

The part of the phase diagram between Mn_3O_4 and Mg_2MnO_4 , figure 4.29, is binary since all phases that appear have compositions that also lie on this join. They have the spinel stoichiometry AB_2O_4 with fixed oxygen stoichiometry, but their variable

Mg:Mn ratio requires the average Mn oxidation state to vary from 2.67+ in Mn_3O_4 to 4.00+ in Mg_2MnO_4 .

MnO_2 and Mn_2O_3 are both stable manganese oxides at lower temperatures but we found no evidence for either of these, or solid solutions derived from them in Mg-doped compositions (figure 4.29). Similarly, MnO is a stable, high temperature manganese oxide but was not encountered here for temperatures up to at least 1400 °C in Mn-rich compositions. DSC results on MnO_2 showed three endotherms on heating (figure 4.20) attributed to transitions between MnO_2 , Mn_2O_3 , tetragonal Mn_3O_4 and cubic Mn_3O_4 at 600, 950 and 1180 °C, respectively. On cooling, a single exotherm at 1130 °C is seen, attributed to the cubic to tetragonal transition in Mn_3O_4 . This tetragonal phase is regarded as the end-member of the T1 solid solution series (figure 4.29), whose compositional extent increases with decreasing temperature to e.g. $x \leq \sim 0.28$ at ~ 600 °C.

HTXRD confirmed the existence of the tetragonal to cubic transition at high temperature in Mn_3O_4 and also showed that an extensive solid solution of cubic Mg-doped compositions formed, which could not be preserved on quenching to room temperature. Instead, the materials changed to the tetragonal polymorph, T2. From the XRD results on a given composition, say $x = 0.20$, either T1 or T2 single phase polymorphs with significantly different lattice parameters was obtained, depending on quench temperature. Further, the T2 to T1 transformation took place on annealing T2 quenched polymorph at, say 800 °C (table 4.5) and as shown by the DSC results at ~ 375 °C (figure 4.25).

The phase field of cubic spinel, C1 solid solution (figure 4.29), extends over the composition range $0 < x \leq 0.40$ but is limited at lower temperatures by a eutectoid where it transforms to a mixture of T1 and a cubic phase of composition $x \leq 0.50$ at ~ 760 °C.

At higher temperature, quenched samples (T2) over the range $0.44 \leq x \leq 0.48$ show a gradual reduction in tetragonality before entering the range of C2 (figure 4.15) which covers the range $0.50 \leq x < 0.86$. Further work is required to fully characterise the materials in this region of reduced tetragonality and especially determine whether there is a morphotropic phase boundary or a two-phase region between C1 and C2 phases.

The cubic solid solution region, C2, extends to the approximate composition of the Suzuki phase Mg_6MnO_8 and appears to be single phase over the entire composition range above $\sim 900^\circ\text{C}$. The composition $x = 0.67$ would correspond, ideally, to the limit of solid solutions with spinel stoichiometry since at $x = 0.67$, the formula is $\text{Mg}_2\text{Mn}^{4+}\text{O}_4$. For $x > 0.67$, a different solid solution mechanism is required and is speculated to involve the replacement mechanism $\text{Mn}^{4+} \rightarrow 2\text{Mg}^{2+}$ and involve the location of extra cations in interstitial sites that are unoccupied in the spinel structure. Results of initial structural studies in these compositions are presented in chapter 6.

The C2 solid solutions are not stable over the whole composition range, $\leq 850^\circ\text{C}$ but decompose into two different cubic compositions, as shown by an immiscibility dome with an upper consolute temperature of 850°C (figure 4.29).

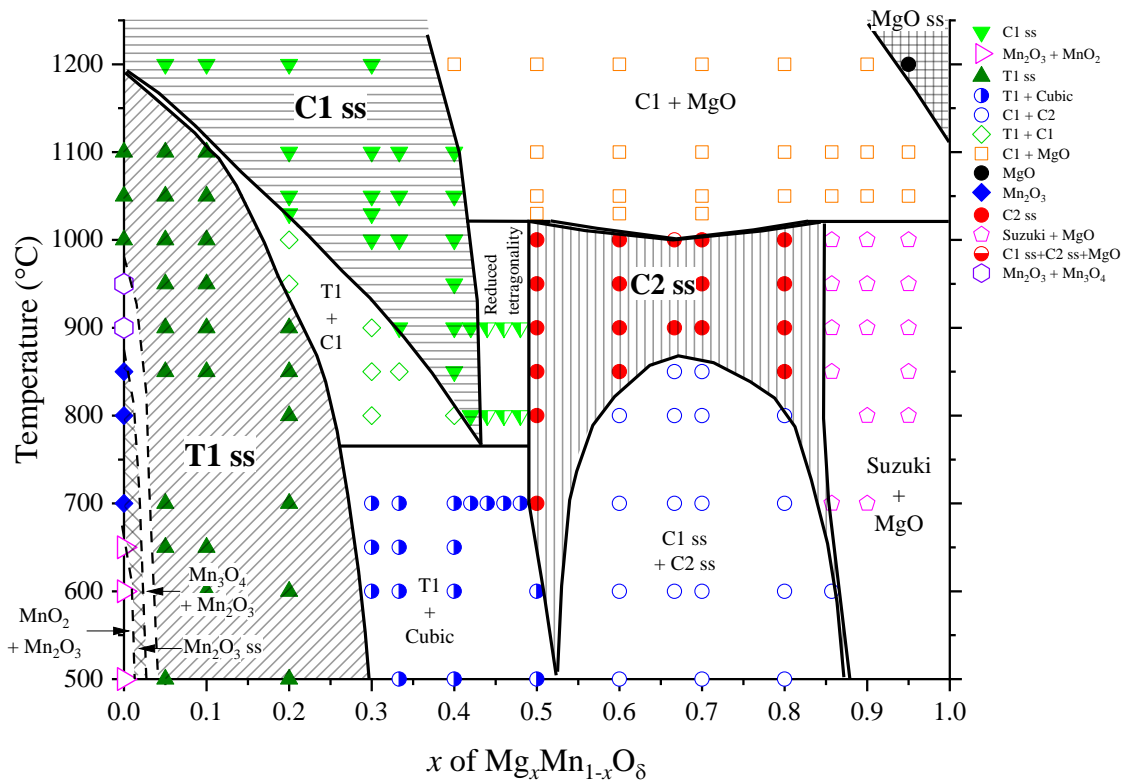


Figure 4.29 Pseudo-binary phase diagram of $\text{Mg}_x\text{Mn}_{1-x}\text{O}_\delta$ over the range 500 to 1200 $^\circ\text{C}$. The solid-lines represent the possible phase boundaries based on XRD data for samples quenched in liquid N_2 . The broken-lines are predicted boundaries.

4.8 Discussion

Manganese exhibits various oxidation states within the MgO-MnO_8 system. The expected Mn oxidation states, chemical compensation and general chemical formula are shown in figure 4.30. These cover the cation:oxygen ratio of 3:4 for spinel structures for $0 \leq x \leq 0.67$ and rock salt-related structures with $x > 0.67$.

For $x < 0.33$, it is expected that Mn exhibits both 2+ and 3+ oxidation states with partial substitution of Mn^{2+} by Mg^{2+} with increasing x . At $x = 0.33$, only Mn^{3+} is expected due to replacement of Mn^{2+} by Mg^{2+} ions. Over the range $0.33 < x < 0.67$, it is expected that partial substitution of two Mn^{3+} ions with a pair of Mg^{2+} and Mn^{4+} ions occurs. Therefore, within this domain, it is expected that Mn exhibits a mixture of 3+ and 4+ oxidation states. Beyond $x = 0.67$, it is expected that the Mn only exhibits a 4+ oxidation state and a further increase in x results in the creation of Mg^{2+} interstitials accompanied by the reduction in the number of Mn^{4+} ions. These expectations assume that there are no changes in oxygen content and the oxygen sublattice in cubic close packed throughout. It also assumes that there is no disproportionation of Mn^{3+} into a mixture of Mn^{2+} and Mn^{4+} , such as has been suggested [9, 10].

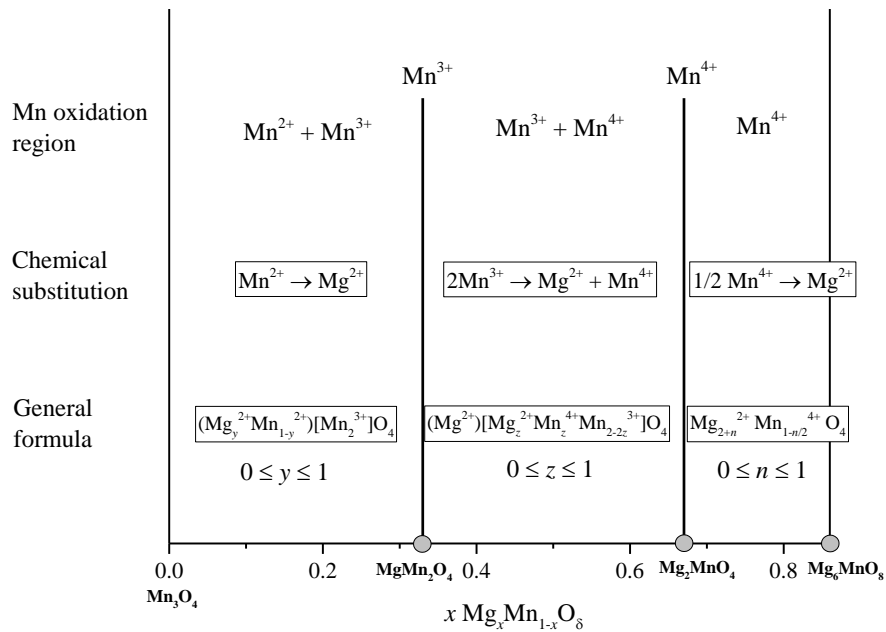


Figure 4.30 The expected Mn oxidation states, chemical substitution and general formulae within $\text{Mg}_x\text{Mn}_{1-x}\text{O}_8$

The x-ray diffraction patterns for slow-cooled samples of $x = 0.33$ (MgMn_2O_4), $x = 0.67$ (Mg_2MnO_4) and $x = 0.86$ (Mg_6MnO_8) indicate that attempts to prepare these stoichiometric compositions through solid state method were not really successful since phase mixtures were observed at these compositions.

Studies on the quenched samples showed that there are two major discrepancies compared to the reported literature [7, 11]. First is the formation of a tetragonal T2 ss on quenching compositions in the range $0 < x \leq 0.42$ instead of a cubic spinel. However, based on HTXRD, a cubic spinel was observed at high temperature instead of a tetragonal T2. Therefore, it appears that a rapid polymorphic transition from cubic spinel to T2 occurs during quenching (and the temperature at which this occur is very much dependent on x).

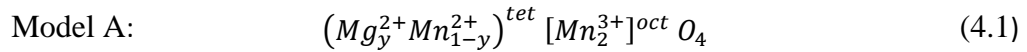
Both polymorphs (T1 and T2) were indexed using the same $I4_1/amd$ space group but with different unit cell parameters. These vary differently with composition, T1 (figure 4.7) and T2 (figure 4.11). T1 showed a slight decrease in unit cell size with increasing x while maintaining its tetragonality whereas T2 showed a more prominent change of its unit cell shifting away from tetragonal towards a pseudo-cubic structure, with increasing x .

It has been reported that Mn_3O_4 has lattice parameter $a = b = 5.7621 \text{ \AA}$, $c = 9.4696 \text{ \AA}$, $c/a = 1.64$, $V = 314.41 \text{ \AA}^3$ [12, 13] and MgMn_2O_4 has $a = b = 5.728 \text{ \AA}$, $c = 9.346 \text{ \AA}$, $c/a = 1.63$, $V = 306.64 \text{ \AA}^3$ [13, 14]. Both have the same tetragonal spinel crystal structure of $I4_1/amd$, but with a smaller unit cell for MgMn_2O_4 . The tetragonal spinel for both compounds is attributed to the distortion of the crystal structure due to the presence of Mn^{3+} ions in the octahedral sites known as Jahn-Teller effect [14, 15]. The difference between these compositions is that the tetrahedral site is occupied by Mn^{2+} and Mg^{2+} respectively, in Mn_3O_4 and MgMn_2O_4 . The reported axial c/a ratio showed a slight decrease from 1.64 in Mn_3O_4 to 1.63 in MgMn_2O_4 .

An ideal spinel has formula of AB_2O_4 where the A and B cations occupy tetrahedral and octahedral sites, respectively, within the oxide array environment. The B_2O_4 part is simply a rock salt structure but with B ions occupying alternate octahedral sites. The B cation is surrounded by six anions in the octahedral environment.

There are two possible sites for Mg^{2+} when doped into Mn_3O_4 : either the tetrahedral site or the octahedral site. In the Mn_3O_4 compound, the Mn^{3+} ion tends to be on the octahedral site due to its higher Crystal Field Stabilisation Energy, CFSE, and as a direct consequence, the Mn^{2+} ion will place itself tetrahedrally. Therefore, the formula of Mn_3O_4 can be rewritten as $(Mn^{2+})^{tet}[Mn_2^{3+}]^{oct}O_4$.

Substitution of the Mg^{2+} on the octahedral site would result in a drastic reduction of the axial c/a ratio due to the reduction in number of Mn^{3+} ions responsible for the Jahn-Teller distortion of Mn_3O_4 . Since there is no such reduction observed in the T1 sample (figure 4.7), the most probable compensation mechanism is by an isovalent substitution of Mn^{2+} with Mg^{2+} at the tetrahedral sub-lattice. Therefore, the proposed chemical formula would be:



As a result, the T1 unit cell parameter decreased with increase in Mg content ($0 < x \leq 0.20$) at 850 °C, since the ionic radius of Mg^{2+} (0.72 Å) is slightly smaller than Mn^{2+} (0.80 Å) in their tetrahedral environment ^[16]. The subtle decrease in lattice parameters and axial c/a ratios of T1 are consistent with the reported literature ^[17].

Data for compositions within T1 solid solution domain (table 4.4), showed that the axial c/a ratio is generally constant with increasing temperature. This suggested the validity of model A as compensation mechanism for T1 solid solution.

Further increase in temperature results in transformation of T1 to C1 cubic as shown by the HTXRD and upon quenching, a rapid C1 → T2 transformation occurs. A dramatic decrease in axial c/a ratio from T1 to T2 was observed, attributed to a reduction in number of Mn^{3+} ions in the octahedral environment which is responsible for the Jahn-Teller distortion. The tentative explanation for these results, confirmed by the crystallographic studies presented in chapter 5, concerns the nature of the structural changes associated with the tetragonal to cubic phase transition in Mg-doped Mn_3O_4 . In particular, the Mg-dopants are located solely on the tetrahedral A sites in T1 but are distributed over both tetrahedral and octahedral sites in T2; since the C1 → T2 transition

occurs very rapidly during quenching there may be insufficient time for cation site occupancies to change and therefore, the Mg distribution over the two sets of sites in T2 is likely to be the same as that in C1 prior to quenching. On annealing T2 at lower temperatures, there is sufficient time for cation reorganisation to occur, giving the distribution in the low temperature equilibrium polymorph, T1. The T2 structure has higher entropy than T1 due to the greater Mn/Mg disorder and is kinetically stable at low temperature after quenching, but is thermodynamically metastable.

A non-linear change in lattice parameters was observed for T2 with increasing x ($0.20 \leq x \leq 0.40$), with a small ‘kink’ observed at $x \sim 0.33$. Unlike T1, the c/a ratio of T2 showed a more dramatic change with increasing x . This could be associated with a further reduction in number of Mn^{3+} ion in the octahedral site with increasing x . It is expected that ideally, at $x = 0.33$, all the Mn^{2+} ion has been replaced by Mg^{2+} ion at the tetrahedral site and the Mn^{3+} ion is fully occupied at the octahedral site. Beyond $x = 0.33$, two Mn^{3+} ions will be replaced by a pair of Mg^{2+} and Mn^{4+} ions, thus reducing in number of Mn^{3+} at the octahedral site, up to $x = 0.67$ (figure 4.30).



Therefore, at $x \leq 0.33$, the reduction in number of Mn^{3+} at the octahedral site depends solely on the high temperature site exchange but at $x > 0.33$, a combination of chemical substitution (4.2) and site exchange could be responsible for the reduction in the axial c/a ratio observed in T2.

Reversibility of transformation between T1 and T2 was studied for $x = 0.20$. It can be concluded that the T1 and T2 phases transform reversibly and no change in weight was observed indicating that any possible loss of oxygen is negligible.

Based on XRD data of quenched samples and HTXRD data, the presence of T2 was only observed when there is a presence of Mg in the samples. The quenched data collected on MnO_2 at 1300 °C indicates only a single phase of Mn_3O_4 is observed which has a similar diffraction pattern to T1. However, the HTXRD data showed the formation of Mn_3O_4 cubic spinel had occurred instead of the Mn_3O_4 tetragonal spinel.

The formation of cubic spinel at high temperature as observed from HTXRD could probably be attributed to the Mn^{3+}O_6 octahedra being randomly oriented within the spinel structure at high temperature. These octahedra share common edges, and at low temperatures, a cooperative distortion with neighboring complexes arises in T1 in a direction that maximized the Jahn-Teller distortion. At high temperature, each complex can be oriented independently because of higher entropy. Therefore, at any instant, a cubic spinel-like structure can be statistically observed when the randomly-oriented complexes are equally distorted in each of the three cubic axes. On quenching, the C1 to T2 transition is very rapid and probably only involves orientational distortion of octahedral complexes within the crystal structure.

The DSC results, showed a single exothermic peak on cooling, even at a rate of $50\text{ }^\circ\text{C}/\text{min}$ (figure 4.25). Due to the vast different in cooling rate between quenching ($\sim 200\text{ }^\circ\text{C}/\text{s}$)^[8] and DSC measurements, we are unable to determine whether this single exothermic peak corresponds to either the C1 cubic spinel \rightarrow T2 or the C1 cubic spinel \rightarrow T1 transformation.

Nevertheless, the temperature at which C1/T2 was observed decreases with increasing x . This could probably be attributed to the cation site exchange between tetrahedral and octahedral sites which result in the reduction in number of Mn^{3+} ion at the octahedral site. As a result, the efficiency for cooperative orientation of the Jahn-Teller distortion is reduced, hence the transformation temperature is lowered. Therefore, it is suggested that the formation of C1/T2 spinel depends on the number of Mn^{3+} ion present at the octahedral site. The possible compensation mechanisms are described in chapter 5.

The minimum temperature at which T2 was observed in quenched samples was $\sim 760\text{ }^\circ\text{C}$, over the range $0.30 \leq x < 0.50$. Below this temperature, a mixture of T1 and a cubic spinel was observed. This could be attributed to:

- a) the “freeze-in” of a small number of randomly oriented Mn^{3+}O_6 octahedra.
- b) the “freeze-in” of a small amount of Mg^{2+} ion in the octahedral site as a result of site exchange.
- c) the reduction in number of Mn^{3+} ion at the octahedral site due to the replacement with Mg^{2+} and Mn^{4+} (figure 4.30).

The second major discrepancy with literature data was the formation of a temperature dependent cubic-Suzuki phase solid solution, C2, over the range $0.50 \leq x < 0.86$ instead of a phase mixture of cubic spinel and Suzuki phase^[11] of fixed composition.

The lattice parameter measurements show a non-linear relationship with change in composition (i.e., Mg content) (figure 4.17). The change in lattice parameter is probably due to the change in compensation mechanisms as shown in figure 4.30. Structural analysis is described in chapter 6.

The formation of C2 solid solution was initially observed at $x = 0.50$ with increasing x . This is probably due to the reduced influence of Mn^{3+} ion in distorting the structure as it was suppressed by the increase in number of Mg^{2+} and Mn^{4+} ions in the octahedral environment (figure 4.30).

An immiscibility dome was observed at a lower temperature of the C2 solid solution range with an upper consolute temperature ~ 850 °C at $x \sim 0.67$. On cooling, the C2 phase became unstable and separated into two solid solutions: cubic spinel solid solution and Suzuki phase solid solution.

4.9 Conclusions

A pseudo-binary phase diagram for $Mg_xMn_{1-x}O_\delta$ has been constructed using a combination of quenching, x-ray diffraction and thermal analysis. Many compositions on the MgO-MnO₈ join, were successfully synthesized *via* solid state reaction. Appropriate reaction conditions have been identified to ensure the reaction reached thermodynamic equilibrium due to the reduced mobility of Mg^{2+} ion in solid state diffusion.

For Mn_3O_4 , the high temperature cubic spinel transformed instantaneously into its low tetragonal Mn_3O_4 phase on quenching, without any formation of an intermediary metastable phase. It is suggested that the high temperature, non-quenchable cubic Mn_3O_4 structure is due to the randomization of the $Mn^{3+}O_6$ octahedron which equally distorted in all of the three axes.

Two tetragonal spinel solid solutions were observed on quenching and both phases were indexed using tetragonal space group of $I4_1/amd$ with different unit cell parameters. The low temperature T1 was observed in the Mn-rich region with proposed compensation mechanism by a direct substitution of $Mn^{2+} \rightarrow Mg^{2+}$ at the tetrahedral site. The high temperature T2 shows the possibility of cation site exchange between the tetrahedral and octahedral sites that causes a structural disorder as a result of an increase in the configurational entropy.

HTXRD data shows the presence of cubic spinel at high temperatures instead of T2 tetragonal phase. On quenching, a rapid transition from cubic spinel to T2 tetragonal phase was observed. In combination with the DSC result showing only a single exotherm, this suggested that T2 ss is probably metastable and thus does not appear in the phase diagram.

A limited range of temperature dependent cubic solid solution, C2 was observed over the range $0.5 \leq x \leq 0.8$. This cubic solid solution was indexed using either cubic space group of $Fd\bar{3}m$ and $Fm\bar{3}m$, but later found by neutron diffraction (chapter 6) that the $Fm\bar{3}m$ best described for the indexing of C2. A non-linear change in lattice parameters with compositions was observed. The C2 ss appears to be unstable as it decomposed into two different cubic phases below ~ 850 °C, where they co-exist within an immiscibility dome.

4.10 References

1. Tukamoto, H. and A. West, *Electronic conductivity of LiCoO_2 and its enhancement by magnesium doping*. Journal of The Electrochemical Society, 1997. **144**(9): p. 3164-3168.
2. Truong, Q.D., M. Kempaiah Devaraju, P.D. Tran, Y. Gambe, K. Nayuki, Y. Sasaki, and I. Honma, *Unravelling the Surface Structure of MgMn_2O_4 Cathode Materials for Rechargeable Magnesium-Ion Battery*. Chemistry of Materials, 2017. **29**(15): p. 6245-6251.
3. Yin, J., A.B. Brady, E.S. Takeuchi, A.C. Marschilok, and K.J. Takeuchi, *Magnesium-ion battery-relevant electrochemistry of MgMn_2O_4 : crystallite size effects and the notable role of electrolyte water content*. Chemical Communications, 2017. **53**(26): p. 3665-3668.
4. Taguchi, H. and M. Nagao, *Synthesis of Mg_6MnO_8 through the sol-gel process*. Journal of Materials Science Letters, 1991. **10**(11): p. 658-659.
5. Taguchi, H., A. Ohta, M. Nagao, H. Kido, H. Ando, and K. Tabata, *Crystal structure and magnetic properties of $(\text{Mg}_{6-x}\text{Li}_x)\text{MnO}_8$* . Journal of Solid State Chemistry, 1996. **124**(2): p. 220-223.
6. Barkhatov, V., Y.V. Golikov, A. Zalazinskii, V. Balakirev, and G. Chufarov. *Phase Diagram of the Mg-Mn-O System*. in *Doklady Physical Chemistry*. 1980.
7. Joshi, S., C. Silva, P. Wang, Y. Mozharivskyj, and A. Petric, *Copper-Magnesium-Manganese spinel coatings for solid oxide fuel cell interconnects*. Journal of The Electrochemical Society, 2014. **161**(3): p. F233-F238.
8. Reeves-McLaren, N., J. Sharp, H. Beltrán-Mir, W.M. Rainforth, and A.R. West, *Spinel-rock salt transformation in $\text{LiCoMnO}_{4-\delta}$* . Proc. R. Soc. A, 2016. **472**(2185): p. 20140991.
9. Dorris, S. and T.O. Mason, *Electrical properties and cation valencies in Mn_3O_4* . Journal of the American Ceramic Society, 1988. **71**(5): p. 379-385.
10. Rosenberg, M. and P. Nicolau, *Electrical properties and cation migration in MgMn_2O_4* . physica status solidi (b), 1964. **6**(1): p. 101-110.
11. Barkhatov, V.P., Y.V. Golikov, A.G. Zalazinskii, V.F. Balakirev, and G.I. Chufarov, *System Mg-Mn-O*. Dokl. Chem., 1980. **252**(2): p. 370-370.
12. Jensen, G. and O. Nielsen, *The magnetic structure of Mn_3O_4 Hausmannite between 4.7 K and Neel point, 41 K*. Journal of Physics C: Solid State Physics, 1974. **7**(2): p. 409.
13. ICDD (2018) and PDF-4+ 2019 (Database), *International Centre for Diffraction Data*. Newtown Square, Pennsylvania, USA, edited by Dr. Soorya Kabekkodu, 2018.

14. Mănăilă, R. and P. Păușescu, *Structural changes in $MgMn_2O_4$ at high temperatures*. *physica status solidi (b)*, 1965. **9**(2): p. 385-394.
15. Jahn, H.A. and E. Teller, *Stability of polyatomic molecules in degenerate electronic states-I—Orbital degeneracy*. *Proceedings of the Royal Society of London. Series A-Mathematical and Physical Sciences*, 1937. **161**(905): p. 220-235.
16. Shannon, R.T. and C.T. Prewitt, *Effective ionic radii in oxides and fluorides*. *Acta Crystallographica Section B: Structural Crystallography and Crystal Chemistry*, 1969. **25**(5): p. 925-946.
17. Rosenberg, M., P. Nicolau, R. Manaila, and P. Pausescu, *Preparation, electrical conductivity and tetragonal distortion of some manganite-systems*. *Journal of Physics and Chemistry of Solids*, 1963. **24**(12): p. 1419-1434.

Chapter 5: Structural analysis of tetragonal polymorphs T1 and T2

5.1 Structural refinement of Mn₃O₄

The initial structural refinement was performed on a known sample composition to validate the refinement steps; subsequent refinements of other compositions would then follow. An XRD dataset of standard Mn₃O₄ (Sigma Aldrich, 97% purity) was used. The Mn positions were restricted by symmetry at tetrahedral (*4b*) and octahedral (*8c*) sites and O in (*16h*) site.

The structural refinement proceeded as described in the methodology section. The starting model and the parameters used were as listed in table 5.1. The R values and atomic coordinates at different stages of refinement are summarised in table 5.2. The scale factor, background (6 terms of Chebyshev function) and lattice parameter were refined first and were allowed to refine in the subsequent refinements, followed by zero-point and peak profile coefficients which were fixed after convergence, column 1. The atomic *y* and *z* coordinates of O1 were refined next and were also fixed after convergence, column 2. After that, the occupancy of Mn1 and Mn2 were refined together and showed values slightly higher than unity, column 3. The occupancies of Mn1 and Mn2 were then fixed to unity. Next, the occupancy of oxygen was refined and gave a value slightly lower than unity, column 4. However, at this step, no obvious improvements were observed in the χ^2 , R_p and R_{wp} values. The occupancy of O1 was then fixed to unity.

In order to test the reliability of all site occupancies, the Mn1, Mn2 and O1 occupancies were fixed with full occupancy and their U_{iso} values were refined in turn. First, the U_{iso} of Mn1 and Mn2 were refined giving a value higher than the default value as shown in column 5. Then the U_{iso} of O1 was refined and also gave value higher than the default value, column 6. As a final step, the atomic coordinates of O1, thermal parameters of Mn1, Mn2 and O1 and profile parameters were refined simultaneously and smaller U_{iso} values closer to the default values were observed, column 7.

The final result, column 7, shows a good fit between the observed and calculated data (table 5.1) with good statistical parameters: $\chi^2 = 1.27$, $R_p = 2.88\%$ and $R_{wp} = 3.65\%$ and realistic isotropic thermal parameters (table 5.2). The refined lattice parameters are $a = 5.7605(1) \text{ \AA}$ and $c = 9.4660(2) \text{ \AA}$ with lattice c/a ratio = 1.64326(4), which are in good agreement with that reported in the literature [1-5].

It is well-established that Mn_3O_4 has two coordination environments for the manganese with Mn^{2+} and Mn^{3+} ions accommodated in the tetrahedral and octahedral sites respectively [4, 6-8]. The Mn^{2+} ions do not have any site preference, unlike Mn^{3+} ions which prefer to be on the octahedral site due to its higher crystal field stabilization energy (CFSE) [9]. The presence of Mn^{3+} in an octahedral environment tends to induce a Jahn-Teller distortion which results in the lengthening of its two axial bonds (with respect to the other four equatorial bonds). This can be clearly seen in the refined bond lengths of Mn1 and Mn2 to the oxide ion (table 5.3a).

The tetrahedrally-coordinated Mn1_O1 gave four bond lengths of 2.048 \AA , whereas, Mn2_O1 gave four bond lengths of 1.929 \AA and two bond lengths of 2.277 \AA in the octahedral environment. Based on the oxide ion radius in the tetrahedral environment (1.24 \AA) [10], the calculated radius of Mn1 is 0.808 \AA , which is similar to the reported Mn^{2+} ionic radius, within errors [10]. The Mn2 radius cannot be directly calculated due to its different bond lengths which result in a distorted octahedron.

Further to this, the valences of the cations were calculated based on the sum of the bond valences, bvs , of all the bonds associated with the cations.

$$bvs = \exp \frac{r_0 - r}{B} \quad (5.1)$$

where r_0 and B are empirically determined parameters, r is the bond length, r_0 is the bond valence parameter and B is a constant with a value of 0.37. r_0 for Mn^{2+} and Mn^{3+} are 1.790 \AA and 1.760 \AA respectively [11, 12].

The calculated valences for Mn1 and Mn2 were 1.99 and 3.02 respectively and therefore suggests their oxidation states to be 2+ (Mn1) and 3+ (Mn2).

Table 5.1 Starting model of Mn_3O_4 (PDF: 00-024-0734)

Atom	Multiplicity	x	y	z	Occupancy	$100 \times U_{iso} (\text{\AA}^2)$
Mn1	$4b$	0	0.25	0.375	1	1.0
Mn2	$8c$	0	0	0	1	1.0
O1	$16h$	0	0.5278	0.2411	1	1.0

$a = b = 5.7621 \text{ \AA}; c = 9.4696 \text{ \AA}; \text{Space group} = I4_1/amd$

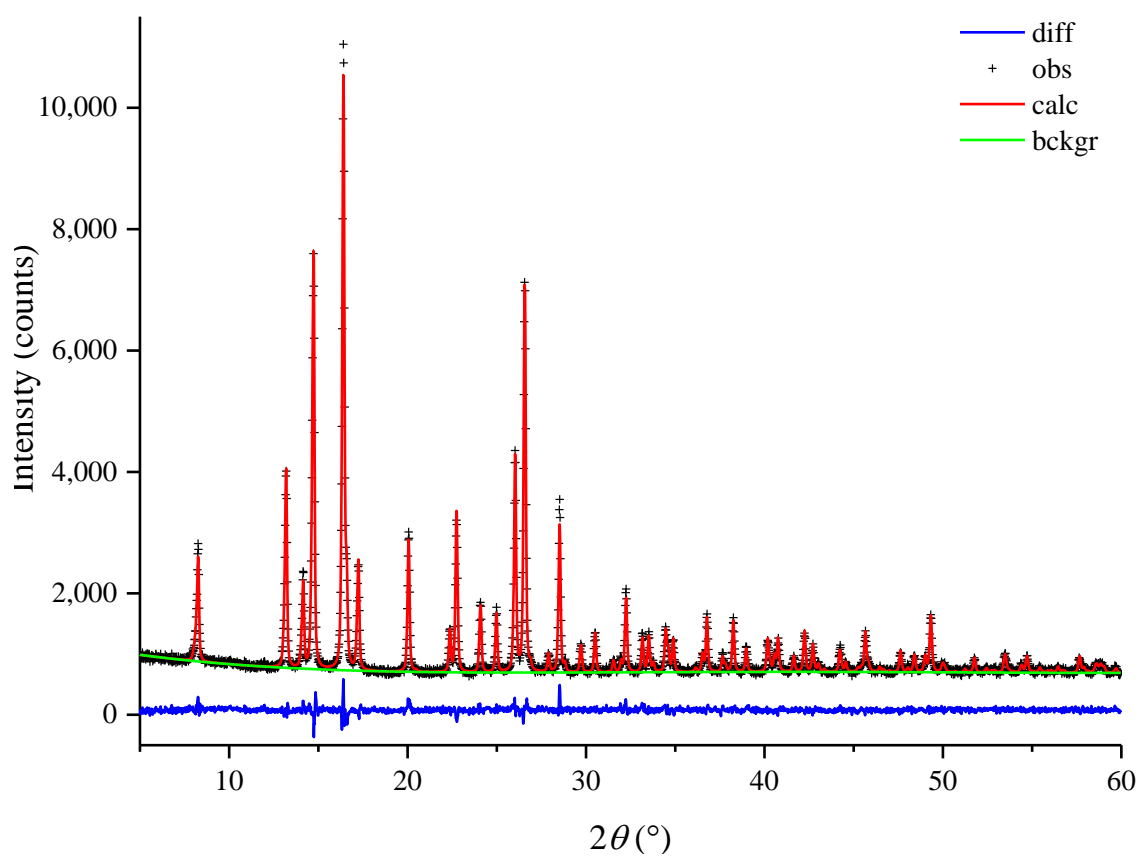
Figure 5.1 Rietveld refinement data for observed (obs), calculated (calc) and difference (diff) profiles of Mn_3O_4 at room temperature

Table 5.2 Structural refinement of Mn₃O₄ at room temperature

			1	2	3	4	5	6	7	
1	Mn1	4b	Occupancy	1.00	1.00	1.02 (1)	1.00	1.00	1.00	1.00
			100×U_{iso}(Å²)	1.00	1.00	1.00	1.00	1.27 (5)	1.27	1.09 (4)
2	Mn2	8c	Occupancy	1.00	1.00	1.05 (1)	1.00	1.00	1.00	1.00
			100×U_{iso}(Å²)	1.00	1.00	1.00	1.00	1.01 (3)	1.01	0.88 (3)
3	O1	16h	Occupancy	1.00	1.00	1.00	0.98 (1)	1.00	1.00	1.00
			100×U_{iso}(Å²)	1.00	1.00	1.00	1.00	1.00	1.32 (8)	1.16 (6)
			y	0.5278	0.5287 (4)	0.5287	0.5287	0.5287	0.5287	0.5278 (3)
			z	0.2411	0.2399 (3)	0.2399	0.2399	0.2399	0.2399	0.2400 (2)
		a (Å)	5.7623 (1)	5.7623 (1)	5.7624 (1)	5.762 (1)	5.7624 (1)	5.7624 (1)	5.7605 (1)	
		c (Å)	9.4703 (2)	9.4703 (2)	9.4702 (2)	9.4703 (2)	9.4703 (2)	9.4703 (2)	9.4660 (2)	
		Volume (Å³)	314.45 (1)	314.45 (1)	314.46 (1)	314.46 (1)	314.46 (1)	314.46 (1)	314.11 (2)	
		χ²	2.04	2.02	1.95	2.01	2.00	1.98	1.27	
		R_p	3.58%	3.59%	3.53%	3.58%	3.56%	3.55%	2.88%	
		R_{wp}	4.63%	4.62%	4.53%	4.60%	4.59%	4.57%	3.65%	

Table 5.3 (a) bond lengths, (b) bond angles of refined Mn₃O₄

(a)		(b)	
Mn ₃ O ₄		Mn ₃ O ₄	
Vector	Length (Å)	Angle	Degree (°)
(4) x Mn1_O1	2.048 (2)	(4) x O1_Mn1_O1	112.9 (1)
(4) x Mn2_O1	1.929 (1)	(2) x O1_Mn1_O1	102.8 (1)
(2) x Mn2_O1	2.277 (2)	(4) x O1_Mn2_O1	90
		(4) x O1_Mn2_O1	90
		(2) x O1_Mn2_O1	96.9 (1)
		(2) x O1_Mn2_O1	83.1 (1)

5.2 Structural refinement of T1 tetragonal spinel polymorphs

A sample of $x = 0.20$ of Mg_xMn_{1-x}O₈, quenched from 500 °C was used to study the structure of the T1 tetragonal spinel polymorph. Based on the refinement result on Mn₃O₄ (section 5.1), it was suggested that Mn²⁺ and Mn³⁺ occupy the tetrahedral and octahedral sites, respectively. Thus, the formula of Mn₃O₄ can be represented by (Mn²⁺)^{tet}[Mn³⁺]^{oct}O₄. There are two possible sites for Mg²⁺ when doped into Mn₃O₄: tetrahedral 4*b*- or octahedral 8*c*-site, as shown in table 5.4.

Table 5.4 Possible sites of Mg²⁺ doped into Mn₃O₄

	Tetrahedral (4 <i>b</i>)		Octahedral (8 <i>c</i>)	
	Mg ²⁺	Mn ²⁺	Mg ²⁺	Mn ³⁺
Ionic radii (Å) ^[10]	0.72	0.80	0.86	0.785

5.2.1 T1 tetragonal spinel quenched from 500 °C ($x = 0.20$)

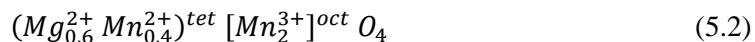
The Rietveld refinement has been performed using a similar procedure to that described for Mn_3O_4 . The same starting model was used (table 5.1). Two models were tested which correspond to the Mg being introduced to either tetrahedral site (Mg1 – model A) or octahedral site (Mg2 – model B).

In order to test the first model (model A), Mg1 was introduced to the Mn1 tetrahedral $4b$ -site. The R values and atomic coordinates at different stages of refinement are summarised in table 5.5. The occupancy of Mg1 and Mn1 were set to be 0.6 and 0.4 respectively (constraints to full occupancy), consistent with the chemical composition of $x = 0.20$. The Mn2 was set to be fully occupied at the octahedral $8c$ -site. First, the scale factor, background, cell parameter, zero-point and profile parameters were refined in turn, column 1. Next, the O1 atomic coordinate was refined, column 2. Then, the occupancy of Mn2 was refined and gave a value of unity within error, column 3. After that, the occupancies of Mg1 and Mn1 were refined, and gave slight increase and decrease in values respectively, column 4. The occupancy ratio of Mg1:Mn1 was fixed at 0.6:0.4.

The occupancy of O1 was then refined and gave a value slightly higher than unity, column 5. The occupancy of O1 was then fixed to unity. After that, the thermal parameters of Mn2, Mg1:Mn1 and O1 were refined in turn, columns 6,7 and 8. Finally, the O1 atomic coordinate, thermal parameters for all atoms and profile parameters were refined simultaneously, column 9.

The final refinement result shows a good fit between the observed and calculated data (figure 5.2) and good statistical parameters: $\chi^2 = 1.47$, $R_p = 3.38\%$ and $R_{wp} = 4.28\%$ with realistic isotropic thermal parameters (column 9, table 5.5). The refined lattice parameters were $a = 5.7320$ (1) Å and $c = 9.3487$ (3) Å with lattice c/a ratio = 1.63097 (6).

This refinement indicates that Mg^{2+} was successfully substituted into the Mn^{2+} tetrahedral $4b$ -site through an isovalent compensation mechanism with the chemical formula:



The tetrahedrally-coordinated (Mg,Mn)1_O1 gave an average of four bond lengths of 2.008 Å, whereas the Mn2_O1 gave four bond lengths of 1.927 Å and two bond lengths of 2.272 Å in the octahedral environment (table 5.6). The reduction in the bond length at the tetrahedral site compared to Mn_3O_4 resulted in a decrease in the unit cell parameter (table 5.7).

In order to test the possible location of Mg on the octahedral $8c$ -site (model B), the occupancy ratios of Mg1:Mn1 and Mg2:Mn2 were set to be 0:1 and 0.3:0.7 respectively (constraint to full occupancy) consistent with the stoichiometric chemical composition at $x = 0.2$. The U_{iso} value for Mg2 was set to be the same as Mn2.

The Mg1:Mn1 and Mg2:Mn2 ratios were then refined simultaneously and gave values of 0.6:0.4 and 0:1 respectively, within error, column 10. This indicates that the probability of Mg^{2+} ions to be at the octahedral $8c$ -site is very unlikely. Therefore, this model (model B) is no longer under consideration for subsequent refinements.

Table 5.5 Structural refinement of T1: $x = 0.20$ quenched from 500 °C. Model A (Mg on 4*b*-site) represented by column 1 to 9 and model B (Mg on 8*c*-site) by column 10

			1	2	3	4	5	6	7	8	9	10	
1	Mg1	4 <i>b</i>	Occupancy	0.60	0.60	0.60	0.614 (5)	0.60	0.60	0.60	0.60	0.606 (3)	
			$100 \times U_{iso}(\text{\AA}^2)$	1.00	1.00	1.00	1.00	1.00	1.00	1.25 (9)	1.25	0.63 (6)	0.63
2	Mn1		Occupancy	0.40	0.40	0.40	0.386 (5)	0.40	0.40	0.40	0.40	0.40	0.394 (3)
			$100 \times U_{iso}(\text{\AA}^2)$	1.00	1.00	1.00	1.00	1.00	1.00	1.25 (9)	1.25	0.63 (6)	0.63
3	Mg2	8 <i>c</i>	Occupancy	-	-	-	-	-	-	-	-	-	-0.003 (2)
			$100 \times U_{iso}(\text{\AA}^2)$	-	-	-	-	-	-	-	-	-	0.81
4	Mn2		Occupancy	1.00	1.00	1.006 (4)	1.00	1.00	1.00	1.00	1.00	1.00	1.003 (2)
			$100 \times U_{iso}(\text{\AA}^2)$	1.00	1.00	1.00	1.00	1.00	1.27 (5)	1.27	1.27	0.81 (4)	0.81
5	O1	16 <i>h</i>	Occupancy	1.00	1.00	1.00	1.00	1.012 (6)	1.00	1.00	1.00	1.00	1.00
			$100 \times U_{iso}(\text{\AA}^2)$	1.00	1.00	1.00	1.00	1.00	1.00	1.00	0.94 (9)	0.49 (7)	0.49
			<i>y</i>	0.5278	0.5266 (5)	0.5266	0.5266	0.5266	0.5266	0.5266	0.5266	0.5256 (4)	0.5256
			<i>z</i>	0.2411	0.2424 (4)	0.2424	0.2424	0.2424	0.2424	0.2424	0.2424	0.2425 (3)	0.2425
<i>a</i> (Å)			5.7350 (1)	5.7350 (1)	5.7350 (1)	5.7350 (1)	5.7350 (1)	5.7350 (1)	5.7350 (1)	5.7350 (1)	5.7320 (1)	5.7320 (1)	
<i>c</i> (Å)			9.3531 (3)	9.3531 (3)	9.3531 (3)	9.3531 (3)	9.3531 (3)	9.3532 (3)	9.3531 (3)	9.3531 (3)	9.3487 (3)	9.3486 (2)	
Volume (Å ³)			307.63 (1)	307.63 (1)	307.63 (1)	307.63 (1)	307.63 (1)	307.63 (1)	307.63 (1)	307.63 (1)	307.16 (2)	307.16 (1)	
χ^2			2.61	2.59	2.59	2.58	2.59	2.55	2.54	2.54	1.47	1.47	
R_p			4.32%	4.30%	4.30%	4.29%	4.30%	4.27%	4.26%	4.26%	3.38%	3.37%	
R_{wp}			5.70%	5.68%	5.68%	5.68%	5.68%	5.64%	5.63%	5.63%	4.28%	4.28%	

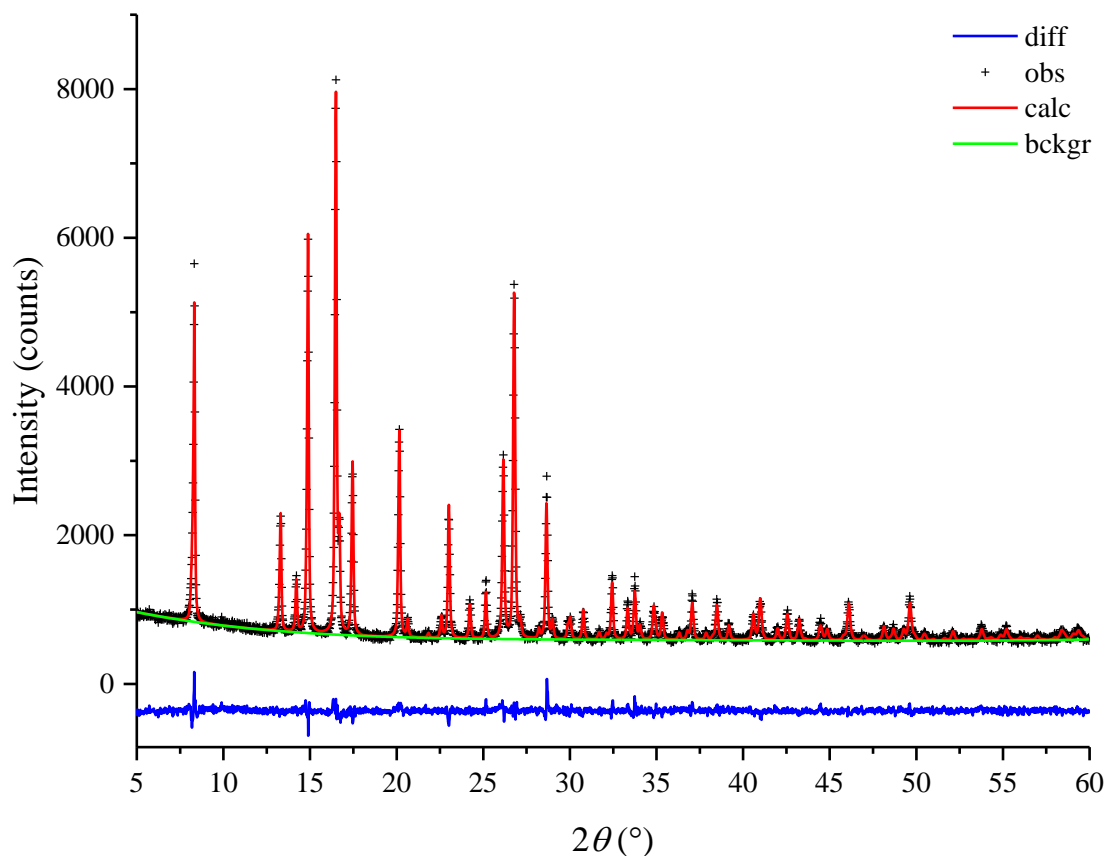


Figure 5.2 Rietveld refinement data (model A) for observed (obs), calculated (calc) and difference (diff) profiles of T1: $x = 0.20$ quenched from 500 °C

Table 5.6 (a) bond lengths, (b) bond angles of T1, $x = 0.20$ quenched from 500 °C (model A)

(a)		(b)	
	$x = 0.20$		$x = 0.20$
Vector	Length (Å)	Angle	Degree (°)
(4) x (Mg,Mn)1_O1	2.008 (2)	(4) x O1_(Mg,Mn)1_O1	112.4 (1)
(4) x Mn2_O1	1.927 (2)	(2) x O1_(Mg,Mn)1_O1	103.8 (1)
(2) x Mn2_O1	2.272 (3)	(4) x O1_Mn2_O1	90
		(4) x O1_Mn2_O1	90
		(2) x O1_Mn2_O1	96.3 (1)
		(2) x O1_Mn2_O1	83.7 (1)

Table 5.7 Comparison of bond lengths of Mn₃O₄ and T1, $x = 0.20$

	Mn ₃ O ₄	$x = 0.20$ (500 °C)
Vector	Bond Length (Å)	Bond Length (Å)
(4) Mn1_O1	2.048 (2)	-
(4) (Mg,Mn)1_O1	-	2.008 (2)
(4) Mn2_O1	1.929 (1)	1.927 (2)
(2) Mn2_O1	2.277 (2)	2.272 (3)

5.2.2 T1 tetragonal spinel quenched from different temperature ($x = 0.20$)

Samples of $x = 0.20$, quenched from 500, 700 and 850 °C were used to study the structure of T1 at different temperatures. A similar refinement procedure was implemented as described in section 5.2.1. The comparison of final structural refinement results is summarised in table 5.8.

The final refinement results show a good fit between the observed and calculated data (figure 5.3) with good statistical parameters (χ^2 , R_p and R_{wp}) and with realistic isotropic thermal parameters (table 5.8). The lattice c/a ratios were generally constant at 1.63, within errors (figure 5.4).

These results indicate that the Mg:Mn ratio (0.6:0.4) is relatively stable at the tetrahedral $4b$ -site up to 850 °C and the probability of Mg migration into octahedral $8c$ -site is minimal and less likely to occur. This is consistent with the XRD patterns (figure 4.6), in which no peak shifts were observed up to 900 °C.

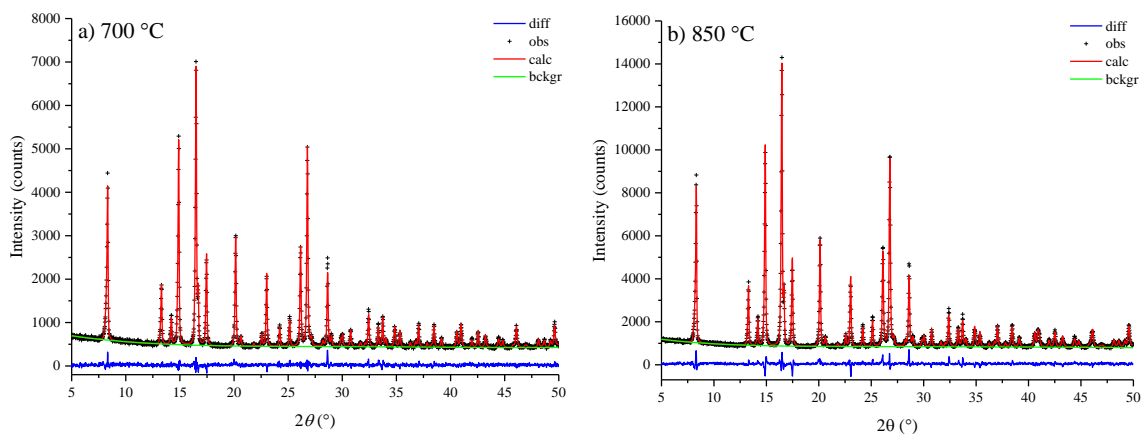


Figure 5.3 Rietveld refinement data for observed (obs), calculated (calc) and difference (diff) profiles of T1: $x = 0.20$ quenched from:

a) 700 °C and b) 850 °C

Table 5.8 Comparison of final structural refinement results of T1: $x = 0.20$ quenched from 500 °C, 700 °C and 850 °C

				500 °C	700 °C	850 °C
1	Mg1	4b	Occupancy	0.60	0.60	0.60
			$100 \times U_{iso}(\text{\AA}^2)$	0.63 (6)	0.87 (6)	0.44 (6)
2	Mn1	4b	Occupancy	0.40	0.40	0.40
			$100 \times U_{iso}(\text{\AA}^2)$	0.63 (6)	0.87 (6)	0.44 (6)
3	Mn2	8c	Occupancy	1.00	1.00	1.00
			$100 \times U_{iso}(\text{\AA}^2)$	0.81 (4)	0.98 (3)	0.75 (3)
4	O1	16h	Occupancy	1.00	1.00	1.00
			$100 \times U_{iso}(\text{\AA}^2)$	0.49 (7)	0.74 (7)	0.57 (6)
			y	0.5256 (4)	0.5255 (4)	0.5236 (4)
			z	0.2425 (3)	0.2427 (2)	0.2424 (2)
a (Å)				5.7320 (1)	5.7347 (1)	5.7408 (1)
c (Å)				9.3487 (3)	9.3496 (3)	9.3386 (3)
Volume (Å ³)				307.16 (2)	307.48 (2)	307.77 (2)
c/a				1.63097 (6)	1.63036 (6)	1.62671 (6)
χ^2				1.47	1.26	2.32
R_p				3.38%	3.48%	3.36%
R_{wp}				4.28%	4.43%	4.35%

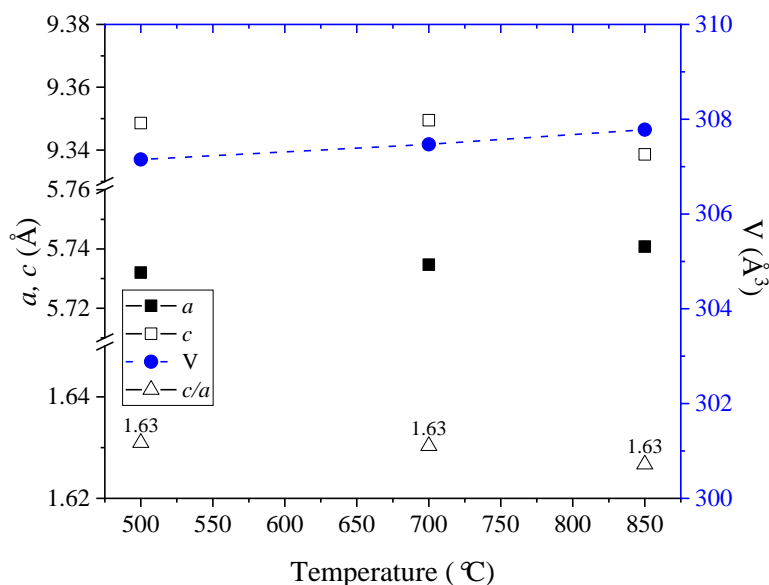


Figure 5.4 Lattice parameters, a , c , cell volume, V , and axial ratio, c/a , of T1 structure: $x = 0.20$ quenched from 500 °C, 700 °C and 850 °C into liquid N₂. Error bars are smaller than the data points.

5.2.3 T1 tetragonal spinel quenched from 850 °C with different compositions ($x = 0.05, 0.10$ and 0.20)

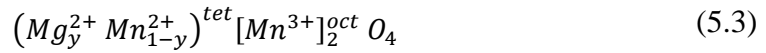
Samples of $x = 0.05, 0.10$ and 0.20 quenched from 850 °C were used to study the structure of T1 at different compositions. A similar refinement procedure was implemented to that described in section 5.2.1. The comparison of final structural refinement results is summarised in table 5.9.

The final refinement results show a good fit between the observed and calculated data (figure 5.5) with good statistical parameters (χ^2 , R_p and R_{wp}) and with realistic isotropic thermal parameters (table 5.9).

A decrease in lattice parameters: a and c , was observed with an increase in Mg content. The lattice c/a ratio decreased slightly with increasing x (figure 5.6). These changes were attributed to the isovalent substitution of Mn^{2+} with Mg^{2+} at the tetrahedral $4b$ -site as shown by the final refinement results. This is due to the fact that Mg^{2+} ($r_{Mg} = 0.72$ Å) has slightly smaller ionic radius than Mn^{2+} ($r_{Mn} = 0.80$ Å) in a tetrahedrally-

coordinated environment ^[10]. This result is consistent with the XRD patterns (figure 4.1), where all the peaks were shifted to higher 2θ angle with increasing x (for $x < 0.30$).

The main structural result for these compositions of T1 solid solution is that the Mn2 site remains fully occupied by Mn whereas the Mn1 site shows increasing occupancy by Mg with increasing x (figure 5.7). Therefore, it is expected that at $x = 0.33$, the Mn at tetrahedral $4b$ -site will be fully substituted by Mg and thus give the chemical formula:



For $x > 0.33$, another compensation mechanism is therefore needed with increasing x . It was suggested that this mechanism would be: the replacement of two Mn^{3+} ions with a pair of Mg^{2+} and Mn^{4+} at the octahedral $8c$ -site (table 5.10). This gives the formula:

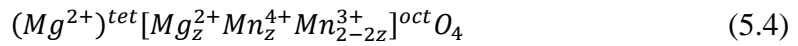


Table 5.9 Comparison of final structural refinement results of T1 with varying Mg content: $x = 0.05, 0.10$ and 0.20 quenched from $850\text{ }^{\circ}\text{C}$.

 As reference, Mn_3O_4 was the final refined result at room temperature, (RT)

			Mn_3O_4 (RT)	$x = 0.05$	$x = 0.10$	$x = 0.20$	
1	Mg1	4b	Occupancy	-	0.15	0.30	0.60
			$100 \times U_{iso}(\text{\AA}^2)$	-	0.93 (4)	0.89 (5)	0.44 (6)
2	Mn1	4b	Occupancy	1.00	0.85	0.70	0.40
			$100 \times U_{iso}(\text{\AA}^2)$	1.09 (4)	0.93 (4)	0.89 (5)	0.44 (6)
3	Mn2	8c	Occupancy	1.00	1.00	1.00	1.00
			$100 \times U_{iso}(\text{\AA}^2)$	0.88 (3)	0.92 (3)	1.10 (4)	0.75 (3)
4	O1	16h	Occupancy	1.00	1.00	1.00	1.00
			$100 \times U_{iso}(\text{\AA}^2)$	1.16 (6)	0.74 (6)	0.90 (7)	0.57 (6)
			y	0.5278 (3)	0.5269 (4)	0.5254 (4)	0.5236 (4)
			z	0.2400 (2)	0.2410 (2)	0.2421 (3)	0.2424 (2)
			a (Å)	5.7605 (1)	5.7533 (1)	5.7481 (1)	5.7408 (1)
			c (Å)	9.4660 (2)	9.4277 (2)	9.3862 (3)	9.3386 (3)
			Volume (Å ³)	314.13 (2)	312.06 (2)	310.12 (2)	307.77 (2)
			c/a	1.64326 (4)	1.63866 (4)	1.63292 (6)	1.62671 (6)
			χ^2	1.21	1.27	1.83	2.32
			R_p	2.81%	3.37%	4.19%	3.36%
R_{wp}	3.57%	4.32%	5.27%	4.35%			

 Table 5.10 Summary of possible compensation mechanisms between $0 < x < 0.67$

x	0	$0 < x < 0.33$	0.33	$0.33 < x < 0.67$
Mechanism	-	$\text{Mn}^{2+} \rightarrow \text{Mg}^{2+}$	-	$2\text{Mn}^{3+} \rightarrow \text{Mg}^{2+} + \text{Mn}^{4+}$
Chemical formula	Mn_3O_4	$(\text{Mg}_y\text{Mn}_{1-y})\text{Mn}_2\text{O}_4$	MgMn_2O_4	$\text{Mg}[\text{Mg}_z\text{Mn}_{2-z}]\text{O}_4$

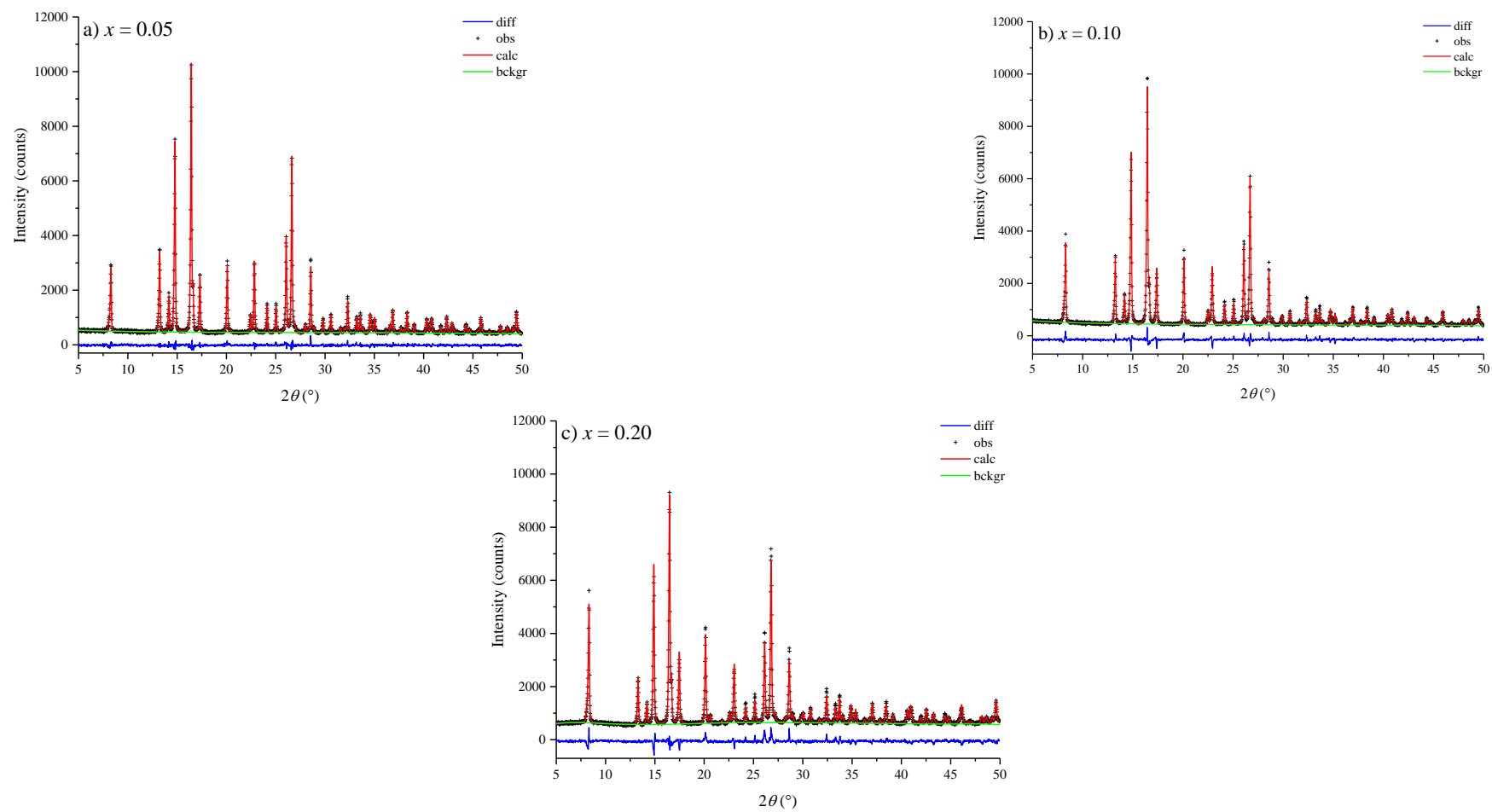


Figure 5.5 Rietveld refinement data for observed (obs), calculated (calc) and difference (diff) profiles of T1:

a) $x = 0.05$, b) $x = 0.10$ and c) $x = 0.20$ quenched from 850 $^\circ\text{C}$

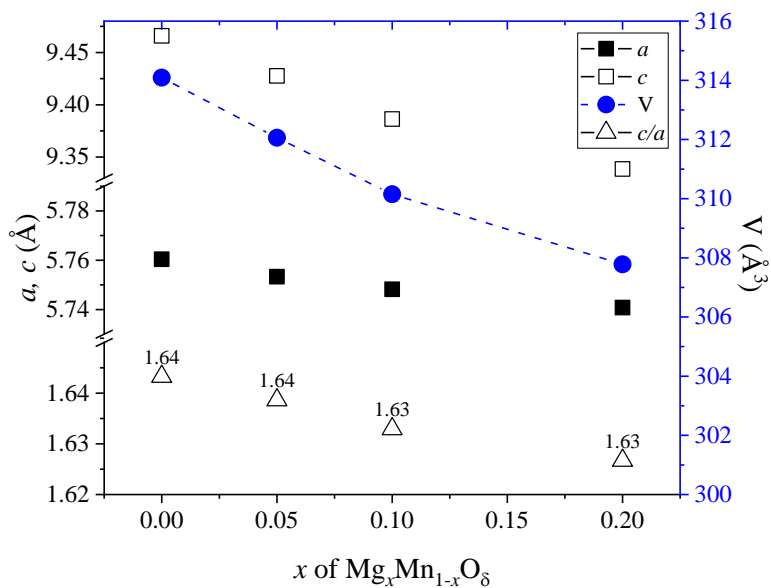


Figure 5.6 Lattice parameters, a , c , cell volume, V , and axial ratio, c/a , of T1 for $0.05 \leq x \leq 0.20$ quenched from 850°C into liquid N_2 . Error bars are smaller than the data points

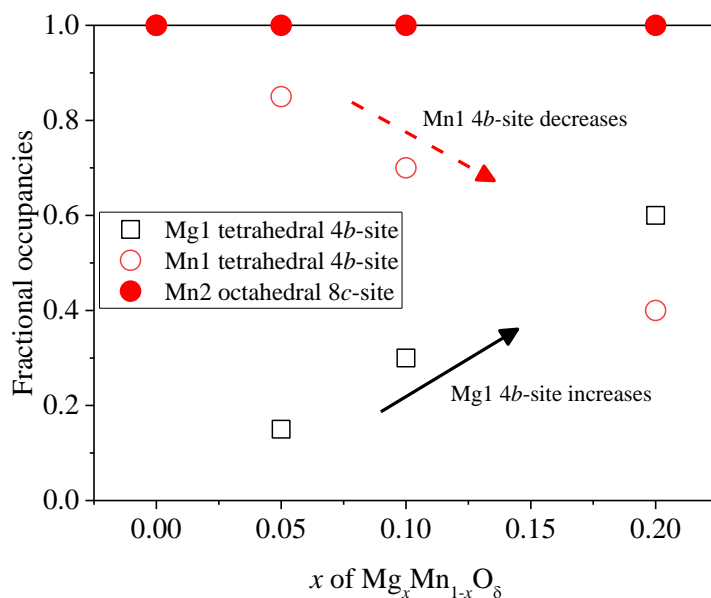


Figure 5.7 Fractional occupancies of Mg1:Mn1 at tetrahedral $4b$ -site and Mn2 at octahedral $8c$ -site of the T1 structure for $0.05 \leq x \leq 0.20$ quenched from 850°C into liquid N_2

5.3 Structural refinement of T2 tetragonal spinel polymorphs

A sample of $x = 0.20$, quenched from 1050 °C was used to study the structure of T2 tetragonal spinel polymorphs. T1 and T2 have similar XRD patterns and were indexed with the same $I4_1/amd$ space group. However, their refined lattice parameters indicate that they have different unit cell size (section 4.4).

5.3.1 T2 tetragonal spinel quenched from 1050 °C ($x = 0.20$)

A similar approach was adopted for the refinement of the T2 tetragonal spinel for sample $x = 0.20$. The same starting model was used (table 5.1) but with occupancy ratio Mg1:Mn1 set to be 0.6:0.4 (based on the refinement result from section 5.2.1) and the lattice parameter set to be $a = 5.7866 \text{ \AA}$ and $c = 9.1466 \text{ \AA}$ (section 4.4). The R values and atomic coordinates at different stages of refinement are summarised in table 5.11.

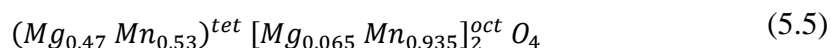
First, the scale factor, cell parameter, zero-point and profile parameters were refined in turn, column 1. Next, the O1 atomic coordinate was refined, column 2. Then, the occupancy of Mn2 was refined and gave a value of less than unity, column 3. After that, the occupancy of Mg1 and Mn1 were refined and showed a decrease and increase in occupancy respectively, column 4 (the overall site occupancy was constrained to be unity). The increase in refined occupancy of Mn1 probably correlates with the decreased occupancy of Mn2 and thus, suggests that a partial site-exchange might have occurred.

Therefore, Mg2 was added to the Mn2 octahedral $8c$ -site. The occupancy ratio of Mg1:Mn1 and Mg2:Mn2 were set to be 0.54:0.46 and 0.03:0.97 respectively (values are given based on Mg1:Mn1 ratio and to keep the stoichiometric composition). Constraints with full occupancy were applied to $4b$ - and $8c$ -sites. Next, all the cation occupancies were refined together and showed that Mg1:Mn1 and Mg2:Mn2 occupancy ratios were 0.47:0.53 and 0.065:0.935 respectively, within errors, column 5. Then, the occupancy of O1 was refined and gave a value of unity within errors, column 6. After that, the thermal parameters of Mg2:Mn2, Mg1:Mn1 and O1 were refined in turn and gave reasonable U_{iso} values, column 7, 8 and 9 respectively. Finally, the atomic positional parameter of O, the

thermal parameters of all atoms and profile parameters were refined simultaneously, column 10.

The final refinement result shows a good fit between the observed and calculated data (figure 5.8) and good statistical parameters: $\chi^2 = 1.57$, $R_p = 3.91\%$ and $R_{wp} = 5.02\%$ with realistic isotropic thermal parameters (table 5.11). The refined lattice parameters are $a = 5.7768(2) \text{ \AA}$ and $c = 9.1680(4) \text{ \AA}$ with lattice c/a ratio = 1.5870 (1).

This refinement indicates that partial counter migration of Mg^{2+} and Mn^{3+} ions had occurred between the tetrahedral $4b$ -site and octahedral $8c$ -site. This partial migration corresponded to an inversion degree, $\gamma = 0.13$, which could be referred to the amount of Mg^{2+} ions migrated into the octahedral site. The refined chemical formula is:



A reduction in lattice c/a ratio was observed (from T1 to T2 for $x = 0.20$ of $\text{Mg}_x\text{Mn}_{1-x}\text{O}_8$) which is probably attributable to the reduction in number of Mn^{3+} ions in the octahedral site. Since Mn^{3+} ions in the octahedral environment are responsible for the Jahn-Teller distortion which results in the tetragonal structure of T1, the decrease in number of Mn^{3+} ions in T2 (by the increase in number of Mg^{2+}) in the octahedral site will have an overall effect in the reduction of c/a ratio (table 5.12).

The tetrahedrally-coordinated (Mg,Mn)1_O1 gave an average of four bond lengths of $1.996(3) \text{ \AA}$, whereas, the (Mg,Mn)2_O1 gave an average of four bond lengths of $1.952(2) \text{ \AA}$ and two bond lengths of $2.218(3) \text{ \AA}$ in the octahedral environment (table 5.13). As the amount of Mn^{3+} ions in the octahedral site decreases, the average of the two axial bonds also decreases. The increase of Mg^{2+} ions in the octahedral site increases the average of the four equatorial bonds since Mg^{2+} (0.86 \AA) has larger ionic radius than Mn^{3+} (0.785 \AA) in the octahedral environment ^[10].

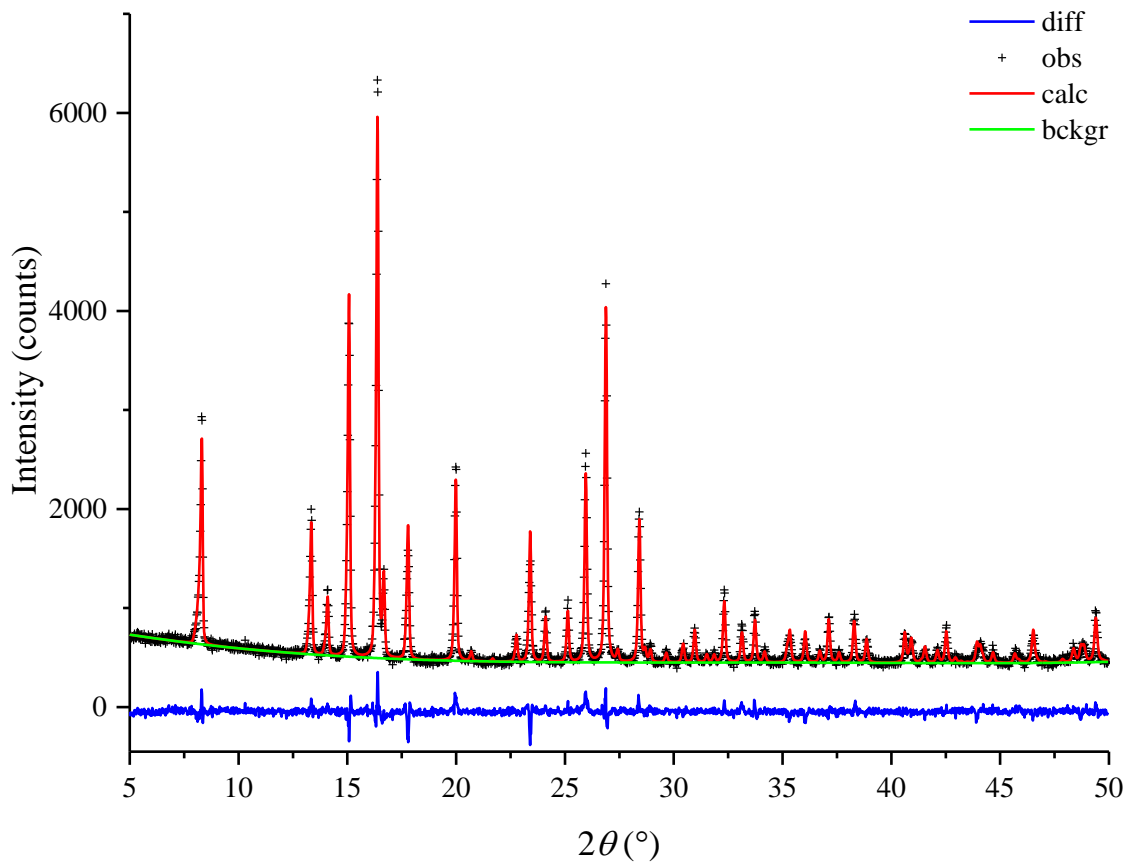


Figure 5.8 Rietveld refinement data for observed (obs), calculated (calc) and difference (diff) profiles of T2: $x = 0.20$ quenched from 1050 °C

Table 5.11 Structural refinement of T2: $x = 0.20$ quenched from 1050 °C

			1	2	3	4	5	6	7	8	9	10		
1	Mg1	4b	Occupancy	0.60	0.60	0.60	0.545 (6)	0.474 (5)	0.47	0.47	0.47	0.47	0.47	
			$100 \times U_{iso} (\text{\AA}^2)$	1.00	1.00	1.00	1.00	1.00	1.00	1.00	1.00	1.09 (8)	1.091	0.58 (7)
2	Mn1	4b	Occupancy	0.40	0.40	0.40	0.455 (6)	0.526 (5)	0.53	0.53	0.53	0.53	0.53	
			$100 \times U_{iso} (\text{\AA}^2)$	1.00	1.00	1.00	1.000	1.00	1.00	1.00	1.00	1.09 (8)	1.09	0.58 (7)
3	Mg2	8c	Occupancy	-	-	-	-	0.063 (2)	0.065	0.065	0.065	0.065	0.065	
			$100 \times U_{iso} (\text{\AA}^2)$	-	-	-	-	1.00	1.00	1.55 (6)	1.55	1.55	0.92 (5)	
4	Mn2	8c	Occupancy	1.00	1.00	0.901 (5)	0.90	0.937 (2)	0.935	0.935	0.935	0.935	0.935	
			$100 \times U_{iso} (\text{\AA}^2)$	1.00	1.00	1.00	1.00	1.00	1.00	1.55 (6)	1.55	1.55	0.92 (5)	
5	O1	16h	Occupancy	1.00	1.00	1.00	1.00	1.00	0.994 (7)	1.00	1.00	1.00	1.00	
			$100 \times U_{iso} (\text{\AA}^2)$	1.00	1.00	1.00	1.00	1.00	1.00	1.00	1.00	1.5 (1)	0.80 (9)	
			y	0.5278	0.5187 (7)	0.5187	0.5187	0.5187	0.5187	0.5187	0.5187	0.5187	0.5187	0.5230 (5)
			z	0.2411	0.2439 (4)	0.2439	0.2439	0.2439	0.2439	0.2439	0.2439	0.2439	0.2439	0.2415 (3)
			$a (\text{\AA})$	5.7784 (1)	5.7784 (1)	5.7783 (1)	5.7783 (1)	5.7784 (1)	5.7784 (1)	5.7784 (1)	5.7784 (1)	5.7784 (1)	5.7768 (2)	
			$c (\text{\AA})$	9.1705 (4)	9.1706 (3)	9.1706 (3)	9.1706 (3)	9.1705 (3)	9.1705 (3)	9.1705 (3)	9.1705 (3)	9.1705 (3)	9.1705 (3)	9.1680 (4)
			Volume (\AA^3)	306.20 (2)	306.20 (1)	306.20 (1)	306.20 (1)	306.20 (1)	306.20 (1)	306.20 (1)	306.20 (1)	306.20 (1)	305.95 (3)	
			χ^2	3.17	2.88	2.41	2.33	2.22	2.22	2.13	2.13	2.11	1.57	
			R _p	5.11%	4.98%	4.65%	4.59%	4.53%	4.53%	4.49%	4.49%	4.49%	3.91%	
			R _{wp}	7.15%	6.81%	6.23%	6.13%	5.98%	5.98%	5.86%	5.85%	5.83%	5.02%	

Table 5.12 Comparison of refined results of structural formulae and c/a ratio of Mn_3O_4 , T1 and T2 phases

Phase	Compositions of refinement result	c/a ratio
Mn₃O₄ $x = 0$	$(Mn)^{tet}[Mn]_2^{oct}O_4$ $\boxed{Mn^{2+}}$ $\boxed{Mn^{3+}}$	1.64326 (4)
T1 $x = 0.20$ at 500 °C	$(Mn_{0.4}Mg_{0.6})^{tet}[Mn]_2^{oct}O_4$ $\boxed{Mn^{2+}}$ $\boxed{Mn^{3+}}$	1.62671 (6)
T2 $x = 0.20$ at 1050 °C	$(Mn_{0.53}Mg_{0.47})^{tet}[Mn_{0.935}Mg_{0.065}]_2^{oct}O_4$ $\boxed{Mn^{2+ ?}}$ $\boxed{Mn^{3+}}$	1.58704 (9)

 Table 5.13 (a) bond lengths, (b) bond angles of T2, $x = 0.20$ quenched from 1050 °C

(a)		(b)	
	$x = 0.20$		$x = 0.20$
Vector	Length (Å)	Angle	Degree (°)
(4) x (Mg,Mn)1_O1	1.996 (3)	(4) x O1_(Mg,Mn)1_O1	112.1 (1)
(4) x (Mg,Mn)2_O1	1.952 (2)	(2) x O1_(Mg,Mn)1_O1	104.4 (2)
(2) x (Mg,Mn)2_O1	2.218 (3)	(4) x O1_(Mg,Mn)2_O1	94.8 (1)
		(4) x O1_(Mg,Mn)2_O1	85.2 (1)
		(2) x O1_(Mg,Mn)2_O1	95.6 (1)
		(2) x O1_(Mg,Mn)2_O1	84.4 (1)

5.3.2 T2 tetragonal spinel quenched from 1050 °C with different compositions ($x = 0.20, 0.30, 0.33, 0.36$ and 0.40)

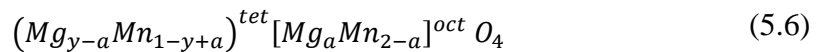
Samples of $x = 0.20, 0.30, 0.33, 0.36$ and 0.40 , quenched from 1050 °C were used to study the structure of T2 at different compositions. A similar refinement procedure was implemented as described in section 5.3.1. The comparison of final structural refinement results is summarised in table 5.15.

The final refinement results show a reasonably good fit between the observed and calculated data (figure 5.9) with acceptable statistical parameters (χ^2 , R_p and R_{wp}) and isotropic thermal parameters (table 5.15). An increase in a and decrease in c with increasing x was observed with an overall decrease in unit cell volume. The lattice c/a ratio decreased with increasing x (figure 5.10).

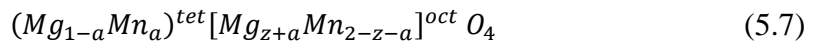
This refinement indicates that partial site exchange occurred between tetrahedral $4b$ -site and octahedral $8c$ -site (figure 5.11). This partial site exchange corresponded to an inversion degree, γ , which gave partial occupancy of Mg and Mn on both sites.

The reduction in the lattice c/a ratio of T2 (quenched from 1050 °C) was probably attributed to the reduction in number of Mn^{3+} ions at the octahedral sites due to:

- a) for $x \leq 0.33$: (i) site exchange.



- b) for $0.33 < x \leq 0.67$: (i) $2Mn^{3+} \rightarrow Mg^{2+} + Mn^{4+}$ (table 5.10), and
(ii) site exchange.



where a represents the number of ions involved in the site-exchange.

The summary of the possible compensation mechanisms for T1 and T2 are shown in table 5.14. However, there are still uncertainties concerning the mechanism of site exchange for T2. The reduction in the number of Mn³⁺ ions at the octahedral sites, could be as a result of partial migration of Mn³⁺ ions to the tetrahedral sites or Mn³⁺ ions itself undergo a disproportionation reaction to a pair of Mn²⁺ and Mn⁴⁺ ions.

Table 5.14 Summary of possible compensation mechanisms of T1 and T2

	$0 < x \leq 0.33$	$0.33 < x \leq 0.67$
T1	$(Mg_y Mn_{1-y})^{tet} [Mn_2]^{oct} O_4$	-
T2	$(Mg_{y-a} Mn_{1-y+a})^{tet} [Mg_a Mn_{2-a}]^{oct} O_4$	$(Mg_{1-a} Mn_a)^{tet} [Mg_{z+a} Mn_{2-z-a}]^{oct} O_4$

Table 5.15 Comparison of structural refinement results of T2 with varying Mg content: $x = 0.20, 0.30, 0.33, 0.36$ and 0.40 quenched from $1050\text{ }^{\circ}\text{C}$. γ represent the degree of inversion

			$x = 0.20$	$x = 0.30$	$x = 0.33$	$x = 0.36$	$x = 0.40$	
1	Mg1	4b	Occupancy	0.47	0.57	0.59	0.63	0.70
			$100 \times U_{iso} (\text{\AA}^2)$	0.58 (7)	0.69 (6)	1.42 (7)	1.26 (8)	1.39 (7)
2	Mn1	4b	Occupancy	0.53	0.43	0.41	0.37	0.30
			$100 \times U_{iso} (\text{\AA}^2)$	0.58 (7)	0.69 (6)	1.42 (7)	1.26 (8)	1.39 (7)
3	Mg2	8c	Occupancy	0.065	0.165	0.205	0.225	0.250
			$100 \times U_{iso} (\text{\AA}^2)$	0.92 (5)	1.20 (4)	1.15 (4)	1.06 (5)	0.97 (4)
4	Mn2	8c	Occupancy	0.935	0.835	0.795	0.775	0.750
			$100 \times U_{iso} (\text{\AA}^2)$	0.92 (5)	1.20 (4)	1.15 (4)	1.06 (5)	0.97 (4)
5	O1	16h	Occupancy	1.00	1.00	1.00	1.00	1.00
			$100 \times U_{iso} (\text{\AA}^2)$	0.80 (9)	1.22 (7)	1.50 (8)	1.50 (9)	1.51 (9)
			y	0.5230 (5)	0.5230 (4)	0.5250 (4)	0.5236 (5)	0.5238 (5)
			z	0.2415 (3)	0.2404 (3)	0.2394 (3)	0.2384 (3)	0.2386 (3)
			$a (\text{\AA})$	5.7768 (2)	5.8219 (1)	5.8294 (2)	5.8340 (2)	5.8534 (2)
			$c (\text{\AA})$	9.1680 (4)	8.8836 (2)	8.8221 (3)	8.7472 (3)	8.6821 (3)
			Volume (\AA^3)	305.95 (3)	301.10 (2)	299.80 (2)	297.72 (3)	297.47 (2)
			c/a	1.58704 (9)	1.52589 (4)	1.51338 (7)	1.50012 (7)	1.48326 (7)
			χ^2	1.57	1.80	1.87	2.33	2.29
			R_p	3.91%	4.36%	5.13%	3.53%	4.69%
			R_{wp}	5.02%	5.62%	6.46%	4.82%	6.03%
			γ	0.13	0.33	0.41	0.37	0.30

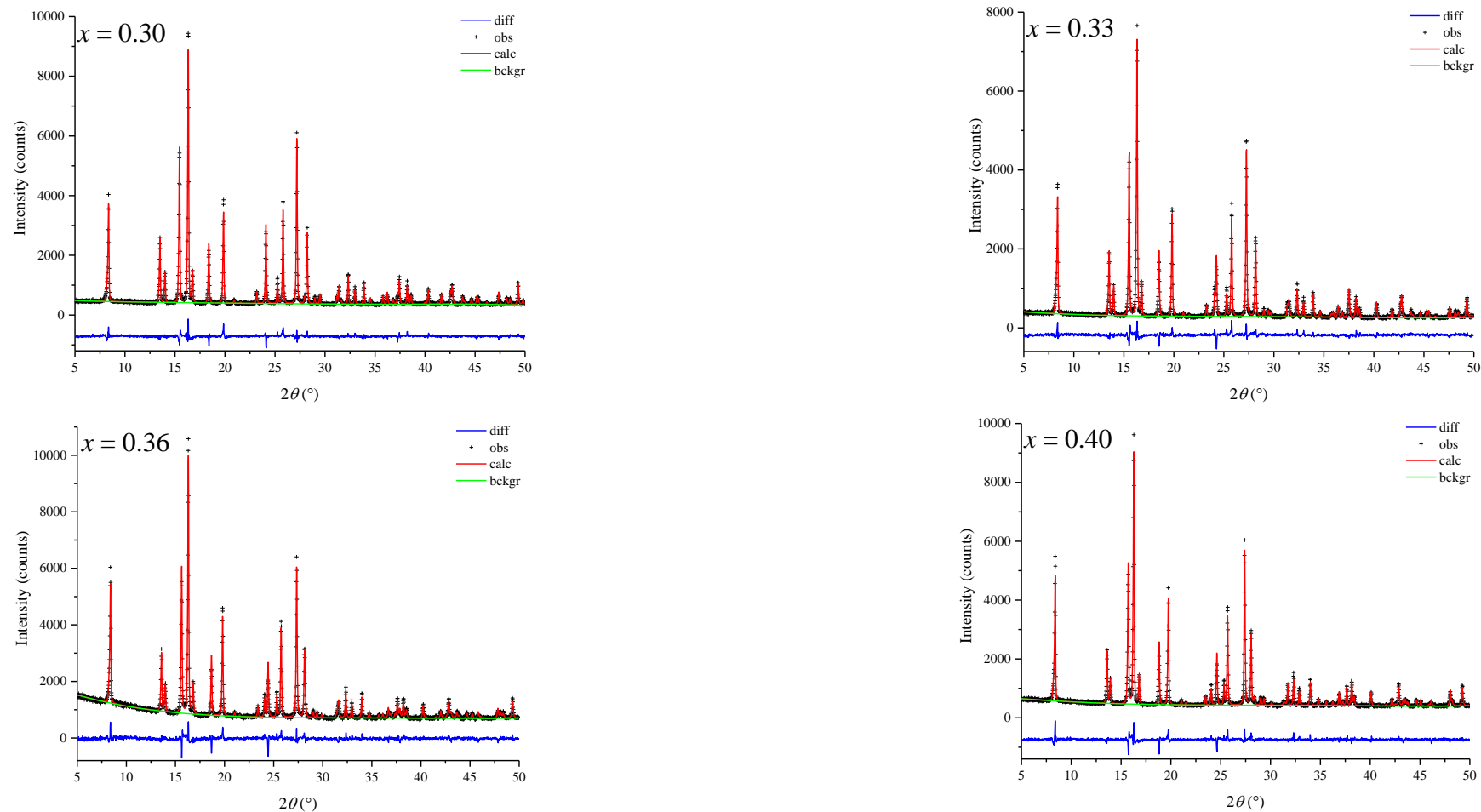


Figure 5.9 Rietveld refinement data for observed (obs), calculated (calc) and difference (diff) profiles of T2:

$x = 0.30, 0.33, 0.36$ and 0.40 quenched from 1050°C

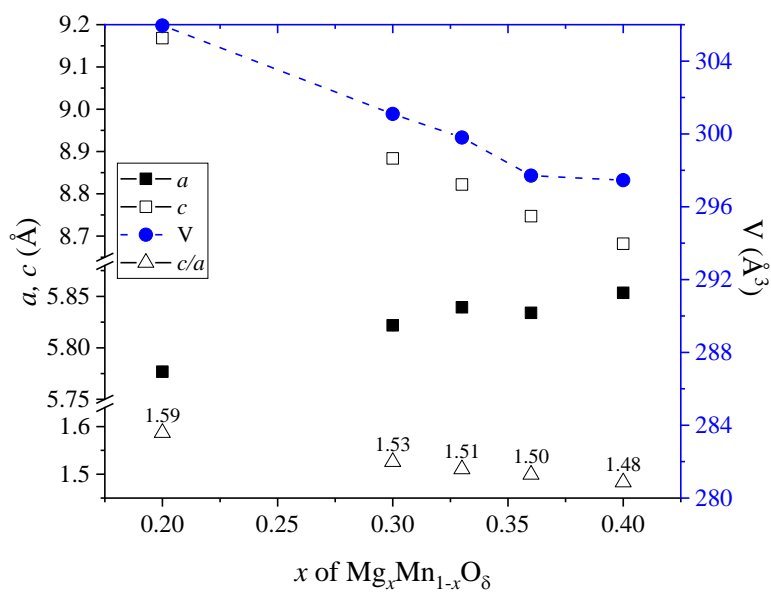


Figure 5.10 Lattice parameters, a , c , cell volume, V , and axial ratio, c/a , of T2 for $0.20 \leq x \leq 0.40$ quenched from 1050°C into liquid nitrogen. Error bars are smaller than the data points

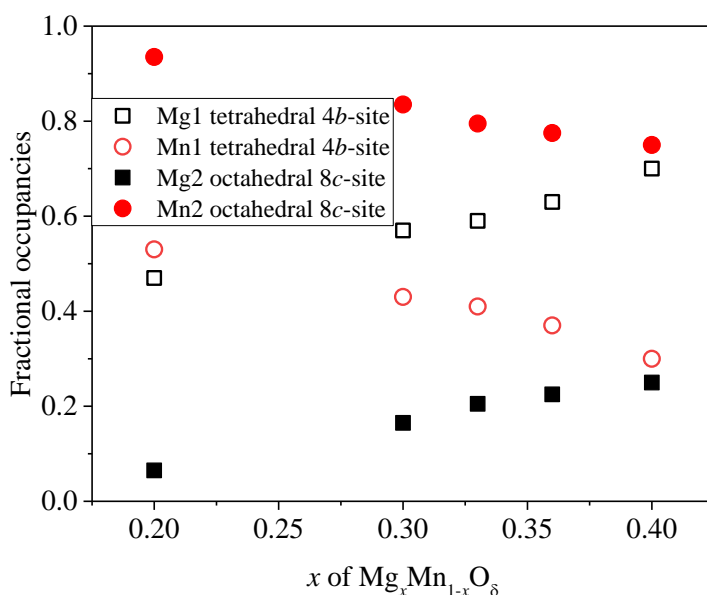


Figure 5.11 Fractional occupancies of Mg1:Mn1 at tetrahedral $4b$ -site and Mg2:Mn2 at octahedral $8c$ -site of the T2 structure for $0.20 \leq x \leq 0.40$ quenched from 1050°C into liquid N_2

5.4 XANES analysis of tetragonal spinel polymorphs

Samples of $x = 0.20$ quenched from 700 and 1100 °C were used to study the manganese oxidation state for T1 and T2 respectively. Reference samples with known valence(s): MnO (+2), Mn₃O₄ (+2, +3), Mn₂O₃ (+3) and MnO₂ (+4), were used as a comparison (table 2.3). The maxima of the absorption Mn K-edge of the samples were compared with the reference.

Figure 5.12 (a) shows the absorption Mn K-edge for the reference samples. The absorption maximum for MnO is clearly distinguish at lower absorption energy, $E_0 = 6554.0$ eV. However, the absorption maxima for Mn₃O₄, Mn₂O₃ and MnO₂ are close to each other, $E_0 = 6558.3$ eV, $E_0 = 6558.0$ eV and $E_0 = 6559.6$ eV respectively. This makes the determination of the average oxidation states of manganese by using the absorption maxima in the samples rather difficult.

However, at the rising-edge or edge at half height of the absorption spectra, it can be observed that the spectra were shifted systematically to higher absorption energy with increasing average oxidation state of manganese (figure 5.12 (b)). Therefore, from here onwards, the absorption energy is compared using half-height of the absorption spectra.

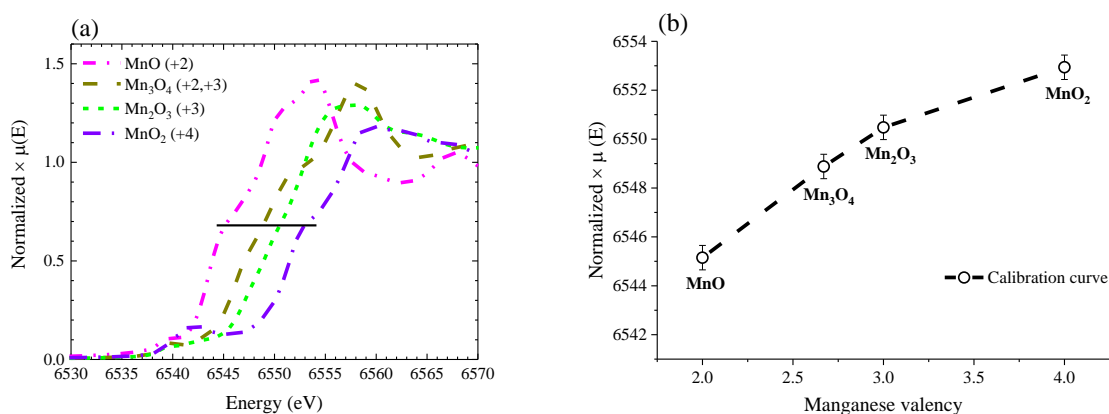


Figure 5.12 (a) XANES spectra of Mn K-edge for reference samples: MnO, Mn₃O₄, Mn₂O₃ and MnO₂. (b) Calibration curve of Mn K-edge absorption at half height for reference samples

Mn K-edge spectra for $x = 0.20$ quenched from 700 and 1100 °C (figure 5.13) showed a similar pattern to the Mn_3O_4 reference. They gave Mn K-edge at half height that was slightly higher than the $\text{Mn}^{2+,3+}$ reference ($E_0 = 6548.9$ eV) corresponding to an increase in the average Mn oxidation state. Both have a similar absorption energy, $E_0 = 6549.2$ eV and $E_0 = 6549.4$ eV respectively, within error. The error was estimated based on the size of a data point, ± 0.5 eV [13]. Plotting the E_0 for $x = 0.20$ on the calibration curve, gave the average oxidation states of manganese to be 2.74+ (700 °C) and 2.77+ (1100 °C) (figure 5.14).

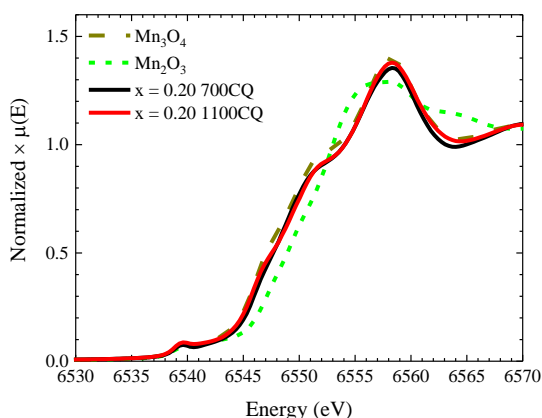


Figure 5.13 XANES spectra of Mn K-edge for $x = 0.20$ quenched from 700 °C (T1) and 1100 °C (T2)

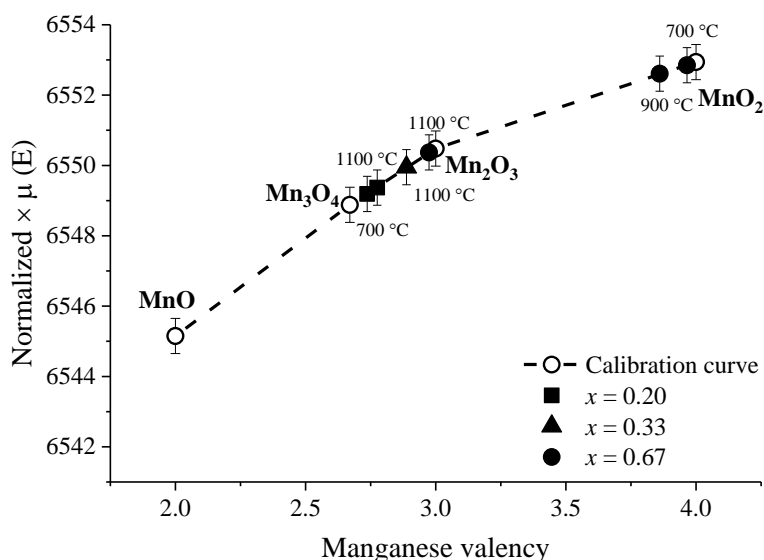


Figure 5.14 Average Mn oxidation states for $x = 0.20$, 0.33 and 0.67 quenched from different temperatures (shown on graph) plotted on the calibration curve of reference samples

The slight increase in energy observed (when compared to $\text{Mn}^{2+,3+}$ reference) was attributed to the reduction in number of Mn^{2+} at the tetrahedral $4b$ -site as it was partially replaced with Mg^{2+} . Therefore, this result is in agreement with the refined data (section 5.2) which showed that at $x = 0.20$, the valence ratio of $\text{Mn}^{2+}:\text{Mn}^{3+}$ to be 0.4:2 (Table 5.16), based on the replacement mechanism: $\text{Mn}^{2+} \rightarrow \text{Mg}^{2+}$. The result also indicates that the average oxidation state of manganese at both temperatures is close to that of the expected value of 2.83+.

Table 5.16 Comparison of expected (a) valence ratio $\text{Mn}^{2+}:\text{Mn}^{3+}$, and (b) the average oxidation states of Mn, with XANES results, for $x = 0.20$ with reference Mn_3O_4

		Mn_3O_4	$x = 0.20$
(a)	Valence ratio ($\text{Mn}^{2+}:\text{Mn}^{3+}$) ($4b:8c$)	1.0 : 2.0	0.4 : 2.0
(b)	Average Mn oxidation states	2.67	2.83

XANES results:

1	Quenched 700 °C	-	2.74
2	Quenched 1100 °C	-	2.77

In order to investigate further the valence of Mn in the T2 polymorph, two additional compositions were prepared, $x = 0.33$ and 0.67 and quenched from 1100 °C. A single phase of T2 was observed at $x = 0.33$ but a mixture of T2 and MgO at $x = 0.67$ (figure 4.26). The half-heights of Mn K-edge absorption maxima were again compared with the reference.

The pattern shapes are similar to $\text{Mn}^{2+,3+}$ reference but with half heights of the K-edge shifted to higher energies with increasing x , $x = 0.33$ ($E_0 = 6549.9$ eV) and $x = 0.67$ ($E_0 = 6550.4$ eV) (figure 5.15). The shift to higher energies thus corresponds to an increase in the average Mn oxidation state. Plotting the E_0 for $x = 0.33$ and 0.67 on the calibration curve, gave the average oxidation states of Mn to be 2.89+ and 2.97+, respectively (figure 5.14).

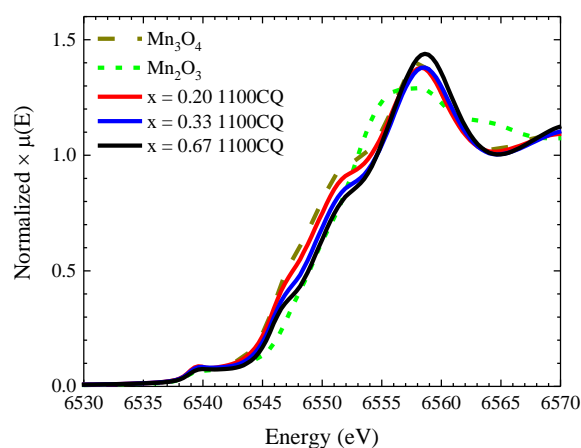


Figure 5.15 XANES spectra of Mn K-edge for $x = 0.20, 0.33$ and 0.67 quenched from $1100\text{ }^{\circ}\text{C}$ (T2)

The energy at half-height of the K-edge absorption maximum for sample $x = 0.33$, is close to the Mn^{3+} reference, within error. At $x = 0.33$, it is expected that there is only Mn^{3+} present in the sample since all the Mn^{2+} on the tetrahedral site has been replaced by Mg^{2+} , and the Mn oxidation state would therefore be 3+.

The energy at half-height of the K-edge absorption maximum for sample $x = 0.67$, matched well with the Mn^{3+} reference, within errors. It was initially expected that the Mn oxidation state at this composition to be 4+ since all the Mn^{3+} will be replaced by Mn^{4+} and Mg^{2+} . However, at $1100\text{ }^{\circ}\text{C}$, a mixture of T2 and MgO was observed on quenched sample. With reference to the phase diagram (figure 4.29), it can be assumed that MgO started to precipitate over the range $0.40 < x < 0.50$. Assuming MgO precipitates at $x = 0.42$, the calculated valence ratio of $\text{Mn}^{3+}:\text{Mn}^{4+}$ to be 1.48:0.26 (based on compensation $2\text{Mn}^{3+} \rightarrow \text{Mg}^{2+} + \text{Mn}^{4+}$) and it was expected that the average Mn oxidation state to be 3.15+.

In order to investigate the presence of Mn^{4+} at $x = 0.67$, two additional samples were prepared from $x = 0.67$ which were quenched from 700 and $900\text{ }^{\circ}\text{C}$. At $700\text{ }^{\circ}\text{C}$, a mixture of cubic spinel solid solution and Suzuki phase solid solution was observed, both of which were expected to have Mn oxidation state of 4+. A single phase cubic solid solution was observed at $900\text{ }^{\circ}\text{C}$ with similar expected Mn oxidation state.

The pattern shapes for $x = 0.67$ at 700 and 900 °C (figure 5.16) were similar and overlapped with each other with Mn K-edge absorption maxima to be $E_0 = 6552.9$ eV and $E_0 = 6552.6$ eV, respectively (slightly higher compared to $x = 0.67$ at 1100 °C). Plotting the E_0 for $x = 0.67$ at 700 and 900 °C on the calibration curve, gave the average oxidation states of Mn to be 3.97+ and 3.86+, respectively (figure 5.14).

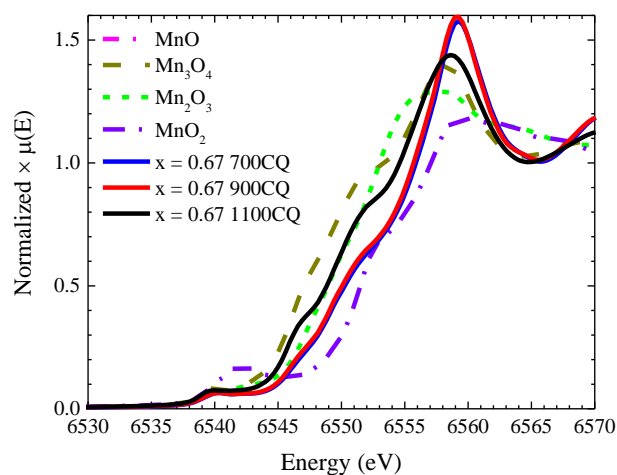


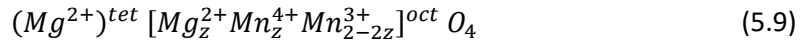
Figure 5.16 XANES spectra of Mn K-edge for $x = 0.67$ quenched from 700, 900 and 1100 °C.

5.5 Conclusions

The T1 refinement results showed that Mn^{2+} was partially substituted by Mg^{2+} at the tetrahedral site. The octahedral site is always fully occupied by Mn^{3+} and there was no evidence of oxygen loss. Thus, the chemical compensation mechanism is suggested to be through isovalent substitution:



Based on this mechanism, it was expected that at $x = 0.33$, there would be no more Mn^{2+} left at the tetrahedral sites as it has been fully replaced by Mg^{2+} . Therefore, for $x > 0.33$, another compensation mechanism was proposed with two Mn^{3+} ions substituted by a pair of Mg^{2+} and Mn^{4+} ions on the octahedral site. This indicates the presence of Mn^{4+} ions for $x > 0.33$.



A small decrease in unit cell size was observed with increasing x up to $x = 0.20$ due to the smaller ionic radius of Mg^{2+} compared to Mn^{2+} in the tetrahedral environment. Within the T1 domain, there was no obvious change in axial ratio c/a with increasing temperature up to 850 °C. The result matches well with the XRD pattern observed in chapter 4.

At higher temperature, T2 refinement indicates that partial site exchange occurred between tetrahedral and octahedral sites. As a result, both sites were partially occupied by Mg and Mn. The reduction in number of Mn^{3+} ions at the octahedral sites thus responsible for the observed decrease in the axial c/a ratio. However, it is still unclear whether the Mn^{3+} ions itself migrated to the tetrahedral sites or a disproportionation reaction ($2Mn^{3+} \rightarrow Mn^{2+} + Mn^{4+}$) took place at the octahedral sites, whereby the Mn^{2+} ions then migrated to the tetrahedral site.

The determination of Mn valence state from the Mn K-edge absorption maxima in XANES spectra is rather difficult. Mn K-edge also exhibits a wide variation of E_0 as reported by Manceau *et al.* ^[14] (figure 5.17). Thus, the rising-edge or edge at half height of the absorption spectra were used as it shows better systematic shifts of the spectra.

The measurements for $x = 0.20$ suggested that the average Mn oxidation state for T1 (700 °C) and T2 (1100 °C) was a mixture of +2 and +3, within error. This was attributed to the isovalent substitution of $Mn^{2+} \rightarrow Mg^{2+}$ at the tetrahedral site.

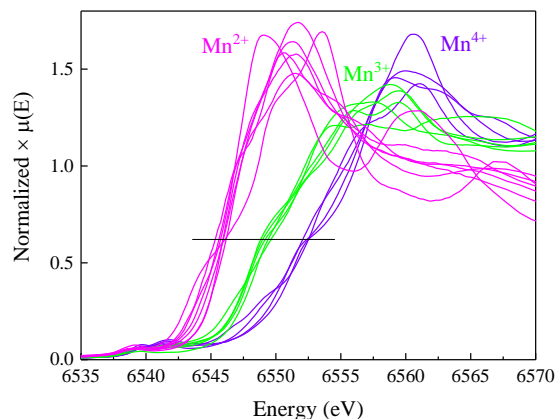


Figure 5.17 XANES spectra of Mn K-edge for Mn^{2+} , Mn^{3+} and Mn^{4+} from different polyvalent manganates in various coordination environment

The measurement of T2 phase at 1100 °C for $x = 0.20, 0.33$ and 0.67 showed an increase in the average Mn oxidation state with increasing x from $\text{Mn}^{2+,3+}$ to Mn^{3+} , within error. For $x > 0.33$, the increase in the average oxidation state was attributed to the decrease in Mn^{3+} by substitution of Mg^{2+} and Mn^{4+} (until the phase boundary of T2 and MgO). Since at $x = 0.67$, a two-phase mixture of T2 and MgO was observed, the average Mn oxidation state at this composition will be the same as at the phase boundary at which MgO started to precipitate, $x \sim 0.42$.

5.6 References

1. Kasper, J., *Magnetic structure of hausmannite, Mn_3O_4* . Bulletin of the American Physics Society, 1959. **4**: p. 178.
2. Boucher, B., R. Buhl, and M. Perrin, *Propriétés et structure magnétique de Mn_3O_4* . Journal of Physics and Chemistry of Solids, 1971. **32**(10): p. 2429-2437.
3. Jensen, G. and O. Nielsen, *The magnetic structure of Mn_3O_4 Hausmannite between 4.7 K and Neel point, 41 K*. Journal of Physics C: Solid State Physics, 1974. **7**(2): p. 409.

4. Gopalakrishnan, I., N. Bagkar, R. Ganguly, and S. Kulshreshtha, *Synthesis of superparamagnetic Mn₃O₄ nanocrystallites by ultrasonic irradiation*. Journal of Crystal Growth, 2005. **280**(3-4): p. 436-441.
5. Hu, C.-C., Y.-T. Wu, and K.-H. Chang, *Low-temperature hydrothermal synthesis of Mn₃O₄ and MnOOH single crystals: determinant influence of oxidants*. Chemistry of Materials, 2008. **20**(9): p. 2890-2894.
6. Guo, L., D. Peng, H. Makino, K. Inaba, H. Ko, K. Sumiyama, and T. Yao, *Structural and magnetic properties of Mn₃O₄ films grown on MgO (0 0 1) substrates by plasma-assisted MBE*. Journal of magnetism and magnetic materials, 2000. **213**(3): p. 321-325.
7. Boucher, B., R. Buhl, and M. Perrin, *Magnetic structure of Mn₃O₄ by neutron diffraction*. Journal of Applied Physics, 1971. **42**(4): p. 1615-1617.
8. Dubal, D., D. Dhawale, R. Salunkhe, S. Pawar, and C. Lokhande, *A novel chemical synthesis and characterization of Mn₃O₄ thin films for supercapacitor application*. Applied Surface Science, 2010. **256**(14): p. 4411-4416.
9. Dunitz, J.t. and L. Orgel, *Electronic properties of transition-metal oxides-II: cation distribution amongst octahedral and tetrahedral sites*. Journal of Physics and Chemistry of Solids, 1957. **3**(3-4): p. 318-323.
10. Shannon, R.T. and C.T. Prewitt, *Effective ionic radii in oxides and fluorides*. Acta Crystallographica Section B: Structural Crystallography and Crystal Chemistry, 1969. **25**(5): p. 925-946.
11. Brown, I. and D. Altermatt, *Bond-valence parameters obtained from a systematic analysis of the Inorganic Crystal Structure Database*. Acta Crystallographica Section B, 1985. **41**(4): p. 244-247.
12. Sidey, V., *Universal 'bond valence versus bond length' correlation curve for manganese–oxygen bonds*. Acta Crystallographica Section B: Structural Science, Crystal Engineering and Materials, 2014. **70**(3): p. 608-611.
13. Reeves-McLaren, N., J. Sharp, H. Beltrán-Mir, W.M. Rainforth, and A.R. West, *Spinel–rock salt transformation in LiCoMnO_{4-δ}*. Proc. R. Soc. A, 2016. **472**(2185): p. 20140991.
14. Manceau, A., M.A. Marcus, and S. Grangeon, *Determination of Mn valence states in mixed-valent manganates by XANES spectroscopy*. American Mineralogist, 2012. **97**(5-6): p. 816-827.

Chapter 6: Structural analysis of a cubic solid solution

6.1 Introduction

The cubic phase solid solution was observed between the immiscibility dome (~ 850 °C) and a subsolidus temperature (~ 1000 °C) over the range $0.50 \leq x < 0.86$ of $\text{Mg}_x\text{Mn}_{1-x}\text{O}_8$ (figure 4.29). The XRD patterns for $x = 0.50, 0.60, 0.67, 0.70$ and 0.80 of the cubic solid solution were indexed using space group either $Fd\bar{3}m$ or $Fm\bar{3}m$ which indicates that they form a single phase solid solution with face-centred cubic (*fcc*) symmetry. In order to proceed with structural analysis, the space group that best describes the symmetry of the cubic solid solution needs to be determined.

The space groups $Fd\bar{3}m$ and $Fm\bar{3}m$ have been reported for known phases with composition Mg_2MnO_4 ^[1] and Mg_6MnO_8 ^[2] respectively. Both describe a face centred cubic unit cell with 32 oxygen atoms. The difference is that the space group $Fd\bar{3}m$ has an extra symmetry element of a body diagonal *d*-glide plane. Therefore, the space group $Fd\bar{3}m$ has an additional rule for reflections to be observed compared to the space group $Fm\bar{3}m$ ^[3] (table 6.1).

Table 6.1 Systematic absences for different lattice type ^[4]

Lattice type		Rule for reflection to be observed
Primitive	P	None
Body-centred	I	$hkl; h+k+l = 2n$ (must be even)
Face-centred	F	$hkl; h, k, l$ either all odd or all even
		<i>d</i> -glide plane reflection to be observed $0kl: k+l = 4n$ ^[3]

The reflections observed in the XRD patterns of samples $x = 0.50$ and 0.67 quenched from $950\text{ }^{\circ}\text{C}$ (figure 6.1), showed the absence of peaks (200), (420) and (640) over the range $5^{\circ} \leq 2\theta \leq 40^{\circ}$, which satisfied the rule of systematic absence for the d -glide plane. This led to the initial assumption that the patterns would satisfy the space group $Fd\bar{3}m$ instead of $Fm\bar{3}m$.

However, the absence of these peaks could also mean that an incomplete destructive interference had occurred in the cubic structure.

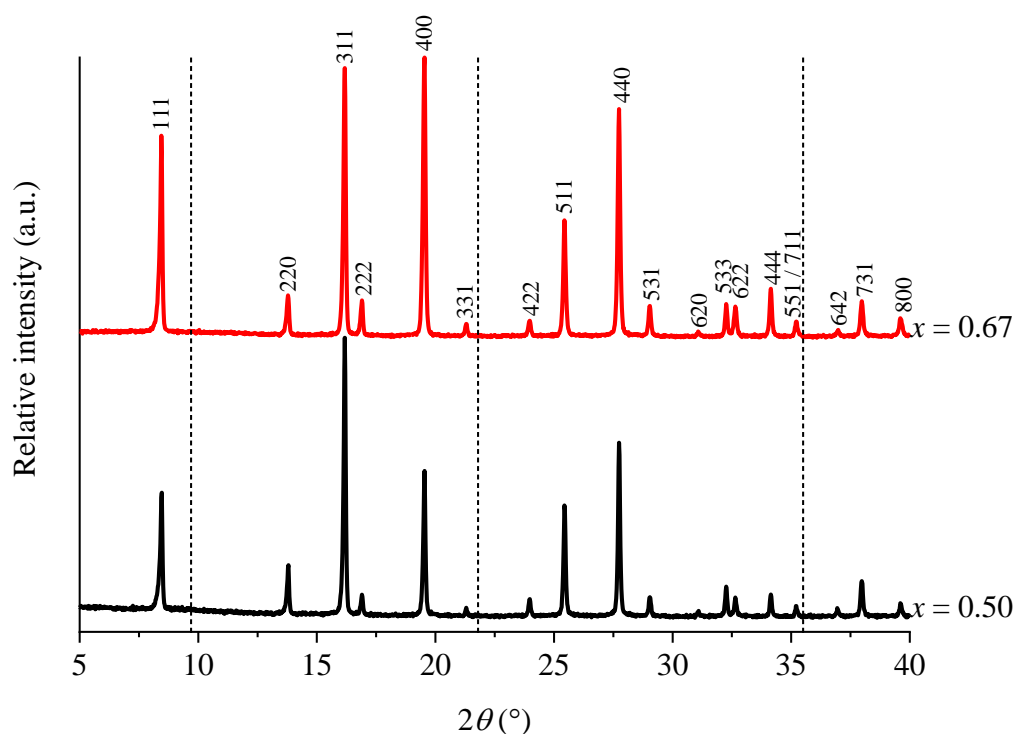


Figure 6.1 The XRD patterns for $x = 0.50$ and 0.67 quenched from $950\text{ }^{\circ}\text{C}$. The vertical dash lines indicate the positions of unobserved peaks (200), (420) and (640) at 2θ ca 9.7° , 21.8° and 35.4° respectively based on ICDD 04-006-8397 [2, 5]

Two conditions have to be fulfilled for a systematic absence to be observed:

- (i) An equal number of diffracted beams to be out-of-phase by half of a wavelength ($\lambda/2$).
- (ii) An equal number of diffracted beams have the same amplitude (governed by the form factors).

Thus, an incomplete destructive interference could be due to either one or both of these conditions not being met ^[4].

The uses of XRD thus possess certain limitations whereby the unobserved peaks of (200), (420) and (640) are either due to systematic absences of the d -glide plane symmetry of the $Fd\bar{3}m$ space group or of reduced intensity as a result of almost complete cancellation of certain reflections in the $Fm\bar{3}m$ space group. Therefore, in order to determine which of these two space groups best describe the symmetry of the observed cubic solid solution, neutron diffraction was used.

6.2 Neutron diffraction on a cubic solid solution

Neutron diffraction data were collected using the Polaris powder diffractometer on samples $x = 0.50$ and 0.67 quenched from $950\text{ }^{\circ}\text{C}$. A preliminary XRD analysis was conducted on both samples prior to the ND experiment to ensure that the samples were single phase cubic without the presence of any impurities (figure 6.1).

The ND data showed the presence of peaks (200), (420) and (640) that were unobserved in the XRD reflections. These peak intensities increased with increasing x (relatively weak for $x = 0.50$ compared to $x = 0.67$) (figure 6.2). Since these peaks were observed in the ND data, they do not satisfy the rule of reflections to be observed for the d -glide plane of the $Fd\bar{3}m$ space group. Hence, the space group for the cubic solid solution was concluded to be $Fm\bar{3}m$.

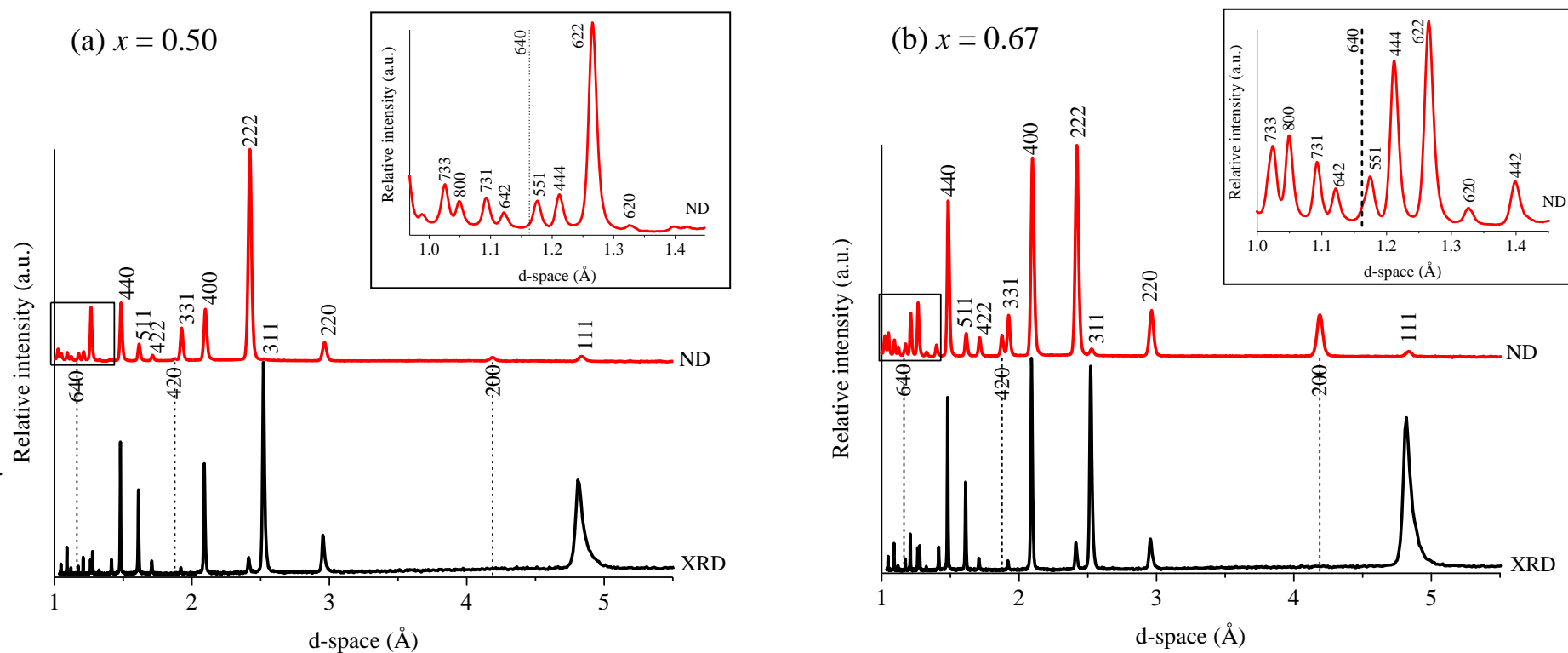


Figure 6.2 The comparison between ND and XRD patterns for (a) $x = 0.50$ and (b) $x = 0.67$ quenched from $950\text{ }^{\circ}\text{C}$. The vertical dashed lines indicate the positions of peaks (200), (420) and (640) at d -space *ca* 4.2, 1.9 and 1.2 \AA respectively. The XRD data collected in 2θ were converted to d -space using Bragg's law.

6.3 Structural refinement of cubic solid solutions

The structural refinement of the cubic solid solution was performed on samples of $x = 0.50, 0.60, 0.67, 0.70$ and 0.80 quenched from $950\text{ }^{\circ}\text{C}$ into liquid nitrogen. Since the space group of the cubic solid solution was concluded to be $Fm\bar{3}m$, the Suzuki phase structure of Mg_6MnO_8 was chosen as a starting model (table 6.2). Mg_6MnO_8 has a cubic rock salt superstructure of MgO by substituting two of the Mg^{2+} ions with a pair of Mn^{4+} ions and a vacancy. Both the Mg^{2+} and Mn^{4+} are octahedrally coordinated at $24d$ - and $4a$ -sites respectively and the oxygen is distributed at $8c$ - and $24e$ -sites. The initial thermal parameters are set to be 0.025 \AA^2 .

Table 6.2 Starting model of Mg_6MnO_8 (ICDD: 04-006-8397) ^[5]

Atom	Multiplicity	x	y	z	Occupancy	$100 \times U_{iso} (\text{\AA}^2)$
Mg1	$24d$	0	0.25	0.25	1	2.5
Mn2	$4a$	0	0	0	1	2.5
O1	$8c$	0.25	0.25	0.25	1	2.5
O2	$24e$	0.23	0	0	1	2.5

$$a = 8.381\text{ \AA}; \text{ Space group} = Fm\bar{3}m$$

In figure 4.14, the XRD pattern showed that attempts to prepare a phase-pure stoichiometric Suzuki phase with composition $x = 0.86$ of $\text{Mg}_x\text{Mn}_{1-x}\text{O}_8$ was unsuccessful, because of the appearance of a second phase, MgO . The nearest phase-pure composition that was prepared was at $x = 0.80$, which showed a single-phase cubic structure between 850 and $1000\text{ }^{\circ}\text{C}$ (figure 4.29). The initial structural refinement was carried out on $x = 0.80$ quenched from $950\text{ }^{\circ}\text{C}$, in order to establish the refinement strategy. Subsequent structural refinement of other cubic solid solution compositions would then follow.

6.3.1 Structural refinement of $x = 0.80$ quenched from 950 °C

The structural refinement has been performed on XRD data using a similar procedure to that described in section 2.4. The R values and atomic coordinates at different stages of refinement are summarised in table 6.3. The occupancy of Mg1, Mn1, O1 and O2 were initially set to full occupancy.

The scale factor, background (6 terms of Chebyshev function) and lattice parameter were refined first and were allowed to refine in the subsequent refinements, followed by zero-point and peak profile coefficient, column 1. The O2 atomic coordinate (x) was refined and fixed after convergence, column 2. Next, the occupancy of Mn2 was refined and gave a value higher than unity, column 3. The occupancy of Mn2 was fixed to full occupancy. Then, the occupancy of Mg1 was refined and gave a value of 0.919 (7), column 4. At composition $x = 0.80$, there were two possible compensation mechanisms that could approximate the occupancy of Mg1:



These mechanisms (6.1) and (6.2) would give the expected occupancy of Mg1 to be 0.933 and 0.889 respectively. An increase in Mn occupancy was also expected and if Mg1 is partially occupied (as shown by the refined value), there is a probability that Mn occupies a different site.

A Difference Fourier map (figure 6.3) was performed in order to locate a possible new site for the extra Mn ions. A new $32f$ -site (0.375, 0.375, 0.375) was found to be partially occupied and thus assigned to the additional Mn ions (Mn3), with the occupancy set to be 0.061, consistent with the reduction in occupancy of Mg1.

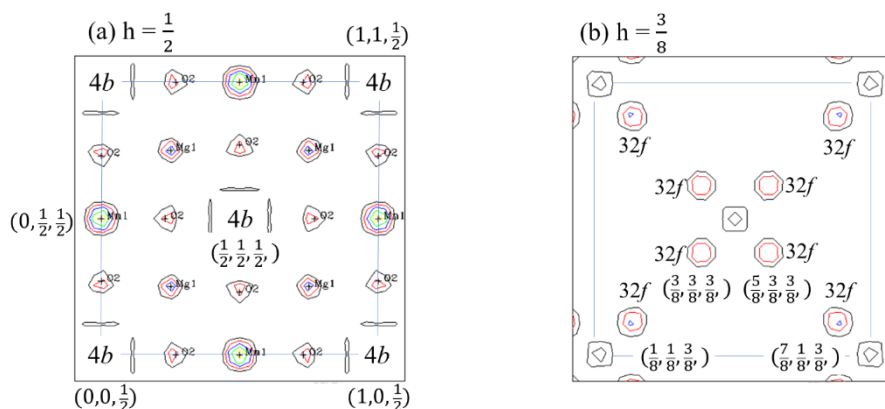


Figure 6.3 A Difference Fourier map of $x = 0.80$ showing electron-density in a unit cell taken at cross-section height, h (a) $h = 0.5$ and (b) $h = 0.375$. The $4b$ -site is empty whilst the $32f$ is occupied. The number in parentheses represent site coordinates in the unit cell

The atomic coordinates of Mn3 (x, y, z) and O2 (x) were refined in turn and were fixed after convergence, column 5 and 6. Next, the occupancies of Mn2 and Mn3 were refined and showed values higher than unity for Mn2 while that of Mn3 remained unchanged, column 7. The occupancy of Mn2 was fixed to full occupancy and the occupancy of Mn3 refined but its value was unchanged within errors, column 8. After that, the occupancy of Mg1 was refined and fixed after convergence, column 9. The occupancies of O1 and O2 were then refined together and gave values of higher and lower than unity, respectively; column 10. The occupancy of O1 was fixed to full occupancy and the occupancy of O2 refined to a value less than unity, column 11. The U_{iso} of Mn2 was refined and gave a reasonable value, column 12. After that, the U_{iso} of O1 was refined, showed a value of ~ 0.006 (2) \AA^2 , column 13. Finally, the atomic coordinates of Mn3 (x, y, z) and O2 (x), the occupancy of Mg1, Mn3, O2, the U_{iso} of Mn2, O1 and the profile parameters were refined simultaneously, column 14. A subsequent refinement check of the U_{iso} values of Mg1, Mn3 and O2 with fixed atomic coordinates and occupancies gave reasonable values for Mg1 and O2 but a higher value for Mn3 than the default 0.025\AA^2 .

The thermal parameter of Mg1, Mn3 and O2 were fixed to a default value of $\sim 0.025 \text{\AA}^2$, and their site fractional occupancy were refined, in order to determine the compensation mechanism, with refined values of 0.910 (5), 0.047 (1) and 0.975 (7), respectively. A slight decrease in occupancy of O2 may indicate the possibility of oxygen vacancies in the structure. The refined lattice parameter is $a = 8.3815$ (2) \AA . The final

result, column 14, shows a reasonable fit between the observed and calculated data (table 6.3) with statistical parameters: $\chi^2 = 2.34$, $R_p = 5.44\%$ and $R_{wp} = 7.31\%$ and realistic isotropic thermal parameters for Mn2 and O1 (table 6.3).

The bond lengths of Mg1_O1, Mg1_O2 and Mn2_O2 are similar to the reported literature [2], within errors, showing a slightly distorted Mg1 octahedron (with O1 and O2). The Mn3 has one bond length with O1, 1.70 (2) Å and three bond lengths with O2, 1.940 (6) Å, indicating a distorted tetrahedron, which are highly correlated to the atomic positions of Mn3 and O2. The presence of tetrahedral Mn3 indicates the possibility of a cubic rock-salt to spinel transformation with decreasing x . The refined chemical composition indicates an oxygen non-stoichiometry, $Mg_{21.8}Mn_{5.5}O_{31.4}$.

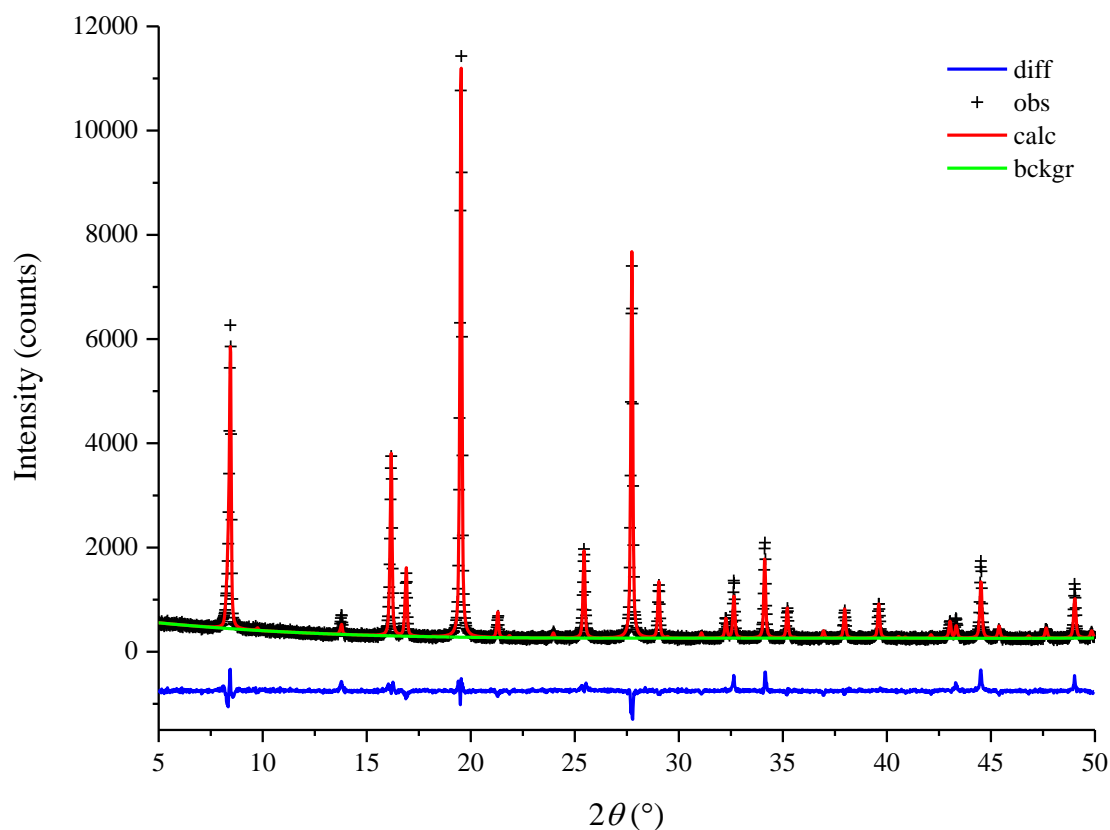


Figure 6.4 Rietveld refinement data for observed (obs), calculated (calc) and difference (diff) profile for $x = 0.80$ quenched from 950 °C

Table 6.3 Structural refinement of $x = 0.80$ quenched from 950 °C

			1	2	3	4	5	6	7	
1	Mg1	24d	Occupancy	1.000	1.000	1.000	0.919 (7)	0.919	0.919	0.919
			$100 \times U_{iso}$ (Å ²)	2.500	2.500	2.500	2.500	2.500	2.500	2.500
2	Mn2	4a	Occupancy	1.000	1.000	1.083 (9)	1.000	1.000	1.000	1.042 (6)
			$100 \times U_{iso}$ (Å ²)	2.500	2.500	2.500	2.500	2.500	2.500	2.500
3	Mn3	32f	Occupancy	-	-	-	-	0.061	0.061	0.061 (2)
			$100 \times U_{iso}$ (Å ²)	-	-	-	-	2.500	2.500	2.500
			x	-	-	-	-	0.3521 (9)	0.3521	0.3521
			y	-	-	-	-	0.3521 (9)	0.3521	0.3521
			z	-	-	-	-	0.3521 (9)	0.3521	0.3521
4	O1	8c	Occupancy	1.000	1.000	1.000	1.000	1.000	1.000	1.000
			$100 \times U_{iso}$ (Å ²)	2.500	2.500	2.500	2.500	2.500	2.500	2.500
5	O2	24e	Occupancy	1.000	1.000	1.000	1.000	1.000	1.000	1.000
			$100 \times U_{iso}$ (Å ²)	2.500	2.500	2.500	2.500	2.500	2.500	2.500
			x	0.2300	0.2340 (5)	0.2340	0.2340	0.2340	0.2335 (4)	0.2335
			a (Å)	8.3832 (3)	8.3832 (1)	8.3832 (1)	8.3832 (1)	8.3832 (1)	8.3833 (1)	8.3833 (1)
			Volume (Å ³)	589.16 (6)	589.16 (3)	589.16 (3)	589.16 (3)	589.17 (2)	589.17 (2)	589.17 (2)
			χ^2	7.18	7.00	6.74	6.62	4.07	4.07	3.99
			R_p	9.33%	9.28%	9.12%	9.07%	7.39%	7.38%	7.28%
			R_{wp}	12.81%	12.65%	12.41%	12.31%	9.65%	9.65%	9.55%

Continue to next page

			8	9	10	11	12	13	14	
1	Mg1	24d	Occupancy	0.919	0.900 (5)	0.900	0.900	0.900	0.900	0.910 (5)
			$100 \times U_{iso} (\text{\AA}^2)$	2.500	2.500	2.500	2.500	2.500	2.500	2.500
2	Mn2	4a	Occupancy	1.000	1.000	1.000	1.000	1.000	1.000	1.000
			$100 \times U_{iso} (\text{\AA}^2)$	2.500	2.500	2.500	2.500	1.15 (6)	1.15	0.48 (5)
3	Mn3	32f	Occupancy	0.062 (2)	0.062	0.062	0.062	0.062	0.062	0.047 (1)
			$100 \times U_{iso} (\text{\AA}^2)$	2.500	2.500	2.500	2.500	2.500	2.500	2.500
			<i>x</i>	0.3521	0.3521	0.3521	0.3521	0.3521	0.3521	0.367 (1)
			<i>y</i>	0.3521	0.3521	0.3521	0.3521	0.3521	0.3521	0.367 (1)
			<i>z</i>	0.3521	0.3521	0.3521	0.3521	0.3521	0.3521	0.367 (1)
4	O1	8c	Occupancy	1.000	1.000	1.18 (2)	1.000	1.000	1.000	1.000
			$100 \times U_{iso} (\text{\AA}^2)$	2.500	2.500	2.500	2.500	2.500	0.6 (2)	0.3 (2)
5	O2	24e	Occupancy	1.000	1.000	0.906 (7)	0.949 (7)	0.949	0.949	0.975 (7)
			$100 \times U_{iso} (\text{\AA}^2)$	2.500	2.500	2.500	2.500	2.500	2.500	2.500
			<i>x</i>	0.2335	0.2335	0.2335	0.2335	0.2335	0.2335	0.2318 (4)
			<i>a</i> (Å)	8.3833 (1)	8.3833 (1)	8.3833 (1)	8.3833 (1)	8.3833 (1)	8.3833 (1)	8.3815 (2)
			Volume (Å ³)	589.17 (2)	589.17 (2)	589.17 (2)	589.17 (2)	589.17 (2)	589.17 (2)	588.81 (4)
			χ^2	4.07	4.04	3.76	3.95	3.39	3.24	2.34
			R _p	7.38%	7.33%	7.14%	7.30%	6.82%	6.74%	5.44%
			R _{wp}	9.65%	9.62%	9.27%	9.50%	8.80%	8.61%	7.31%

Table 6.4 (a) Bond lengths, (b) Bond angles of refined $x = 0.80$ quenched from 950 °C

(a) Bond length		(b) Bond angle	
	$x = 0.80$		$x = 0.80$
Vector	Length (Å)	Angle	Degree (°)
(2) × Mg1_O1	2.0954 (1)	(8) × O1_Mg1_O2	90
(4) × Mg1_O2	2.1009 (3)	(2) × O2_Mg1_O2	81.7 (2)
(6) × Mn2_O2	1.943 (3)	(2) × O2_Mg1_O2	98.3 (2)
(1) × Mn3_O1	1.70 (2)	(12) × O2_Mn2_O2	90
(3) × Mn3_O2	1.940 (6)	(3) × O1_Mn3_O2	108.9 (6)
		(3) × O2_Mn3_O2	110.0 (6)

6.3.2 Structural refinement of $x = 0.50, 0.60, 0.67$ and 0.70 quenched from 950 °C

Samples of $x = 0.50, 0.60, 0.67$ and 0.70 quenched from 950 °C were used to study the structure of cubic solid solution at different compositions. A similar refinement procedure was implemented to that described in section 6.3.1. The comparison of final structural refinement results is summarised in table 6.5.

The main structural result for these compositions is that there is a decrease and increase in occupancy at Mg1 (24*d*) and Mn3 (32*f*) sites, respectively with decreasing x . The 32*f*-site corresponds to the new tetrahedral site that was initially unoccupied in the stoichiometry Mg₆MnO₈. The Mn2 (4*a*) and O1 (8*c*) sites remain fully occupied, although O1 shows an increase in thermal parameters with decreasing x which may indicate that this site becomes less than fully occupied as shown at $x = 0.50$ and 0.60 . However, subsequent refinement check of the U_{iso} at these two compositions showed that O1 is still fully occupied. The O2 (24*e*) site shows a decrease in occupancy with decreasing x .

Poor fits between the observed and calculated data (figure 6.5) were obtained for all compositions which worsened with decreasing x . This was particularly shown by the poor fit of peaks (311) and (440). A disorder might exist since the Mg1 and Mn3 are partially occupied. However, attempts to refine the possibility of site exchange were not

feasible since there are three occupancy variables available at any one site, Mg, Mn and vacancy.

Two possible compensation mechanisms (6.1) and (6.2) were initially expected for $x < 0.67$ and $x > 0.67$, respectively. Neither mechanism would explain the observed reduction in oxygen occupancies. However, a reduction in cation:anion ratio could only be observed in mechanism (6.2), assuming that the oxygen is fully occupied.

A decrease and increase in occupancy of Mg1 and Mn3 are expected with decreasing x , respectively, although the refined values does not satisfy either of the proposed mechanisms. The decrease in oxygen occupancy with decreasing x could probably be associated with either an increase in number of cation vacancies or increase in number of reduced Mn oxidation states, both of which referred to mechanisms (6.2) and (6.1), respectively.

The highest O2 vacancy was observed at composition $x = 0.50$. It has been reported ^[6-8] that at this composition, an oxygen-deficient cubic structure may form after heat treatment between 600 and 1000 °C. A similarity exists between the refined occupancy of O2 and literature, which shows an oxygen non-stoichiometry, $\text{MgMnO}_{3-\delta}$, despite having inconclusive Mg:Mn ratio.

Table 6.5 Comparison of final structure refinement results of cubic solid solution with varying Mg content, $x = 0.50, 0.60, 0.67, 0.70$ and 0.80 quenched from $950\text{ }^{\circ}\text{C}$ into liquid nitrogen

			$x = 0.50$	$x = 0.60$	$x = 0.67$	$x = 0.70$	$x = 0.80$	
1	Mg1	24d	Occupancy	0.541 (4)	0.592 (4)	0.654 (5)	0.697 (5)	0.910 (5)
			$100 \times U_{iso} (\text{\AA}^2)$	2.500	2.500	2.500	2.500	2.500
2	Mn2	4a	Occupancy	1.000	1.000	1.000	1.000	1.000
			$100 \times U_{iso} (\text{\AA}^2)$	0.88 (8)	0.92 (7)	0.76 (9)	0.76 (7)	0.48 (5)
3	Mn3	32f	Occupancy	0.150 (2)	0.120 (1)	0.103 (1)	0.089 (1)	0.047 (1)
			$100 \times U_{iso} (\text{\AA}^2)$	2.500	2.500	2.500	2.500	2.500
			x	0.3735 (5)	0.3738 (6)	0.3725 (7)	0.3735 (8)	0.367 (1)
			y	0.3735 (5)	0.3738 (6)	0.3725 (7)	0.3735 (8)	0.367 (1)
			z	0.3735 (5)	0.3738 (6)	0.3725 (7)	0.3735 (8)	0.367 (1)
4	O1	8c	Occupancy	1.000	1.000	1.000	1.000	1.000
			$100 \times U_{iso} (\text{\AA}^2)$	3.0 (2)	2.9 (2)	2.3 (2)	1.9 (2)	0.3 (2)
5	O2	24e	Occupancy	0.637 (7)	0.691 (7)	0.736 (7)	0.780 (7)	0.975 (7)
			$100 \times U_{iso} (\text{\AA}^2)$	2.500	2.500	2.500	2.500	2.500
			x	0.2262 (8)	0.2284 (7)	0.2313 (7)	0.2313 (6)	0.2318 (4)
			$a (\text{\AA})$	8.3740 (3)	8.3800 (3)	8.3812 (4)	8.3781 (3)	8.3815 (2)
			$V (\text{\AA}^3)$	587.23 (7)	588.47 (7)	588.73 (7)	588.28 (6)	588.81 (4)
			χ^2	4.52	3.02	5.89	2.20	2.34
			R_p	6.91%	6.33%	7.90%	5.92%	5.44%
			R_{wp}	9.59%	8.25%	10.37%	7.64%	7.31%

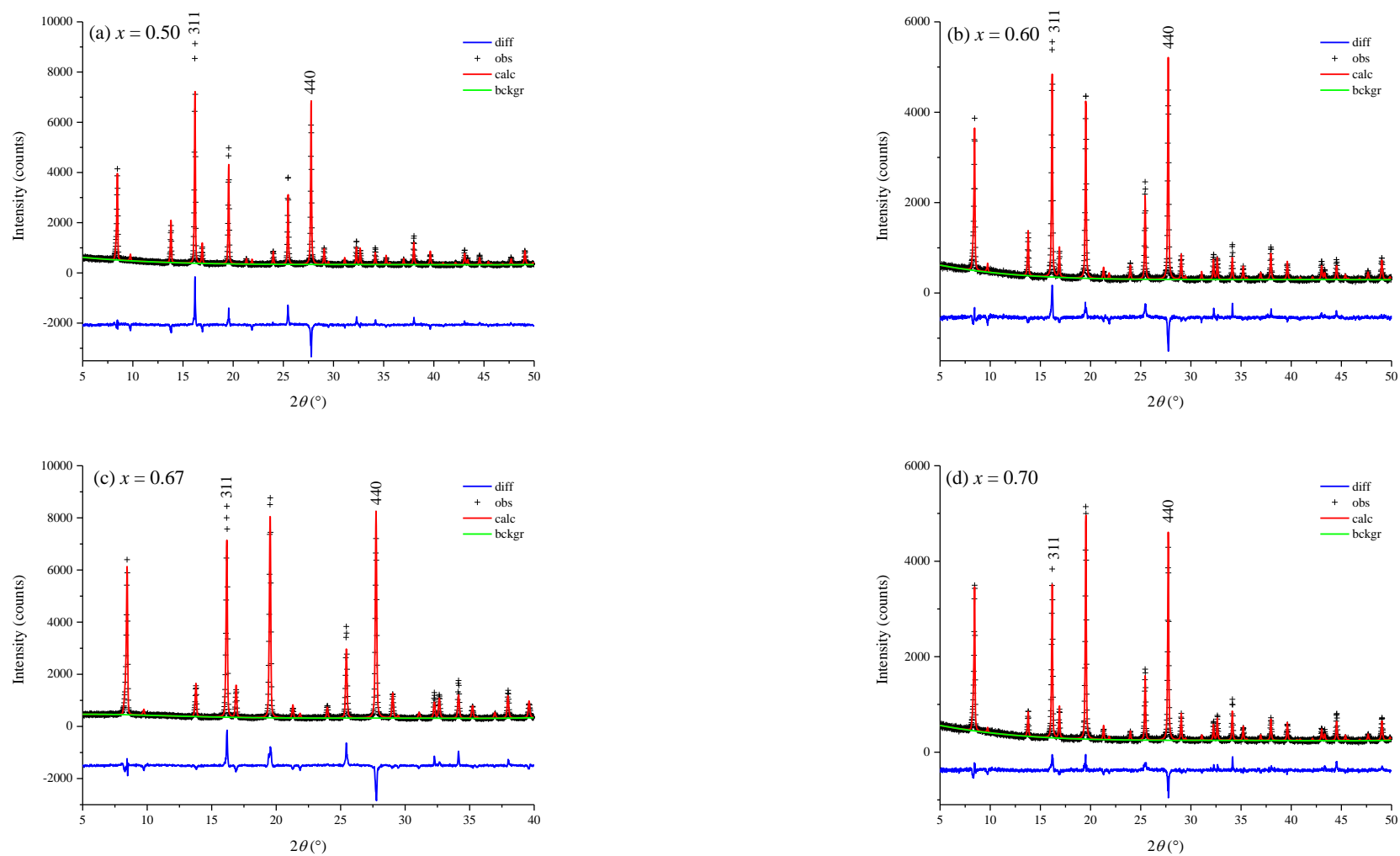


Figure 6.5 Rietveld refinement data for observed (obs), calculated (calc) and difference (diff) profile for $x = 0.50$, 0.60 , 0.67 and 0.67 quenched from $950\text{ }^{\circ}\text{C}$ into liquid nitrogen

Table 6.6 Refined chemical compositions, cation:anion ratio comparison, and the expected cation:anion ratio from the two possible compensation mechanisms

	$x = 0.50$	$x = 0.60$	$x = 0.67$	$x = 0.70$	$x = 0.80$
Mg	13.0	14.2	15.7	16.7	21.8
Mn	8.8	7.8	7.3	6.8	5.5
O	23.3	24.6	25.7	26.7	31.4
cation:anion (oxygen non- stoichiometry)	0.93 : 1	0.90 : 1	0.90 : 1	0.88 : 1	0.87 : 1
cation:anion (Expected from (6.2))	0.67 : 1	0.71 : 1	0.75 : 1	0.77 : 1	0.83 : 1
cation:anion (Expected from (6.1))	0.88 : 1	0.88 : 1	0.88 : 1	0.88 : 1	0.88 : 1

6.4 Conclusions

The C2 cubic solid solution can be indexed on XRD data by using either $Fd\bar{3}m$ or $Fm\bar{3}m$ space groups. However, ND data on compositions $x = 0.50$ and 0.67 showed additional peaks (200), (420) and (640) which were initially unobserved in the XRD patterns. Since, the appearance of these additional peaks does not satisfy the rule of reflections to be observed for $Fd\bar{3}m$ space group, the cubic solid solution was therefore assigned to space group $Fm\bar{3}m$.

Structural analysis was carried out using Mg_6MnO_8 as starting model. A new tetrahedral $32f$ -site (assigned to Mn3) was found to be partially occupied and its occupancy increased with decreasing x . At the same time, the occupancies of Mg1 (24d) and O2 (24e) decreased with decreasing x . Therefore, for any given composition over the range $0.50 \leq x \leq 0.80$, these three sites are always partially occupied.

The refinement results showed poor fits between the observed and calculated data and worsened with decreasing x . This indicated that there is a possibility of structural disorder as a result of site exchange between Mg1 and Mn3 as both of these sites are partially occupied. The disorder increased with decreasing x , probably due to the increase in cation vacancies, cation interstitials and anion vacancies. It is impossible to refine Mg1

and Mn³⁺ due to the presence of three occupancy variables: Mg, Mn and vacancy. Hence, the Mg:Mn ratio could not be determined conclusively.

The increase in O₂ vacancy was observed with decreasing x , to a maximum at $x = 0.50$. The refined O₂ occupancy at this composition is similar to that reported for oxygen-deficient cubic MgMnO_{3- δ} [6-8].

6.5 References

1. Garg, N., K.V. Ramanujachary, S.E. Lofland, and A.K. Ganguli, *Nanostructured dimagnesium manganese oxide (Spinel): Control of size, shape and their magnetic and electro catalytic properties*. Journal of Solid State Chemistry, 2013. **197**: p. 392-397.
2. Kasper, J. and J. Prener, *The crystal structure of Mg₆MnO₈*. Acta Crystallographica, 1954. **7**(3): p. 246-248.
3. Hahn, T. and H. Wondratschek, *Symmetry of crystals: Introduction to International Tables for Crystallography Vol. A*. Acta Cryst, 1997. **53**: p. 252.
4. West, A.R., *Solid state chemistry and its applications*. 2014: John Wiley & Sons.
5. ICDD (2018) and PDF-4+ 2019 (Database), *International Centre for Diffraction Data*. Newtown Square, Pennsylvania, USA, edited by Dr. Soorya Kabekkodu, 2018.
6. Chamberland, B., A. Sleight, and J. Weiher, *Preparation and characterization of MgMnO₃ and ZnMnO₃*. Journal of Solid State Chemistry, 1970. **1**(3-4): p. 512-514.
7. Arjomand, M. and D. Machi, *The preparation and magnetic properties of ternary oxides ABO₃ (A= alkaline earth metal, B= Ti, Zr, Mn, Fe, Co) and quaternary oxides ATi_{1-x}(Zr_{1-x})B_xO₃*. Journal of the Less Common Metals, 1978. **61**(1): p. 133-149.
8. Pavlyuchkov, D., D. Dilner, G. Savinykh, and O. Fabrichnaya, *Phase equilibria in the ZrO₂-MgO-MnO_x system*. Journal of the American Ceramic Society, 2016. **99**(9): p. 3136-3145.

Chapter 7: Electrical properties of tetragonal polymorphs (T1 and T2) and C2 cubic solid solution

7.1 Introduction

Mn_3O_4 spinel exists in two stable structures: the low temperature distorted tetragonal structure ($T_c < \sim 1170$ °C) and the high temperature cubic structure. Doris and Mason ^[1] proposed that the electrical conductivity of Mn_3O_4 were due to disproportionation of Mn^{3+} to give a mixture with Mn^{2+} and Mn^{4+} at the octahedral site. Metselaar *et al.* ^[2] reported that the conductivity was due to the presence of impurities (Cu, Mg, Fe, Al and Si) in the sample. Keller and Dieckmann ^[3] showed that a small oxygen non-stoichiometry might have minimal effect on the electrical properties.

Driessens ^[4] reported that any disproportionation of a solid solution into a two-phase mixture is a slow process and the formation of a single metastable phase is possible, when quenching from a high temperature. This would contradict the conduction model proposed by Doris and Mason ^[1] as there was no evidence of a metastable phase formation for Mn_3O_4 upon quenching from 1000 to 1300 °C (section 4.5.1). In fact, the high temperature quenched phase resembles the Mn_3O_4 tetragonal structure.

The electrical properties of tetragonal and cubic spinel MgMn_2O_4 have been investigated by several authors. Rosenberg and Nicolau ^[5] proposed that the conductivity was attributed to the presence of mixed valency of Mn^{3+} and Mn^{4+} on the octahedral site (due to site exchange). Malavasi *et al.* ^[6] reported that the conductivity could be due to both the site exchange (led by a disproportionation of Mn^{3+} ions) and oxygen non-stoichiometry with the latter playing a minor role in the conductivity. Keer *et al.* ^[7] also reported that the conductivity was dependent on the number of Mn^{3+} - Mn^{4+} pairs present on the octahedral site due to extrinsic dopant but without any disproportionation reaction.

The inversion process occurs when there is a partial site exchange between cations on the tetrahedral and octahedral sites. In the case of MgMn_2O_4 , it was suggested that a small number Mg^{2+} ions migrated from the tetrahedral to octahedral site. The presence of

Mg^{2+} ions on the octahedral site appears to trigger a disproportionation process of two Mn^{3+} to give Mn^{2+} and Mn^{4+} . The same number of Mn^{2+} ions then migrated to the tetrahedral site. Since inversion is a slow process, there is also a possibility that the cations are in their “frozen-in” states even during a slow-cooling. This may result in conductivity dependency on the cooling rate.

The oxygen non-stoichiometry in $\text{MgMn}_2\text{O}_{4-\delta}$ would result in a partial reduction of Mn^{3+} to Mn^{2+} for electroneutrality. The presence of mixed valency of Mn thus creates a pathway for electrons or holes hopping which results in electronic conduction.

However, there are few reports on the electrical properties of Mg_2MnO_4 and Mg_6MnO_8 . Similar to Li_2MnO_3 , the Mn ions in these compositions are ideally in tetravalent states and highly unlikely to be oxidised to Mn^{5+} .

In this chapter, we investigate the electrical property variations in the T1, T2 and C2 cubic solid solution, to determine their relationship with the crystal structure.

7.2 Experimental

In order to study the effect of composition on the conductivity of the T1 phase, pellets of $x = 0.05, 0.10$ and 0.20 of $\text{Mg}_x\text{Mn}_{1-x}\text{O}_\delta$ were heated at $900\text{ }^\circ\text{C}$ for 10 h and slowly cooled in the muffle furnace to room temperature. InGa electrodes were printed on these pellets and the impedance data were collected using Solartron Modulab analyser with 100 mV of AC, in the frequency range of 10^{-2} to 10^6 Hz, within temperature range from room temperature to $300\text{ }^\circ\text{C}$. At the end of the measurement, the InGa electrodes were removed from the pellets with acetone.

The same pellet of composition $x = 0.20$ was then used to study the effect of annealing temperature on conductivity. The pellet was heated at $700\text{ }^\circ\text{C}$ for 10 h and quenched into liquid nitrogen. Similar steps as described above were implemented starting from the application of InGa electrode, the impedance measurements and the removal of electrode from the pellet. The steps were repeated at two additional quench

temperatures of 900 and 1050 °C. The pellet quenched from 1050 °C, represented the T2 phase (figure 4.6).

Two additional pellets of $x = 0.33$ and 0.40 were prepared in order to study the effect of composition of T2 on conductivity. The pellets were heated at 1050 °C for 10 h and quenched into liquid nitrogen. The impedance data were collected using the same Solartron Modulab analyser.

To investigate the effect of composition on the electrical properties of C2 cubic solid solution, pellets of $x = 0.50, 0.60, 0.70$ and 0.80 were prepared. The pellets were heated at 1000 °C and quenched into liquid nitrogen.

7.3 Electrical properties of tetragonal spinel polymorphs

7.3.1 Effect of composition on conductivity of slow-cooled T1 polymorph

Impedance spectroscopy was conducted on samples of $x = 0.05, 0.10$ and 0.20 . The pellets were heated at 900 °C for 10 h and slowly cooled to room temperature.

The impedance complex plane, Z^* plots of $x = 0.05, 0.10$ and 0.20 with their respective spectroscopic Y' , C' and $-Z''$, M'' plots at two temperatures are shown in figure 7.1, figure 7.2, and figure 7.3 respectively.

The Z^* plots for all samples show similar characteristics. A single semicircle was observed which could be attributed to the bulk response. The resistance of the samples decreased with increasing temperature as shown by the low frequency intercept on the Z' axis. The absence of a low frequency spike in the Z^* plots could indicate that the mobile charge carrier is dominated by electronic conduction.

The Y' plots against frequency for all samples show a single plateau, followed by a dispersion at a higher frequency. This high frequency dispersion could be associated with a Jonscher power law behaviour.

The C' plots as a function of frequency show a similar pattern with a plateau observed at high frequency of $\sim 10^{-12} \text{ F cm}^{-1}$ attributed to the bulk response, followed by a large and noisy dispersion at lower frequency.

The Z'' and M'' versus frequency plots show overlapping peak maxima of Z'' and M'' at a higher frequency indicating a good electrical homogeneity of the samples.

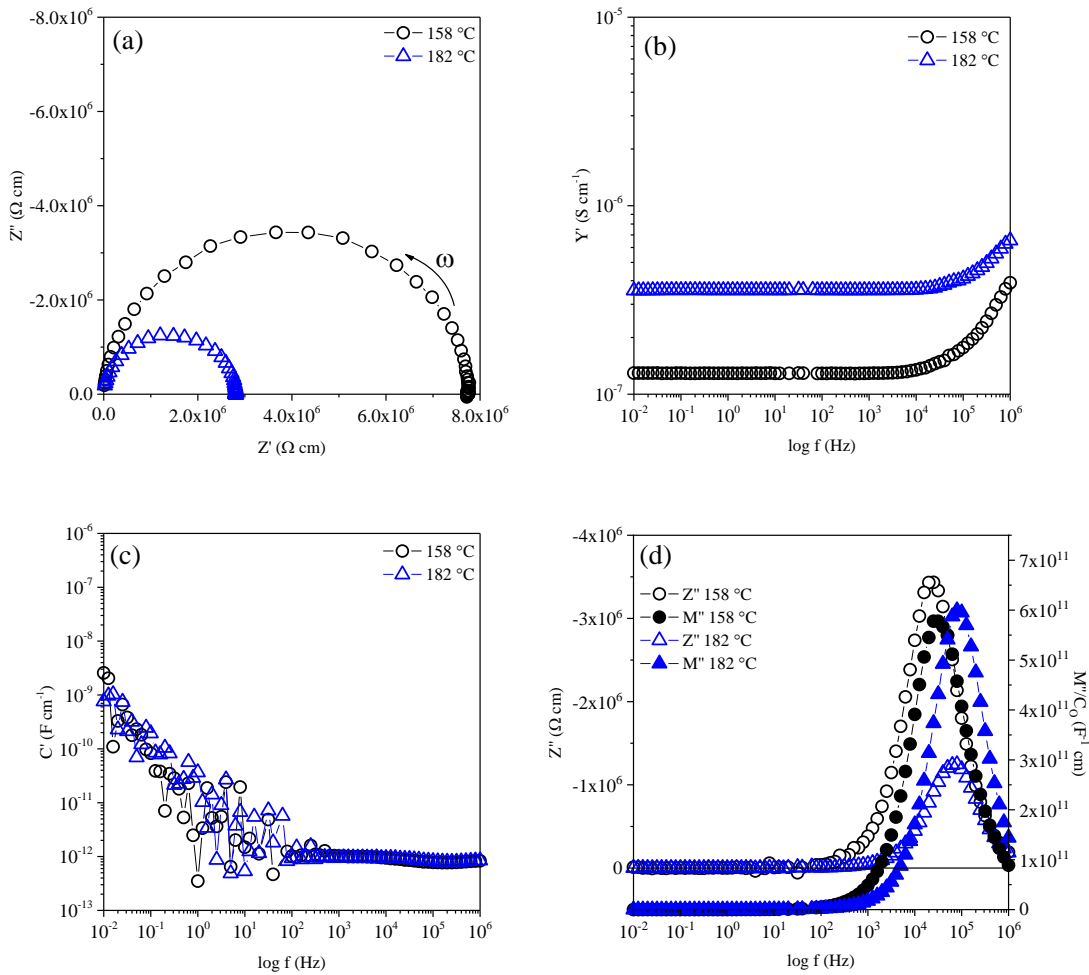


Figure 7.1 A slow-cooled sample of T1 from 900 °C: $x = 0.05$,
 (a) Impedance complex plane, Z^* plots and spectroscopic plots (b) Y' , (c) C' ,
 (d) $-Z''$ and M'' at 158 °C and 182 °C

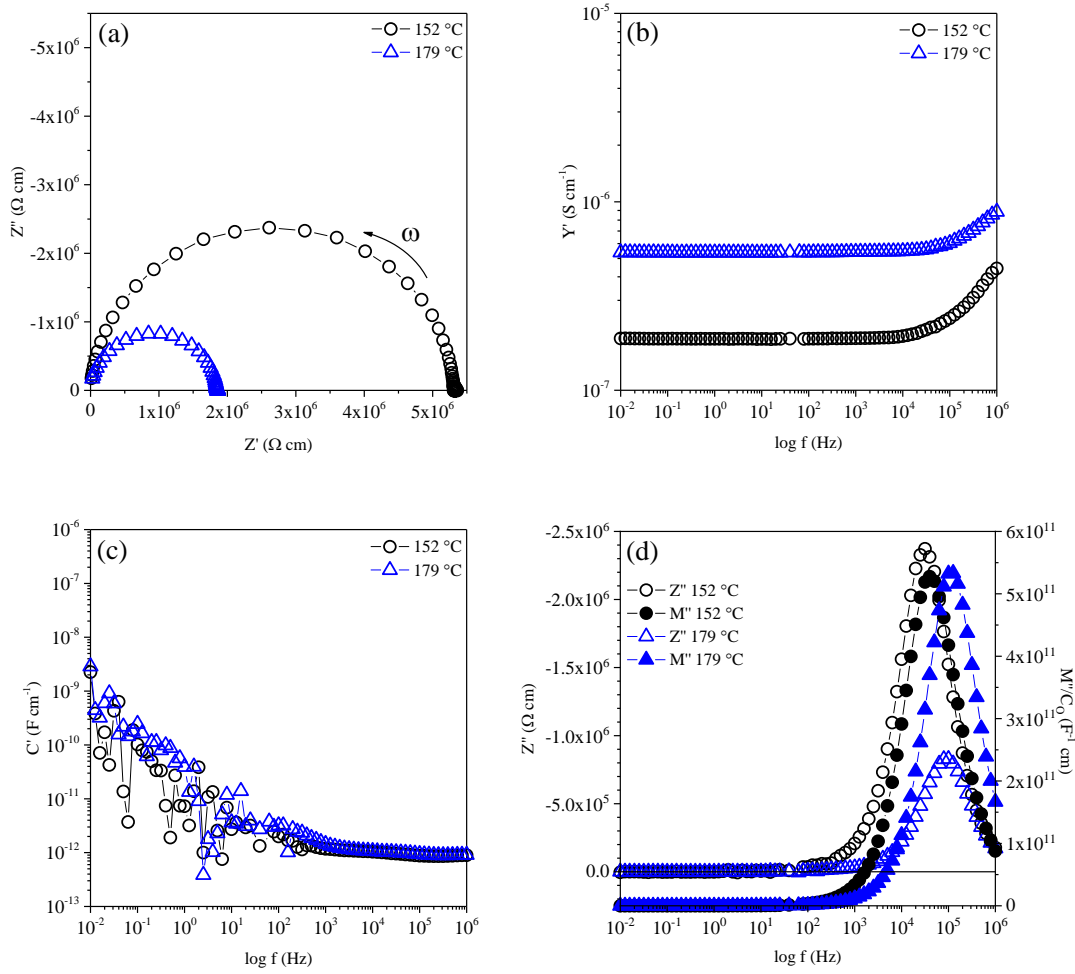


Figure 7.2 A slow-cooled sample of T1 from 900 °C: $x = 0.10$,
 (a) Impedance complex plane, Z^* plots and spectroscopic plots (b) Y' , (c) C' ,
 (d) $-Z''$ and M'' at 152 °C and 179 °C

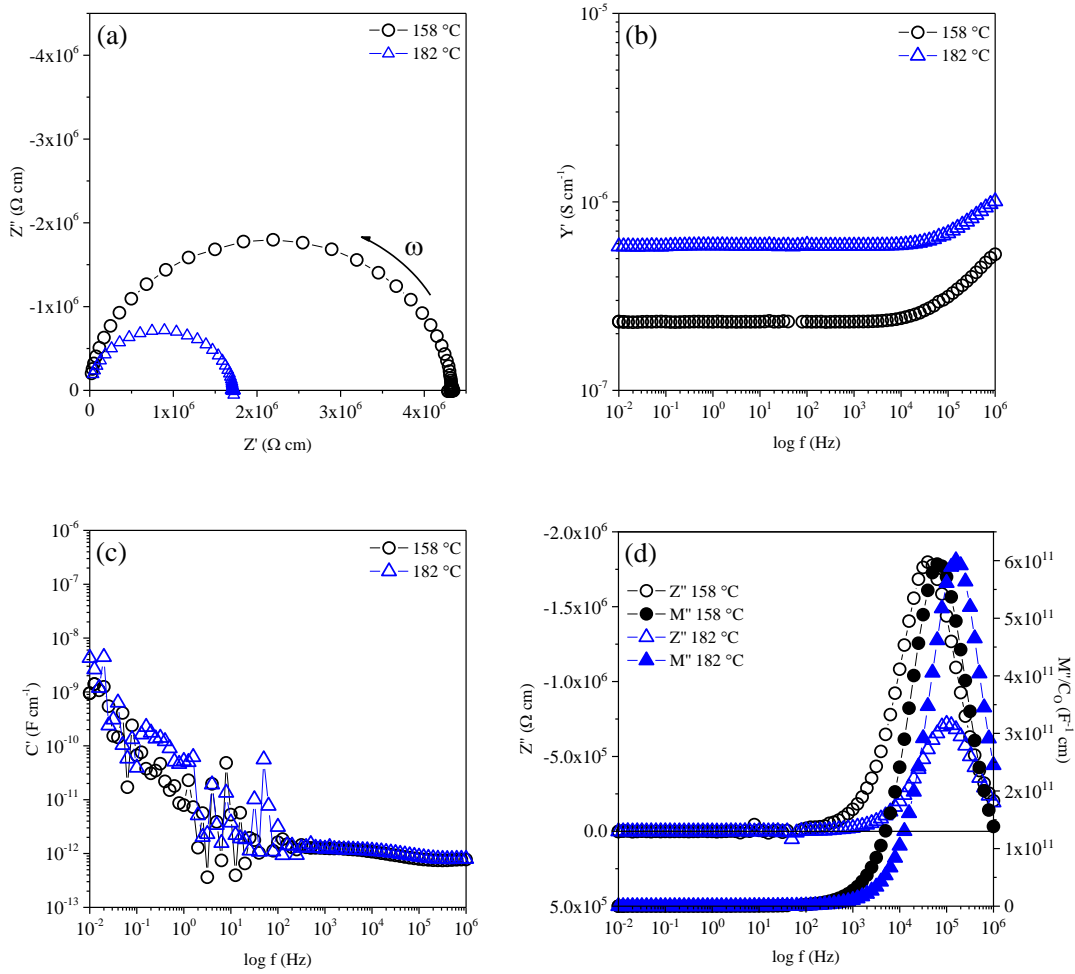


Figure 7.3 A slow-cooled sample of T1 from 900 °C: $x = 0.20$,
 (a) Impedance complex plane, Z^* plots and spectroscopic plots (b) Y' , (c) C' ,
 (d) $-Z''$ and M'' at 158 °C and 182 °C

The Arrhenius plots (figure 7.4) show three linear parallel lines overlapping each other. The conductivity of the slow-cooled T1 samples of $x = 0.05$, 0.10 and 0.20 are similar, within errors, with activation energy of 0.662 ~ 0.687 eV. At room temperature, it is expected that the conductivities of these samples are $\sim 7.7 \times 10^{-12} \text{ S cm}^{-1}$ (extrapolated).

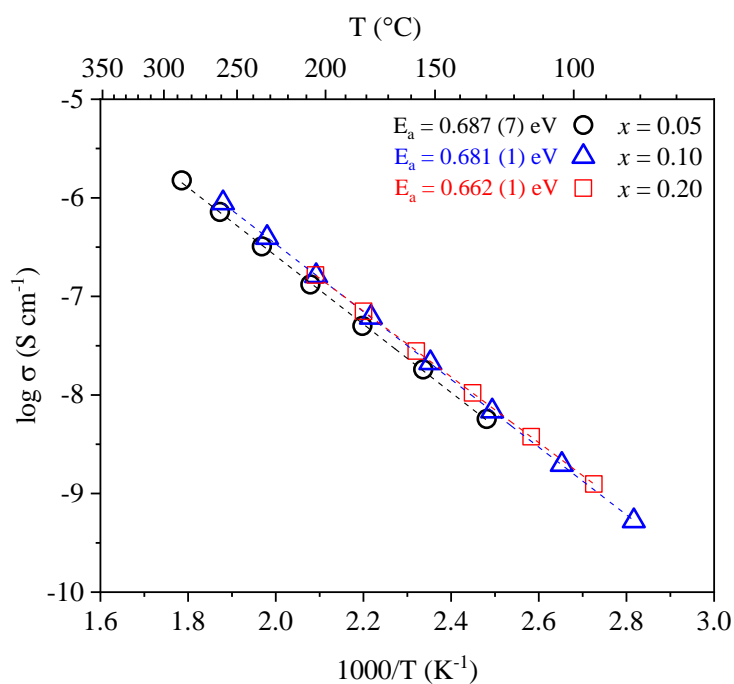


Figure 7.4 Arrhenius plots of T1: $x = 0.05$, 0.10 and 0.20 for slow-cooled samples with their respective activation energy, E_a

7.3.2 Effect of temperature on conductivity of $x = 0.20$ $\text{Mg}_x\text{Mn}_{1-x}\text{O}_8$

Impedance spectroscopy was conducted on a sample of $x = 0.20$. The pellet was heated for 10 h and quenched from 700, 900 and 1050 °C into liquid nitrogen. The electrical properties were measured after each quench.

The impedance complex plane, Z^* plots of $x = 0.20$ with their respective spectroscopic Y' , C' and $-Z''$, M'' plots are shown in figure 7.5 (700 °C), figure 7.6 (900 °C), and figure 7.7 (1050 °C) respectively.

The Z^* plots for samples quenched from 700 and 900 °C show similar characteristics with the slow-cooled sample. A single semicircle was observed which could be attributed to the bulk response. However, the sample quenched from 1050 °C shows two arcs which could be attributed to the grain boundary and bulk response at low and high frequency respectively. Again, no low frequency spike was observed at these quenched temperatures which could be associated with the ionic conduction. Therefore, the conductivity was dominated by electronic conduction.

The Y' plots against frequency for samples quenched from 700 and 900 °C show a single plateau, followed by a dispersion at a higher frequency. However, for sample quenched at 1050 °C, two nearly similar plateaus were observed at low and intermediate frequency. High frequency dispersions were observed for data collected at 23 and 44 °C but a small lower frequency dispersion was observed only at 44 °C.

The C' plots as a function of frequency show a similar pattern to the slow-cooled sample. A single plateau was observed at high frequency attributed to the bulk response, followed by a large and noisy dispersion at a lower frequency. For the sample quenched from 1050 °C, two plateaus were observed at high and intermediate frequency attributed to the bulk ($\sim 10^{-12}$ F cm^{-1}) and grain boundary ($\sim 10^{-9}$ F cm^{-1}) response respectively. The low frequency capacitance of $10^{-7} \sim 10^{-8}$ F cm^{-1} may be attributed to the sample-electrode interface response.

The Z'' and M'' *versus* frequency plots for samples quenched from 700 and 900 °C show overlapping peak maxima of Z'' and M'' at a higher frequency indicating a good

electrical homogeneity of the samples. However, for the sample quenched at 1050 °C, two peaks were observed for Z'' with the small intermediary frequency peak attributed to the grain boundary response.

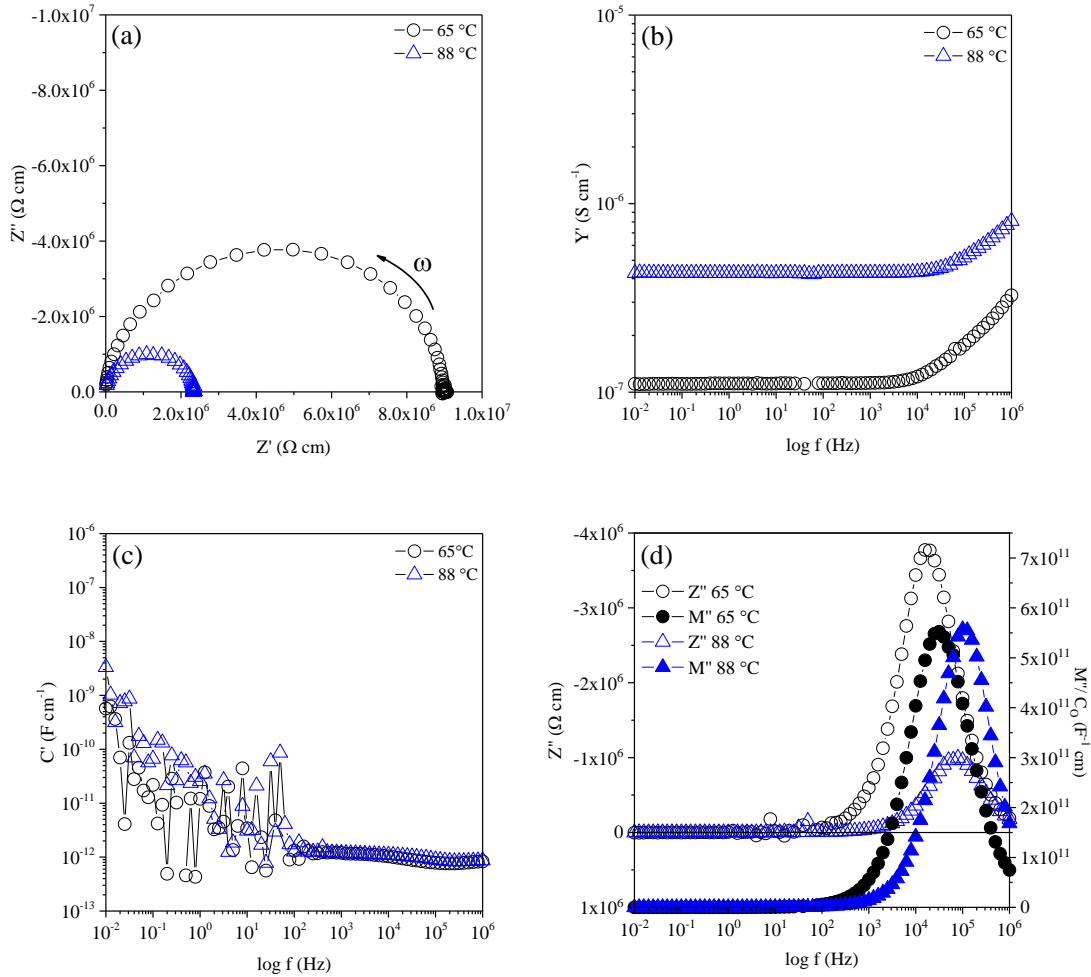


Figure 7.5 A quenched sample of T1 at 700 °C: $x = 0.20$,
 (a) Impedance complex plane, Z'' plots and spectroscopic plots (b) Y' , (c) C' ,
 (d) $-Z''$ and M'' at 65 °C and 88 °C

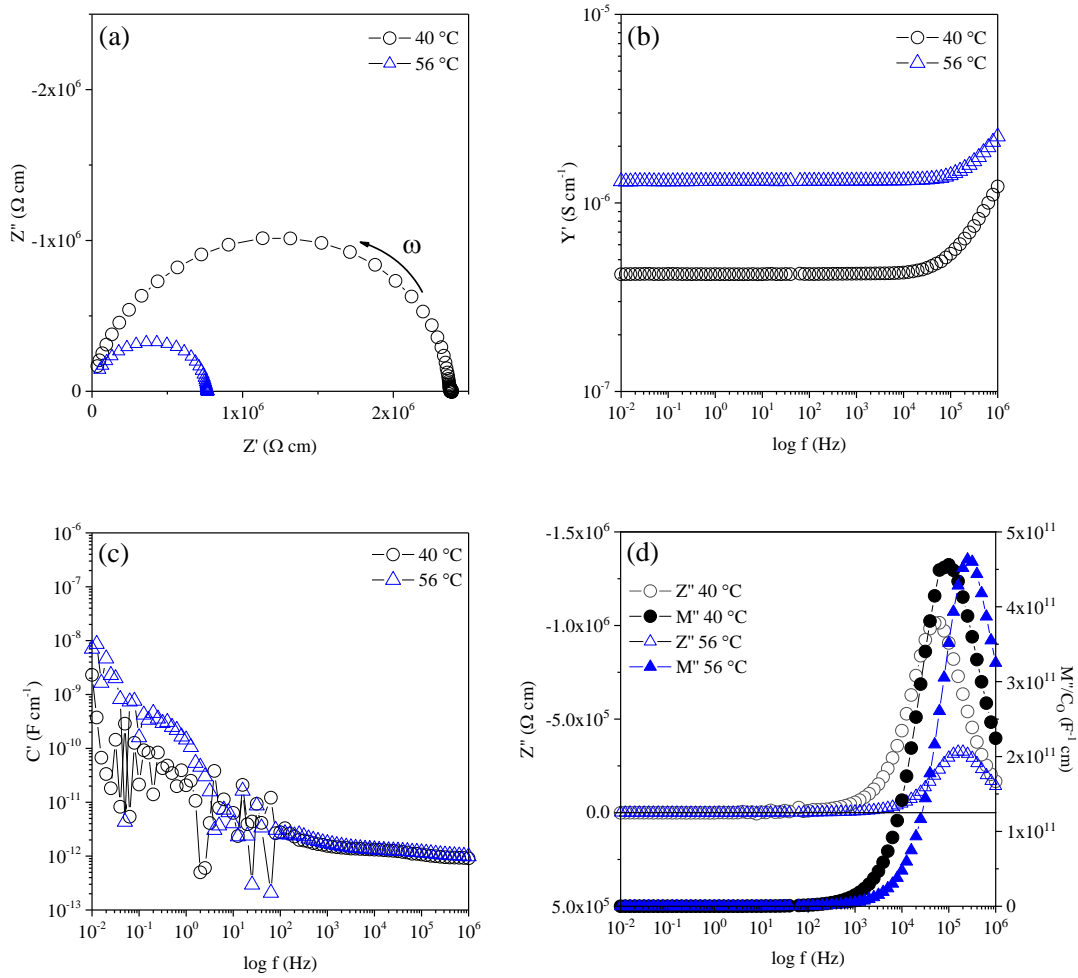


Figure 7.6 A quenched sample of T1 at 900 °C: $x = 0.20$,
 (a) Impedance complex plane, Z^* plots and spectroscopic plots (b) Y' , (c) C' ,
 (d) $-Z''$ and M'' at 40 °C and 56 °C

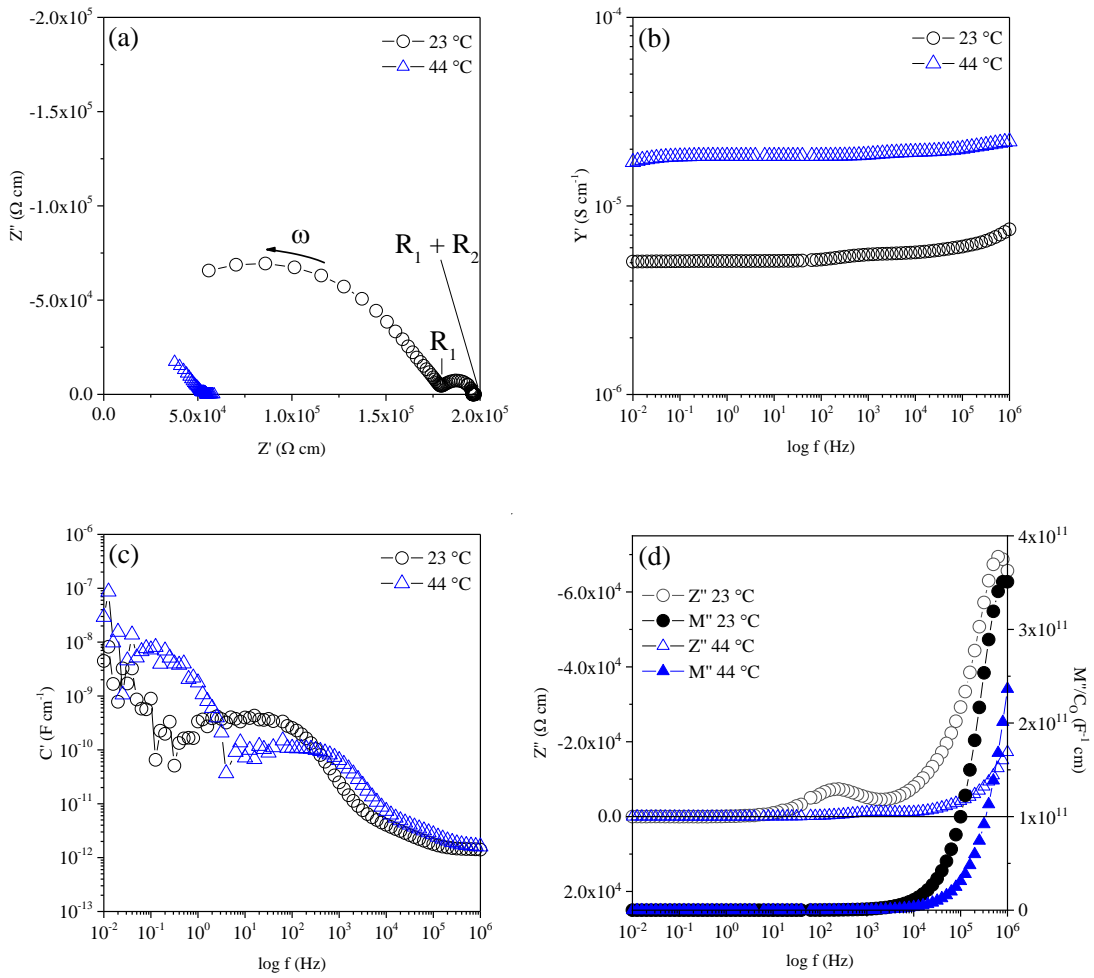


Figure 7.7 A quenched sample of T2 at 1050 °C: $x = 0.20$,
 (a) Impedance complex plane, Z^* plots and spectroscopic plots (b) Y' , (c) C' ,
 (d) $-Z''$ and M'' at 23 °C and 44 °C

The Arrhenius plots (figure 7.8) show a linear behaviour for all samples. The slow-cooled sample has the lowest conductivity with activation energy of 0.662 (1) eV. The conductivity for the quenched samples increased within the temperature range 20 to 200 °C with increasing quench temperature. A small reduction in activation energy was observed from 0.662 (1) to 0.44 (1) eV with increasing quench temperature, although the samples quenched from 700 and 900 °C showed a relatively similar value of 0.56 ~ 0.59 eV, within errors.

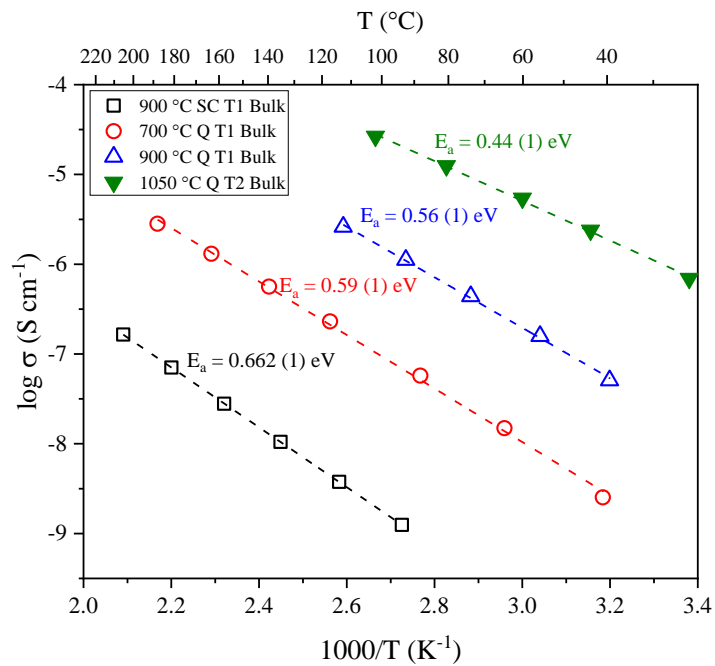


Figure 7.8 Arrhenius plots of $x = 0.20$ for slow-cooled (SC) in air from 900 °C and quenched (Q) samples for T1 at 700 and 900 °C, and T2 at 1050 °C with their respective activation energy, E_a

7.3.3 Effect of composition on conductivity of T2 polymorph

Impedance spectroscopy was conducted on samples of $x = 0.33$ and 0.40 . The pellets were heated at $1050\text{ }^{\circ}\text{C}$ for 10 h and quenched into liquid nitrogen.

The Z^* plot of $x = 0.33$ and 0.40 with their respective spectroscopic Y' , C' and Z'' , M'' plots at two temperatures are shown in figure 7.9, and figure 7.10 respectively.

The Z^* plots for both samples show similar characteristics to $x = 0.20$ quenched from $1050\text{ }^{\circ}\text{C}$ (figure 7.7). Two semicircles were observed which could be attributed to the grain boundary and bulk response at low and high frequency respectively.

The Y' plots against frequency for both samples show two nearly similar plateaux at low and intermediate frequency. A small dispersion at high frequency was observed for $x = 0.33$, for data collected at $22\text{ }^{\circ}\text{C}$ but a small lower frequency dispersion was observed for $x = 0.40$, for data collected at $44\text{ }^{\circ}\text{C}$. With increase in temperature, the high frequency dispersion is shifted-out of the measured window whereas the low frequency dispersion shifted-in.

The C' plots as a function of frequency show two plateaux at high and intermediate frequency attributed to the bulk ($\sim 10^{-12}\text{ F cm}^{-1}$) and grain boundary ($\sim 10^{-9}\text{ F cm}^{-1}$) response respectively. The low frequency capacitance of $10^{-6} \sim 10^{-7}\text{ F cm}^{-1}$ may be attributed to the sample-electrode interface response.

The Z'' and M'' *versus* frequency plots for both samples does not show the overlapping peak maxima of Z'' and M'' since it is shifted out of the measured windows. However, a small peak was observed for Z'' at intermediate frequency which could be attributed to the grain boundary response.

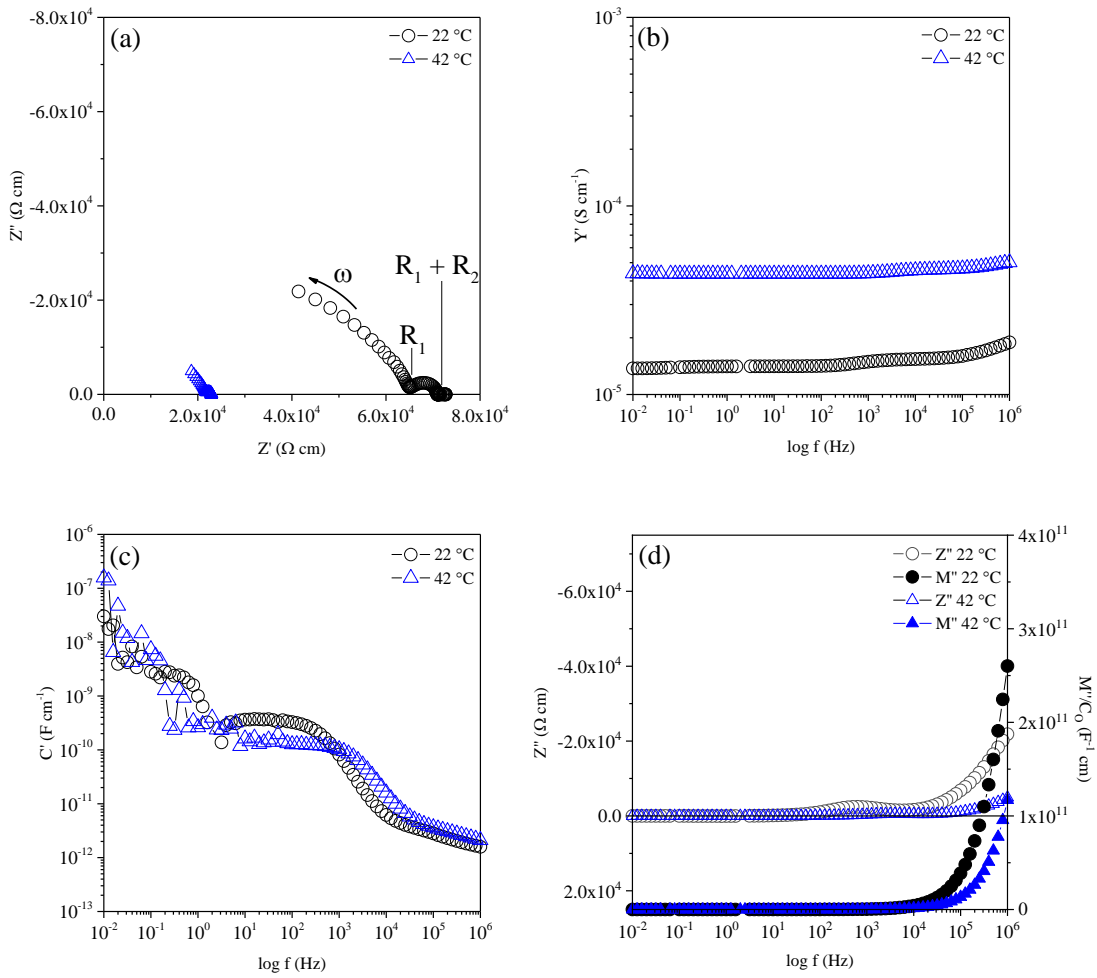


Figure 7.9 A quenched sample of T2 at 1050 °C: $x = 0.33$,
 (a) Impedance complex plane, Z^* plots and spectroscopic plots (b) Y' , (c) C' ,
 (d) $-Z''$ and M'' at 22 °C and 42 °C

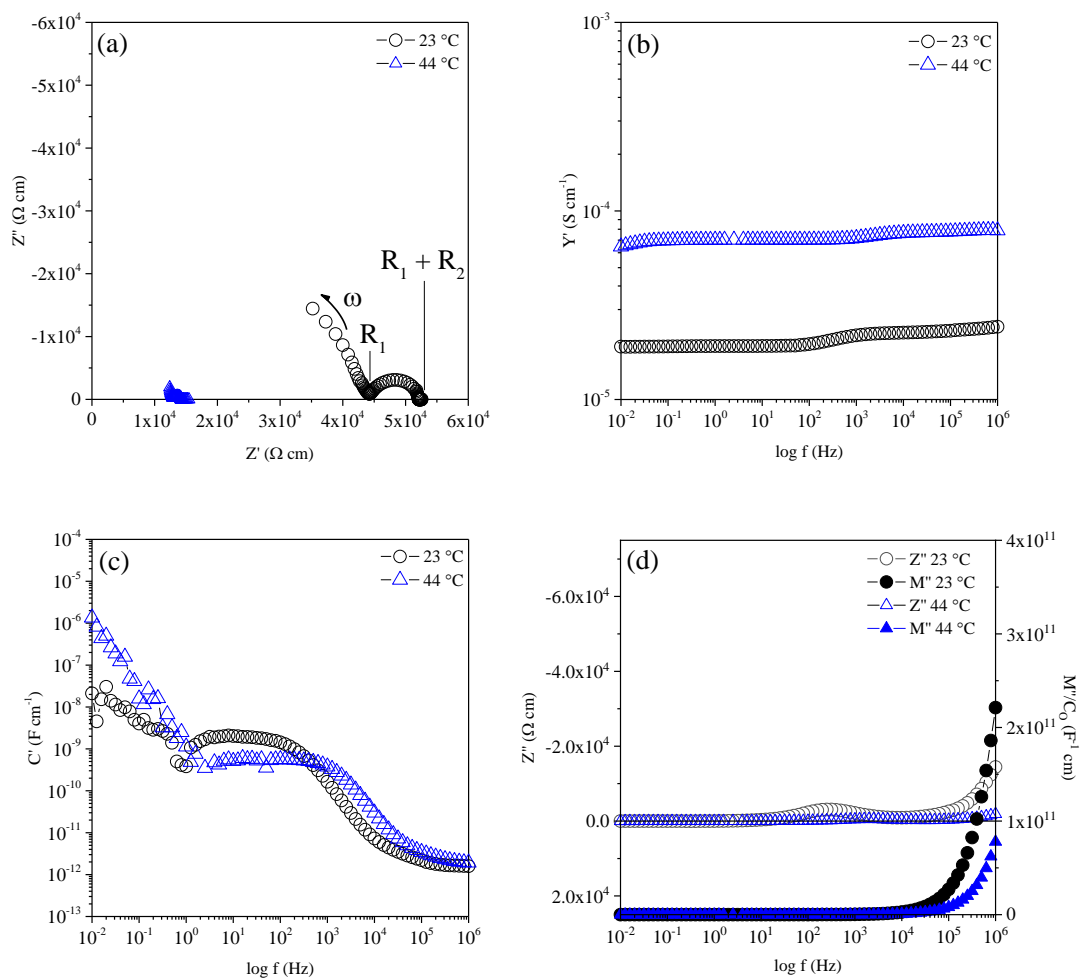


Figure 7.10 A quenched sample of T2 at 1050 °C: $x = 0.40$,
 (a) Impedance complex plane, Z^* plots and spectroscopic plots (b) Y' , (c) C' ,
 (d) $-Z''$ and M'' at 23 °C and 44 °C

The conductivity data, $\log \sigma$ versus T^{-1} (figure 7.11) show a linear behaviour for all samples. The T2 samples of $x = 0.20, 0.33$ and 0.40 , quenched at $1050\text{ }^\circ\text{C}$, show a similar activation energy of $0.42 \sim 0.44\text{ eV}$, within errors. The conductivities for these T2 quenched samples increased with increasing x . The highest conductivity measured at room temperature is shown by $x = 0.40$ with $\sigma = 3.8 \times 10^{-6}\text{ S cm}^{-1}$ (table 7.1).

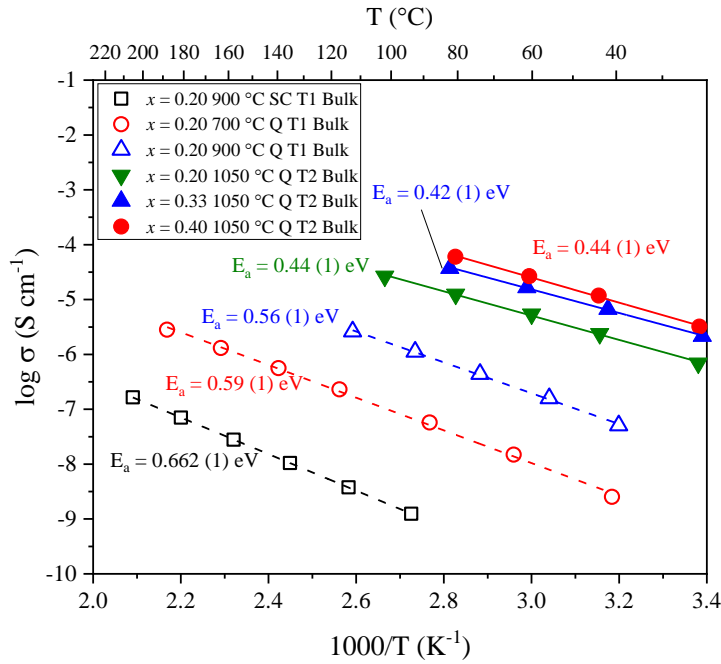


Figure 7.11 Arrhenius plots comparison between T1 and T2. T1 represented by open symbols of $x = 0.20$ at different temperatures. T2 represented by closed symbols: $x = 0.20, 0.33$ and 0.40 quenched (Q) at $1050\text{ }^\circ\text{C}$. Not shown here are the plots of slow-cooled (SC) T1 of $x = 0.05$ and 0.10 since they overlap with the slow-cooled T1 $x =$

0.20

Table 7.1 Comparison of activation energy and conductivities of $x = 0.20, 0.33$ and 0.40 . # represent extrapolated data with the assumption that the activation energy remains constant with temperature

Sample	State	Activation energy, E_a (eV)	Conductivity ($S\text{ cm}^{-1}$) at RT ($^{\circ}\text{C}$)
$x = 0.20$	Slow-cooled (T1)	0.662 (1)	7.7×10^{-12} (22°C) #
	Quenched from 700°C (T1)	0.59 (1)	7.3×10^{-10} (22°C) #
	Quenched from 900°C (T1)	0.56 (1)	1.6×10^{-8} (22°C) #
	Quenched from 1050°C (T2)	0.44 (1)	6.9×10^{-7} (23°C)
$x = 0.33$	Quenched from 1050°C (T2)	0.42 (1)	2.3×10^{-6} (22°C)
$x = 0.40$	Quenched from 1050°C (T2)	0.44 (1)	3.8×10^{-6} (23°C)

In order to identify the behaviour of the electronic conduction, the conductivity of the slow-cooled pellet $x = 0.20$ of $\text{Mg}_x\text{Mn}_{1-x}\text{O}_8$ was measured at different oxygen partial pressure ($p\text{O}_2$), O_2 ($p\text{O}_2 \sim 1$ bar) and nitrogen, N_2 ($p\text{O}_2 \sim 10^{-3}$ bar). The impedance data were collected using Impedance Gain-Phase Analyzer (SI 1260) with 100 mV of AC, in the frequency sweep of 10^{-2} to 10^6 Hz, within temperature range from room temperature to 200°C . The Z^* plots (figure 7.12) showed that the conductivity increased with increasing $p\text{O}_2$, indicating a p -type conduction behaviour.

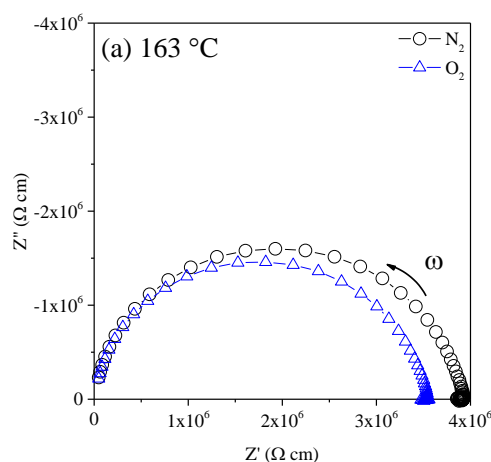


Figure 7.12 The impedance complex plane, Z^* plots of $x = 0.20$ for slow-cooled sample measured at 163°C in different atmospheres, O_2 and N_2

7.4 Electrical properties of C2 cubic solid solution

7.4.1 Effect of temperature on conductivity of $x = 0.50$ $\text{Mg}_x\text{Mn}_{1-x}\text{O}_8$

Impedance spectroscopy was conducted on a sample of $x = 0.50$. The pellet was heated for 10 h and quenched from 700, 900 and 1000 °C into liquid nitrogen. The electrical properties were measured after each quench.

The Z^* plots of $x = 0.50$ with their respective spectroscopic Y' , C' and $-Z''$, M'' plots at two temperatures are shown in figure 7.13 (700 °C), figure 7.14 (900 °C), and figure 7.15 (1000 °C).

The Z^* plots for all samples show similar characteristics. Data collected at room temperature show a single semicircle at high frequency followed by an incomplete arc at low frequency which could be attributed to the grain boundary and bulk response, respectively.

The Y' plots against frequency show two frequency independent plateaux observed at low and high frequency with a small higher frequency dispersion for data collected at room temperature.

The capacitance plots show two plateaux at high and intermediate frequency which could be attributed to the bulk and grain boundary response, followed by a noisy dispersion at a lower frequency.

The Z'' and M'' against frequency plots for all samples show a small Z'' peak at intermediate frequency which could be attributed to the grain boundary response. The overlapping peak maxima of Z'' and M'' at high frequency was shifted out of the measured window.

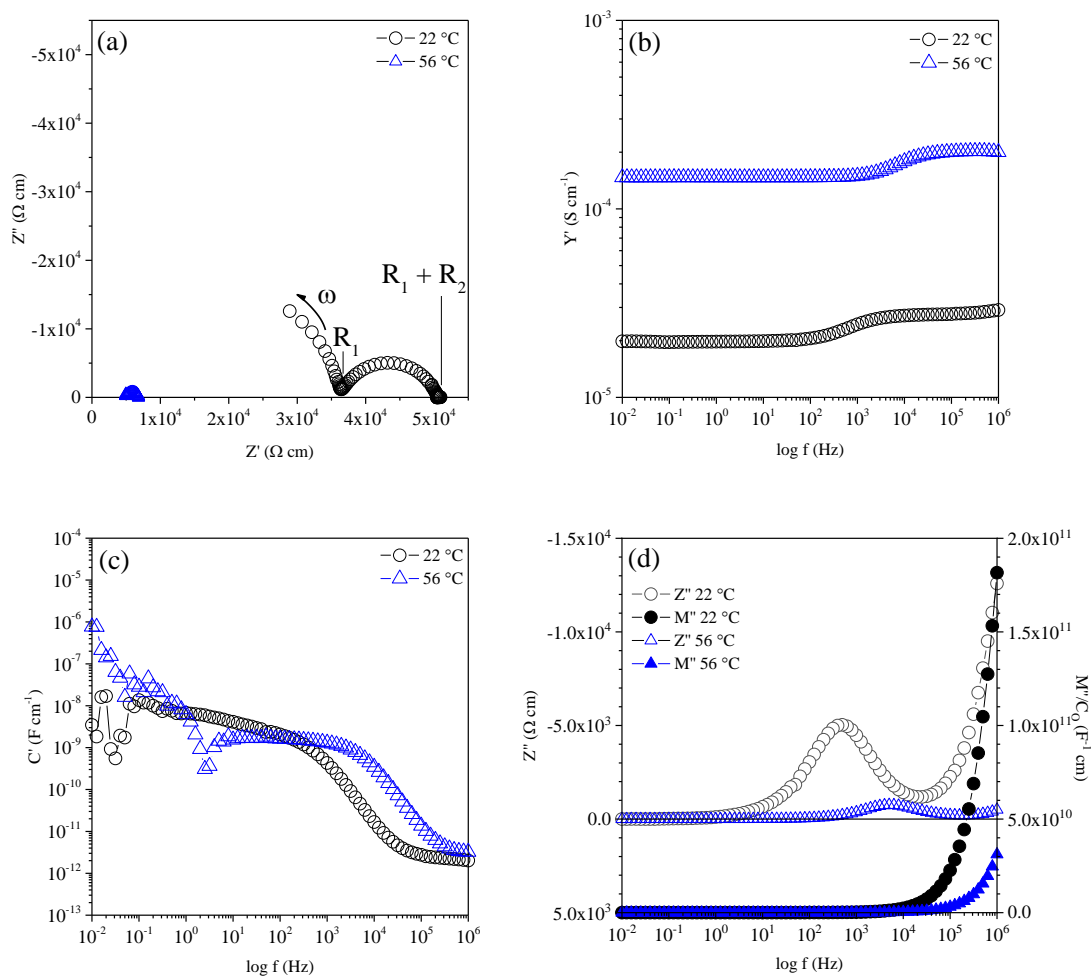


Figure 7.13 A quenched sample of $x = 0.50$ at $700\text{ }^{\circ}\text{C}$:

- (a) Impedance complex plane, Z^* plots and spectroscopic plots (b) Y' , (c) C' ,
 (d) $-Z''$ and M'' at 22 and $56\text{ }^{\circ}\text{C}$

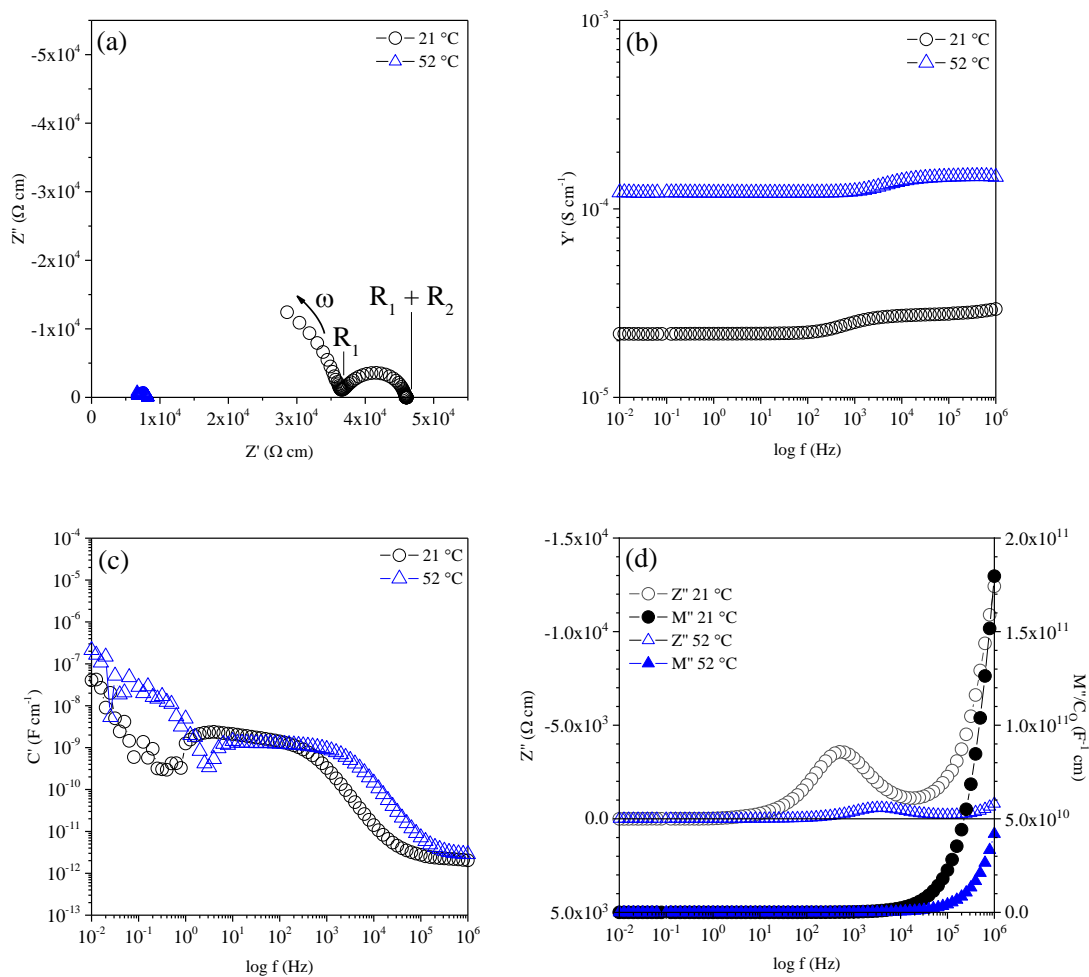


Figure 7.14 A quenched sample of $x = 0.50$ at $900\text{ }^{\circ}\text{C}$:

- (a) Impedance complex plane, Z^* plots and spectroscopic plots (b) Y' , (c) C' ,
 (d) $-Z''$ and M'' at 21 and $52\text{ }^{\circ}\text{C}$

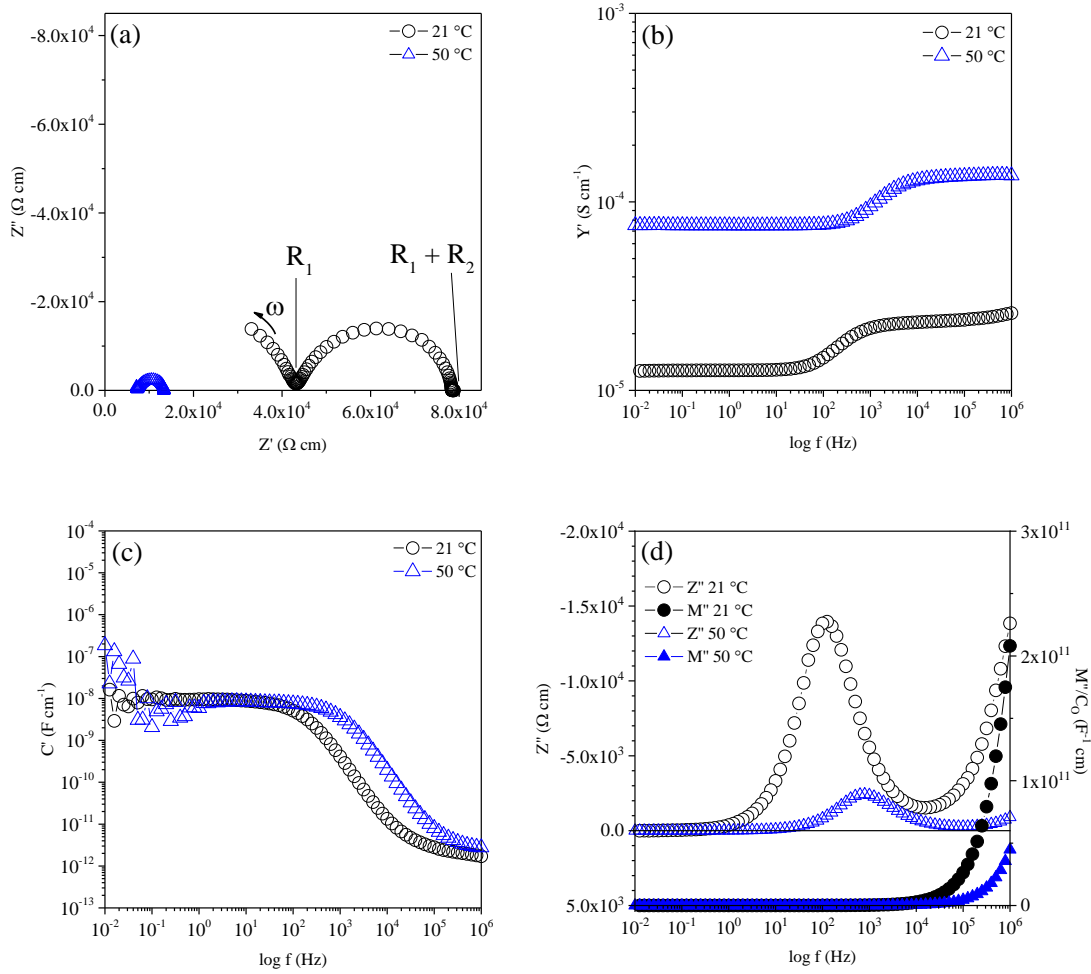


Figure 7.15 A quenched sample of $x = 0.50$ at $1000\text{ }^{\circ}\text{C}$:

- (a) Impedance complex plane, Z^* plots and spectroscopic plots (b) Y' , (c) C' ,
 (d) $-Z''$ and M'' at 21 and $50\text{ }^{\circ}\text{C}$

The Arrhenius plots (figure 7.16) show three linear parallel lines overlapping each other, with similar activation energy of 0.43 (1) eV, within errors. The conductivity for composition $x = 0.20$ is independent of quench temperature between 700 to 1000 °C.

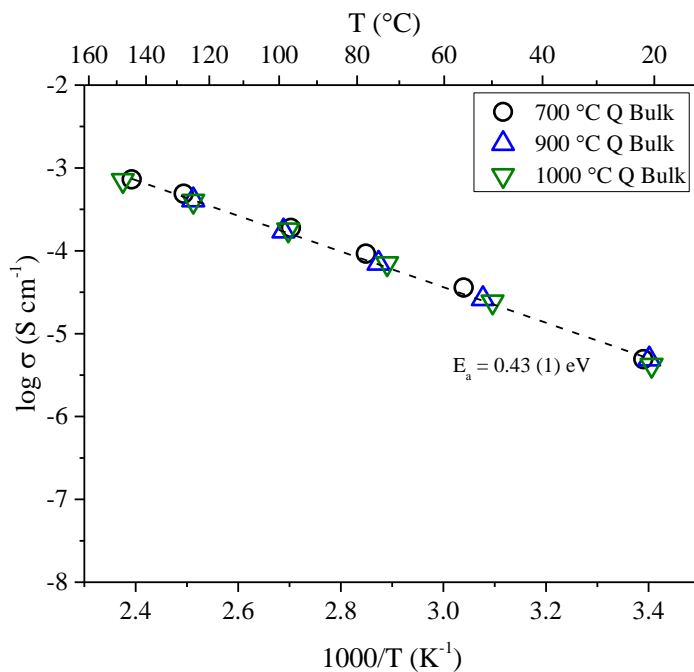


Figure 7.16 Arrhenius plots of $x = 0.50$ Mg_xMn_{1-x}O_δ quenched at 700, 900 and 1000 °C showed the same activation energy, $E_a = 0.43$ (1) eV

7.4.2 Effect of composition on conductivity of C2 cubic solid solution

Impedance spectroscopy was conducted on samples of $x = 0.60, 0.70$ and 0.80 . The pellets were heated at $1000\text{ }^\circ\text{C}$ for 10 h and quenched into liquid nitrogen. Data were collected over temperature range 20 to $200\text{ }^\circ\text{C}$.

The Z^* plot of $x = 0.60, 0.70$ and 0.80 with their respective spectroscopic Y' , C' and $-Z''$, M'' plots are shown in figure 7.9, and figure 7.10 respectively.

The Z^* plots for $x = 0.60$ show similar characteristics to the $x = 0.50$ quenched at $1000\text{ }^\circ\text{C}$ (figure 7.15). For composition $x = 0.70$, a large depressed semicircle was observed at intermediate frequency which could be represented by a two components of parallel RC elements, followed by a small semicircle at low frequency attributed to the grain boundary response. At $x = 0.80$, only a single depressed semicircle was observed which could be attributed to the bulk and grain boundary response.

The Y' plots against frequency show two plateaux at low and intermediate frequency for $x = 0.60$, followed by a small dispersion at high frequency for data collected at $20\text{ }^\circ\text{C}$. For composition $x = 0.70$, two nearly similar plateaux were observed particularly at $20\text{ }^\circ\text{C}$, followed by a high frequency dispersion. At $x = 0.80$, a single plateau was observed with a dispersion at high frequency.

The C' plots as a function of frequency, for $x = 0.60$ show two plateaux at high and intermediate frequency attributed to the bulk ($\sim 10^{-12}\text{ F cm}^{-1}$) and grain boundary ($10^{-8} \sim 10^{-9}\text{ F cm}^{-1}$) response respectively. For composition $x = 0.70$, the high frequency plateau was shifted out of the measure window, followed by an unresolved plateau at $\sim 10^{-11} \sim 10^{-12}\text{ F cm}^{-1}$. A lower frequency plateau was observed at $\sim 10^{-11}\text{ F cm}^{-1}$ which could be attributed to the grain boundary response. At $x = 0.80$, two plateaux were observed at high and low frequency attributed to the bulk and grain boundary response. Data collected at room temperature for $x = 0.70$ and 0.80 show a continuous dispersion (without noisy data) at a lower frequency which could be associated with a protonic conduction due to moisture adsorption onto the sample surface. As the measured temperature increased, the moisture dissipated and the sample become resistive at lower frequency.

The Z'' and M'' versus frequency plots for $x = 0.60$ does not show the overlapping peak maxima of Z'' and M'' since it is shifted out of the measured windows. However, a small peak was observed for Z'' at intermediate frequency which could be attributed to the grain boundary response. For composition $x = 0.70$, the separated peak maxima of Z'' and M'' by a decade could indicate a two components of parallel RC element, followed by a small peak at $\sim 10^2$ Hz which could be attributed to the grain boundary response. At $x = 0.80$, the well separated peak maxima of Z'' and M'' indicating the bulk and grain boundary response at high and low frequency respectively.

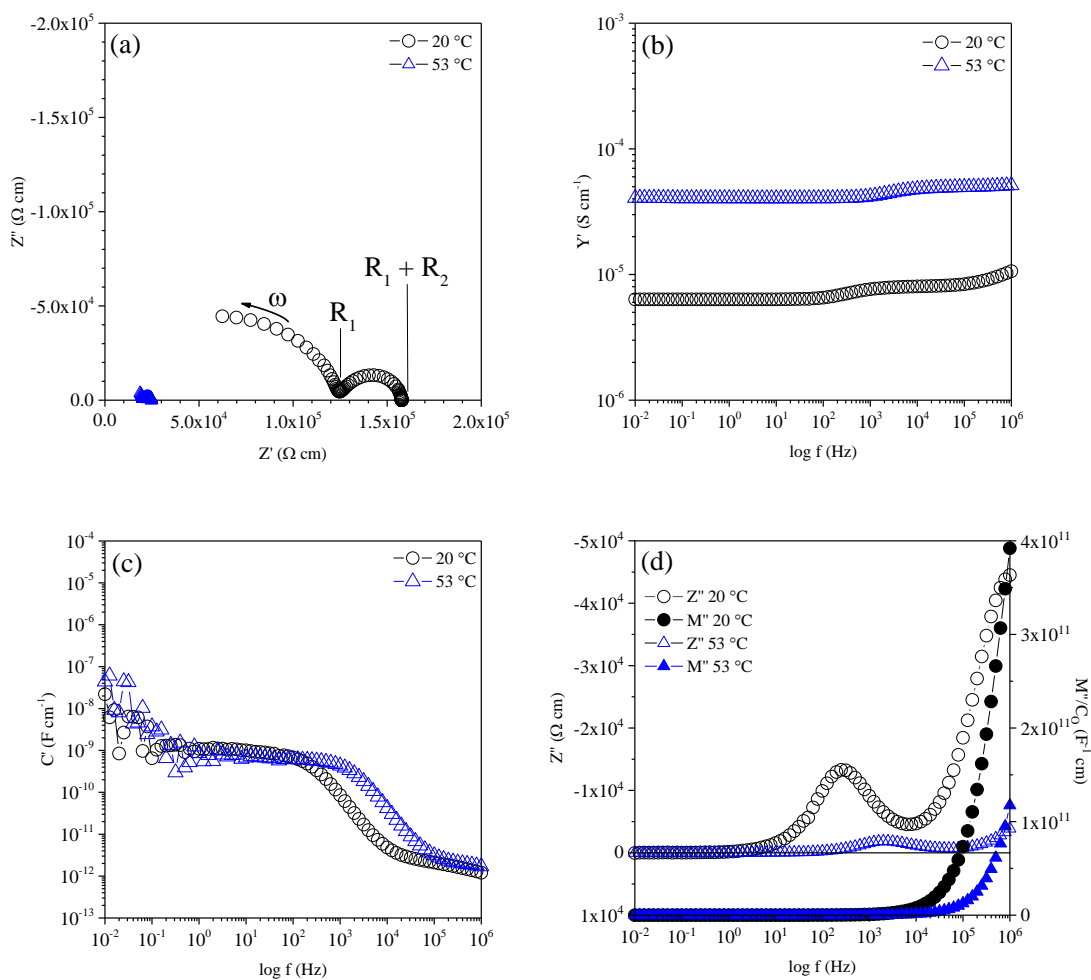


Figure 7.17 A quenched sample of $x = 0.60$ at $1000\text{ }^\circ\text{C}$:

- (a) Impedance complex plane, Z^* plots and spectroscopic plots (b) Y' , (c) C' ,
 (d) $-Z''$ and M'' at 20 and $53\text{ }^\circ\text{C}$

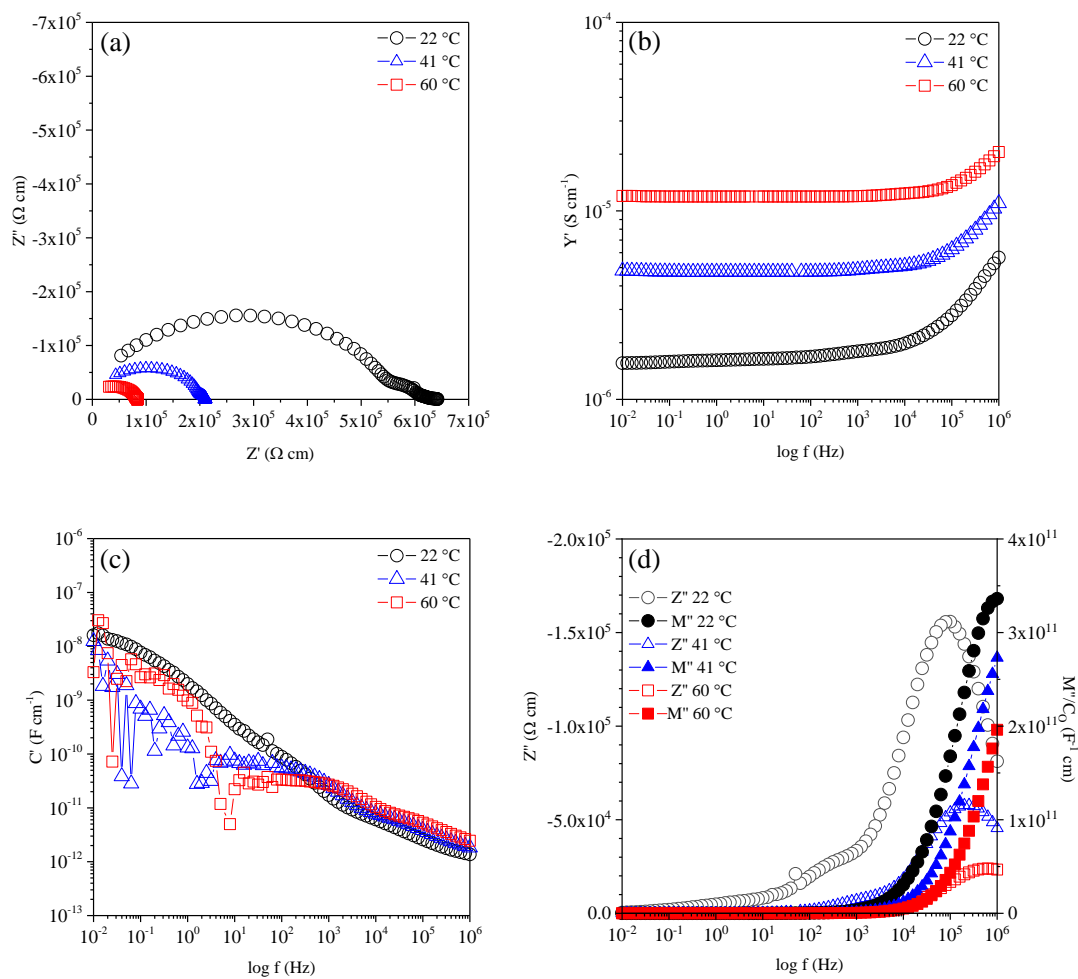


Figure 7.18 A quenched sample of $x = 0.70$ at $1000\text{ }^{\circ}\text{C}$:

- (a) Impedance complex plane, Z^* plots and spectroscopic plots (b) Y' , (c) C' ,
 (d) $-Z''$ and M'' at $22, 41$ and $60\text{ }^{\circ}\text{C}$

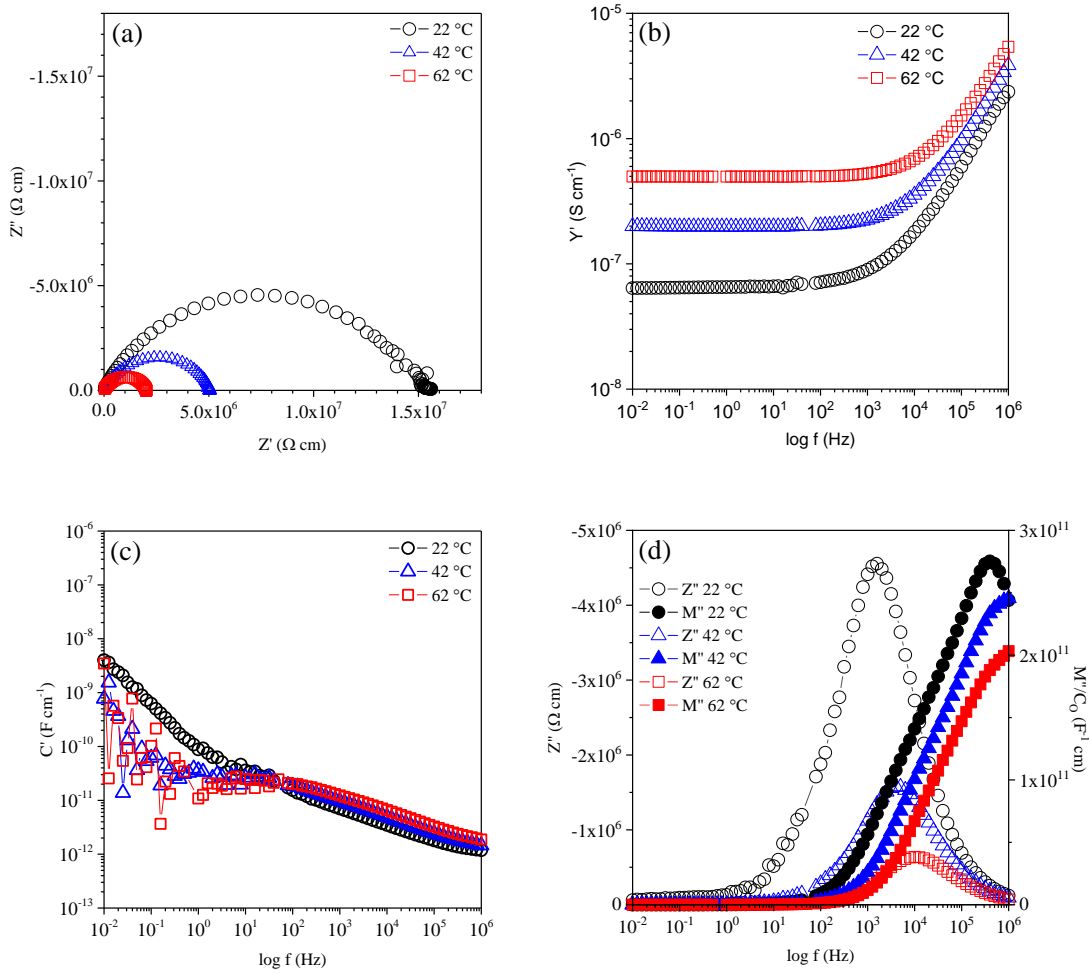


Figure 7.19 A quenched sample of $x = 0.80$ at $1000\text{ }^\circ\text{C}$:

- (a) Impedance complex plane, Z^* plots and spectroscopic plots (b) Y' , (c) C' ,
 (d) $-Z''$ and M''

The Arrhenius plots (figure 7.20) show linear behaviour for all samples. The conductivity increases with increasing x up to $x = 0.50$, before it decreases until $x = 0.80$. The highest conductivity measured at room temperature is shown by $x = 0.50$ with $\sigma = 4.2 \times 10^{-6} \text{ S cm}^{-1}$. The C2 samples have the same activation energy as T2 samples of $0.42 \sim 0.44 \text{ eV}$.

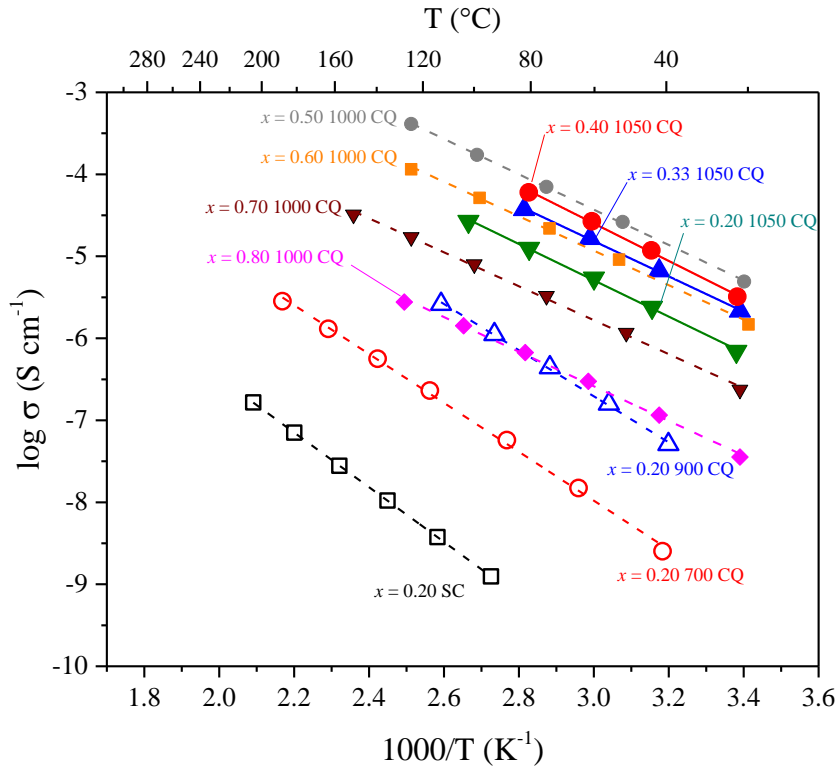
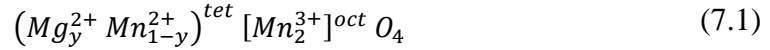


Figure 7.20 Arrhenius plots comparison between T1, T2 and C2 cubic solid solution. T1 represented by open symbols of $x = 0.20$ at different temperatures. T2 represented by closed symbols with solid lines: $x = 0.20, 0.33$ and 0.40 quenched (Q) from $1050 \text{ }^\circ\text{C}$. C2 represented by closed symbols with dash lines: $x = 0.50, 0.60, 0.70$ and 0.80 quenched from $1000 \text{ }^\circ\text{C}$. Not shown here are the plots of slow-cooled (SC) T1 of $x = 0.05$ and 0.10 since they overlap with the slow-cooled T1 $x = 0.20$

7.5 Discussion

The electrical properties of cubic, C2 and tetragonal polymorphs (T1 and T2) solid solutions, under various conditions, have been studied by impedance spectroscopy. In the T1 domain, for samples $x = 0.05, 0.10$ and 0.20 of $Mg_xMn_{1-x}O_\delta$, the measured conductivity was relatively similar with activation energies of 0.662 (1) to 0.687 (7) eV. It was clear that from the structural analysis on T1 samples (section 5.2.3), that Mn (presumably Mn^{2+}) on the tetrahedral site was partially replaced by Mg^{2+} through isovalent substitution $0.05 \leq x \leq 0.20$. Following the same trend, it was expected that a complete substitution of Mn^{2+} ions at the tetrahedral site would occur at $x = 0.33$. The proposed chemical compensation is therefore:

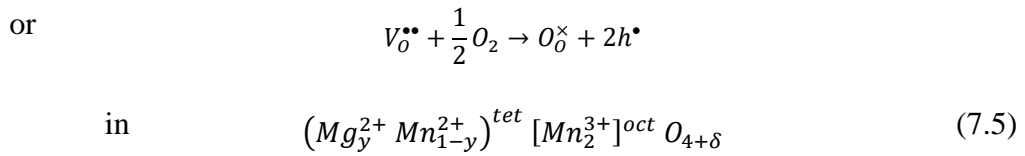
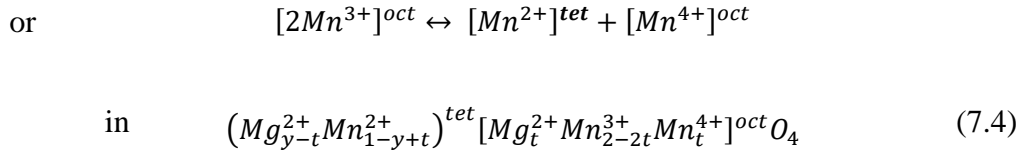
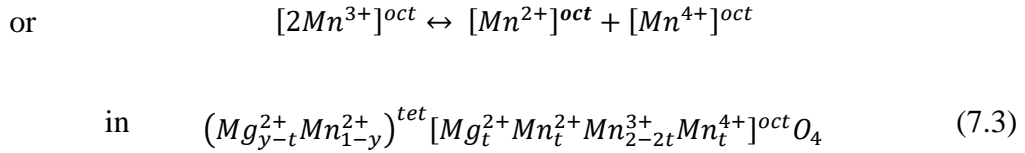


where y represents Mg content.

The conductivity, therefore, is independent of the number of Mn^{2+} ions in the tetrahedral sites. Since a decrease in conductivity was not observed with decreasing Mn^{2+} content, it can be concluded that the electronic conduction between the tetrahedral sites and also between tetrahedral and octahedral sublattices is negligible. Therefore, any conductivity within the spinel T1 and T2 domain could only occur on the octahedral sites, the conduction on tetrahedral site is less favorable due to a longer hopping distance between neighboring sites.

When the same pellet with composition $x = 0.20$ was re-heated and quenched from three different temperatures, $700, 900$ and 1050 °C, an increase in conductivity was observed with an activation energy of 0.59 (1), 0.56 (1) and 0.44 (1) eV respectively. Possible mechanisms, ideally, include:





where t represents the number of cations involved in site-exchange.

Mechanism (7.2) is highly unlikely for the reasons described earlier. Since the possibility of oxygen loss is negligible (table 4.6), the mechanism (7.5) thus can be excluded. Therefore, the increase in conductivity with temperature could involve migration of Mg^{2+} ions to the octahedral sites which appears to trigger disproportionation of Mn^{3+} ions as shown by mechanisms (7.3) and (7.4). The presence of mixed valence of Mn at the octahedral sites provides a conduction pathway for electron or hole hopping. However, the mechanism (7.3) would result in occupancy at the tetrahedral sites to be less than fully occupied, no such conditions were observed based on the refinement data (table 5.8). Since Mn^{3+} and Mn^{4+} ions both have high octahedral sites preference, it can be assumed that the Mn^{2+} ions in the octahedral sites would then migrate to the tetrahedral sites instead of Mn^{3+} and Mn^{4+} ions. This suggest that the mechanism (7.4) is highly likely to occur with increasing temperature.

Within the T1 domain, it was shown by the refinement data that the site exchange is negligible (table 5.8). However, there is still a possibility that the Mn at the octahedral sites has a mixed valency.

Conductivity is governed by the equation:

$$\sigma = n q \mu \quad (7.6)$$

where : σ = conductivity

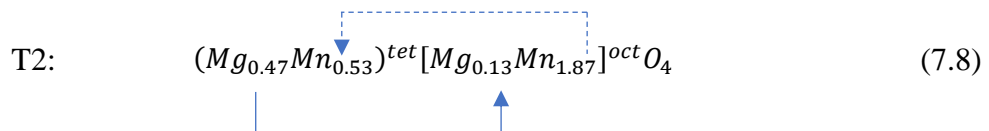
n = number of mobile charge carrier

q = electronic charge (1.602×10^{-19} C)

μ = mobility of charge carrier (temperature dependent)

Since the samples at 700 and 900 °C has the same activation energy, within errors, the increase in conductivity with temperature is governed by the charge carrier mobility.

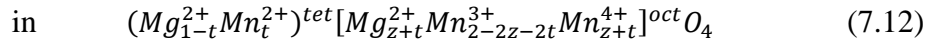
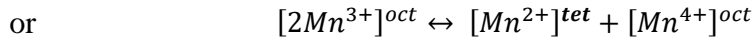
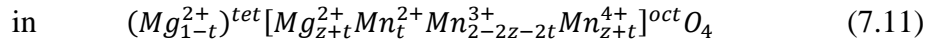
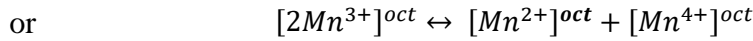
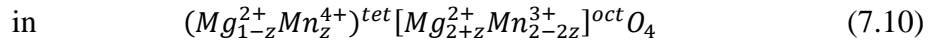
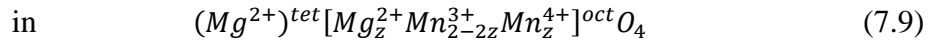
For $x = 0.20$ quenched from 1050 °C, the increase in conductivity compared to T1 is probably due to mechanism (7.4) as shown by the refinement result in table 5.11 The structural analysis shows a possible site-exchange had occurred with a degree of inversion, $\gamma = 0.13$. The refined chemical formula between T1 (room temperature) and T2 (1050 °C) as shown:



The effect of conductivity with composition was further investigated with $x = 0.20, 0.33, 0.40, 0.50, 0.60, 0.70$ and 0.80 . A steady increase in conductivity (~ 1 order of magnitude) was observed with increasing x to a maximum at $x = 0.50$.

The conductivity for sample $x = 0.50$ does not vary with temperature indicating that the conductivity is intrinsic rather than extrinsic, therefore the effect of oxygen activity is negligible.

At $x = 0.33$, it is expected that all Mn^{2+} ions at the tetrahedral site has been replaced by Mg^{2+} ions. Another compensation mechanism is needed for $x \geq 0.33$. It was proposed that two Mn^{3+} ions is replaced by a pair of Mg^{2+} and Mn^{4+} ions. Therefore, an increase in conductivity is expected as the charge concentration carrier, Mn^{3+} - Mn^{4+} pair increases with increasing x at the octahedral site. The possible mechanisms, include:



where z represents Mg content.

t represents the number of cations involved in site-exchange.

Of these four mechanisms, (7.12) is more likely since it shows the site exchange with mixed valence of Mn at octahedral site and full occupancy at the tetrahedral site.

The similarities in activation energy (0.40 ~ 0.44 eV) of these samples indicate that the mobility of the charge carrier is similar. Hence, the increase in conductivity could be attributed to the increase in number of mobile charge carrier present in the samples.

A direct relationship exists between the charge concentration carrier and the electrical properties. On the basis of this relationship, a cation concentration distribution, based on site exchange was plotted with increasing x (figure 7.21). Data were taken from the refinement results in chapter 5, and the cation distributions were calculated based on the number of Mg^{2+} ions migrated from tetrahedral to the octahedral sites.

An increase in conductivity with increasing x ($0.20 \leq x \leq 0.50$) was observed, as shown by the gradual increase in number of $\text{Mn}^{3+}\text{-Mn}^{4+}$ pairs at the octahedral site. This is consistent with the conductivity data shown by the Arrhenius plot (figure 7.20). A small ‘kink’ was observed at $x \sim 0.33$ probably due to two different conduction mechanisms, (7.4) and (7.12) for high temperature T2 and cubic spinel

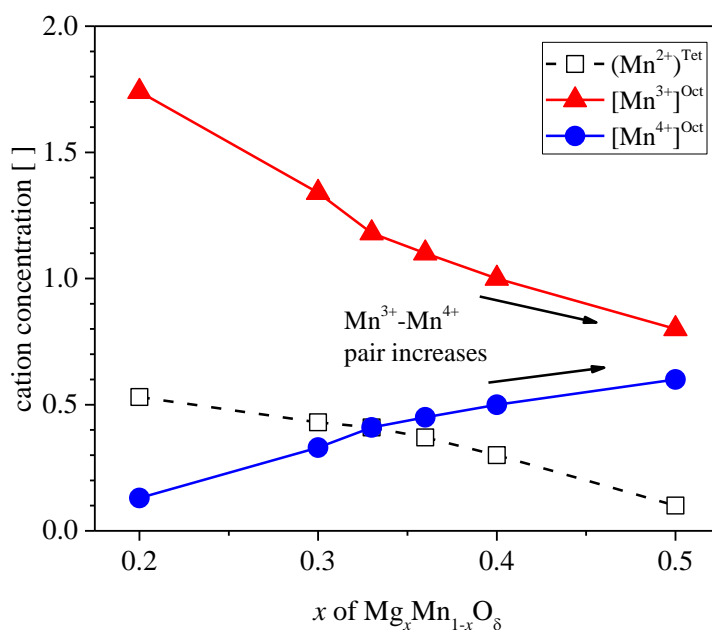


Figure 7.21 A cation concentration from refinement data, distributed based on site-exchange and disproportionation reaction ($2\text{Mn}^{3+} \rightarrow \text{Mn}^{2+} + \text{Mn}^{4+}$)

7.6 Conclusions

The electrical properties of T1, T2 and C2 have been measured, under various conditions. It is clear that the conductivity on tetrahedral sites is highly unlikely due to the longer jump distance between neighbouring sites.

The electrical properties within T1 domain remain unchanged with increasing x . However, an increase in conductivity was observed with increasing temperature. This is probably due to the presence of small amount of mixed valence of Mn at the octahedral site.

An increase in conductivity by four orders of magnitude was observed for sample $x = 0.20$, between room temperature, T1 and high-temperature T2 (at 1050 °C). This increase in conductivity is mainly due to the increase in mobile charge carrier concentration (Mn³⁺-Mn⁴⁺ pair) at the octahedral site as a result of site exchange and disproportionation reaction.

An increase in conductivity within T2 domain was also observed with increasing x up to $x = 0.50$. Beyond $x = 0.50$, the electrical conductivity decreases. Two possible conduction mechanisms were proposed, (7.4) for $x < 0.33$ and (7.12) for $x \geq 0.33$.

7.7 References

1. Dorris, S. and T.O. Mason, *Electrical properties and cation valencies in Mn_3O_4* . Journal of the American Ceramic Society, 1988. **71**(5): p. 379-385.
2. Metselaar, R., R. Van Tol, and P. Piercy, *The electrical conductivity and thermoelectric power of Mn_3O_4 at high temperatures*. Journal of Solid State Chemistry, 1981. **38**(3): p. 335-341.
3. Keller, M. and R. Dieckmann, *Defect Structure and Transport Properties of Manganese Oxides:(II) The Nonstoichiometry of Hausmannite ($Mn_{3-\delta}O_4$)*. Berichte der Bunsengesellschaft für physikalische Chemie, 1985. **89**(10): p. 1095-1104.
4. Driessens, F., *Place and valence of the cations in Mn_3O_4 and some related manganates*. Inorganica Chimica Acta, 1967. **1**: p. 193-201.
5. Rosenberg, M. and P. Nicolau, *Electrical properties and cation migration in $MgMn_2O_4$* . physica status solidi (b), 1964. **6**(1): p. 101-110.
6. Malavasi, L., P. Ghigna, G. Chiodelli, G. Maggi, and G. Flor, *Structural and transport properties of $Mg_{1-x}Mn_xMn_2O_{4\pm\delta}$ spinels*. Journal of Solid State Chemistry, 2002. **166**(1): p. 171-176.
7. Keer, H., M. Bodas, A. Bhaduri, and A. Biswas, *Electrical and magnetic properties of the $MgMn_2O_4$ - $MgAl_2O_4$ system*. Journal of Physics D: Applied Physics, 1974. **7**(15): p. 2058.

Chapter 8: Conclusions and future work

8.1 Mg-doped Li_2MnO_3

Li_2MnO_3 has been successfully doped with Mg by solid state reaction using two possible solid solution formulae, $\text{Li}_{2+2m}\text{Mg}_m\text{Mn}_{1-m}\text{O}_3$ and $\text{Li}_2\text{Mg}_m\text{Mn}_{1-m}\text{O}_{3-m}$, $0 \leq m \leq 0.10$. The proposed charge compensation in the second mechanism involves the creation of oxygen vacancies but without change in Li content, and it is expected that Mn^{4+} would be partially reduced to Mn^{3+} to maintain electroneutrality.

An increase in electrical conductivity for the Mg-doped samples was observed and is likely to be attributed to the presence of $\text{Mn}^{3+}\text{-Mn}^{4+}$ pair, as a result of either oxygen vacancy creation and/or Mg substitution. Further loss of oxygen, shown by quenching samples from higher temperatures, resulted in additional increase in electronic conductivity, as the number of $\text{Mn}^{3+}\text{-Mn}^{4+}$ pairs increases.

The electrical properties of Mg-doped Li_2MnO_3 are, therefore, dependent on the oxygen content, and the number of mobile charge carrier associated with $\text{Mn}^{3+}\text{-Mn}^{4+}$ pairs.

8.2 Phase diagram of the $\text{MnO}_\delta\text{-MgO}$ system

A pseudo-binary phase diagram of the system $\text{MnO}_\delta\text{-MgO}$ has been constructed. It shows three large single-phase solid solution regions: tetragonal spinel, T1; cubic spinel, C1; Suzuki phase solid solution, C2. The presence of C1 solid solution could only be determined by *in-situ* HTXRD, as quenching from high temperature resulted in a rapid transformation from C1 to tetragonal spinel, T2, which is believe to be a metastable phase. Due to this, it can be assumed that the cation site occupancies of C1 and T2 are likely to be the same since there may be insufficient time for them to be redistributed.

Both T1 and T2 have the same tetragonal structure but T2 has slightly smaller c/a ratio. Crystallographic studies confirmed that site exchange exists in the T2 structure,

whereby Mg^{2+} ions are distributed over both tetrahedral $4b$ - and octahedral $8c$ -sites. As a direct consequence, the number of Mn^{3+} ions in the octahedral sites is reduced, which are responsible for the Jahn-Teller distortion of the tetragonal structure.

At a much slower cooling rate, T1 appears, as there is sufficient time for the cations to be redistributed, and the Mg^{2+} ions are thus located only at the tetrahedral $4b$ -sites.

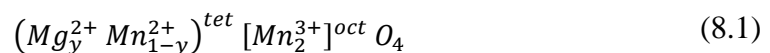
It is yet to be determined whether the single exothermic peak observed by DSC on cooling corresponds to the transition of $C1 \rightarrow T1$ directly or $C1 \rightarrow T2$. Nevertheless, the rapid nature of the $C1 \rightarrow T2$ transition is proposed due to the collective orientational distortion of $Mn^{3+}O_6$ octahedra in the direction that maximized the Jahn-Teller effect. At lower temperature, the slower $T2 \rightarrow T1$ transition is proposed due to cation site exchange between tetrahedral and octahedral sites.

Within the Mg-rich region, the Suzuki phase C2 solid solution was observed over the entire range $0.50 \leq x \leq 0.80$ over the range $900 \sim 1000$ °C. Below this temperature, an immiscibility dome of two cubic phases exists with an upper consolute temperature ~ 850 °C. The cubic spinel C1 solid solution is therefore, expected to be limited to a maximum at composition $x \sim 0.50$.

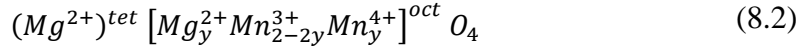
8.3 Structural analysis of T1 and T2 solid solution

Crystallographic studies on Mn_3O_4 suggested that the tetrahedral $4b$ - and octahedral $8c$ -sites were occupied by Mn^{2+} and Mn^{3+} ions respectively. This was shown by the result of the structural refinement and their respective calculated bond lengths.

Structural refinements on T1 samples for compositions $x = 0.05, 0.10$ and 0.20 of $Mg_xMn_{1-x}O_8$ showed that the Mn^{2+} ion had been replaced by Mg^{2+} ions at the tetrahedral sites, leaving the octahedral sites fully occupied by Mn^{3+} ions. The compensation mechanism was therefore proposed to be:

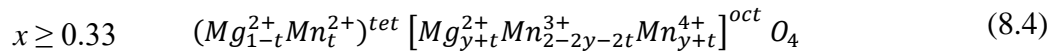
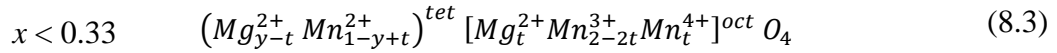


This compensation mechanism is however, limited to a maximum of $x = 0.33$. Beyond $x = 0.33$, another compensation mechanism was expected, $Mn^{3+} \rightarrow Mg^{2+} + Mn^{4+}$.



Structural refinement on T2 samples for compositions $x = 0.20, 0.30, 0.33, 0.36$ and 0.40 of $Mg_x Mn_{1-x} O_\delta$ showed that a partial site exchange occurred between tetrahedral and octahedral sites. The migration of Mg^{2+} ions from the tetrahedral to octahedral sites appears to trigger a disproportionation reaction, $2Mn^{3+} \rightarrow Mn^{2+} + Mn^{4+}$, shown by the electrical property measurements. The Mn^{2+} ions then reciprocate and migrate to the tetrahedral sites.

Therefore, the T2 site exchange compensation mechanisms are proposed to be:



where y represents Mg content

t represents number of cations involved in site exchange.

8.4 Structural analysis on cubic spinel-Suzuki phase, C2 solid solution

The C2 space group was determined to be $Fm\bar{3}m$ using ND data as shown by the extra reflections at (200), (440) and (640), which do not satisfy the rule of reflections to be observed for the d -glide plane symmetry of $Fd\bar{3}m$ space group.

Although C2 has cubic symmetry, the structural refinement faces some challenges since it has partially occupied sites due to cation vacancies, mixed cation valency and anion vacancies. There is a possibility that Mg, Mn and vacancies are present at each of the tetrahedral $32f$ - and octahedral $24d$ -sites, thus refining three variables at any one site is impossible. As a result, the Mg:Mn ratio of C2 solid solution and their compensation mechanism(s) could not be determined conclusively.

8.5 Electrical properties of T1, T2 and C2 solid solutions

Impedance measurements have been conducted on T1, T2 and C2 solid solution series as a function of composition and temperature. All samples showed that the conductivity is dominated by electronic conduction with the possibility of *p*-type behaviour.

The T1 conductivity does not change with composition but increases with increasing temperature. This is probably due to the presence of a small amount of mobile charge carrier (holes) in the sample and the increase in conductivity with temperature is due to the increased mobility of the charge carrier.

The T2 samples have higher conductivity than T1 at any given composition. This was attributed to the partial site exchange between tetrahedral and octahedral sites as explained in section 8.3. The conductivity of T2 also increased with increasing x , with the highest conductivity observed at $x = 0.50$ (C2). This is probably because this composition has the highest concentration of Mn^{3+} - Mn^{4+} pair for hole hopping.

The proposed chemical compensation mechanisms for T2 are shown by equations (8.3) and (8.4).

Beyond $x = 0.50$, the conductivity decreases with further increase in x probably due to the decrease in mobile charge carrier.

8.6 Suggestion for future work

8.6.1 Mg-doped Li_2MnO_3

It has been reported in this thesis that there are uncertainties related to the synthesis condition that might result in the possibility of either Li_2O loss and/or oxygen loss, both of which occur during heat treatment. A small amount of Li_2O loss will generally result in different stoichiometry of Li:Mn ratio. Any loss of oxygen will result in a partial reduction of Mn^{4+} to Mn^{3+} . Therefore, an alternative synthesis method without using any heat treatment is preferred such as mechanosynthesis (attrition ball mill) that uses high-energy ball milling for reaction to occur at room temperature. Substitute ion of oxygen with monovalent anions such as F^- , would probably result in a similar partial reduction of Mn^{4+} to Mn^{3+} for charge compensation.

It has been suggested that an increase in electrochemical properties is expected due to the presence of Mn^{3+} ions and thus it would be interesting to investigate the electrochemical behaviour of Mg-doped Li_2MnO_3 as potential cathode materials.

8.6.2 $\text{Mg}_x\text{Mn}_{1-x}\text{O}_8$

Attempts to prepare stoichiometric composition of Mg_6MnO_8 has not been successful by using solid state reaction. The use of an alternative synthesis route without the use of heat treatment such as mechanosynthesis could provide a better result. Preparation of Mg_6MnO_8 in high oxygen partial pressure could also avoid any reduction of Mn oxidation states at high temperatures.

The transition from T2 to C2 has been proposed to be reduced in tetragonality. However, there is uncertainty whether this transition is a morphotropic or a mixture of two-phase region. Further synthesis, quenching at different temperature and phase analysis thus necessary to fully characterize this region.

The structural analysis on T2 showed a partial site exchange exists between tetragonal and octahedral sites, the extent of which varies with x . It is still unclear what governs the site exchange to occur partially. It would be interesting to investigate the effect on T2 of increasing temperature.

Appendices

Part A Spinel types

The spinel structure can be classified into two types: normal spinel and inverse spinel. This section is summarised from the book: *Solid-state chemistry and its applications: second edition* by Anthony R West ^[1].

1.1.1 Normal spinel structure

The normal spinel structures have a general formula of AB_2X_4 , where A and B cations can have various combinations of cation charge but with overall cation:anion ratio of 3:4. Generally, spinels exhibit a large cubic unit cell with formula unit, $Z = 8$, corresponding to $A_8B_{16}X_{32}$ (figure 9.1). For every octahedral site, there are two interstitial tetrahedral sites (T_+ and T_-) (figure 9.2). Therefore, in a cubic close packed (*ccp*) oxide array, one-eighth of the tetrahedral sites are occupied by A, and half of the octahedral sites are occupied by B. Thus, the A cations typically have smaller ionic radius compared to B cations since tetrahedral interstices are smaller than the octahedral sites. An example of a normal spinel structure oxide is $LiMn_2O_4$, Mn_3O_4 and $MgMn_2O_4$ ^[2].

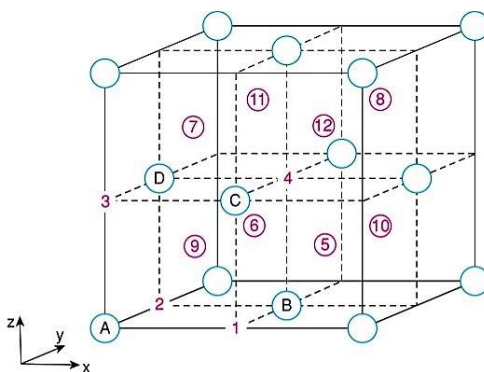


Figure 9.1 Face centered cubic (*fcc*) anion array (blue circle) with available cation sites. The number 1-4 and 5-12 referred to octahedral and tetrahedral sites respectively. The cation number 9 is tetrahedrally coordinated with anions A-D ^[1]

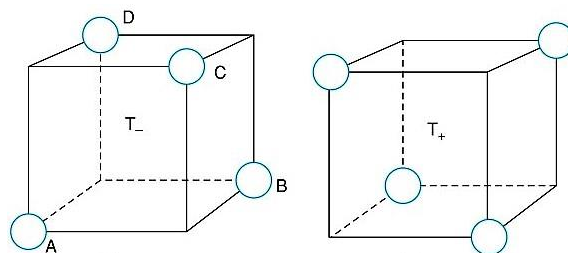


Figure 9.2 Two possible tetrahedral sites T_+ , T_- with respect to *fcc* anion array in figure 2.6 ^[1]

The spinel LiMn_2O_4 has been commercialized as cathode material in the LIB industry. It has monovalent lithium occupying tetrahedral sites and manganese occupying the octahedral sites with the Mn average oxidation state of +3.5 ^[3].

The spinel ss Mn_3O_4 and MgMn_2O_4 have divalent A^{2+} and trivalent B^{3+} cations occupying the tetrahedral and octahedral sites respectively. In the case of Mn_3O_4 , the manganese has two possible oxidation states and the composition could be rewritten as $(\text{Mn}^{2+})^{tet}[\text{Mn}^{3+}]_2^{oct}\text{O}_4$. Therefore, for a normal spinel structure, the general formula can be denoted as $(A)^{tet}[B]_2^{oct}X_4$ ^[2].

1.1.2 Inverse spinel structure

The inverse spinel structure occurs when there is different cation distribution than in normal spinel structure. This (extreme) cation distribution results in all A cations occupying the octahedral site and half of the B cations occupying the tetrahedral site, creating a mixture of A and B on the octahedral site. The distribution of A and B at the octahedral site is usually random. Therefore, the inverse spinel structure can be described by the general formula $(B)^{tet}[AB]^{oct}X_4$. An example of an inverse spinel structure is Mg_2MnO_4 which can be rewritten as $(\text{Mg}^{2+})^{tet}[\text{Mg}^{2+}\text{Mn}^{4+}]^{oct}\text{O}_4$ ^[2].

In between these two extremes, a variation of A and B distribution over both tetrahedral and octahedral sites is possible. This intermediate distribution may be quantified by a parameter known as the degree of inversion, γ , corresponding to the amount of A ions which have migrated from the tetrahedral site into the octahedral site (table 9.1).

Table 9.1 Spinel type, general formula and inversion degree ^[1]

Spinel Type	General formula	Inversion degree, γ
Normal	$(A)^{tet}[B_2]^{oct}X_4$	0
Inverse	$(B)^{tet}[A, B]^{oct}X_4$	1
Random	$(A_{0.33}B_{0.67})^{tet}[B_{1.33}A_{0.67}]^{oct}X_4$	0.67

1.1.3 Jahn-Teller distortions in a spinel structure

The spinel structure usually exists in the cubic form but it is known that it can often show some tetragonal distortion which is attributable to a different length of one of its cell edges, from the other two. The lengthening or shortening of this cell edge in a spinel structure is a consequence of the Jahn-Teller effect ^[4].

1.1.3.1 Octahedral coordination

In an octahedral environment, the five d orbitals are not degenerate (due to the presence of ligand or anion) and split into two groups: the t_{2g} group of lower stabilized energy and the e_g group of higher destabilized energy (9.3). The lower t_{2g} group consists of three orbitals: d_{xy} , d_{xz} and d_{yz} and the higher e_g group consists of two orbitals: $d_{x^2-y^2}$ and d_z^2 . The e_g orbitals are of higher energy (relative to t_{2g}) since they directly interact with the surrounding ligands (figure 9.4).

In the presence of electrons, according to Hund's rule, the orbitals are filled singly with electrons in order to maximize multiplicity (i.e. increase the number of unpaired electrons). Therefore, two possible configurations exist for d^4 to d^7 (d refer to orbital and the superscript refer to the number of electrons) elements in the transition metal group: low-spin (LS) and high-spin (HS) states.

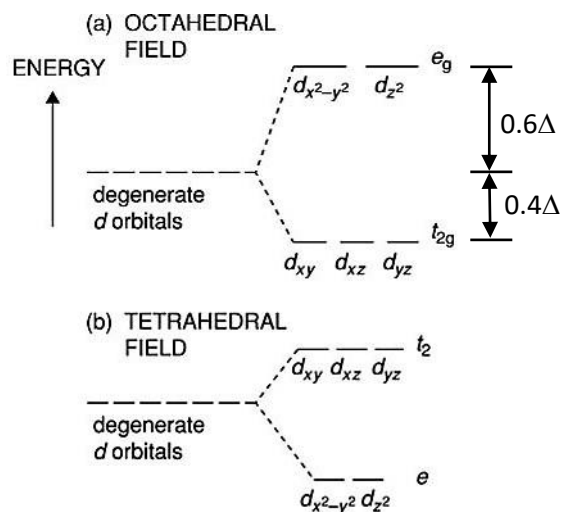


Figure 9.3 The splitting of *d* orbitals and their respective energy levels in (a) octahedral and (b) tetrahedral coordination ^[1]

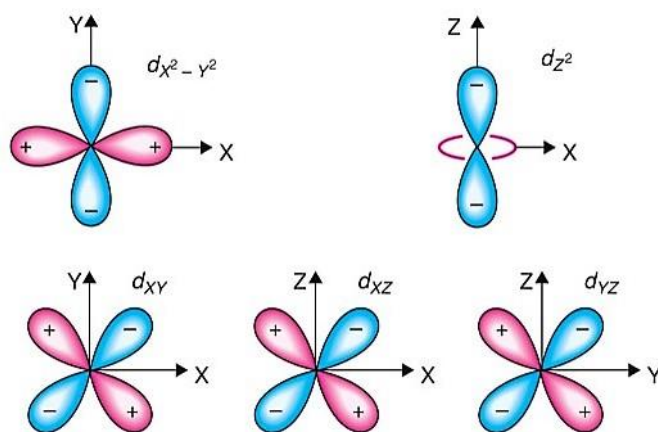


Figure 9.4 The five *d* orbitals in octahedral coordination. The three orbitals d_{xy} , d_{xz} and d_{yz} lie in-between their respective axes at 45° angle. The two orbitals $d_{x^2-y^2}$ and d_{z^2} point directly to the ligand on their respective axes ^[1]

The splitting of d orbitals results in the energy difference, Δ , between t_{2g} and e_g . The total energy of the five orbitals is the same after the splitting which means that the t_{2g} orbitals are stabilized by 0.4Δ and the e_g orbitals are destabilized by 0.6Δ , both relative to the five degenerate orbitals without splitting (figure 9.3). In order to put an electron in e_g orbitals, Δ must be balanced with the pairing energy, P . The pairing energy refer to the amount of energy needed to pair up electrons in the same orbitals.

Consider a d^4 ion Mn^{3+} in an octahedral complex. The first three electrons will occupy the t_{2g} orbitals one in each and be parallel to each other as expected from Hund's rule. For the fourth electron, there are two possibilities. It can occupy the e_g orbitals giving rise to a HS state or it can occupy one of the three t_{2g} orbitals, pairing up with an electron that already there, giving rise to LS state. The two set of configurations can be denoted as: HS $(t_{2g})^3 (e_g)^1$ or LS $(t_{2g})^4 (e_g)^0$.

In order to know which of the spin complexes is more favorable, a crystal field stabilization energy (CFSE) can be calculated for the two possibilities. For the d^4 HS state, the CFSE is $3 \times 0.4\Delta - 1 \times 0.6\Delta = 0.6\Delta$. For the LS state, the CFSE is $4 \times 0.4\Delta - 0 \times 0.6\Delta = 1.6\Delta + P$, where P is the pairing energy of one pair of electrons. Therefore, which of these possibilities is favoured depends on the relative magnitude of Δ and the value of P . If $P > \Delta$, the electron will occupy the e_g orbitals, hence the HS state and *vice versa*.

In the HS state, the electron can occupy either $d_{x^2-y^2}$ or d_z^2 orbitals. Since the electrons occupy unequally the e_g orbitals, they are no longer degenerate and split into two energy levels (figure 9.5). It is not clear which of the two e_g orbitals is preferable. If the electron preferred the d_z^2 orbital, this orbital will experience stronger repulsion and the two metal-ligand bond length increases in the direction of the singly occupied d_z^2 orbital, i.e. lengthening of the z -axis in respect to the other four metal-ligand bonds. As a consequence, the energy of the d_z^2 orbital is lower than the unoccupied $d_{x^2-y^2}$ orbital, which stabilized by the amount of $\frac{1}{2}\delta_2$ relatives to the normal degenerate e_g orbitals. The d_{xz} and d_{yz} orbitals in the t_{2g} level will also experience an almost similar effect since they are indirectly connected to the z -axis, unlike the d_{xy} orbital. The lowering of the energy of the d_{xz} and d_{yz} orbitals is stabilized by the amount of $\frac{1}{2}\delta_1$ relative to the normal

degenerate t_{2g} orbitals. Hence the distorted spinel structure was observed which due to the odd number of electrons in the e_g orbitals. Therefore, the Jahn-Teller effect can be observed in d^4 (HS), d^7 (LS) and d^9 ions in the octahedral environment.

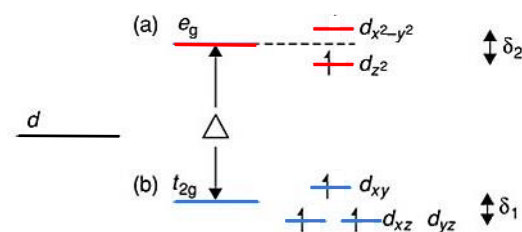


Figure 9.5 The splitting of d orbital for d^4 Mn^{3+} ion in the octahedral environment [1]

1.1.3.2 Tetrahedral coordination

In the tetrahedral environment, the splitting of the two sets of levels is reversed. The t_2 is now at the higher energy level with the three orbitals (d_{xy} , d_{xz} and d_{yz}) and e is at the lower energy with two orbitals ($d_{x^2-y^2}$ and d_z^2) (figure 9.). Note that the subscript g was omitted from the denotation for the energy level in the tetrahedral coordination.

None of the orbitals is pointed directly to their surrounding ligands, but the t_2 orbitals are much closer to the surrounding ligands than the e orbitals. Hence, the splitting of the two sets with a smaller magnitude of Δ^{tet} was observed compared to octahedral coordination. The tetrahedral complexes are normally in HS state since P is appreciably larger than Δ^{tet} . A Jahn-Teller effect can still be observed when an odd number of electrons occupy the three t_2 orbitals but may exhibit various distorted structure such as tetragonal or trigonal distortion.

1.1.3.3 Octahedral versus tetrahedral coordination

The preferred site for a transition metal ion to reside in, either in the octahedral or tetrahedral environment can be estimated based on the CFSE. Consider a HS state of d^4 ion Mn^{3+} . In the octahedral environment, the calculated CFSE is equal to $0.6\Delta^{\text{oct}}$. In tetrahedral environment, the calculated CFSE is $2 \times 0.6\Delta - 2 \times 0.4\Delta = 0.4\Delta^{\text{tet}}$. Since the magnitude of Δ^{tet} is smaller than Δ^{oct} , the preferred coordination for the Mn^{3+} ions is in the octahedral site.

$$\Delta^{\text{tet}} \approx \frac{4}{9} \Delta^{\text{oct}} \quad (9.1)$$

1.1.4 References

1. West, A.R., *Solid state chemistry and its applications*. 2014: John Wiley & Sons.
2. Chandrasekaran, S., C. Bowen, P. Zhang, Z. Li, Q. Yuan, X. Ren, and L. Deng, *Spinel photocatalysts for environmental remediation, hydrogen generation, CO₂ reduction and photoelectrochemical water splitting*. *Journal of Materials Chemistry A*, 2018. **6**(24): p. 11078-11104.
3. Ouyang, C., S. Shi, and M. Lei, *Jahn–Teller distortion and electronic structure of LiMn₂O₄*. *Journal of Alloys and Compounds*, 2009. **474**(1-2): p. 370-374.
4. Dunitz, J. and L. Orgel, *Electronic properties of transition-metal oxides—I: Distortions from cubic symmetry*. *Journal of Physics and Chemistry of Solids*, 1957. **3**(1-2): p. 20-29.